# Experimental study of carrier gas and pressure effects on homogeneous water nucleation

*Document status and date:*
Published: 27/09/2021

*Document Version:*
Publisher's PDF, also known as Version of Record (includes final page, issue and volume numbers)

*Please check the document version of this publication:*

• A submitted manuscript is the version of the article upon submission and before peer-review. There can be important differences between the submitted version and the official published version of record. People interested in the research are advised to contact the author for the final version of the publication, or visit the DOI to the publisher's website.
• The final author version and the galley proof are versions of the publication after peer review.
• The final published version features the final layout of the paper including the volume, issue and page numbers.

[Link to publication](#)

# *Experimental study of carrier gas and pressure effects on homogeneous water nucleation*

M.M. Campagna

*Experimental study of carrier gas and pressure effects on homogeneous water nucleation*

PROEFSCHRIFT

ter verkrijging van de graad van doctor aan de Technische Universiteit Eindhoven, op gezag van de rector magnificus prof.dr.ir. F.P.T. Baaijens, voor een commissie aangewezen door het College voor Promoties, in het openbaar te verdedigen op Maandag 27 September 2021 om 16:00 uur

door

Mauro Michele Campagna

geboren te San Giovanni Rotondo (FG), Italië

Dit proefschrift is goedgekeurd door de promotoren en de samenstelling van de promotiecommissie is als volgt:

| | |
|---|---|
| voorzitter: | prof.dr. L.P.H. de Goey |
| 1$^e$ promotor: | prof.dr.ir. D.M.J. Smeulders |
| co-promotor: | prof.dr.ir. M.E.H. van Dongen |
| co-promotor: | dr. J. Hrubý (Czech Academy of Sciences) |
| leden: | prof.dr. B.E. Wyslouzil (The Ohio State University) |
| | prof.dr.ing. C. Tropea (Technical University of Darmstadt) |
| | prof.dr. A.A. Darhuber |
| | prof.dr.ir. J.A.M. Kuipers |

Het onderzoek of ontwerp dat in dit proefschrift wordt beschreven is uitgevoerd in overeenstemming met de TU/e Gedragscode Wetenschapsbeoefening.

# Summary

**Experimental study of carrier gas and pressure effects on homogeneous water nucleation**

The effects of pressure and carrier gases on homogeneous water nucleation are investigated experimentally by means of a Pulse Expansion Wave Tube (PEWT).

A novel PEWT high pressure section is first designed and tested. The main difference with earlier designs consists in a test section with flat walls, which avoids that optical windows and pressure transducers locally affect the flow field. The test section is also shorter so that less gas is needed and the duration of an experimental run is reduced. The flow phenomena are simulated with a 2D numerical model. The model correctly predicts the gas-dynamic features of the PEWT and the effects of the diaphragm opening process. Nucleation rates for water in helium at 240 K and two pressure conditions, 0.1 MPa and 1 MPa, are in good agreement with those from the earlier version of the PEWT.

With the new PEWT, homogeneous nucleation of water is investigated in argon and in nitrogen at about 240 K and 0.1 MPa, 1 MPa and 2 MPa. At high pressures, the nucleation rates increase, which can be explained by the reduction of the water surface tension due to the adsorption of carrier gas molecules at the cluster surface. At low pressure, there is not enough carrier gas available to ensure that the growing clusters are adequately thermalized by collisions with carrier gas molecules, so that the nucleation rate is lower than under isothermal conditions. Reasonable agreement between experiments and theoretical model for imperfect thermalization is found for argon and nitrogen as carrier gases. For helium as carrier gas, the observed nucleation rate decrease appears to be stronger than predicted by theory. The temperature dependence of the nucleation rates at 0.1 MPa follows the scaling model proposed in literature. Moreover, the number of water molecules in the critical clusters is determined from the experimental data according to the nucleation theorem. The results are in reasonable agreement with the Gibbs-Thomson equation, as also documented in literature. In addition, it is found that all our experimental data could be described by a correlation function based on the Classical Nucleation Theory (CNT) with empirical extrapolations of the surface tension to our experimental conditions.

Next, experiments are carried out for water in carrier gas mixtures of nitrogen with carbon dioxide molar fractions of 5%, 15% and 25% at 240 K and 0.1 MPa, 1 MPa and 2 MPa. Additional 0.1 MPa experiments are carried out at 234 K and 236 K for a water-nitrogen mixture with 25% of carbon dioxide. As pressure and carbon dioxide content are increased, the nucleation rate increases accordingly. As discussed before, this behavior is attributed to the reduction of the water surface tension by adsorption of carrier gas molecules. The experimental data

are compared with theoretical predictions based on CNT and on extrapolations of empirical surface tension data to the supercooled condition of 240 K. The extrapolation is performed on the basis of a theoretical adsorption/surface tension model, extended to multi-component mixtures. The theoretical prediction of the nucleation rate shows the expected trend, but appears to strongly overestimate the pressure and composition dependence. At 0.1 MPa, a reduction of the nucleation rates is found due to an incomplete thermalization of colliding clusters and carrier gas molecules. The observed nucleation rate decrease is supported by the theoretical model for imperfect thermalization, generalized here for nucleation in multi-component carrier gas mixtures.

The water nucleation experiments in nitrogen – carbon dioxide mixtures are used to derive the critical cluster compositions by means of the nucleation theorem. In this way, a macroscopic quantity - nucleation rate - reveals properties of clusters consisting of a few tens of molecules. Two different methods are presented. The first method is a multi-component extension of the approach used in literature for mixtures of two components. The second method is more straightforward and general. Both methods are found to lead to the same composition of the critical clusters.

# Contents

# Chapter 1

# Introduction

## 1.1 Motivation and theoretical highlights

Condensation is the well-known phase transition of a substance from gas to liquid. Condensation phenomena have been investigated for over a century,[1] but they remain an important research area with many environmental and industrial applications.[2] For the oil and gas industry, the gas-to-liquid phase transition plays a crucial role. Natural gas consists of methane, nitrogen, and numerous other components, such as carbon dioxide, heavy hydrocarbons (pentane, nonane, benzene, etc.), sulphates and water vapor. Design and performances of impurity separators,[3] or the development of devices coupling removal of contaminants and gas liquefaction, require a profound understanding of the condensation process under a large variety of conditions. Effects of condensation are also present in chemical reactors, aircraft, turbines and engine applications. In addition, a full comprehension of this phase transition is also important in modeling formation, persistence, and properties of clouds.

The condensation process can be heterogeneous or homogeneous. Heterogeneous condensation takes place when surfaces or foreign particles are present, providing the starting points for the condensation to initiate. In this case, a vapor pressure $p_v$ slightly above the saturated vapor pressure $p_s$ is sufficient to enable the gas-to-liquid phase transition. In absence of foreign particles or surfaces, aggregates of vapor molecules (clusters) must act as condensation centers and the gas-to-liquid phase transition is considered homogeneous.[1] Unlike heterogeneous condensation, a condition of strong supersaturation ($p_v \gg p_s$) must be reached. The clusters can grow (condensation) or shrink (evaporation) by catching or releasing free vapor molecules in a stochastic process. A cluster becomes critical when the probabilities of growth and decay are equal. If adequate supersaturation conditions are met in absence of foreign particles or macroscopic surfaces, the largest clusters overcome the critical size in a stochastic process of condensation and evaporation events and become growing droplets. The process of critical cluster formation is called homogeneous nucleation. The present work focuses on homogeneous nucleation of water.

A key parameter in nucleation studies is the homogeneous nucleation rate $J$, defined as the number of droplets formed per units of time and volume. This quantity depends on pressure, temperature and supersaturation $S$, which represents the driving force of nucleation and quantifies how far the actual vapor state is from its corresponding equilibrium condition. More details on the supersaturation definition can be found in Chapter 2. The homogeneous nucleation rate $J$ can be measured by experimental means. Several experimental techniques have

been used since the pioneering work of Wilson in 1897.[1] An in depth overview of these techniques was recently published by Wyslouzil and Wölk.[2] With reference to this work, the range of pressures, temperatures, supersaturations and homogeneous water nucleation rates investigated by various authors over the years is described in Sec. 1.2. The Classical Nucleation Theory (CNT)[4–10] is currently the most used model, as it provides a simple way for quantifying the homogeneous nucleation rate $J$ by means of measurable bulk (macroscopic) quantities (capillarity approximation). On the other hand, relying on the capillarity approximation remains physically unrealistic, especially for small clusters (typically few tens of molecules). As a result, the nucleation rates predicted by the CNT lead to a disagreement with the experiments by several orders of magnitude. Thus, many researchers modified and extended the CNT over the years.[10–35]

## 1.2   Experimental overview

This section focuses on the state of the art in homogeneous water nucleation studies from the experimental prospective. The range of pressures, temperatures, supersaturations and homogeneous water nucleation rates currently covered by the various authors is described. As for an in depth description of the different experimental techniques, more details can be found in the recent review paper by Wyslouzil and Wölk.[2] The various techniques can be categorized based on the way the supersaturated state is obtained.

Diffusion based methods can be static, thermal diffusion cloud chamber (TDCC), or can involve flows, laminar flow tube reactor (LFTR).[2] The TDCC was designed by Langsdorf in 1939.[36] This technique was later used by other authors[37,38] to study homogeneous water nucleation. More recent TDCC experimental data were reported by Brus *et al.* in 2008[39] and 2009[40] for water in helium between 290 K and 320 K and from 0.05 MPa to 0.17 MPa. In the two papers, the same experimental conditions were investigated applying two different techniques for measuring the nucleation rate: digital photography and image processing in one case and a photomultiplier method in the second paper. Somewhat comparable results were found. The measured nucleation rates ranged from $3 \cdot 10^4$ m$^{-3}$s$^{-1}$ to $3 \cdot 10^8$ m$^{-3}$s$^{-1}$ for supersaturation values between 2.8 and 4.3.

Homogeneous water nucleation experiments carried out with the LFTR device were reported by Mikheev *et al.* in 2002.[41] Water nucleation in helium was investigated between 210 K and 250 K at ambient pressure conditions, with measured nucleation rates ranging from $10^{10}$ m$^{-3}$s$^{-1}$ to $10^{13}$ m$^{-3}$s$^{-1}$ for supersaturations between 7 and 50. The LFTR - or equivalently called laminar flow diffusion chamber (LFDC) - was later used by Manka *et al.* in 2010[42]. They reproduced and extended the data of Mikheev *et al.*[41] up to 270 K, with nucleation rates ranging from $10^8$ m$^{-3}$s$^{-1}$ to $10^{12}$ m$^{-3}$s$^{-1}$ for supersaturations between 5 and 11. The results compared well with other literature sources at the same pressure and temperature conditions.[39–41,43–47] The LFDC was also used by Hyvärinen *et al.*[48] to analyze pressure effects, in the low pressure regime, on the water nucleation rates with helium as carrier gas. The temperature was varied from 240 K to 270 K, with the nucleation rates ranging from $10^8$ m$^{-3}$s$^{-1}$ to $10^{13}$ m$^{-3}$s$^{-1}$ for supersaturations between 4.5 and 10. At 270 K, the nucleation rates decreased by a factor 10 with decreasing the pressure from 0.2 MPa to 0.07 MPa. A smaller effect was observed at lower temperatures. They argued that this effect is due to the carrier gas acting as a better thermalizer at higher pressures.

Expansion based devices were the first techniques developed to study nucleation phenom-

ena. The expansion cloud chamber (ECC), designed by Wilson in 1897,[1] was later improved by Allard and Kassner in 1965.[49] The new design allowed to stop the nucleation process after 10-200 ms, followed by droplet growth to sizes detectable by photographic means. Quantitative nucleation rate measurements of water in helium were enabled at about 268 K and ambient pressure. Nucleation rates between $10^6$ m$^{-3}$s$^{-1}$ to $10^9$ m$^{-3}$s$^{-1}$ were obtained for supersaturations between 4.5 and 5.6. The ECC was later used by Allen and Kassner in 1969[50] to analyze temperature and carrier gas effects. In argon, homogeneous water nucleation rates of about one order of magnitude larger than in helium were found. In a refined version of the ECC by Schmitt,[51] temperatures between 268 K and 318 K were investigated with nucleation rates ranging from $10^8$ m$^{-3}$s$^{-1}$ to $10^{11}$ m$^{-3}$s$^{-1}$. In this case, the analyzed condensing components were ethanol, nonane, and toluene.

A modified version of the ECC was designed by Strey and Wagner in 1981,[52–54] the two pistons expansion chamber (TPEC), in which the application of the nucleation pulse method by Allard and Kassner[49] was improved. The nucleation time was reduced to about 1 ms, thus more effectively decoupling nucleation and droplet growth. With the TPEC, the vapor-gas mixture was prepared outside of the TPEC chamber. In addition, the so-called Constant Angle Mie Scattering (CAMS) method was introduced for measuring nucleation rates.[55] Various studies were conducted with the TPEC by Strey, Wagner and Viisanen on unary water nucleation,[52] as well as on binary and ternary nucleation including water.[56–59]

In 1993, Viisanen *et al.*[45] used a slightly modified version of the TPEC, the two valve expansion chamber (TVEC), to investigate homogeneous water nucleation between 220 K and 260 K at about 0.07 MPa for different carrier gases: helium, neon, argon, krypton and xenon. No difference in the *J-S* isotherms was observed by changing the carrier gas. In addition, the CNT was found not to quantitatively predict the nucleation rate as a function of supersaturation and temperature. In 2001, Wölk and Strey[43] investigated unary water nucleation in argon with the same setup (TVEC). The temperature was systematically varied from 220 K to 260 K, keeping the pressure at approximately 0.06 MPa. The nucleation rates were found to vary between $10^{11}$ m$^{-3}$s$^{-1}$ to $10^{15}$ m$^{-3}$s$^{-1}$ for supersaturations ranging from 7 to 25. An empirical temperature correction of the CNT was introduced, based on their experimental data, which holds for the available literature data obtained at the same pressure and temperature conditions.[39–42,44–47,60,61]

Another expansion based option to study unary water nucleation is represented by the supersonic nozzles (SSN). First introduced by Oswatitsch in 1942[62], the SSN technique was later used by Wyslouzil and co-workers.[63–67] Typical unary water nucleation rates - in nitrogen carrier gas - from $10^{22}$ m$^{-3}$s$^{-1}$ to $10^{23}$ m$^{-3}$s$^{-1}$ were observed for supersaturations between 50 and 300, the temperature ranging from 200 K to 230 K with pressures below ambient conditions. A good agreement was found with the empirical temperature correction of the CNT proposed by Wölk and Strey.[43] In 1994, Wyslouzil *et al.*[63] also investigated the pressure effect on water nucleation in the atmospheric pressure range, but no relevant variation was observed.

Shock tubes are expansion based devices largely exploited for nucleation studies. The first homogeneous water nucleation data obtained with a shock tube device were reported by Barschdorff in 1975.[68] He analyzed the effect of various carrier gases (air, helium, argon) at temperatures between 225 K and 282 K and pressures up to 8 kPa. No relevant variations were found for the different carrier gases. In 1983, Peters[69] was the first to propose a modified shock tube to apply the nucleation pulse method.[49] This idea was later perfected by van Dongen and co-workers,[70] leading to the first version of the pulse expansion wave tube (PEWT).

This device has been improved and successfully used for almost 30 years to investigate homogeneous nucleation of different vapors in a large variety of carrier gases and for a wide range of pressure and temperature conditions: from 0.1 MPa to 4 MPa and between 200 K and 260 K.[44,60,61,70–85] Typical nucleation rates obtained with the PEWT range from $10^{12}$ m$^{-3}$s$^{-1}$ to $10^{18}$ m$^{-3}$s$^{-1}$ with supersaturations between 7 and 20. An overview of the homogeneous water nucleation studies carried out with the PEWT is reported in TABLE 1.1.

**TABLE 1.1.** Homogeneous water nucleation experiments carried out with the PEWT.

| Authors and references | Year | p (MPa) | T (K) | Carrier gas |
|---|---|---|---|---|
| Looijmans and van Dongen, Ref. 60 | 1997 | 0.03-0.09 | 200-260 | $N_2$ |
| Luijten et al., Ref. 73 | 1997 | 1, 2.5, 4 | 230-250 | $N_2$ |
| Luijten et al., Ref. 78 | 1999 | 1, 2.5, 4 | 240 | $N_2$, He |
| Peeters et al., Ref. 82 | 2004 | 1.1, 4.4 | 242, 247 | $CH_4$ |
| Holten et al., Ref. 44 | 2005 | 0.1 | 200-240 | He |
| Holten and van Dongen, Ref. 84 | 2010 | 1 | 235 | $CH_4 + CO_2$ (0%,3%,25%) |
| Fransen et al., Ref. 61 | 2014 | 0.1, 1 | 240 | He |
| Fransen et al., Ref. 85 | 2015 | 1 | 240 | $N_2$ |

Based on the experimental overview reported in this section, the following considerations can be made.

- At about ambient pressure, several homogeneous water nucleation studies in different carrier gases have been reported for various temperatures.[39–42,44–47,60,61,64–67] They all agree with the empirical temperature correction of the CNT proposed by Wölk and Strey[43] and later perfected by Hale.[86]

- A few studies investigate the effect of the carrier gases at low pressure[45,50,68] and only Allen and Kassner in 1969[50] observed lower water nucleation rates in argon than in helium. They argued that argon offers a somewhat lower binding energy since it would interact with a greater number of water molecules through van der Waals forces. The small size of the helium atom causes it to experience a much smaller interaction energy with the water molecules, thus explaining the lower nucleation rates.[50]

- Pressure effects were analyzed at low pressure (<0.2 MPa).[48,63,68] At these conditions, there is not enough carrier gas to adequately thermalize the condensing clusters. Thus, at low pressure, insufficient thermalisation is the only phenomena responsible for the nucleation rate differences observed as a function of pressure.[a]

- At high pressure (>0.2 MPa), the only systematic analysis of the pressure effects was carried out by Luijten et al.[78] and by Fransen et al.[61,85] for water in nitrogen and in helium, respectively, and by Peeters et al.[82] for water in methane. The dependence of the

---

[a] Surface tension variations as a function of pressure are negligible at low pressure (<0.2 MPa) for any carrier gas and, thus, thermalisation becomes the only effect playing a role at this conditions. On the contrary, at high pressure (>0.2 MPa) the surface tension reduction with pressure is predominant, while thermalisation phenomena become negligible. These aspects will be discussed more in detail in Chapters 4 and 5.

homogeneous water nucleation rates on pressure and type of carrier gas was attributed to the surface tension variation.[a]

## 1.3 Research goal and thesis overview

The experimental overview presented in Sec. 1.2 underlines that pressure and carrier gas effects remain two puzzling aspects in homogeneous water nucleation studies. The aim of the present work is to give a better understanding of these two effects by experimental means. To this end, the thesis is structured as follows:

**Chapter 2** The two key parameters characterizing the nucleation phenomena, supersaturation $S$ and homogeneous nucleation rate $J$, are described. First, the equilibrium vapor molar fraction and the enhancement factor are specified in order to define the supersaturation parameter. Then, the CNT expression of the nucleation rate $J$ is obtained starting from elementary thermodynamics and the kinetic theory of cluster formation. Finally, the CNT $J$-expression is extended to non-ideal mixtures by accounting for the presence of the carrier gases and their effects on the nucleation rate.

**Chapter 3** A novel design of the PEWT test section is presented. The effect of the thermal insulation on the piezoelectric pressure sensor and the thickness of the diaphragm, initially separating the PEWT high and low pressure sections, are experimentally analyzed. The flow phenomena are simulated with a 2D numerical model, which correctly predicts the gas-dynamic features of the PEWT and the effects of the diaphragm opening process. Homogeneous water nucleation experiments in helium at 240 K are carried out for 0.1 MPa and 1 MPa. They are shown to be in agreement with the experimental data obtained at the same conditions by Fransen *et al.*[61] with the previous version of the test section.

**Chapter 4** Homogeneous water nucleation rate data are obtained in argon and in nitrogen at about 240 K and 0.1 MPa, 1 MPa and 2 MPa, using the PEWT. The surface tension reduction at high pressure qualitatively explains the observed $J$ increase. At low pressure, the effect of type of carrier gas and of pressure on the measured $J$ is ascribed to imperfect thermalization phenomena as predicted by theory. The Gibbs-Thomson equation is used to compute the number of water molecules in the critical clusters. The theoretical predictions are in reasonable agreement with experimentally calculated critical cluster sizes as reported by Wölk and Strey.[43] Finally, an empirical correction of the CNT $J$-expression is proposed, accounting for pressure, temperature and carrier gas effects experimentally investigated in this chapter.

**Chapter 5** Homogeneous water nucleation experiments are carried out at 240 K in mixtures of nitrogen and 5%, 15% and 25% of carbon dioxide. Three pressure conditions are tested: 0.1 MPa, 1 MPa and 2 MPa. A restricted series of water nucleation experiments is presented with the 25% of carbon dioxide at 0.1 MPa for 234 K and 236 K. Increasing pressure and carbon dioxide content leads to a nucleation rate increase. A theoretical adsorption/surface tension model, extended to multi-component mixtures, is derived. The $J$ values predicted by the CNT in combination with the presented surface tension model agrees with the pressure and composition dependence experimentally observed,

but appears to strongly overestimate it. At 0.1 MPa, the measured nucleation rates decrease as predicted by the theoretical model for imperfect thermalization,[87] generalized here for water in multi-component carrier gas mixtures. The scaling model proposed by Hale[86] is shown to agree with the observed temperature dependence of the experimental nucleation rates at 0.1 MPa.

**Chapter 6**  The homogeneous nucleation data presented in Chapters 4 and 5 for water in nitrogen and 0%, 5%, 15% and 25% of carbon dioxide are further analyzed. The experimental nucleation rate dependencies on supersaturation, pressure and mixture composition at constant temperature can be used to derive the critical cluster composition by employing the nucleation theorem. This theorem is exploited to derive two methodologies. One extends the method used in literature for two components to mixtures of $N$ components. The other method is more straightforward and can be used for unary as well as for binary and multi-component nucleation cases. Within the experimental uncertainty, the same critical nuclei compositions is found with both methods. At fixed temperature and supersaturation, the calculated water content of the critical clusters decrease with pressure and carbon dioxide fractions. On the contrary, the numbers of nitrogen and carbon dioxide molecules adsorbed at the cluster surface increase. This increase cause the surface tension to decrease, which explains the observed nucleation rate increase with increasing pressure and carbon dioxide molar fraction at constant temperature and supersaturation.

# Chapter 2

# Theoretical background

In this chapter, a theoretical insight of nucleation is given by introducing the two key parameters describing the phenomenon: supersaturation $S$ and nucleation rate $J$. Starting from phase equilibrium of a single condensing component in a non-ideal mixture, the equilibrium vapor molar fraction $y_{eq}$ and the enhancement factor $f_e$ are first derived in order to define the supersaturation $S$. The classical formulation of the nucleation rate $J$ then follows from elementary thermodynamics and the the kinetic theory of cluster formation. For non-ideal mixtures, the classical formulation is extended by accounting for the presence of the carrier gases and their effects on the nucleation phenomenon.

## 2.1 Phase equilibrium

Consider a non-ideal mixture of $N$ components and a single condensing component with its liquid and vapor phases in equilibrium. This condition can be described by the equality of chemical potentials in the coexisting phases at the actual total pressure $p$ and temperature $T$ of the mixture[88]

$$\mu_1^g(p, T, y_{1,eq}) = \mu_1^\ell(p, T, x_{1,eq}), \tag{2.1}$$

where $y_{1,eq}$ and $x_{1,eq}$ are the vapor and liquid molar fractions of the condensing component (subscript '1') at phase equilibrium (subscript 'eq') and with the superscripts '$g$' and '$\ell$' denoting its gas and liquid phases. A property directly related to $\mu$ is the fugacity $\mathscr{F}$. For the condensing component '1', the relation is [a]

$$\mu_1^g(p, y_1) = \mu_1^g(p_{1,s}) + kT \ln\left[\frac{\mathscr{F}_1^g(p, y_1)}{\mathscr{F}_1^g(p_{1,s})}\right], \tag{2.2}$$

where $p_{1,s}$ is the saturation pressure of the pure condensing component '1', taken as reference state for both phases, and $k$ is the Boltzmann constant. The quantity denoted as $\mathscr{F}_1^g$ in Eq. 2.2 is the fugacity of component '1' in its gas phase and is formulated with respect to the fugacity coefficient $\phi_1$ as follows

$$\mathscr{F}_1^g(p, y_1) = \phi_1 y_1 p. \tag{2.3}$$

---

[a] Note that, by definition, the chemical potential of component $i$ is $\mu_i = dG/dn_i$ with $n_{j \neq i}$, $p$ and $T$ kept constant, $n_i$ the number of molecules of component $i$ and $G$ the Gibbs free energy.

It can be interpreted as a partial pressure $p_1^g = y_1 p$ corrected to account for the actual molecular interactions taking place in the mixture.[89] At low total pressure $p \to 0$, $\phi_1 \to 1$ so that $\mathscr{F}_1^g \to y_1 p$. For the liquid phase of the condensing component, its molar liquid fraction $x_{1,\mathrm{eq}} \to 1$ for our practical applications (small concentration of the other $(N-1)$ components in the liquid phase - see Sec. 2.1.1). Therefore, the Raoult's law applies, leading to

$$\mu_1^\ell(p, x_1) = \mu_1^\ell(p) + kT \ln x_1, \tag{2.4}$$

where the chemical potential $\mu_1^\ell(p)$ can be expressed with respect to the reference saturated state of the pure component as

$$\mu_1^\ell(p) = \mu_1^\ell(p_{1,\mathrm{s}}) + \int_{p_{1,\mathrm{s}}}^{p} v_1^\ell \, dp, \tag{2.5}$$

with $v_1^\ell$ the bulk liquid molecular volume of component '1'.

At the condition of chemical equilibrium between gas and liquid phases, the equality of chemical potentials in Eq. 2.1 applies, with $\mu_1^g(p, y_{1,\mathrm{eq}})$ and $\mu_1^\ell(p, x_{1,\mathrm{eq}})$ as given in Eqs. 2.2 and 2.4, the fugacity in the form of Eq. 2.3 and with $\mu_1^g(p_{1,\mathrm{s}}) = \mu_1^\ell(p_{1,\mathrm{s}})$. This leads to the general chemical equilibrium expression

$$kT \ln \left( \frac{\phi_{1,\mathrm{eq}} y_{1,\mathrm{eq}} p}{\phi_{1,\mathrm{s}} p_{1,\mathrm{s}}} \right) = kT \ln x_{1,\mathrm{eq}} + \int_{p_{1,\mathrm{s}}}^{p} v_1^\ell \, dp. \tag{2.6}$$

Finally, the equilibrium vapor molar fraction $y_{1,\mathrm{eq}}$ for the condensing component (subscript '1') of a non-ideal mixture can be now derived from Eq. 2.6 as

$$y_{1,\mathrm{eq}} = \frac{p_{1,\mathrm{s}}}{p} \frac{\phi_{1,\mathrm{s}}}{\phi_{1,\mathrm{eq}}} x_{1,\mathrm{eq}} \exp \int_{p_{1,\mathrm{s}}}^{p} \frac{v_1^\ell}{kT} \, dp. \tag{2.7}$$

From Eq. 2.7, it follows that, for a non-ideal mixture, the equilibrium vapor molar fraction is enhanced by two contributions:

  (i) the real gas effect ($\phi_{1,\mathrm{s}}/\phi_{1,\mathrm{eq}}$) accounting for the interaction of the condensing component molecules with the other condensing component molecules and with the molecules of the other $(N-1)$ components in the non-ideal mixture
     and
 (ii) the so-called Poynting correction ($\exp \int_{p_{1,\mathrm{s}}}^{p} v_1^\ell / kT \, dp$), which takes into consideration the effect of the total pressure on the liquid phase.

An additional effect considered in the $y_{1,\mathrm{eq}}$ definition of Eq. 2.7 is

 (iii) the equilibrium liquid molar fraction $x_{1,\mathrm{eq}}$, accounting for the solubility of the surrounding $(N-1)$ components into the liquid phase.

It mast be noted that the effect (iii) is responsible for a decrease of $y_{1,\mathrm{eq}}$, which is often much less important than the real gas effect (i) and the Poynting contribution (ii). Under the incompressibility assumption of the liquid phase, Eq. 2.7 simplifies as follows

$$y_{1,\mathrm{eq}} = \frac{p_{1,\mathrm{s}}}{p} \frac{\phi_{1,\mathrm{s}}}{\phi_{1,\mathrm{eq}}} x_{1,\mathrm{eq}} \exp \left[ \frac{v_1^\ell(p - p_{1,\mathrm{s}})}{kT} \right]. \tag{2.8}$$

### 2.1.1 Enhancement factor

The heteromolecular interactions taking place in a non-ideal mixture between the condensing component and the surrounding carrier gases are responsible for an increase of the equilibrium vapor molar fraction $y_{1,\mathrm{eq}}$. In order to quantify this increase, we now introduce an additional parameter, the so-called enhancement factor $f_e$. With reference to Eq. 2.8, it is defined as

$$f_e \equiv \frac{y_{1,\mathrm{eq}}\, p}{p_{1,\mathrm{s}}} = \frac{\phi_{1,\mathrm{s}}}{\phi_{1,\mathrm{eq}}}\, x_{1,\mathrm{eq}}\, \exp\left[\frac{v_1^\ell (p - p_{1,\mathrm{s}})}{kT}\right], \tag{2.9}$$

where the three aspects discussed in Sec. 2.1 are taken into account: (i) the real gas effect, (ii) the Poynting contribution and (iii) the solubility of the $(N-1)$ carrier gases into the liquid phase by means of the equilibrium liquid molar fraction $x_{1,\mathrm{eq}}$.

As far as the real gas effect is concerned, the fugacity coefficient of the pure condensing component at the saturated state is [90]

$$\ln \phi_{1,\mathrm{s}} = \frac{B_{11}\, p_{1,\mathrm{s}}}{RT}, \tag{2.10}$$

with $B_{11}$ the second virial coefficient of the pure component '1'. The fugacity of the condensing component in presence of the $(N-1)$ carrier gases $\phi_{1,\mathrm{eq}}$ takes into account the interactions with the other components of the non-ideal mixture:

$$\ln \phi_{1,\mathrm{eq}} = \left[y_{1,\mathrm{eq}}B_{11} + \sum_{j=2}^{N} y_j B_{1j}\right]\frac{2}{V} - \ln Z, \tag{2.11}$$

where $y_j$ is the molar fraction of the $j$-th carrier gas, $B_{1j}$ is the second cross-virial coefficient for the condensing component in presence of the $j$-th carrier gas, with $V$ the molar volume and $Z = pV/RT$ the compressibility factor of the mixture. The latter accounts for the non-ideality of the mixture and can be reformulated by means of the virial equation of state [89]

$$Z = 1 + \frac{B}{V}, \tag{2.12}$$

with

$$B = \sum_{i=1}^{N}\sum_{j=1}^{N} y_i y_j B_{ij}. \tag{2.13}$$

For $j = i$, $B_{ij}$ is the second virial coefficient of the pure $i$-th component and, for $j \neq i$, $B_{ij}$ denotes the second cross-virial coefficient of the $i$-th and $j$-th interacting components.

In the present work, water is investigated as condensing component in four different carrier gas mixtures: helium, argon, nitrogen and carbon dioxide with nitrogen. The corresponding virial and cross-virial coefficients as functions of temperature are shown in FIGS. 2.1 and 2.2. The values obtained from the literature sources used in the present work [91] are represented with a black solid line. For the whole set of investigated mixtures, the used values are shown to be in agreement with the other data available in literature. [91–101]

The liquid fraction of the condensing component in Eq. 2.9 can be expressed as

$$x_{1,\mathrm{eq}} = 1 - \sum_{i=2}^{N} x_{i,\mathrm{eq}}, \tag{2.14}$$

with $x_{i,eq}$ the fraction of the *i*-th carrier gases into the liquid phase at equilibrium. The solubility in water has been analyzed for each of the carrier gases used in this work.
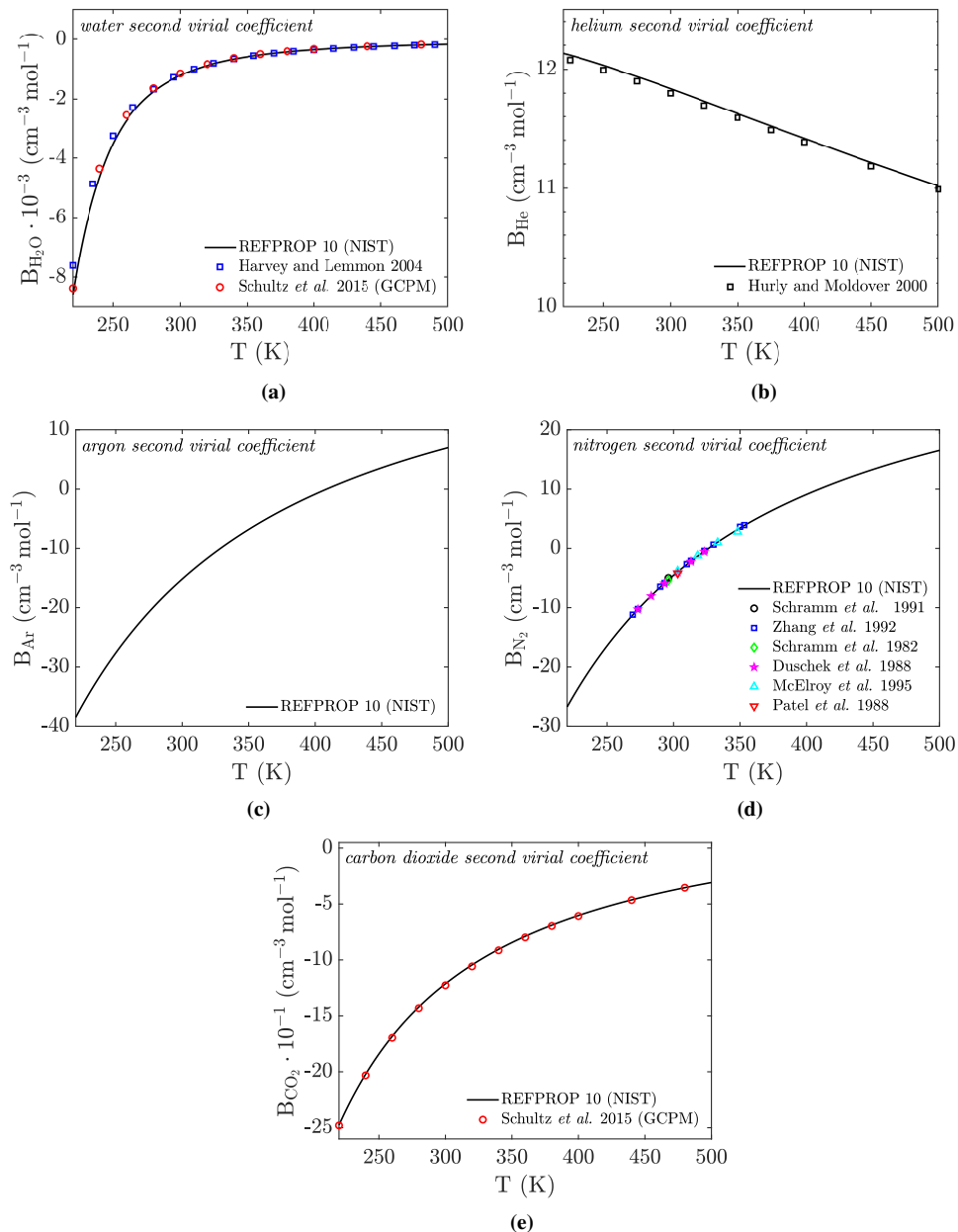


**FIG. 2.1.** Second virial coefficients: present work values (black solid lines)[91] compared to literature data.[95,96,102–110]
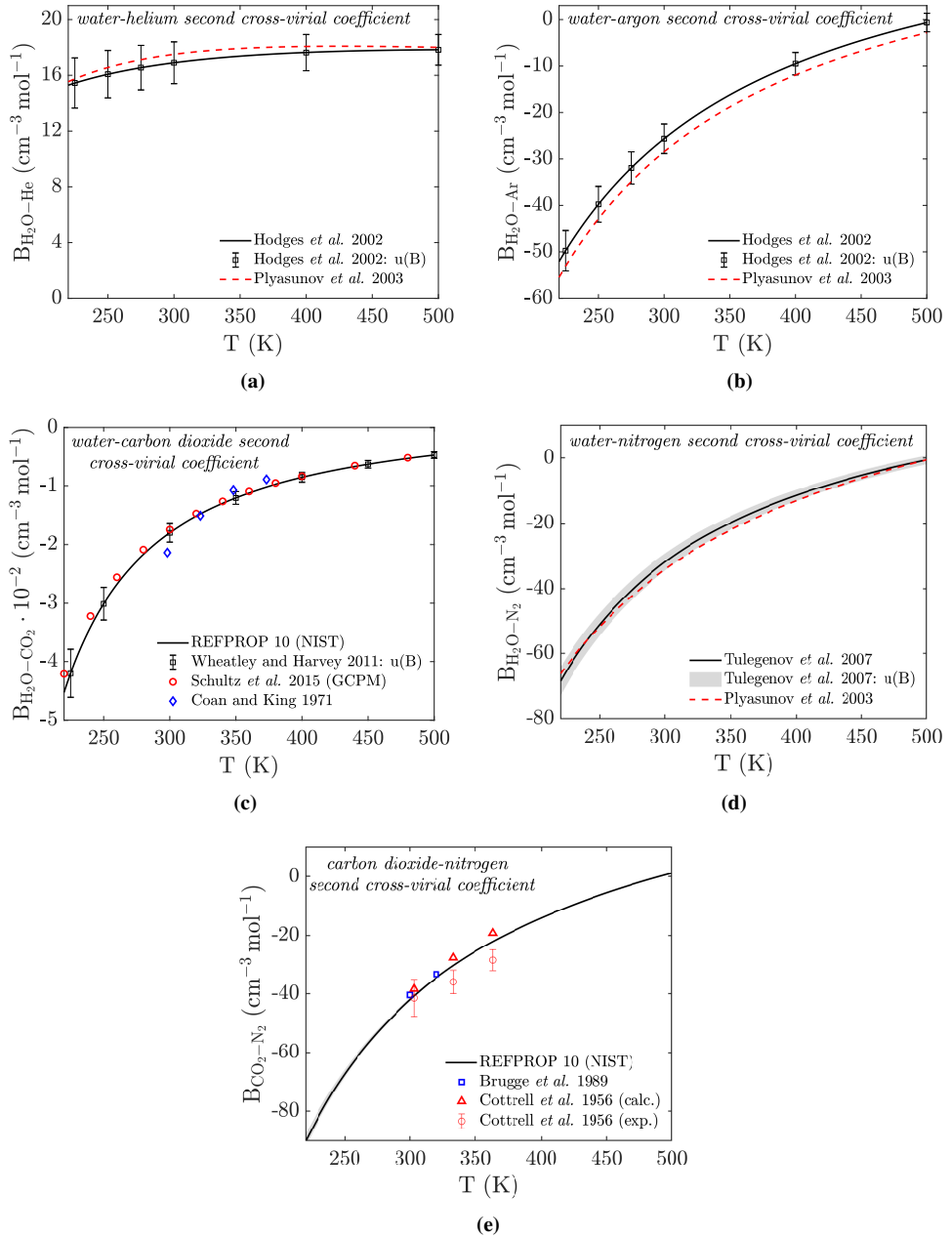
**FIG. 2.2.** Second cross-virial coefficients: present work values (black solid lines)[91] compared to literature data.[90,96–98,100,101,111,112]

For helium, argon and nitrogen, it is found to be negligibly small, as shown in FIG. 2.3 for nitrogen as an example. On the contrary, for the case of carbon dioxide, the solubility in water cannot be neglected, being an order of magnitude higher with respect to the other carrier gases

at the reference temperature of 240 K and at the investigated pressure conditions (0.1 MPa, 1 MPa, and 2 MPa). The software REFPROP 10[91] is employed to calculate the carrier gas liquid fractions in water as a function of temperature and pressure. The results of these computations for carbon dioxide in water are compared with the data available in literature[92–94] and the outcome is reported in FIG. 2.4. Taking this comparison into consideration, REFPROP 10[91] is chosen for the $x_{i,eq}$ calculations of the present work.
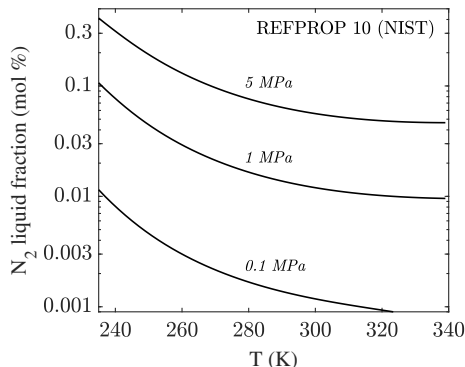


**FIG. 2.3.** Solubility of nitrogen in water as a function of temperature for different pressures.[91]
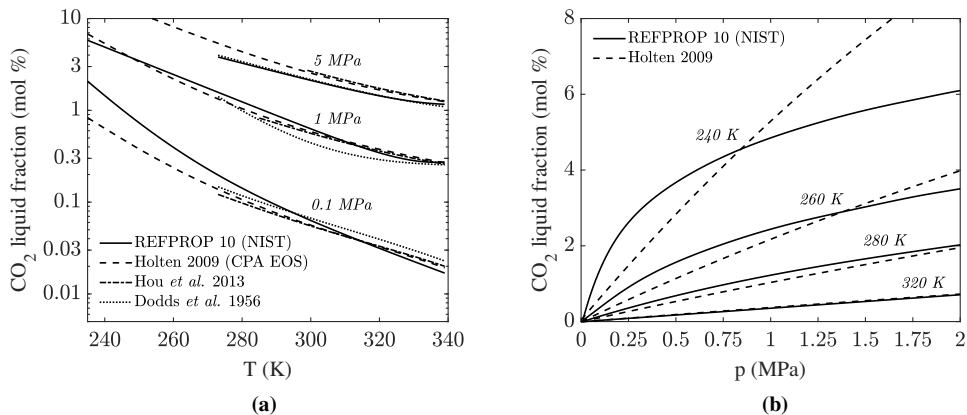


**FIG. 2.4.** Solubility of carbon dioxide in water for water-carbon dioxide mixtures. The liquid fraction of carbon dioxide is shown as a function of temperature at different pressures (2.4a) and as a function of pressure at different temperatures (2.4b). The literature data[92–94] are compared with the values obtained with REFPROP 10[91] (black solid lines) at the same pressure and temperature conditions available in literature.

### 2.1.2 Supersaturation

For a non-ideal mixture, the supersaturation of the condensing component '1' is defined here as the ratio of its gas phase fugacities at the actual and at the corresponding - same total (mixture) pressure $p$ and temperature $T$ - equilibrium condition

$$S \equiv \frac{\mathscr{F}_1^{\mathrm{g}}(p,T,y_1)}{\mathscr{F}_1^{\mathrm{g}}(p,T,y_{1,\mathrm{eq}})} = \exp\left[\frac{\mu_1^{\mathrm{g}}(p,T,y_1) - \mu_1^{\mathrm{g}}(p,T,y_{1,\mathrm{eq}})}{kT}\right]. \tag{2.15}$$

The second equality in Eq. 2.15 is derived from the chemical potentials expressed in Eq. 2.2 as a function of the corresponding fugacities. Hence, recalling Eq. 2.3, the supersaturation for the condensing component '1' in a non ideal mixture becomes

$$S = \frac{\phi_1}{\phi_{1,eq}} \frac{y_1}{y_{1,eq}} \approx \frac{y_1}{y_{1,eq}} = \frac{y_1 \, p}{f_e \, p_{1,s}}, \tag{2.16}$$

with the last equality derived from Eq. 2.9. The approximation $\phi_1 \approx \phi_{1,eq}$ in Eq. 2.16 is valid under the assumption that, both at the actual and at the equilibrium condition, the interactions between monomers of the condensing component can be neglected with respect to the molecular interactions with the carrier gas. This condition is fulfilled with a high degree of approximation for the mixtures investigated in the present work, the gas molar fraction of the condensing component being small with respect to that of the carrier gases ($y_1 < 5000$ ppm $\ll y_{i \neq 1}$).

Note that our general definition of supersaturation given in Eqs. 2.15 and 2.16 differs from that by Wedekind *et al.*[113] $S' = y_1 \, p / p_{1,s}$, in which the saturated state of the pure condensing component is taken as reference. While at low pressure $f_e \to 1$ and the two definitions coincide $S' = S f_e \to S$, at high pressures the enhancement effect plays a crucial role ($1 < f_e < 1.3$) as the influence of the surrounding becomes important. This influence is included in the definition of $S$ (see Eqs. 2.15 and 2.16). In addition, at phase equilibrium for a given $p$ and $T$, $S = 1$, while $S' \geq 1$, depending on the pressure.

It must be stressed that the investigated nucleation conditions are chosen such that the carrier gases are always in the undersaturated state. In fact, the saturation pressure of the pure carrier components is always larger than their partial pressure at our experimental conditions $p_{i \neq 1,s} < p \, y_{i \neq 1}$. In addition, $y_{i \neq 1}$ is so large that any carrier component in the gas phase is in chemical equilibrium with the corresponding carrier gas in the cluster and the nucleation kinetics only depends on impingement/evaporation of the condensing component molecules.[77] Luijten and van Dongen[77] have shown that nucleation phenomena of condensable vapors in a carrier gas can be considered as unary nucleation if $x_{i \neq 1,eq} \ll (S - 1)/S$, with $x_{i \neq 1,eq}$ the dissolved gas fraction in the bulk liquid. With the $x_{i \neq 1,eq} < 0.038$ in our experiments (see FIGS. 2.3 and 2.4), this condition is always fulfilled. For carrier gases with much larger $x_{i \neq 1,eq}$, the full binary nucleation model applies.[114] Thus, we consider the nucleation phenomena observed in the current work as essentially unary. Accordingly, '1' being the only (supersaturated) component providing the driving force for the nucleation process, the subscript '1' is omitted in the expression of $S$ (see Eqs. 2.15 and 2.16).

## 2.2 Nucleation model

In this section, the thermodynamics of cluster formation (Sec. 2.2.1), the kinetic model of nucleation (Sec. 2.2.2) and the classical nucleation model (Sec. 2.2.3) are described following the approaches of Vehkamäki[115] and Luijten.[88] In addition, the nucleation model is extended to account for the presence of the carrier gas (Sec. 2.2.4) according to Luijten.[88]

### 2.2.1 Thermodynamics of cluster formation

Consider a single component (vapor) system, kept at constant pressure $p$ and temperature $T$ by its surrounding. The system is closed with respect to the surrounding, with which only work and heat are exchanged and no molecules are flowing through their interface. System

and surrounding together form an isolated macro-system. Assume the system passes from an initial gas state (subscript '0'), where only monomers[b] are present, to a final liquid-gas state (omitted subscript), in which a cluster is formed. It is assumed that the cluster is separated from the vapor monomers by a surface. For the described system, only internal energy, entropy and volume can change when passing from initial $(U_0, \mathbb{S}_0, V_0)$ to final state $(U, \mathbb{S}, V)$.
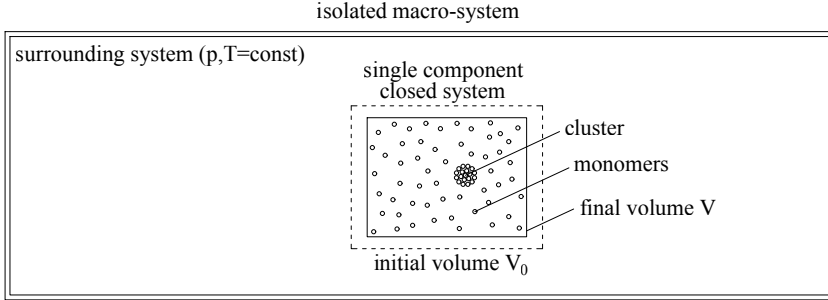


**FIG. 2.5.** Schematic of the considered isolated macro-system (mixture), consisting of a single (condensing) component system and a surrounding system (carrier gas), which keeps pressure and temperature constant. The single component system being closed, it is assumed that no net flow of molecules is present with the surrounding system.

The work of cluster formation can be expressed as the difference of Gibbs free energies between initial and final state $\Delta G = G - G_0$ by combining the first and second law of thermodynamics, which leads to[88,115]

$$\Delta G = (U - U_0) + p(V - V_0) - T(\mathbb{S} - \mathbb{S}_0) \leqslant 0. \tag{2.17}$$

Being extensive quantities, the internal energy $U$, the entropy $\mathbb{S}$ and the system volume $V$ can be seen as result of the contributions from the gas (vapor monomers), liquid (cluster core) and surface (cluster core - vapor monomers interface) subsystems, denoted respectively with superscripts 'g', '$\ell$' and 's'. It follows that $V = V^g + V^\ell$, $\mathbb{S} = \mathbb{S}^g + \mathbb{S}^\ell + \mathbb{S}^s$ and equivalently

$$U = U^g + U^\ell + U^s \tag{2.18}$$

where

$$U^g = -p^g V^g + T\mathbb{S}^g + n^g \mu^g, \tag{2.19a}$$
$$U^\ell = -p^\ell V^\ell + T\mathbb{S}^\ell + n^\ell \mu^\ell, \tag{2.19b}$$
$$U^s = \sigma A_{<\mathrm{n}>} + T\mathbb{S}^s + n^s \mu^s, \tag{2.19c}$$

at the final state and that, at the initial state,

$$U_0 = -pV_0 + T\mathbb{S}_0 + n_0 \mu_0, \tag{2.20}$$

with $A_{<\mathrm{n}>}$ the surface area of the cluster consisting of $n$ molecules, $n_0 = n^g + n^\ell + n^s$ the total number of molecules in the system at the initial state and $n^g$, $n^\ell$ and $n^s$ the number of

---

[b]Here and in the forthcoming discussions, the terms 'molecule' and 'monomer' will be used interchangeably, with a 'monomer' that can be seen as a cluster consisting of a single molecule.

molecules in the gas phase, liquid phase and interface at the final state. Additionally, $p = p^g$, therefore $\mu_0 = \mu^g$ and $\mu^\ell = \mu^s$ as the cluster core (liquid phase) is in equilibrium with its surface. Under these circumstances and inserting Eqs. 2.18-2.20 in Eq. 2.17, the work of cluster formation becomes

$$\Delta G = -V^\ell \Delta p + n \Delta \mu + \sigma A_{<n>}, \tag{2.21}$$

with $\Delta p = p^\ell - p^g$, $\Delta \mu = \mu^\ell - \mu^g$ and $n = n^\ell + n^s$.

## 2.2.2 Kinetic model of nucleation

The dynamics of nucleation is characterized by continuous growth and decay of the forming clusters. A single component system at constant temperature $T$ and pressure $p$ is considered in order to describe the nucleation phenomena. Normally, the number density of clusters is much less than the molecular number density in the system (dilute cluster condition). Thus, the cluster formation can be assumed to take place by impingement and release of single molecules, cluster-cluster interactions being negligible. Moreover, the sticking probability is taken equal to one. Note that the clusters consisting of $n$ molecules will be denoted as $n$-mers in the forthcoming. The reader is referred to FIG. 2.6 for the following discussion. Assuming steady state nucleation, the $n$-mer concentration or number density $\rho_{<n>}$ (number of $n$-mers per unit of volume), does not change in time, meaning that

$$\frac{d\rho_{<n>}}{dt} = J_{<n-1>} - J_{<n>} = 0, \tag{2.22}$$

where

$$J_{<n>} = \beta_{<n>} \rho_{<n>} - \gamma_{<n+1>} \rho_{<n+1>} \tag{2.23}$$

is the net transition rate between clusters of size n and size $(n+1)$, with $\beta_{<n>}\rho_{<n>}$ the number of $n$-mers per unit of time and volume catching a single molecule (clusters per unit of time and volume passing from a size $n$ to a size $n+1$), $\gamma_{<n+1>}\rho_{<n+1>}$ the number of $(n+1)$-mers per unit of time and volume loosing a single molecule (clusters per unit of time and volume passing from size $n+1$ to size $n$), $\beta_{<n>}$ and $\gamma_{<n+1>}$ being the condensation and evaporation coefficients. In other words, the condensation coefficient can be interpreted as the number of monomers per unit of time hitting an $n$-mer and is defined as follows

$$\beta_{<n>} = \rho_{<1>} A_{<n>} \sqrt{\frac{kT}{4\pi m}}, \tag{2.24}$$
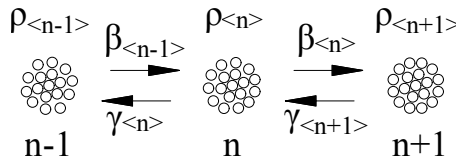


**FIG. 2.6.** Schematic of the condensation and evaporation flows between $n-1$, $n$ and $n+1$, with $\beta_{<n>}$ and $\gamma_{<n>}$ the condensation and evaporation coefficients for size n. [115]

where $A_{<n>}$ is the surface area of an $n$-mer, $m$ is the molecular mass of the system component, $\rho_{<1>}$ is the concentration (number density) of monomers in the system, the term under the square root is the impingement rate of the monomers with a sticking probability equal to one. The steady state assumption in Eq. 2.22 implies that the transition rate is independent of the cluster size and, therefore, $J_{<n-1>} = J_{<n>} = J$, with $J$ the nucleation rate, i.e. the formation rate of critical clusters.

When gas and liquid phases are at equilibrium in the system, the concentration of $n$-mers is constant in time with $d\rho_{<n>}^{eq}/dt = 0$ and, thus, $\rho_{<n>} = \rho_{<n>}^{eq}$. At this condition, the net transition rate $J_{<n>}^{eq} = 0$ and Eq. 2.23 leads to

$$\gamma_{<n+1>} = \gamma_{<n+1>}^{eq} = \frac{\beta_{<n>}^{eq} \rho_{<n>}^{eq}}{\rho_{<n+1>}^{eq}}, \tag{2.25}$$

where it is assumed that the probability of a cluster to release one molecule is independent of the vapor concentration and only depends on $T$ and $n$, i.e. $\gamma_{<n+1>}^{eq} = \gamma_{<n+1>}$. Considering the gas phase to be ideal, the concentration of monomers is given by

$$\rho_{<1>} = \frac{n^g}{V^g} = \frac{p^g}{kT}. \tag{2.26}$$

The Gibbs-Duhem equation applied to the ideal gas phase of the isothermal single-component system under analysis can then be written as $n^g \, d\mu^g = V^g \, dp^g$ and, using Eq. 2.26, the following expression for the difference in chemical potentials between the actual and equilibrium conditions can be derived

$$\mu^g - \mu_{eq}^g = kT \ln\left(\frac{p^g}{p_{eq}^g}\right). \tag{2.27}$$

In this specific case, the supersaturation definition becomes

$$S = \exp\left(\frac{\mu^g - \mu_{eq}^g}{kT}\right) = \frac{p^g}{p_{eq}^g}, \tag{2.28}$$

which finally leads, by recalling Eqs. 2.24 and 2.26, to express the concentration of monomers in the gas phase $\rho_{<1>}$ and the condensation coefficient of the $n$-mers in the system $\beta_{<n>}$ as a function of their corresponding quantities at equilibrium $\rho_{<1>}^{eq}$ and $\beta_{<n>}^{eq}$:

$$\rho_{<1>} = S\rho_{<1>}^{eq} \quad \text{and} \quad \beta_{<n>} = S\beta_{<n>}^{eq}. \tag{2.29}$$

Using the expressions of $\gamma_{<n>}$ given in Eq. 2.25 and $\beta_{<n>}$ given in Eq. 2.29, Eq. 2.23 can be reformulated, at the steady state condition ($J_{<n>} = J$ independent of $n$), as

$$\frac{J}{\beta_{<n>} \rho_{<n>}^{eq} S^n} = \frac{\rho_{<n>}}{\rho_{<n>}^{eq} S} - \frac{\rho_{<n+1>}}{\rho_{<n+1>}^{eq} S^{n+1}}. \tag{2.30}$$

Applying the summation for $n$ from 1 to and an arbitrary value $\mathbb{N} > 1$ to both right and left hand sides of Eq. 2.30 gives the following expression by mutual cancellation of successive terms

$$J\left(\sum_{n=1}^{\mathbb{N}} \frac{1}{\beta_{<n>} \rho_{<n>}^{eq} S^n}\right) = \frac{\rho_{<1>}}{\rho_{<1>}^{eq} S} - \frac{\rho_{<\mathbb{N}+1>}}{\rho_{<\mathbb{N}+1>}^{eq} S^{\mathbb{N}+1}} = 1 - \frac{\rho_{<\mathbb{N}+1>}}{\rho_{<\mathbb{N}+1>}^{eq} S^{\mathbb{N}+1}}, \tag{2.31}$$

where the second equality is obtained knowing that $\rho_{<1>} = S\rho_{<1>}^{\text{eq}}$ from Eq. 2.29. Extending the summation to infinity, $\mathbb{N} \to \infty$, $\rho_{<\mathbb{N}+1>}/(\rho_{<\mathbb{N}+1>}^{\text{eq}} \cdot S^{\mathbb{N}+1}) \to 0$ and the formation (nucleation) rate $J$ can be finally derived as

$$J = \left( \sum_{n=1}^{\infty} \frac{1}{\beta_{<n>} \rho_{<n>}^{\text{eq}} S^n} \right)^{-1} \approx \left( \int_{1}^{\infty} \frac{1}{\beta_{<n>} \rho_{<n>}^{\text{eq}} S^n} \right)^{-1}, \tag{2.32}$$

where the approximation is due to the extension of the summation to continuum limit.

### 2.2.3 Classical nucleation model

The classical cluster model is now introduced for the single component system described in Secs. 2.2.1 and 2.2.2. According to this model, the liquid inside the clusters is considered as a macroscopic hypothetical bulk liquid. Additionally, the cluster size is given solely by the number of molecules in the cluster core $n = n^\ell$. This is justified under the assumption of a curvature-independent surface tension, known as capillarity approximation, which implies that the surface of the cluster is chosen as an equimolar surface and $n^s = 0$ (infinitely thin surface). In the capillarity approximation, the surface tension of strongly curved clusters[c] is taken equal to the flat surface value.[115] Once the capillarity approximation is introduced, the volume of the single cluster can be expressed as $V^\ell = n v^\ell$. The chemical potentials of liquid and gas phases being equal at equilibrium $\mu_{\text{eq}}^\ell(p_{\text{eq}}^g) = \mu_{\text{eq}}^g(p_{\text{eq}}^g)$, the difference of chemical potentials between the two phases $\Delta\mu$ in Eq. 2.21 can be formulated as

$$\Delta\mu = \mu^\ell(p^\ell) - \mu^g(p^g) = [\mu^\ell(p^\ell) - \mu_{\text{eq}}^g(p_{\text{eq}}^g)] + [\mu_{\text{eq}}^g(p_{\text{eq}}^g) - \mu^g(p^g)], \tag{2.33}$$

where $[\mu^g(p^g) - \mu_{\text{eq}}^g(p_{\text{eq}}^g)] = kT \ln S$ (see Eq. 2.28) and

$$\Delta\mu_{\text{eq}}^\ell = \mu^\ell(p^\ell) - \mu_{\text{eq}}^g(p_{\text{eq}}^g) = \mu^\ell(p^\ell) - \mu_{\text{eq}}^\ell(p_{\text{eq}}^g) = v^\ell(p^\ell - p_{\text{eq}}^g) = v^\ell(p^\ell - p^g) \tag{2.34}$$

with the third equality obtained by integrating the Gibbs-Duhem equation applied to the ideal liquid phase of the investigated isothermal system ($n \, \mathrm{d}\mu^\ell = V^\ell \, \mathrm{d}p^\ell$) and with the last equality derived from the consideration that the Laplace pressure $\Delta p = (p^\ell - p^g) \gg (p^g - p_{\text{eq}}^g)$ by several orders of magnitude. Finally the difference of chemical potential

$$\Delta\mu = v^\ell(p^\ell - p^g) - kT \ln S \tag{2.35}$$

and the work of cluster formation defined in Eq. 2.21 becomes

$$W = -nkT \ln S + \sigma A_{<n>}. \tag{2.36}$$

Note that in Eq. 2.36 as in the forthcoming part of this dissertation, the work of cluster formation is denoted by the symbol $W$, instead of $\Delta G$, as it is independent of the kind of free energy that is used.[92,115]

   In the classical model, an additional assumption is made by considering perfectly spherical clusters. Thus, for a generic $n$-mer, the volume $V_{<n>} = V^\ell = (4/3)\pi r_{<n>}^3 = n v^\ell$, the surface area $A_{<n>} = 4\pi r_{<n>}^2 = A_{<1>} n^{2/3}$ and the radius $r_{<n>} = r_{<1>} n^{1/3}$ can be defined, where

---

[c] Typically, the critical clusters consist of few tens of molecules.

$V_{<1>} = v^\ell$, $A_{<1>} = 4\pi r^2_{<1>}$ and $r_{<1>} = (3v^\ell/4\pi)^{1/3}$ are the corresponding quantities for a single monomer. Finally, introducing the non-dimensional surface tension

$$\Theta = \frac{A_{<1>}\sigma}{kT} = \frac{[36\pi(v^\ell)^2]^{1/3}\sigma}{kT},$$
(2.37)

Eq. 2.36 can be reformulated as follows

$$\frac{W}{kT} = -n\ln S + \Theta n^{2/3},$$
(2.38)

with $W/kT$ as a function of $n$ characterized by a maximum at the critical cluster size (Gibbs-Thomson equation)

$$n^* = \left(\frac{2\Theta}{3\ln S}\right)^3 = \frac{32\pi(v^\ell)^2\sigma^3}{3(kT\ln S)^3},$$
(2.39)

which is characterized by equal probabilities of growth and decay. The energy of critical cluster formation (nucleation barrier) can be derived by simply substituting $n = n^*$ in Eq. 2.38:[5]

$$\frac{W^*}{kT} = \frac{4\Theta^3}{27(\ln S)^2} = \frac{16\pi}{3}\left(\frac{v^\ell}{\ln S}\right)^2\left(\frac{\sigma}{kT}\right)^3.$$
(2.40)

The Courtney distribution $\rho^{\text{eq}}_{<n>} = \rho^{\text{eq}}_{<1>}\exp(-\Theta n^{2/3})$ is now introduced to define the concentration of $n$-mers at the equilibrium state, which is a distribution model obeying the law of mass action.[9] Such a distribution leads to the following expression for the term $\rho^{\text{eq}}_{<n>}S^n$ given in Eq. 2.32

$$\rho^{\text{eq}}_{<n>}S^n = \rho^{\text{eq}}_{<1>}\exp(n\ln S - \Theta n^{2/3}) = \rho^{\text{eq}}_{<1>}\exp\left(-\frac{W}{kT}\right),$$
(2.41)

where the second equality is derived by employing Eq. 2.36. Since $\exp(W/kT)$ is characterized by a sharp maximum for $n = n^*$, a second order Taylor expansion around $n^*$ can be applied to $W$. As a result, the corresponding rate of formation (see Eq. 2.32) becomes

$$J = \beta_{<n^*>}\rho^{\text{eq}}_{<1>}\left[\int_1^\infty \exp[-\mathscr{Z}^2\pi(n-n^*)^2]\,\mathrm{d}n\right]^{-1}\exp\left(-\frac{W^*}{kT}\right),$$
(2.42)

where $\mathscr{Z} = [(-2\pi kT)^{-1}(\partial^2 W^*/\partial n^2)_{n^*}]^{1/2} = [(\Theta/\pi)(n^*)^{2/3}]/3$ is the Zeldovich factor.[7] The condensation coefficient $\beta_{<n>}$ is weakly dependent on $n$ and it is therefore not included in the integral, with its value evaluated at $n^*$, i.e. $\beta_{<n>} \approx \beta_{<n^*>}$. Because of the sharp maximum for $n = n^*$, it is possible to extend the lower limit of the integral to $-\infty$. The resulting integral is of Gaussian type with a standard solution given by $1/\mathscr{Z}$ for our specific case. Substituting in Eq. 2.42, the final form of the nucleation rate according to the classical nucleation theory (CNT) becomes

$$J = K\exp\left(-\frac{W^*}{kT}\right),$$
(2.43)

with $W^*/kT$ the non-dimensional work of critical cluster formation given in Eq. 2.40 and $K$ the so-called kinetic prefactor

$$K = \rho_{<1>}\, \rho_{<1>}^{\text{eq}}\, v^\ell \sqrt{\frac{2\sigma}{\pi m}} = \left(\frac{p_\text{s}}{kT}\right)^2 S\, v^\ell \sqrt{\frac{2\sigma N_\text{a}}{\pi M}},$$  (2.44)

where $\rho_{<1>} = S\rho_{<1>}^{\text{eq}}$ (Eq. 2.29) and $\rho_{<1>}^{\text{eq}} = p_{\text{eq}}^{\text{g}}/kT$ (Eq. 2.26), with $p_{\text{eq}}^{\text{g}}$ taken equal to the saturation pressure $p_\text{s}$ of the single component present in the system. In Eq. 2.44, $M = mN_\text{a}$ denotes the molar mass and $N_\text{a}$ the Avogadro's number. According to the classical model, the molecular volume is calculated as a bulk quantity $v^\ell = v_\ell = m/\rho_\ell$ from the liquid mass density $\rho_\ell$. Similarly, regardless of the critical cluster size, $\sigma$ is taken equal to the surface tension of the pure liquid component $\sigma = \sigma_\ell$ (capillarity approximation).

### 2.2.4 Accounting for the carrier gas

The nucleation rate given by Eqs. 2.43, 2.44 and 2.40 according to the CNT refers to a single component system, closed with respect to the surrounding, with which no net flow of molecules is present and only work and heat can be exchanged. For a non-ideal mixture, the actual heteromolecular interactions taking place between condensing component and surrounding carrier gases do strongly influence the nucleation process. This effect has been partially accounted for by means of the enhancement factor discussed in Sec. 2.1.1 and it is included in the definition of supersaturation for a non-ideal mixture given in Sec. 2.1.2.

The surface tension is the other parameter to be affected by the heteromolecular interactions within the mixture. Adsorption of carrier gas molecules at the cluster surface increases the nucleation rate by decreasing the actual surface tension $\sigma$ with respect to the pure condensing component case ($\sigma < \sigma_\ell$). The derivation of the actual surface tension as a function of pressure and temperature for the general case of $(N-1)$ carrier gases is discussed in detail in Appendix A. The surface tension decrease becomes particularly important at high pressure and it will be analyzed for our practical applications in Secs. 4.2.2 and 5.2.1.

At low pressure conditions, adsorption phenomena are negligible, but, on the other hand, thermalisation of the clusters by collisions with the carrier gas molecules is less efficient than at high pressure. Hence, imperfect thermalisation effects become important at low pressure, reducing the nucleation rates with respect to the corresponding - same temperature and supersaturation - isothermal condition. This aspect will be discussed in Secs. 4.2.3 and 5.2.2 and analyzed in detail for the investigated experimental conditions.

In this section, attention will be given to the concentration of monomers at the actual and at the equilibrium condition: $\rho_{<1>}$ and $\rho_{<1>}^{\text{eq}}$ (see Eq. 2.44). For the conditions considered in this work (low temperature nucleation of water in several carrier gases), the gas phase of the condensing component (subscript '1') mainly consists of monomers. Therefore, $\rho_{<1>} \simeq \rho_1 = y_1\rho$, with $\rho$ the total number density of the mixture and with $\rho_1$ and $y_1$ the partial number density and the molar fraction of the condensing component in the gas phase. The compressibility factor of the mixture $Z = p/\rho kT$ must also be taken into account in the case of non-ideal mixtures. In addition, it must be recalled that $y_1$ is much smaller than the carrier gas molar fractions $y_{i\neq1}$ for our applications ($y_1 < 5000$ ppm), so that $\phi_1 \approx \phi_{1,\text{eq}}$ and, thus, $S \approx y_1/y_{1,\text{eq}}$ (see Eq. 2.16). As a result, accounting for the presence of the carrier gases in the non-ideal mixture leads to

$$\rho_{<1>} = \frac{y_1 p}{ZkT} = S\frac{p_{1,\text{s}} f_\text{e}}{ZkT} \quad \text{and} \quad \rho_{<1>}^{\text{eq}} = \frac{f_\text{e}\, p_{1,\text{s}}}{ZkT},$$  (2.45)

with the kinetic prefactor $K$ in Eq. 2.44 that becomes

$$K = \left(\frac{f_e p_{1,s}}{ZkT}\right)^2 S v_\ell \sqrt{\frac{2\sigma_\ell N_a}{\pi M_1}}. \tag{2.46}$$

Note that the liquid phase is considered to be incompressible, although the liquid compressibility may have an influence on the nucleation phenomena in non-ideal mixtures. Not to make the present analysis unnecessary complicated, the Luijten approach[88] is followed here and the molecular volume $v_1^\ell$ is calculated from the pure liquid density $\rho_1^\ell$ of the condensing component as $v_1^\ell = v_\ell = m_1/\rho_\ell$.

# Chapter 3

# Novel test section for homogeneous nucleation studies

The content of this chapter is based on the paper "M.M. Campagna, M.E.H. van Dongen, and D.M.J. Smeulders. Novel test section for homogeneous nucleation studies in a Pulse Expansion Wave Tube. Experimental verification and gas dynamic 2D numerical model. *Exp. Fluids*, 61(4):108, 2020" (Ref. 116). For coherence with the rest of the thesis, some of the symbols reported in Ref. 116 are modified in the present chapter. More details on the experimental procedure are added in Sec. 3.3, extending the corresponding section in Ref. 116.

***Abstract*** *A novel design of a Pulse Expansion Wave Tube (PEWT) for the study of homogeneous nucleation in mixtures of vapors and gases is presented. The main difference with the previous design consists in a test section with flat walls, which avoids that optical windows and pressure transducers do affect the flow field locally. Additionally, the test section length is reduced by a factor two. The performance of the wave tube is investigated both experimentally and numerically. The thermal insulation of the piezoelectric pressure sensor is proved to be beneficial for accurate measurements. The smallest thickness possible of the diaphragm, initially separating the high and low pressure sections of the PEWT, is also shown to be crucial. The flow phenomena are simulated with a 2D numerical model. It is shown to correctly predict the gas-dynamic features of the PEWT and the effects of the diaphragm opening process. Nucleation rates for water in helium are determined as a function of supersaturation for two different pressure conditions, 1 MPa and 0.1 MPa, at a temperature of 240 K. The good agreement with results from previous experiments shows that the geometrical mismatch of optical windows and pressure transducers in the original wave tube did not affect the nucleation rates significantly and that both the original and the new wave tube produce reliable measurement data.*

## 3.1 Introduction

Condensation has been actively studied for several decades, but, nevertheless, it remains an active research area with critical implications for many industrial and environmental applications. Carbon dioxide emission and industrial pollution are just two fields in which a profound knowledge of such phase transition plays a crucial role. Effects of condensation are also present in chemical reactors, aircraft, turbines and engine applications.[2] The oil and gas

industry is another important sector interested in condensation phenomena mainly for performance prediction and design improvement of natural gas impurity separators,[3] or even for the development of integrated devices to couple the removal of contaminants with the gas liquefaction process. Hence, a full comprehension of this phase transition and more accurate models would lead to beneficial consequences in a wide range of scientific and technological fields. A large variety of measurement techniques was applied in the past,[2] not only to verify and validate the theory, but also to elaborate corrections for the existing condensation models. The Pulse Expansion Wave Tube (PEWT) is one of the expansion based devices. Initially designed to cope with the lack of experimental data related to homogeneous condensation of hydrocarbons, it has been largely and effectively used with water as condensing vapor at a later time.[44,60,61,71,73–85] In this chapter we discuss a new PEWT measurement section with flat inner walls to allow a perfectly flush installation of optical windows and pressure sensors. As the rest of the tube remains cylindrical, a coupler section is installed as well, which enables a gradual transition of the cross-sectional shape from square to circular. Results of first wave experiments with the new gasdynamic facility will be presented including nucleation rate data for water-helium mixtures. Two-dimensional numerical simulations will be compared with experimental wave tube observations.

## 3.2   Working principle

Water condensation is considered homogeneous when the vapor to liquid transition takes place in absence of macroscopic surfaces or foreign particles. In heterogeneous condensation, such surfaces or particles act as starting points for the phase transition and a vapor pressure $p_v$ slightly above the saturated vapor pressure $p_s$ is sufficient to trigger the vapor to liquid transition. If such surfaces or impurity particles are absent, a gas-vapor mixture can easily become oversaturated ($p_v > p_s$). Nevertheless, due to the stochastic nature of the gas and the vapor molecules, clusters are formed. While the smallest ones dissolve, the largest clusters reach the so called critical size $n^*$ if adequate supersaturated conditions are met. After that, the critical clusters become stable droplets and grow by collision with the free vapor molecules. The process of critical cluster formation is known as homogeneous nucleation and it is followed by droplet growth. The number of critical clusters formed per unit of volume and time is the so called nucleation rate $J$. The critical size $n^*$ stands for the number of molecules constituting a critical cluster. A key parameter in nucleation research is the supersaturation $S$. Two specific cases are very useful. For an ideal vapor-gas mixture, $S$ is defined as[115]

$$S = \frac{p_v}{p_s}. \tag{3.1}$$

For a dilute non-ideal vapor-gas mixture, $S$ can be approximated as (see Eq. 2.16)

$$S \approx \frac{y}{y_{eq}}, \tag{3.2}$$

with $y$ the vapor molar fraction and $y_{eq}$ the equilibrium vapor molar fraction (see Sec. 2.1).

As shown by experimental evidence and confirmed by the Classical Nucleation Theory (CNT),[4–10,115] the nucleation rate strongly depends on supersaturation and temperature. Exploiting such dependency, the nucleation pulse method[49] is capable of separating in time the processes of nucleation and droplet growth, enabling an accurate determination of the nucleation rate. The working principle is sketched in FIG. 3.1. The initially undersaturated ($S < 1$)

vapor-gas mixture is first adiabatically expanded. The corresponding temperature drop causes the saturation level to increase far above unity ($S \gg 1$). This is due to the fact that, in case of homogeneous condensation, the partial vapor pressure $p_v$ decreases with the temperature much less than the saturated vapor pressure $p_s$. This state is maintained for a short time, the nucleation pulse, indicated in FIG. 3.1 with $\Delta t_p$. The supersaturation level for the pulse is chosen such that an appreciable amount of critical nuclei is formed. At the end of the pulse, the mixture is slightly recompressed, inhibiting the nucleation process to continue, but still keeping a supersaturated level ($S > 1$) for a relatively long period of time, in which the droplets can grow. In order to narrow the size distribution of the clusters, $\Delta t_p$ must be kept much shorter than the growth time interval. In this way, nucleation and droplet growth are effectively decoupled and the clusters can be assumed to be approximately monodisperse.[69]
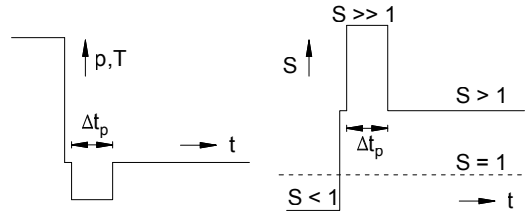


**FIG. 3.1.** Nucleation pulse method: pressure $p$, temperature $T$ and supersaturation $S$ vs. time $t$.

The first application of the nucleation pulse method dates back to 1965, when Allard and Kassner[49] designed a piston expansion chamber to expand and recompress the test mixture, with a pulse duration of 10 ms. In order to limit vapor depletion, polydispersity and the effect of heat released by the nucleating clusters, it is of fundamental importance to have a sufficiently short pulse duration. Therefore, Wagner and Strey[52] later improved the design of Allard and Kassner[49] with a two pistons cloud chamber and a 1 ms nucleation pulse. Peters[69] was the first to implement the nucleation pulse principle in a gasdynamic facility: the wave tube. The Peters' tube consists of two sections, the high pressure (driver section - HPS) and the low pressure (driven section - LPS), separated by a diaphragm. A schematic of the Peters' tube and its corresponding wave diagram is sketched in FIG. 3.2. After the diaphragm rupture, waves are generated: an expansion fan (E) moving towards the end wall of the HPS and a shock wave (sh) in the opposite direction. The idea of Peters was to partially reflect the shock into the HPS, by reducing the LPS cross sectional area, at position C just a few centimeters behind the diaphragm position D. Doing that, the test mixture at the observation point O is first subjected to an adiabatic expansion E. After a short time interval ($\Delta t_p$), the shock reflected at the cross section reduction C reaches the observation point O as a weak shock wave $sh_1$. In this way the mixture undergoes a slight, but sudden, recompression and the nucleation pulse nP ends. The mixture remains at constant pressure, coinciding with the droplet growth stage. The downside of such setup was that E and $sh_1$, reflected at the HPS end wall as rE and $rSh_1$ respectively, interact with the cross section reduction C, generating a second slight expansion $rE_a$ and a second weak shock $rSh_1c$. This may lead to a second nucleation stage (sP) at the observation point O, simultaneously with the droplet growth process.

The PEWT is a modified version of the Peters' wave tube by Looijmans *et al.*[70] The difference with the Peters' tube consisted in the elimination of the second nucleation pulse by replacing the cross sectional area reduction C with a local widening W. In FIG. 3.2 the PEWT configuration and the corresponding wave diagram are also sketched for comparison with the
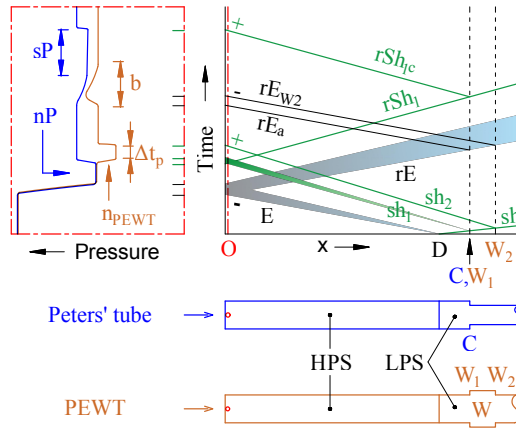
**FIG. 3.2.** Schematic x-t wave diagram for the Peters' tube [69] and for the Looijmans *et al.* PEWT. [70] The waves related to the expansion E are drawn with black solid lines, while the waves due to the shock sh are represented with green solid lines. The resulting pressure-time profiles at the observation point O are sketched in the red dashed-dotted box on the left side of the wave diagram for both the Peter' tube (blue solid line) and the PEWT (light-brown solid line). Below the wave diagram, the geometrical configuration of both tubes is also represented. The observation point O is situated at few mm from the end-wall of the HPS. The length of the HPS for the PEWT of Looijmans *et al.* [70] is about 125 cm, the distance between D and $W_1$ is about 18 cm and the widening (W) length is 15 cm. The diameter of the tube is 36 mm, while the widening diameter is 41 mm. For comparison purposes, the Peters' tube is represented here with the same dimensions of the PEWT and with a diameter of 31 mm for the LPS part on the right-hand-side of C.

Peters' tube. The modifications of Looijmans *et al.* [70] implied a different way for the shock sh to be reflected towards the observation point: at the enlargement $W_1$ as a weak expansion fan $sh_1$, at the restriction $W_2$ as a weak shock $sh_2$. The outcome was an isolated well-defined nucleation pulse $n_{PEWT}$. The end-wall reflected waves interact with the cross-sectional area change also in the PEWT case, with the difference that, beside a small recompression $rE_a$, also a second weak expansion $rE_{W2}$ at $W_2$ is generated because of rE. Nevertheless, no appreciable disturbance on the droplet growth process is present in this case, since the interference consists of a small positive pressure ripple b after the nucleation pulse $n_{PEWT}$. In this way, the resulting PEWT pressure-time profile at the observation point approximates the one prescribed by the nucleation pulse method (FIG. 3.1) and the decoupling of nucleation and droplet growth is achieved. Once the droplets grow to a detectable size, their size and concentration can be measured by optical means (details in Sec. 3.3).

## 3.3   Experimental methodology

The PEWT overall facility consists of three main parts (see FIG. 3.3): the mixture preparation device (MPD), [117] the pulse expansion wave tube PEWT and the optical setup.

The experimental procedure starts with the PEWT evacuation by means of two vacuum pumps (Alcatel Adixen ACP 15) $VP_H$ and $VP_L$, connected respectively to the HPS and the LPS. The two sides of the tube are kept separated by means of a polyester (PET) diaphragm placed at the diaphragm section D. Six possible diaphragm thicknesses from 30 $\mu m$ to 250 $\mu m$ are available, depending on the initial pressure difference. The evacuation procedure continues

until a moderate vacuum of about 2 mbar is obtained, measured via two vacuum manometers (Edwards 600 Barocel) denoted by $P_a$ and $P_b$ in FIG. 3.3. When this condition is reached, the valves $V_{H3}$ and $V_{L3}$ are closed and the evacuation ends. Note that the HPS is connected to the MPD at this stage, thus, the MPD is also evacuated by the vacuum pump at the HPS $VP_H$.

At this point, the valve $V_{hb}$ is closed and the vapor-gas mixture can be prepared in the MPD sketched in FIG. 3.3. The pure gas inside the gas bottle[a] $G_I$ flows in the MPD, where it is split into two flows $Q_A$ and $Q_B$.[b] The latter remains dry, while $Q_A$ is saturated[61] with the pure water[c] contained inside the two saturators $sat_a$ and $sat_b$. Before exiting the MPD, the fully saturated flow $Q'$ ($Q' = Q_A + Q_{H_2O}$) and the dry one $Q_B$ are mixed together. In this way, the mixture composition can be easily controlled by regulating $Q_A$ and $Q_B$ and by keeping constant the temperature $T_{mpd}$ and the pressure $p_{mpd}$ inside the MPD at known values.[d] It follows that the water molar fraction $y$ can be calculated as

$$y = \frac{Q_{H_2O}}{Q_{tot}} = \frac{y'_{eq}}{1 + (1 - y'_{eq})\frac{Q_B}{Q_A}}, \tag{3.3}$$

where $y'_{eq}$ is the equilibrium vapor molar fraction calculated at the MPD conditions as

$$y'_{eq} = \frac{Q_{H_2O}}{Q_{H_2O} + Q_A} = f_e(p_{mpd}, T_{mpd}) \frac{p_s(T_{mpd})}{p_{mpd}}, \tag{3.4}$$

with $f_e(p_{mpd}, T_{mpd})$ the enhancement factor (see Sec. 2.1.1) at $p_{mpd}$ and $T_{mpd}$ and $p_s(T_{mpd})$ the saturation pressure of pure water at $T_{mpd}$. More details on the MPD can be found in Ref. 117.

The total flow coming from the MPD ($Q_{tot} = Q_A + Q_{H_2O} + Q_B$) enters a heated box, where the pressure is reduced by a metering valve $V_{hb}$ from $p_{mpd}$ to $p_0$ in the HPS. In order to avoid condensation, the temperature in the heated box is kept at about 320 K, measured by the platinum resistance thermometer $T_{hb}$. At the exit of the metering valve, in the heated box, a static mixer smooths the fluctuations of the flow.[92]

The HPS is now filled with the prepared mixture, while the LPS is pressurized with the pure gas contained into the gas bottle $G_L$.

When the desired pressure levels are reached in both PEWT sides, valve $V_{L1}$ at the LPS is closed and the so-called flushing procedure starts at the HPS. In this stage, the pressure level inside the HPS is kept constant by means of an upstream pressure controller UPC and saturation of the tube walls takes place. A relative humidity sensor (RH, Vaisala HMP 124 B) constantly monitors the humidity level of the flow at the exit of the HPS, which keeps increasing during this stage. The flushing ends when the RH signal does not change in time anymore, meaning that no more net PEWT wall adsorption takes place. The mixture composition at the test section can be derived by calculating $y$ as in Eq. 3.3.

Once the wall saturation condition is reached, the bypass valve $V_b$ is opened and $V_{H1}$ and $V_{H2}$ are closed, isolating the HPS from the MPD. The wave experiment can be now run. It starts with the fast opening of the diaphragm separating the HPS from the LPS, which leads to the the wave pattern described in section 3.2 and sketched in FIG. 3.2. The concept and design

---

[a]Linde gas bottle with purity $> 99.999\%$ (type 5.0).

[b]Each flow is controlled with a Brooks 5850S mass flow controller (accuracy $\pm 0.2\%$ FS).

[c]Water purified with a demineralization cartridge BWT Ministil P-21 (resistivity $> 1.0\ M\Omega\,cm$).

[d]Pressure and temperature at the MPD are measured via a Druck PMP 4070 pressure transducer (accuracy $\pm 0.04\%$ FS) and two in house calibrated platinum resistance thermometers (accuracy $\pm 0.02$ K).
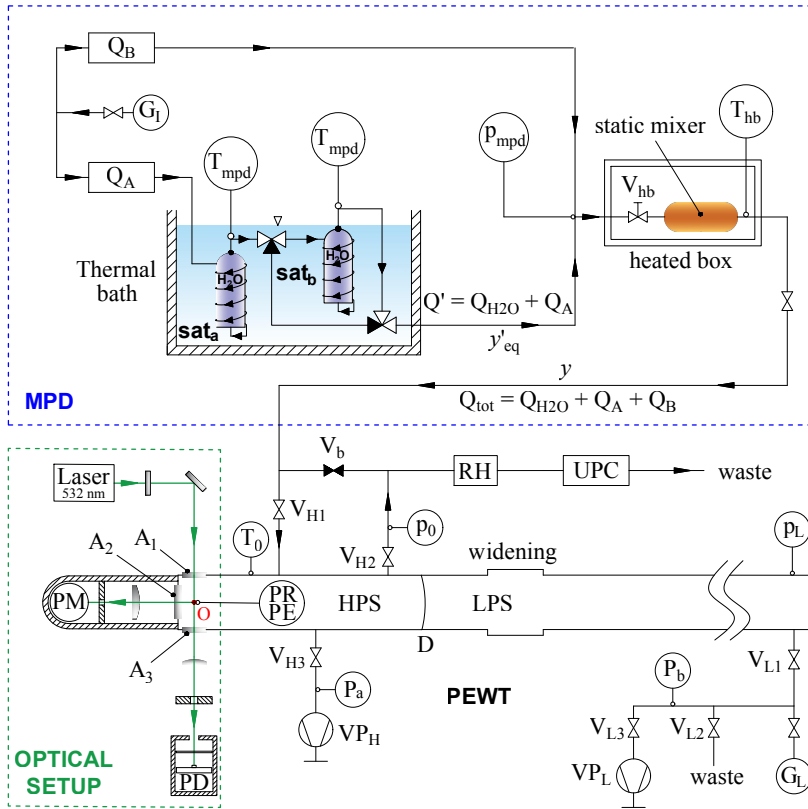
**FIG. 3.3.** Layout of the PEWT facility. The mixture preparation device MPD is indicated with a blue dotted line and the optical setup with a green dotted line. The test section with the flush mounted optical windows ($A_1$, $A_2$ and $A_3$) and the location of the pressure transducers (PR, PE) are the modified parts of the new HPS.

of the diaphragm section D was first introduced by Looijmans and van Dongen in 1977.[60] The present configuration is shown in FIG. 3.4. The fast opening is triggered by an electrical pulse (200 A - 300 A in 60 ms - 80 ms) trough a Kanthal ribbon (150 mm × 1.75 mm × 0.2 mm) positioned in a circumferential groove placed at the section D. The PET diaphragm remains in contact with the 0.2 mm side of the ribbon for the entire experimental procedure, being the LPS clamped to the HPS. The electrical pulse, increasing the Kanthal temperature to about 800 K, weakens the diaphragm, enabling the pressure difference to open it in a short time frame (~180 $\mu$s, see Sec. 3.5.1). It should be noted that the ribbon does not go all the way around the entire diaphragm circumference. At the top, a few millimeters are not wired. There the PET material will remain intact, thus creating a hinge for the diaphragm to rotate around.

After the diaphragm rupture, the pressure as a function of time at the observation point O is as shown in FIG. 3.5. Two transducers are used to measure the pressure at the test section wall, one piezoresistive (PR, Kistler 4073A50)[e] and one piezoelectric (PE, Kistler 603B). Details on the combined PR-PE measuring methodology can be found in Holten *et al.* (2005).[44]

---

[e]This sensor is used for the experiments with a pulse pressure up to 2 MPa. It is replaced by the Kistler 4073A10 for the experiments with a pulse pressure of 0.1 MPa.
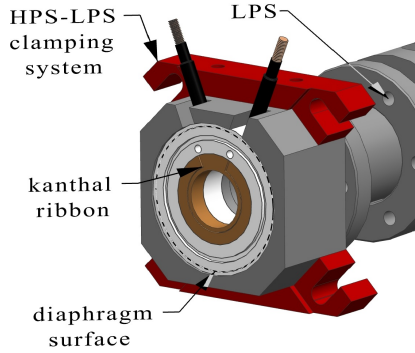
**FIG. 3.4.** 3D view of the PEWT diaphragm section (D).
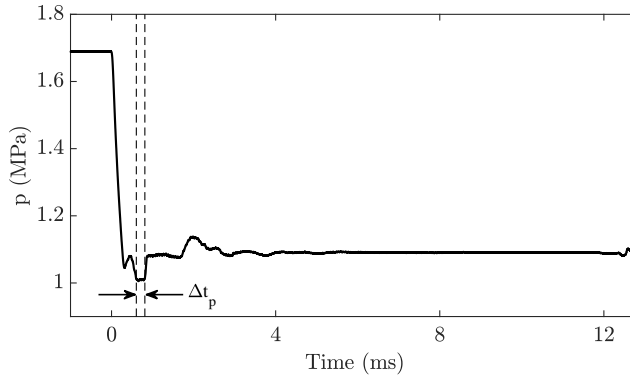


**FIG. 3.5.** PE pressure-time signal.

By using such measuring methodology, the uncertainty on the nucleation pulse pressure is less than 0.2%. Although the PE transducer is specifically suited for measuring rapid pressure variations, as in the case of the nucleation pulse technique, the used sensor suffers from a lack of thermal compensation when a temperature gradient is applied to it. Therefore, a coating layer (Dow Corning 732 black sealant) of half a millimeter has been applied to the PE sensing surface in order to insulate it from heat flow from the wall to the expanding gas. In Sec. 3.5.2, the effect of such coating on the performances of the PE transducer is analyzed. Wave experiments with dry helium have been performed to investigate the contribution of the PE transducer with and without coating layer. The temperature profile is derived from the pressure signal as follows. The initial temperature of the mixture is assumed equal to the test section wall temperature $T_0$, which is measured via two independent thermocouples (Temp-control PT-8316) with an accuracy of $\pm 0.03$ K.[85] Knowing the water molar fraction $y$, the entropy $s_0$ for the actual mixture can be calculated at the initial conditions $p_0$ and $T_0$. Assuming the process to be isentropic $\mathbb{S}(t) = \mathbb{S}(t = 0) = const$, the temperature as a function of time $T(t)$ is finally derived for each known pressure condition $p(t)$.[91]

Once the experimental pressure and temperature signals in time are known, it is possible to derive the pulse duration $\Delta t_{\text{p}}$ (FIG. 3.5). The corresponding supersaturation $S$ follows from equation 3.2, with $y$ the initial vapor molar fraction from the MPD and $y_{eq}$ the equilibrium

vapor molar fraction calculated at the pulse conditions.

Knowing that the experimental form of the nucleation rate is given by the equation

$$J = \frac{n_d}{\Delta t_p},$$ (3.5)

$J$ can be determined if the droplet number density $n_d$ is measured, being $\Delta t_p$ known from $p(t)$.

In order to measure $n_d$, the test section is equipped with the Optical Setup sketched in FIG. 3.3, based on the light scattering and the light beam attenuation. It consists of

- a linearly polarized 100:1 laser (Lasos Lasnova GLK 3220 T01 - wavelength $\lambda = 532$ nm) probing the test section through the optical window $A_1$ (see FIG. 3.3),

- a photomultiplier PM (Hamamatsu 1P28A) recording the $90^o$ scattered irradiance $I_{sca}(t)$ at the optical window $A_2$ (see FIG. 3.3),

- a photodiode PD (Telefunken BPW 34) measuring the transmitted laser light $I(t)$ leaving the test section from the optical window $A_3$ (see FIG. 3.3).

$A_1$, $A_2$ and $A_3$ (see FIG 3.3) are three BK7 glass windows. The laser beam interacts with the nearly monodisperse cloud of droplets generated during the nucleation pulse. As the droplets start to grow to an optically detectable size, $I_{sca}(t)$ and $I(t)$ are detected by the PM and the PD respectively. During the growth process, $I_{sca}(t)$ shows a characteristic peaks and valleys pattern of increasing intensity in time as reported in FIG. 3.6. Such pattern is strictly related to the droplet radius $r(t)$ for a fixed refractive index $m$ of the medium and wavelength $\lambda$ of the laser light. Simultaneously, as $r$ grows in time, $I(t)$ is attenuated proportionally to size and number density of the droplets. In FIG. 3.7, a typical attenuated transmitted light $I(t)/I_0$ is shown, with $I_0$ the initial undisturbed value of $I(t)$. The PM output is compared with the theoretical $90^o$ Mie scattered intensity $I_{sca,th}(\alpha)$, which is function of the non-dimensional droplet radius $\alpha = 2\pi r/\lambda$ at a fixed $\lambda$ and $m$. The $I_{sca,th}(\alpha)$ pattern for $\lambda = 532$ nm and $m = 1.33$ is shown in FIG. 3.8. The almost one to one correspondence between experimental (FIG. 3.6) and theoretical (FIG. 3.8) scatter qualitatively proves that the assumption of nearly monodisperse droplets[52,54,55] is well posed for the new PEWT.[f] Therefore, by comparing $I_{sca}(t)$ in FIG. 3.6 with the theoretical $I_{sca,th}(\alpha)$ in FIG. 3.8, the non-dimensional droplet growth rate $\alpha^2(t)$ in FIG. 3.9 can be obtained.

The $n_d$ determination follows from the Lambert-Beer law

$$\frac{I}{I_0} = \exp(-n_d\, \pi\, r^2\, Q_{ext}\, l),$$ (3.6)

with the the radius $r = \lambda\, \alpha/2\pi$ calculated from $\alpha^2(t)$ as given in FIG. 3.9. The parameter $l$ stands for the extinction length and it is taken equal to the inner diameter of the test section ($\sim 32$ mm for the new HPS, see Figures 3.11 and 3.12). The extinction efficiency term $Q_{ext}(\alpha)$ can be found in literature[118] and is a function of the non dimensional droplet radius $\alpha$ for fixed refractive indices $m$ and wavelengths $\lambda$.

---

[f]A quantitative estimate for the variation of the droplet size within the cloud is found as follows. A droplet formed at time $t_0$ within the pulse period $\Delta t_p$, grows according to $r^2$ proportional to $(t - t_0)$ as illustrated in FIG. 3.9 for diffusion dominated growth. Then, the width of the size distribution function is directly related to the possible variation in $t_0$, which is $\Delta t_p$: $\Delta r^2/r^2 = \Delta t_p/(t - t_0)$. For $\Delta t_p = 0.2$ ms and an average growth time of 6 ms, we find for the relative width: $\Delta r/r = 0.02$
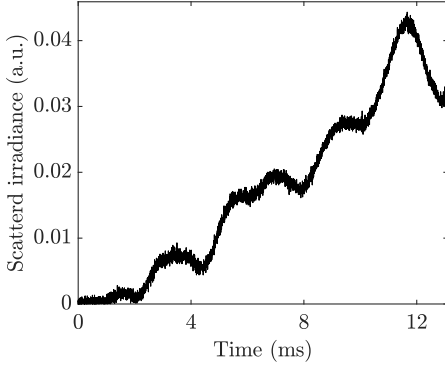
**FIG. 3.6.** PM 90$^o$ scattered light signal as a function of time.
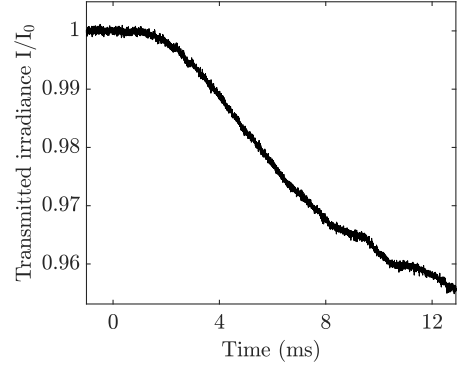


**FIG. 3.7.** PD relative transmitted light signal as a function of time.
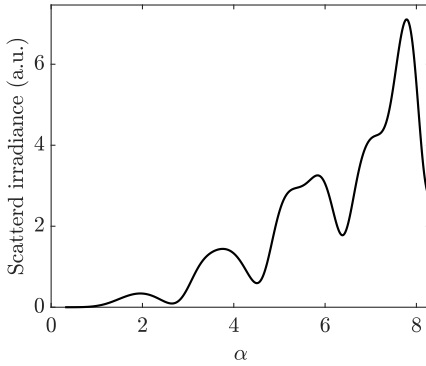


**FIG. 3.8.** Theoretical 90$^o$ Mie scattered intensity as a function of the non dimensional droplet radius $\alpha = 2\pi r/\lambda$ for a refractive index m = 1.33 and a wavelength $\lambda$ = 532 nm.
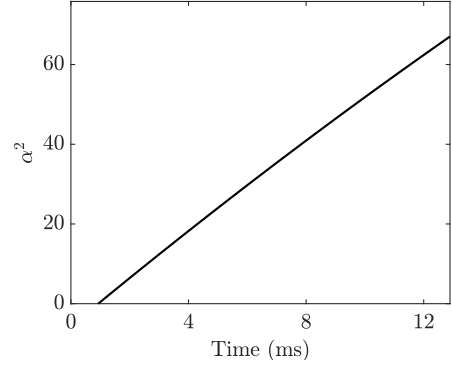


**FIG. 3.9.** Non-dimensional droplet growth rate curve $\alpha^2(t)$ obtained by comparing the experimental $I_{sca}(t)$ in FIG. 3.6 with the theoretical $I_{sca,th}(\alpha)$ in FIG. 3.8.

### 3.3.1 The newly designed HPS

A wide range of experimental conditions, accurate measurements of nucleation rates, droplet growth rates and supersaturation have made the PEWT technique a powerful tool for homogeneous condensation studies. Nucleation rate data can be determined for a wide range of pressures (0.1 MPa - 4 MPa) and temperatures (220 K - 260 K) and for different binary and ternary vapor-gas mixtures. The nucleation rates have a strong dependence on temperature, pressure and measured optical signals. In the previous version of the PEWT, a slight geometrical mismatch between the cylindrical test section wall and the flat surfaces of $A_1$, $A_3$, PE and PR was present. Such geometrical mismatch might generate local flow disturbances. Therefore, the PEWT high pressure section was redesigned, which also allowed for improved optical alignment.

The new design features a rectangular cross-sectional shape (see Figures 3.10 and 3.11). In this way, flat optical windows and measuring surface of the pressure transducers (PE, PR) have been mounted flush to the HPS wall, without any geometrical mismatch. In order to minimize the intersections between the main laser beam and the secondary reflections, the two optical

windows $A_1$ and $A_3$ (see also FIG. 3.3) have been positioned with the axis mutually parallel and $\pm 2$ mm distant from the center of the HPS. Doing that, the laser beam can enter the test section through $A_1$ with an inclination of $7^o$ (see FIG. 3.11), which prevents any possible optical interference.

The PEWT High Pressure Section (HPS) has been also shortened from a length of 1.25 m to about 0.66 m, which speeds up the filling procedure (see Sec. 3.3) and significantly reduces the gas consumption.

Three main parts have been assembled to compose the new HPS: the 0.375 m long test section HPS1 (see FIG. 3.10), which has a square cross area with rounded off corners (r = 2.67 mm) and a width of 32 mm (see FIG. 3.11); the outlet and vacuum valve section HPS3 (see FIG. 3.10) with a circular cross area shape as the LPS, diameter of 36 mm (B-B) and length of 0.167 m; the transition part HPS2, having a length of 0.116 m and designed to facilitate a gradual cross section transition from the circular shape of HPS3 to the square shape of HPS1 (see FIG. 3.10).

The test section distance from the HPS end-wall has been increased to 10 mm as shown in FIG. 3.10. In this way, the thermal boundary layer developing from the walls towards the core of the tube does not represent a possible source of disturbance for the last part of the droplet growth process.[88,119]

The PEWT performances have been examined with two different experimental campaigns. During the first one, the setup has been tested at four different pressure ranges with pure helium, analyzing

- the added value brought to the measurement quality by the PE with respect to the PR,

- the effect of the coating on the PE measuring surface, applied to protect it from exchange of heat with the gas during the wave experiment,

- the influence of the diaphragm thickness on the pressure profile at the observation point.

The above mentioned tests have been exploited as reference to design and verify the 2D numerical model described in Sec. 3.4.
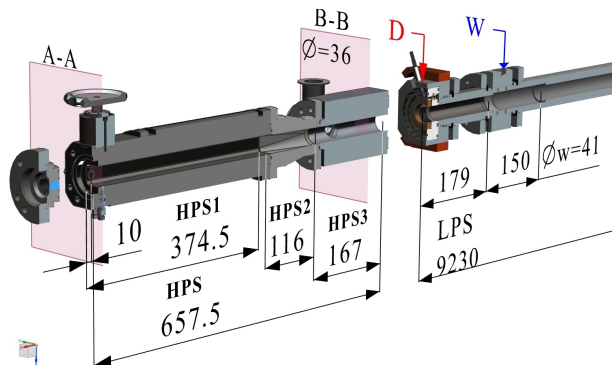


**FIG. 3.10.** New HPS: sectioned 3D view of the PEWT (all dimensions in mm). The diaphragm section and the widening (internal diameter $\Phi_w$ = 41 mm) are indicated with the letters D and W respectively. Details on the observation plane (section A-A) are represented in FIG. 3.11. The rest of the PEWT is characterized by an internal diameter $\Phi$ of 36 mm, specified at the section B-B.
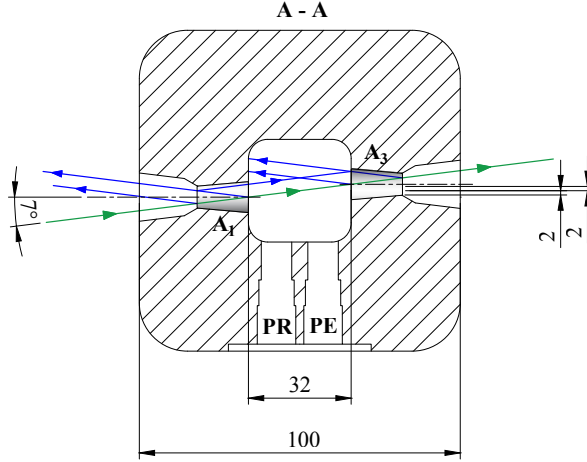
**FIG. 3.11.** New rectangular test section side view (dimensions in mm). The flush mounted optical windows ($A_1$ and $A_3$) and pressure transducers (PE and PR) can be noted. The laser beam (green solid line) enters the test section from the left side (window $A_1$) and exits it from the right side (window $A_3$). The secondary reflections are also represented (blue solid lines).

The second experimental campaign has been executed with the purpose of testing the reliability of the modified PEWT setup by performing homogeneous water nucleation and droplet growth experiments. The tested nucleation pressure and temperature conditions have been 1 MPa and 240 K, respectively. Helium has been chosen as carrier gas and the results have been compared to the data obtained by Fransen *et al.* (2015)[85] at the same experimental conditions with the previous PEWT version. Details on both test campaigns will be given in Sec. 3.5.2.

## 3.4 2D Numerical Model

### 3.4.1 Computational Domain, Numerical Settings and Grid Independence Study

The PEWT has been modeled in a two dimensional manner. Details on the geometrical domain are sketched in FIG. 3.12. The 3D area variation of the PEWT has been modeled in a 2D manner by changing the widening vertical dimension from 41 mm to 46.7 mm. This choice allowed to keep the same relative cross-sectional area ratio when passing from the 3D geometry to the 2D model.

The numerical model is based on non-stationary 2D Euler equations:

$$\frac{\partial \mathbb{U}}{\partial t} + \frac{\partial \mathbf{X}}{\partial x} + \frac{\partial \mathbf{Y}}{\partial y} = 0, \tag{3.7}$$

with $\mathbb{U}$ the vector of unknowns and $\mathbf{X}$ and $\mathbf{Y}$ convective fluxes in x and y direction respectively:

$$\mathbb{U} = \begin{pmatrix} \rho \\ \rho u \\ \rho v \\ \rho E \end{pmatrix}; \ \mathbf{X} = \begin{pmatrix} \rho u \\ \rho u^2 + p \\ \rho uv \\ (\rho E + p)u \end{pmatrix}; \ \mathbf{Y} = \begin{pmatrix} \rho v \\ \rho uv \\ \rho u^2 + p \\ (\rho E + p)v \end{pmatrix}; \tag{3.8}$$
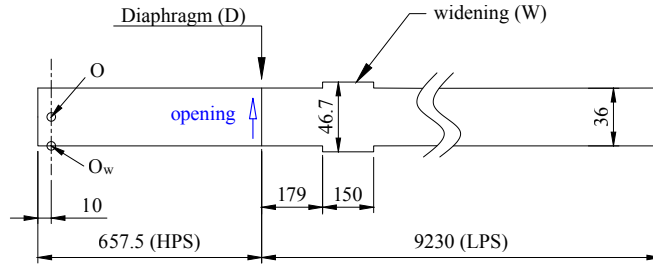
**FIG. 3.12.** 2D model domain (dimensions in mm). The blue arrow (↑) indicates the diaphragm opening direction.

Eqs. 3.8 have been solved in a coupled manner by means of the density-based explicit solution method present in the commercial software ANSYS® Fluent®. The discretization of the convective fluxes **X** and **Y** has been performed by means of the *Advection Upstream Splitting Method* (AUSM). For the spacial discretization, the *Least Squares Cell Based Gradient* has been employed, while the *Third Order Monotone Upstream - Centered Scheme* (MUSCL) has been exploited for the flow discretization. The time integration of the governing equations has been performed by means of a second order implicit formulation. Helium has been chosen as simulated gas and it is assumed to behave as a calorically prefect gas. In order to minimize the numerical errors due to the grid choice, different mesh sizes have been tested for accuracy and computational time ($\Delta x$ and $\Delta y$ both decreasing from 6 mm to 1 mm). Instantaneous opening of the diaphragm has been considered at this stage. A mesh size with $\Delta x = 4$ mm and $\Delta y = 2$ mm has been selected.

Preliminary results of the 2D numerical model are reported in FIG. 3.13, where the pressure (FIG. 3.13a) and the temperature (FIG. 3.13b) profiles in time are compared with the reference experimental results of test 2c* (TABLE 3.1). It should be noticed that the shown numerical results are taken at the observation plane wall $O_w$ at this stage. Such a choice has been possible only after the verification of a perfect overlapping for the results taken at $O_w$ and at the observation point O, when the diaphragm opening process is modeled as instantaneous. The simulated pressure and temperature profiles in time shown in FIG. 3.13 differ from the experimental results in three regions: at the first expansion E, at the pulse $n_{PEWT}$ and at the ripple *b*. Such differences are due to two main reasons. In the first place, the diaphragm opening process has been simulated as instantaneous at this stage, while such assumption is far from the reality. For this reason, the finite diaphragm opening process will be implemented in the 2D numerical model as explained in the next Sec. 3.4.2. Secondly, the presence of the contact discontinuity, clearly visible on the wave diagram in FIG. 3.13b, might have interacted with the reflected expansion rE in the proximity of $W_1$, contributing with a small overshoot to the ripple *b*. The latter hypothesis has been verified by simulating the exact same conditions, but without widening in the geometrical domain. A small recompression has been observed, caused by the interaction between the expansion E and the only contact discontinuity.

### 3.4.2   Modeling of the Diaphragm Opening Process

The 3D opening process of the diaphragm, described in Sec. 3.3, has been simplified for the present 2D model in the following way. It has been assumed that the diaphragm slides away
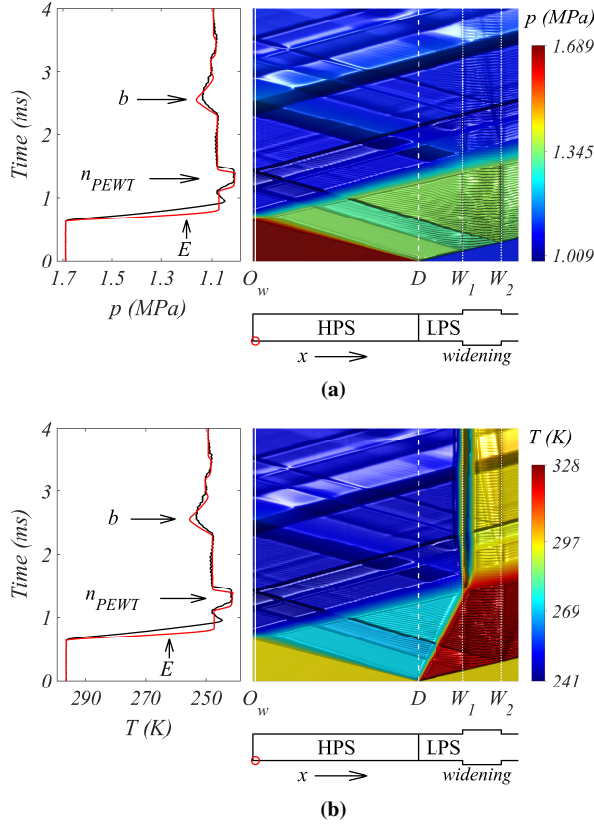
**FIG. 3.13.** Pressure (3.13a) and temperature (3.13b) map on the x-t wave diagram. The latter is derived from the 2D numerical tool described in this chapter, with the represented data taken at the tube wall line in time. The simulated initial conditions are the same as for the test 2c* (TABLE 3.1) and the diaphragm opening process is modeled as instantaneous. On the left side of both figures, the pressure (3.13a) and temperature (3.13b) profiles in time (red solid line) are compared to the experimental results (black solid line) of test 2c* (TABLE 3.1). The simulated profiles are taken at the observation plane wall ($O_w$), where the transducers are placed (red circle).

as indicated by the blue arrow sketched in FIG. 3.12, so that the open area becomes[120]

$$\frac{A}{A_{\text{diaph}}} = \left(\frac{d}{d_{\text{diaph}}}\right)^2 = \left(\frac{t}{t_{\text{diaph}}}\right)^{1/a}, \tag{3.9}$$

with $t_{\text{diaph}}$ the total opening time of the diaphragm, $A$ the open area of the diaphragm ($d$ the open diaphragm dimension in the 2D model) at the time $t$ and $A_{\text{diaph}}$ the total area of the diaphragm ($d_{\text{diaph}}$ the total diaphragm dimension).

The duration of each opening time step has been chosen to be 8 ms. The modeled diaphragm has been divided in 18 segments. The initial boundary condition for the whole diaphragm geometry has been set to be a *wall*, which perfectly separates the HPS from the LPS side. After that, at each consecutive opening time-step, the boundary condition for each piece of the diaphragm has been dynamically changed from *wall* to *interior* type, starting from the bottom piece of the diaphragm. In this way, with such discrete *piece-wise step function*, it has been possible to closely approximate the continuous 3D aperture process of the diaphragm.

A parametric study has been performed on $a$ and $t_{\mathrm{diaph}}$. In first instance the exponent $a$ has been varied from 1/2 to 1/8 (see FIG. 3.14), with $t_{\mathrm{diaph}}$ kept fixed at 136 $\mu$s.[70] The best agreement with the reference pressure-time profile of test 2c* (TABLE 3.1) has been found for $a = 3/8$.
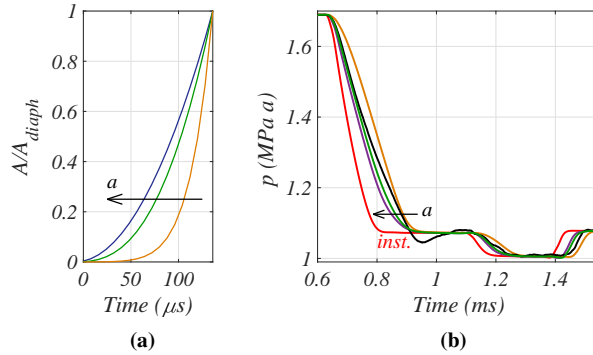


**FIG. 3.14.** Parametric study performed with total opening time $t_{\mathrm{diaph}}$=136 $\mu$s and varying the exponent a: a=1/2 (purple line), a=3/8 (green line) and a=1/8 (brown line). The different diaphragm opening function $A(t)$ are shown in 3.14a. In 3.14b the reference pressure-time profile (black line, test 2c*, TABLE 3.1) is compared to the simulated $p(t)$ in $O$. The pressure profile with instantaneous diaphragm opening is also reported (red line).

Then, $t_{\mathrm{diaph}}$ has been varied from 136 $\mu$s to 232 $\mu$s (see FIG. 3.15), with $a = 3/8$. A perfect agreement with the experimental reference (test 2c*, Table 3.1) has been found for $t_{\mathrm{diaph}}$=184 $\mu$s. The 2D numerical model has been also verified with all the other experimental conditions reported in TABLE 3.1 as reference and a perfect agreement has been obtained at any condition.
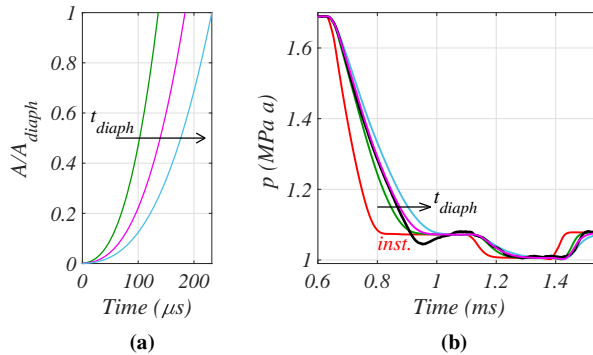


**FIG. 3.15.** Parametric study performed with total opening time a=3/8 and varying the total opening time of the diaphragm: $t_{\mathrm{diaph}} = 136$ $\mu$s (green line), $t_{\mathrm{diaph}} = 184$ $\mu$s (magenta line) $t_{\mathrm{diaph}} = 232$ $\mu$s (cyan line). The different diaphragm opening function $A(t)$ are shown in 3.15a. In 3.15b the reference $p(t)$ profile (black line, test 2c*, Table 3.1) is compared with the simulated ones taken in $O$. The pressure profile with instantaneous diaphragm opening is also reported (red line).

## 3.5 Results and discussion

### 3.5.1 Numerical results

Now that the complete 2D numerical model has been validated, it is possible to analyze the pressure-time profile at the bottom wall of the observation plane (A-A, see FIG. 3.10), namely $O_w$ (see FIG. 3.12), where the pressure transducers are placed. The comparison between the numerical and the reference experimental $p(t)$ and $T(t)$ profiles shows a perfect agreement, when the diaphragm opening process is included in the 2D numerical model (see FIG. 3.16). It must be also underlined that, by modeling the diaphragm opening process, the overshoot of the numerical $p(t)$ with respect to the experimental pressure at the ripple $b$ disappears (compare FIG. 3.13 to FIG. 3.16). This is due to the different position of the contact discontinuity when the reflected expansion wave rE reaches $W_1$ (see FIG. 3.16b). As evident in FIG. 3.17, the experimental oscillations present at the plateau ($t = 1.5 \div 2.2$ ms) and at the bottom of the
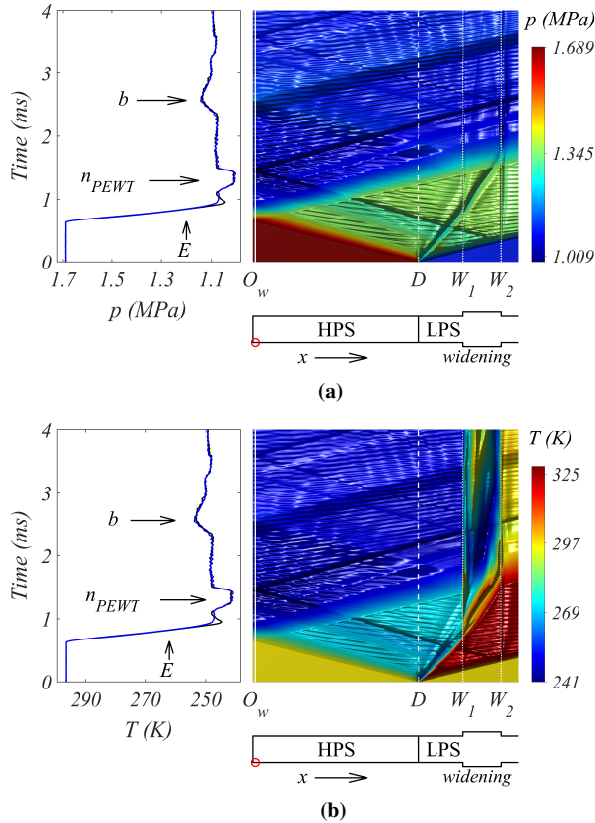


**FIG. 3.16.** Pressure (3.16a) and temperature (3.16a) map on the x-t wave diagram. The latter is derived from the 2D numerical tool described in this chapter, with the represented data taken at the tube wall line in time. The simulated initial conditions are the same as for the test 2c* (TABLE 3.1) and the diaphragm opening process is modeled with a=3/8 and $t_{\text{diaph}}$=184 $\mu$s. On the left side of both figures, the pressure (3.16a) and temperature (3.16b) profiles in time (blue line) are compared to the $p(t)$ and $T(t)$ (black line) of test 2c* (TABLE 3.1). The simulated profiles are taken at the observation plane wall $O_w$, where PR and PE are placed (red circle).
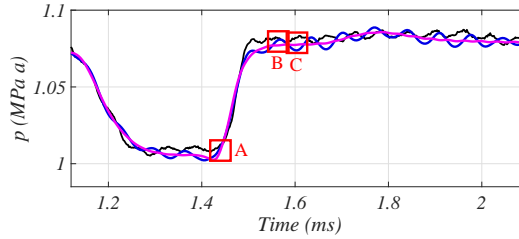
**FIG. 3.17.** Pressure-time profile at $O$ (purple line) and $O_w$ (blue line) with emphasis on the pulse ($t = 1.24 \div 1.44$ ms) and the plateau ($t = 1.5 \div 2.2$ ms). The experimental pressure measured at $O_w$ for the test condition 2c$^*$ (TABLE 3.1) is used as reference (black line).

pulse ($t = 1.24 \div 1.44$ ms) are also appreciable in the numerical results at $O_w$. On the contrary, such oscillations appears to be damped at the observation point $O$ for the numerical results. An additional proof of such pressure oscillations is reported in FIG. 3.18. The position and the shape of the sh$_2$ front wave is highlighted by narrowing the color-map around the pressure value in O at the beginning of the pulse recompression $t_A = 1.44$ ms (see FIG. 3.18b). The evolution in time of such wave is shown by considering the time step before ($t_A$-0.004 ms, see FIG. 3.18a) and after ($t_A$+0.004 ms, see FIG. 3.18c) $t_A$. A typical oscillation over-shoot (B) and under-shoot (C) of the pressure at $O_w$ are shown in FIGS. 3.18d and 3.18e respectively. In these cases, the color-map has been narrowed around the pressure value in O at the time $t_B$ and $t_C$. In this way, it is evident as the pressure in $O_w$ alternatively increases and decreases in time with respect to the pressure in $O$. Moreover, the s-shape of the waves, visible in FIGS. 3.18a, 3.18b and 3.18c, appears to be absent for instantaneous opening of the diaphragm. In the latter case, the waves are parallel to the HPS end-wall and the pressure oscillations are completely absent at $O_w$ (see the wave diagrams in FIGS. 3.13a and 3.13b). The ripples of the pressure at O$_w$ in time are more evident in FIG. 3.19. It can be concluded that the pressure oscillations are caused by the 2D diaphragm opening process. Moreover, such disturbances appear to be sensed by the transducers, placed at the bottom wall of the observation plane A-A, while they are strongly muffled at the observation point O. Therefore, no disturbances are expected to affect the flow field at the observation point $O$.

### 3.5.2 Experimental results

The first experimental campaign with the modified version of the PEWT has been performed by running four sets of wave experiments with pure dry helium. Each set of tests corresponds to a different pulse pressure level $p$. Four levels have been checked. The pressure $p$ and temperature $T$ values, averaged over the pulse duration $\Delta t_p$, are presented in TABLE 3.1. The superscript '$*$' indicates the tests performed applying the coating layer to the PE transducer (Sec. 3.3). The typical temperature profiles are shown in FIG. 3.20. One observes a small but significant difference between the two nucleation temperatures derived from both pressure transducer signals, when the PE is uncoated. It must be noted that a temperature error of 1 K corresponds to a shift in nucleation rate by more than a factor two. The temperature difference disappears when the PE transducer is coated, indicating that the thermal insulation of the coating is effective. Different diaphragm thicknesses have also been tested at 0.5 MPa and 1 MPa and the results are summarized in TABLE 3.1. The 75 $\mu$m and 125 $\mu$m diaphragms show an influence on the pulse duration $\Delta t_p$, reducing the available time for the mixture to
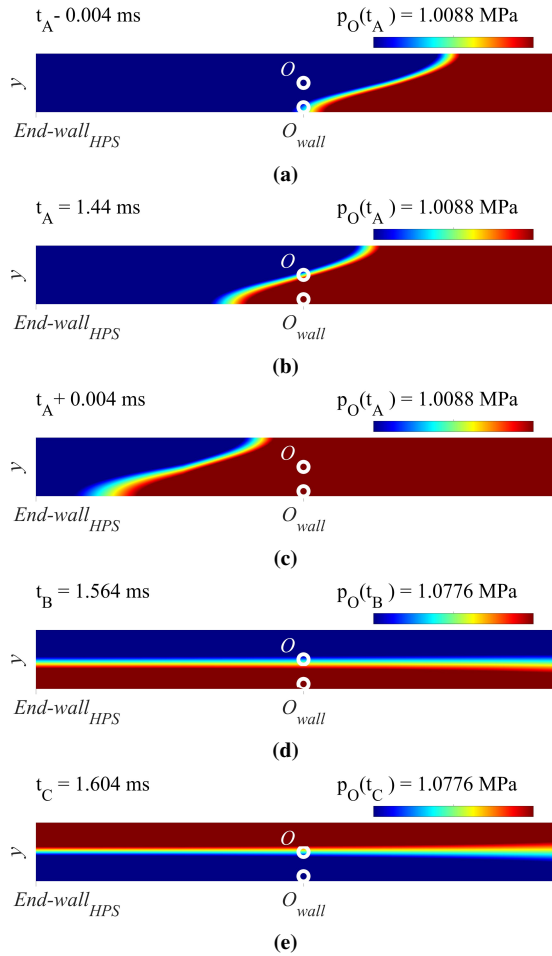
**FIG. 3.18.** Simulated pressure color-map of the HPS, narrowed around the reference pressure $p_0$ at different times: **(a)** $t_A$-0.004 ms, **(b)** $t_A$ = 1.44 ms, **(c)** $t_A$+0.004 ms, **(d)** $t_B$ = 1.564 ms, **(e)** $t_C$ = 1.604 ms. A, B and C are highlighted in FIG. 3.17.
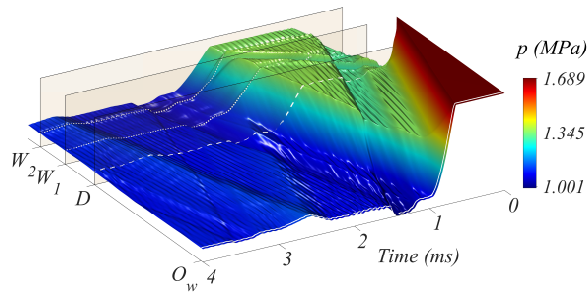


**FIG. 3.19.** Pressure map of FIG. 3.16a in 3D form. The z-direction is representative of the pressure level

**(a)**



**(b)**
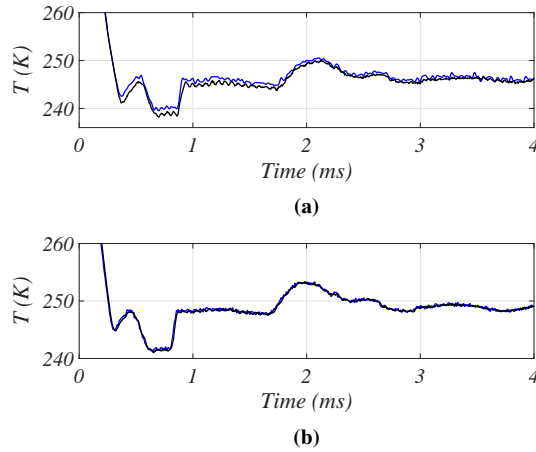
**FIG. 3.20.** Temperature profiles at the nucleation pulse derived from the PR (black line) and from the PE (blue line) pressure signals. In (3.20a) the temperature profiles of the test 2a (TABLE 3.1) with uncoated-PE transducer and in (3.20b) the temperature profiles with the test 2c* (TABLE 3.1) with coated-PE.

**TABLE 3.1.** Wave experiments overview.

| Wave | Diaphragm | $\Delta t_p$ | p | $\Delta p$ | T | $\Delta T$ |
|------|-----------|--------------|------|------------|------|------------|
| Exp. | $\mu$m | msec | MPa | % | K | % |
| 1a | 50 | 0.210 | 0.488 | 1.20 | 237.6 | 0.48 |
| 1c* | 50 | 0.210 | 0.494 | 0.49 | 241.5 | 0.20 |
| 1d* | 75 | 0.205 | 0.492 | 0.38 | 241.4 | 0.15 |
| 2a | 50 | 0.215 | 0.995 | 1.37 | 240.1 | 0.55 |
| 2c* | 50 | 0.208 | 1.012 | 0.19 | 241.7 | 0.08 |
| 2d* | 75 | 0.194 | 1.001 | 0.27 | 240.3 | 0.11 |
| 2e* | 125 | 0.180 | 0.987 | 0.24 | 240.2 | 0.09 |
| 3a | 125 | 0.180 | 1.479 | 1.25 | 238.8 | 0.50 |
| 3c* | 125 | 0.180 | 1.489 | 0.29 | 241.9 | 0.12 |
| 4a | 125 | 0.190 | 1.968 | 1.17 | 238.5 | 0.47 |
| 4c* | 125 | 0.185 | 1.982 | 0.18 | 241.9 | 0.07 |

The superscript "*" denotes the experiments performed with coated PE. Diaphragm and $\Delta t_p$ indicate thicknesses of the diaphragm and pulse duration of each experiment. The superscripts "PR" and "PE" denote the quantities derived from piezoresistive and piezoelectric transducer respectively. $\Delta p = (p^{PR} - p^{PE}) \cdot 100/p^{PR}$ and $\Delta T = (T_{PR} - T_{PE}) \cdot 100/T_{PR}$ are the relative percentage difference between the PR and PE measures.

nucleate. This effect points out the importance of using the thinnest diaphragm possible, provided that it stands the pressure difference existing between HPS and LPS at the beginning of the experiment.

A second experimental campaign has been carried out in order to verify the performances of the novel design. Several homogeneous water nucleation experiments have been run with

helium as carrier gas and a pulse temperature of about 240 K. Two nucleation pressures have been tested, 1 MPa and 0.1 MPa, at different supersaturation levels. In FIG. 3.21 the results for such tests are presented in terms of nucleation rate $J$ - supersaturation $S$ data. A data overview of the nucleation experiments presented in this chapter is given in TABLE 3.2 (see also Appendix B for more details). For both pressure conditions, a coating layer has been applied to the PE sensing surface and a diaphragm thickness of 50 $\mu$m and 40 $\mu$m has been found to be the optimal choice at 1 MPa and 0.1 MPa, respectively. The measured $J$ - $S$ values are compared with the data obtained by Fransen *et al.* (2015)[85] at the same conditions, but with the previous version of the PEWT. The main result to be underlined is the substantial agreement with the literature data,[85] which demonstrates the well functioning of the PEWT, in the new version as in the original one of Looijmans.[70]
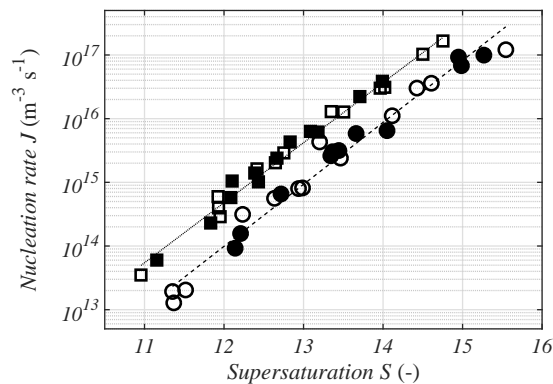


**FIG. 3.21.** Experimental data overview of the water nucleation rates $J$ as a function of the supersaturation $S$ at 240 K in helium. The data obtained with the new version of the PEWT at 1 MPa (filled squares) and 0.1 MPa (filled circles) are presented. A data overview is reported in TABLE 3.2 (see also Appendix B). The data of Fransen *et al.*[85] at 1 MPa (open squares) and 0.1 MPa (open circles), obtained with the previous PEWT version, are also shown for comparison. The two trend lines at 1 MPa (dotted line) and 0.1 MPa (dashed line) have the only purpose of guiding the eye.

## 3.6 Conclusions

The High Pressure Section (HPS) of the PEWT for homogeneous condensation experiments has been redesigned. A square-shape cross-section has been chosen for the test section in order to accommodate, without any geometrical mismatch, the pressure transducers (PR and PE) and two of the three optical windows ($A_1$ and $A_3$). The HPS has been also halved in length with the scope of a faster experimental procedure and a reduced gas consumption. Two test campaigns have been carried out in order to verify, with the first one, the gas-dynamic performances of the modified PEWT and, with the second campaign, the nucleation rate $J$ - supersaturation $S$ data quality when homogeneous condensation experiments are run. The homogeneous water nucleation data $J$ - $S$ obtained at 240 K and at two pressure conditions, 1 MPa and 0.1 MPa, in helium with the newly designed PEWT have been shown to be perfectly aligned with previous measurements performed, at the same experimental conditions, by means of the previous version of the PEWT. This means that the modified wave tube is functioning properly. Moreover,

**TABLE 3.2.** Experimental data overview of the water nucleation experiments performed with the new version of the PEWT discussed in this chapter and reported in FIG. 3.21.

| Test | $p_{mpd}$ | $T_{mpd}$ | $y$ | $p$ | $T$ | $\Delta t_p$ | $n_d$ | $J$ | $S$ |
|------|------|------|------|------|------|------|------|------|------|
|      | MPa | K | ppm | MPa | K | ms | m$^{-3}$ | m$^{-3}$s$^{-1}$ | |
| 1  | 3.20  | 296.38 | 504  | 1.00949 | 241.46 | 0.208 | 2.18E+11 | 1.05E+15 | 12.10 |
| 2  | 3.20  | 296.68 | 514  | 1.00383 | 241.32 | 0.202 | 2.83E+11 | 1.40E+15 | 12.39 |
| 3  | 3.20  | 296.15 | 494  | 0.99907 | 240.41 | 0.206 | 4.94E+11 | 2.40E+15 | 12.67 |
| 4  | 3.20  | 296.14 | 494  | 0.99285 | 239.75 | 0.204 | 1.26E+12 | 6.17E+15 | 13.18 |
| 5  | 3.20  | 296.64 | 509  | 0.99512 | 240.31 | 0.206 | 1.30E+12 | 6.32E+15 | 13.09 |
| 6  | 2.575 | 291.11 | 448  | 0.98943 | 239.85 | 0.200 | 4.60E+10 | 2.30E+14 | 11.83 |
| 7  | 2.575 | 291.08 | 529  | 0.99342 | 239.87 | 0.204 | 7.88E+12 | 3.86E+16 | 13.99 |
| 8  | 2.575 | 291.12 | 489  | 0.98796 | 240.75 | 0.204 | 1.18E+11 | 5.77E+14 | 12.09 |
| 9  | 2.575 | 291.07 | 488  | 0.98861 | 239.89 | 0.202 | 8.69E+11 | 4.30E+15 | 12.83 |
| 10 | 2.558 | 291.08 | 488  | 0.99004 | 240.37 | 0.200 | 2.03E+11 | 1.02E+15 | 12.43 |
| 11 | 2.575 | 291.08 | 447  | 0.99771 | 240.76 | 0.206 | 1.24E+10 | 6.01E+13 | 11.15 |
| 12 | 2.575 | 291.06 | 516  | 0.98930 | 239.75 | 0.210 | 4.67E+12 | 2.22E+16 | 13.71 |
| 13 | 0.3   | 291.02 | 4803 | 0.10405 | 239.92 | 0.142 | 4.29E+11 | 3.02E+15 | 13.37 |
| 14 | 0.3   | 291.03 | 4797 | 0.10453 | 240.67 | 0.148 | 9.71E+10 | 6.56E+14 | 12.72 |
| 15 | 0.3   | 291.02 | 4795 | 0.10317 | 239.80 | 0.146 | 3.82E+11 | 2.61E+15 | 13.34 |
| 16 | 0.3   | 291.02 | 5313 | 0.10494 | 241.39 | 0.152 | 4.80E+11 | 3.16E+15 | 13.44 |
| 17 | 0.3   | 291.01 | 5188 | 0.10269 | 239.22 | 0.148 | 1.37E+13 | 9.26E+16 | 14.95 |
| 18 | 0.3   | 291.02 | 5311 | 0.10247 | 239.22 | 0.144 | 1.43E+13 | 9.95E+16 | 15.27 |
| 19 | 0.3   | 291.02 | 5310 | 0.10252 | 239.50 | 0.142 | 9.65E+12 | 6.80E+16 | 14.99 |
| 20 | 0.3   | 291.01 | 4884 | 0.10424 | 239.47 | 0.134 | 8.69E+11 | 6.48E+15 | 14.05 |
| 21 | 0.3   | 291.01 | 4889 | 0.10432 | 239.90 | 0.142 | 8.30E+11 | 5.85E+15 | 13.66 |
| 22 | 0.4   | 291.01 | 4243 | 0.10397 | 239.52 | 0.138 | 1.28E+10 | 9.24E+13 | 12.14 |
| 23 | 0.4   | 291.01 | 4177 | 0.10387 | 239.20 | 0.136 | 2.14E+10 | 1.57E+14 | 12.21 |

The subscript "mpd" denotes the MPD quantities, while $p$ and $T$ are the pulse pressure and temperature.

it also implies that the quality of the nucleation rate data obtained with the previous version of PEWT, is not significantly affected by the slight mismatch of the flat windows and transducers with the circular walls of the previous test section. Both campaigns have demonstrated the combination of piezoresistive (PR) and fast responding coated-piezoelectric (PE) transducers to be essential for the purpose of providing a much more accurate measuring of the mixture thermodynamic conditions during the PEWT experiments. The importance of the diaphragm has also been pointed out, proving that the choice of the thinnest diaphragm thickness possible is crucial to minimize the intrusiveness of the diaphragm opening process. Additionally, a 2D numerical model has been successfully developed for the PEWT, representing a powerful support for the design of the forthcoming experiments. Such tool has been shown to correctly predict all gasdynamic features of the PEWT, including the opening process and the total opening time of the diaphragm and it has been possible to exclude the presence of any disturbances on the flow field at the observation point.

# Chapter 4

# Homogeneous water nucleation in nitrogen and in argon

The content of this chapter is an unabridged version of the paper "M.M. Campagna, J. Hrubý, M.E.H. van Dongen, and D.M.J. Smeulders. Homogeneous water nucleation: Experimental study on pressure and carrier gas effects. *J. Chem. Phys.* 153(16):164303, 2020" (Ref. 121).

***Abstract*** *Homogeneous nucleation of water is investigated in argon and in nitrogen at about 240 K and 0.1 MPa, 1 MPa and 2 MPa, by means of the Pulse Expansion Wave Tube. The surface tension reduction at high pressure qualitatively explains the observed enhancement of the nucleation rate of water as well in argon as in nitrogen. The differences in nucleation rates for the two mixtures at high pressure are consistent with the differences in adsorption behavior of the different carrier gas molecules. At low pressure, there is not enough carrier gas available to ensure the growing clusters are adequately thermalized by collisions with carrier gas molecules, so that the nucleation rate is lower than under isothermal conditions. This reduction depends on carrier gas, pressure and temperature. A qualitative agreement between experiments and theory is found for argon and nitrogen as carrier gases. As expected, the reduction of the nucleation rates is more pronounced at higher temperatures. For helium as carrier gas, non-isothermal effects appear to be substantially stronger than predicted by theory. The critical cluster sizes are determined experimentally and theoretically, according to the Gibbs-Thomson equation, showing a reasonable agreement as documented in literature. Finally, we propose an empirical correction of the classical nucleation theory for the nucleation rate calculation. The empirical expression is in agreement with the experimental data for the analyzed mixtures (water-helium, water-argon and water-nitrogen) and thermodynamic conditions (0.06 MPa-2 MPa and 220 K-260 K).*

## 4.1 Introduction

Numerous studies have been reported on the dropwise vapor to liquid phase transition since the pioneering work of C.T.R. Wilson in 1879.[1] An extensive overview of the past 100+ years of experimental and theoretical developments in condensation study has been published by Wyslouzil and Wölk (2016).[2] One of the puzzling aspects is the effect of carrier gas and pressure on nucleation.[77,78,87,113,122] A successful facility to study homogeneous nucleation is the Pulse Expansion Wave Tube (PEWT). It offers the possibility to investigate dropwise

condensation in a large variety of vapor-gas mixtures at pressures from 0.1 MPa to 4 MPa and temperatures between 200 K and 260 K.[44,60,61,71,72,74–85] In this chapter, we present new data on homogeneous nucleation of water at 0.1 MPa, 1 MPa and 2 MPa in two different carrier gases: nitrogen at 240 K and argon at 236 K and 240 K. The novel experiments have been carried out with a recently modified version of the PEWT.[116] A comparison is made with the homogeneous water nucleation data by Wölk and Strey[43] in argon between 220 K and 260 K, at about 0.06 MPa, and by Fransen *et al.* at 240 K and 1 MPa in nitrogen,[85] and at 0.1 MPa and 1 MPa in helium.[61,116] We shall discuss several aspects of the role of the carrier gas in the nucleation process. It reduces warming of the growing clusters and causes the nucleation process to be isothermal at sufficiently high pressure. At high pressure, real gas effects become important as well as the reduction of surface tension due to adsorption of gas at the phase interface. Additionally, we shall compare experimental critical cluster sizes with predictions from Classical Nucleation Theory (CNT).[4–10] Finally, an empirical correction of theoretical (CNT) nucleation rate is proposed, which takes into account the influence of the different carrier gases and the effect of the investigated pressure and temperature conditions.

## 4.2   Theoretical background

Nucleation and droplet growth are the two steps in the dropwise condensation process. Nucleation is called homogeneous when aerosol particles and foreign surfaces do not affect the nucleation process. The carrier gas (non-condensing component) acts as heat reservoir, which reduces the warming up of the clusters during nucleation. The key parameter in quantifying the nucleation process is the nucleation rate $J$, which is the number of droplets formed per units of time and volume. The other important parameter in homogeneous nucleation studies is the supersaturation $S$. For a vapor-gas mixture, it quantifies the current state deviation of the vapor component from its corresponding (same $p$ and $T$) phase equilibrium. More details on the $J$ and $S$ definitions will be given further on.

### 4.2.1   Classical Nucleation Theory and Nucleation Theorem

The Classical Nucleation Theory (CNT)[4–10] is the most used model to predict the nucleation rates (see Eq. 2.43)

$$J_{\mathrm{CNT}} = K \, \exp\left(\frac{-W^*}{kT}\right),\tag{4.1}$$

with the work of cluster formation $W^*$ proposed by Becker and Döring[5] (see Eq. 2.40)

$$W^* = \frac{16\pi}{3}\left(\frac{v_\ell}{kT \ln S}\right)^2 \sigma_\ell^3.\tag{4.2}$$

As far as the kinetic prefactor $K$ is concerned, we employ its corrected form suggested by Courtney[9,10] (see Eq. 2.44)

$$K = \left(\frac{p_\mathrm{s}}{kT}\right)^2 S v_\ell \sqrt{\frac{2\sigma_\ell N_\mathrm{a}}{\pi M}},\tag{4.3}$$

In Eqs. 4.1-4.3, $k$ is the Boltzmann constant and the quantities $v_\ell$, $p_\mathrm{s}$ and $\sigma_\ell$ are the molecular liquid volume,[123] the saturation vapor pressure[124] and the surface tension of pure water[125] at the temperature $T$.

Of central importance in the nucleation theory is the so-called critical cluster, which is defined by equal probabilities of growth and decay. The size of the critical cluster (number of vapor molecules forming it) can be determined by the Gibbs-Thomson equation as (Eq. 2.39)

$$n_{GT}^* = \frac{32\pi \, v_\ell^2}{3(kT \, ln \, S)^3} \sigma_\ell^3. \tag{4.4}$$

It should be noted that the CNT stipulates that bulk properties, such as surface tension, are also valid for clusters which may consist of a few molecules only (capillarity approximation). An independent way for the determination of the critical cluster size is provided by the first nucleation theorem[126,127]

$$n^* = \left( \frac{\partial \ln J}{\partial \ln S} \right)_T - 1, \tag{4.5}$$

which enables a straightforward derivation from the experimental $J$-$S$ curves.

## 4.2.2   Pressure and carrier gas influence on the surface tension

The pressure dependency of the water surface tension, in presence of helium, argon and nitrogen, has been largely investigated experimentally[128–132] and, recently, also numerically[131] for different conditions. The surface tension decrease with increasing pressure is generally ascribed to the adsorption of carrier gas molecules on the condensing cluster surfaces.[133] As already pointed out by Fransen *et al.* (2015),[85] adsorption of nitrogen is pronounced at high pressure and mild at ambient pressure.[128–130,132] The analysis was based on the pressure dependency of the water surface tension in presence of nitrogen, available in literature between 273 K and 423 K. Such dependency was linearly extrapolated into the supercooled liquid region of interest, namely 240 K. For the present study, we extend the Fransen analysis[85] with the water interfacial tension data of Chow *et al.* (2016)[131] for nitrogen and argon as diluent gases. Following this approach,[85] the surface tension of water in presence of the diluent gas can be expressed as

$$\sigma(p,T) = \sigma_\ell(T) - \frac{v^A}{A_g} \exp\left( -\frac{u_g^A}{kT} \right) p = \sigma_\ell(T) + \sigma_{p0}(T) \, p, \tag{4.6}$$

with $\sigma_\ell$ the surface tension of pure water, $A_g$ the average surface area per adsorption site ($1.62 \cdot 10^{-19}$ m$^2$ for nitrogen and $1.38 \cdot 10^{-19}$ m$^2$ for argon),[134] $v^A$ the effective volume available for the translation of an adsorbed molecule and $u_g^A$ the interaction potential energy of a gas molecule with the liquid surface. The following values for $v^A$ and $u_g^A$ have been found by fitting the $\sigma_{p0}(T)$ data available in literature[128–132] (see FIG. 4.1): for nitrogen $v^A = 8.85 \cdot 10^{-30}$ m$^3$ and $u_g^A = -1.03 \cdot 10^{-20}$ J, for argon $v^A = 7.13 \cdot 10^{-30}$ m$^3$ and $u_g^A = -1.03 \cdot 10^{-20}$ J. The resulting water surface tension reduction at 240 K ($\sigma_\ell = 79.95 \cdot 10^{-3}$ N·m$^{-1}$) is 1.45% $\pm$ 0.55% for argon at 1 MPa, 2.89% $\pm$ 0.98% for argon at 2 MPa, 1.53% $\pm$ 0.49% for nitrogen at 1 MPa and 3.06% $\pm$ 0.87% for nitrogen at 2 MPa. Thus, the pressure effect on the surface tension of water in argon and in nitrogen are expected to be similar. Additionally, values of surface tension reduction within 0.2% $\pm$ 0.1% confirm a negligible adsorption effect for both diluent gases at pressures up to 0.1 MPa and temperatures between 220 K and 260 K. A negligible effect has been also calculated for helium at pressures up to 1 MPa and 240 K. It should be stressed that this analysis is based on the extrapolation to the supercooled liquid region of the few literature data available only at temperatures above 298 K. This leads to a relatively high uncertainty, as confirmed also by Fransen *et al.*.[85]
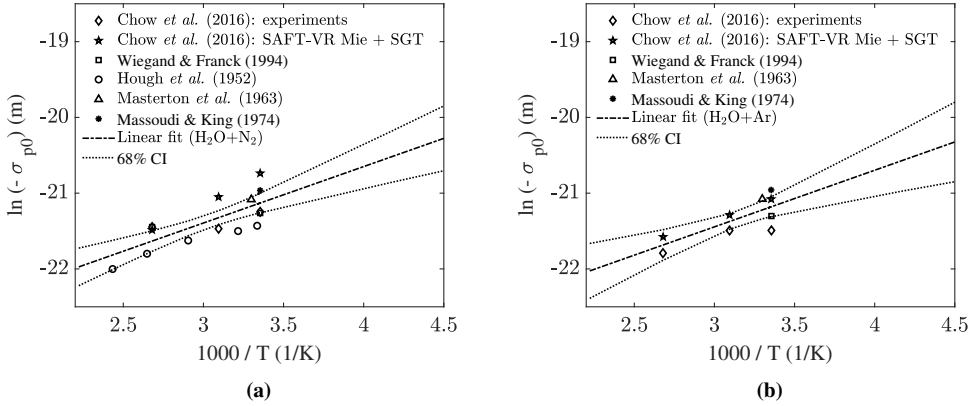
**FIG. 4.1.** Plot of $\sigma_{p0}$ data at different reciprocal temperatures for nitrogen[128–132] (4.1a) and argon[128–131] (4.1b). The linear fit (dashed-dotted line) and the standard uncertainty bands (68% confidence interval CI, dotted line) are also shown.

### 4.2.3    Kinetic model for non-isothermal nucleation

The cluster growth is characterized by two linked aspects: the trapping of vapor monomers by collision with the clusters (size) and the release of latent heat due to impinging and evaporating vapor monomers (energy). For mixtures of vapors and non-condensing carrier gases, the effect of latent heat release is further reduced by collisions of vapor clusters and gas molecules. The non-isothermal nucleation phenomena have been analyzed since 1966 by means of a 2D size-energy space.[87,113,122,135–138] We follow here the analysis of Feder *et al.* (1966),[122] later modified by Barrett and co-workers.[87,137,138] The analytical expression of the non-isothermal nucleation rate, approximated to the first order, reads

$$\frac{J}{J_{\mathrm{iso}}} = \frac{1}{1 + \dfrac{(\hat{c}_{\mathrm{bv}} + H)^2}{\hat{c}_{\mathrm{bv}}(1+\lambda)}} \left[ 1 + \left( \frac{H^4 + 3H^2 + 2\hat{c}_{\mathrm{bv}}H + 1}{(H^2+1)\left((H+\hat{c}_{\mathrm{bv}})^2 + (1+\lambda)\hat{c}_{\mathrm{bv}}\right)} \right) X \right] \tag{4.7}$$

where $J_{\mathrm{iso}}$ is the isothermal nucleation rate, $\hat{c}_{\mathrm{bv}} = c_{\mathrm{bv}}/k$ and $c_{\mathrm{bv}} = c_{\mathrm{v}} + k/2$ is the vapor monomer heat capacity at constant volume $c_{\mathrm{v}}$, accounting also for the increased collision rate of the high energy monomers $k/2$. The non-dimensional parameter $H$ of Eq. 4.7 is defined as

$$H = \frac{ML}{N_{\mathrm{a}}kT} - \frac{1}{2} - \hat{c}_{\mathrm{bv}} + \frac{2}{3(n_{\mathrm{GT}}^*)^{1/3}} T \frac{\mathrm{d}\Theta}{\mathrm{d}T}, \tag{4.8}$$

with $L$ the latent heat of vaporization, $\Theta = A_{<1>}\sigma_\ell/kT$ the non-dimensional surface tension, and $A_{<1>} = (36\pi)^{1/3} v_\ell^{2/3}$ the surface area of the vapor monomer. The parameter $\lambda$ is given by

$$\lambda = \frac{c_{\mathrm{bg}}\, \rho_{\mathrm{g}}\, \overline{v}_{\mathrm{g}}}{c_{\mathrm{bv}}\, \rho_{\mathrm{l}}\, \overline{v}_{\mathrm{l}}}, \tag{4.9}$$

with $c_{\mathrm{bg}} = c_{\mathrm{g}} + k/2$ the enhanced heat capacity of the gas at constant volume, $\rho_{\mathrm{g}}$ and $\rho_{\mathrm{l}}$ the molecular gas and vapor number densities, $\overline{v}_{\mathrm{g}}$ and $\overline{v}_{\mathrm{l}}$ the mean molecular (thermal) velocities

of gas and vapor. Additionally, $X$ is defined as

$$X = \frac{2\Theta\left(n_{GT}^* c_1 + k\right)}{9k\left(n_{GT}^*\right)^{4/3}\left(H^2 + 1\right)}, \tag{4.10}$$

with $c_1$ the heat capacity per molecule in the liquid. FIG. 4.2 shows $J/J_{iso}$ as a function of $(\lambda + 1)$ for a water-carrier gas system at 240 K and a supersaturation of 12. The parameter $\lambda$ strongly increases with pressure and with the reciprocal of the gas molecular mass. As a result, negligible non-isothermal effects are predicted at high pressure ($J/J_{iso} \approx 1$). On the other hand, at low pressures, thermalisation is more pronounced for gases with larger molecular mass ($J/J_{iso} < 1$). Additionally, a larger thermalisation effect is predicted for increasing temperature. The described model[87] will be used for the analysis of the low pressure experiments presented in this chapter. Note that the zeroth order approximation of Eq. 4.7 ($X = 0$) makes a small difference (over the third digit for our conditions) in the calculation of $J/J_{iso}$, as also pointed out by Barrett.[87]
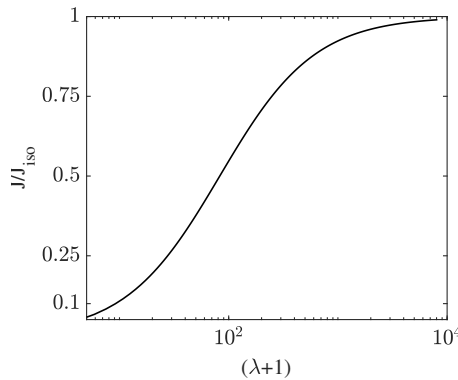


**FIG. 4.2.** Non-isothermal nucleation model of Barrett (Ref. 87): plot of $J/J_{iso}$ (Eq. 4.7) as a function of $\lambda + 1$ (Eq. 4.9), at 240 K and a supersaturation of 12.

### 4.2.4 Enhancement factor and supersaturation definition

The presence of a carrier gas in a vapor-gas mixture in equilibrium with a liquid phase is responsible for the increase of the vapor content. In order to quantify this enhancement effect, we consider the equality of chemical potentials in the coexisting phases. This equilibrium condition leads to the following expression of the equilibrium vapor molar fraction[74,89,90,139,140] (see Sec. 2.1)

$$y_{eq} = \frac{p_s}{p} \frac{\phi_s}{\phi_{eq}} \left(1 - x_g\right) \exp \int_{p_s}^{p} \frac{v_\ell}{kT} \, dp, \tag{4.11}$$

with $p$ the total pressure of the mixture and $p_s$ the equilibrium (saturation) vapor pressure for the pure condensing component at the total (mixture) temperature $T$.[124] The term $x_g$ is the carrier gas molar fraction dissolved in the liquid, which can be assumed negligibly small for the carrier gases investigated at temperatures well above 200 K. The quantities $\phi_s$ and $\phi_{eq}$ are the fugacity coefficients at equilibrium for pure water vapor and for water vapor in presence

of the carrier gas, respectively. Also assuming negligible liquid compressibility, Eq. 4.11 can be reformulated as follows

$$f_e = \frac{y_{eq} p}{p_s} = \frac{\phi_s}{\phi_{eq}} \exp\left[\frac{v_\ell (p - p_s)}{kT}\right], \tag{4.12}$$

The enhancement factor $f_e$ describes the increase of saturated vapor pressure due to the presence of the carrier (real) gas in the non-ideal mixture.[60] It consists of two contributions, both related to the heteromolecular interactions taking place within the mixture. On one hand, $\phi_s/\phi_{eq}$ accounts for the non-ideality of the water vapor in presence of the surrounding carrier gas molecules (real gas effect). The second contribution is the Poynting correction (exponent on the right hand side of Eq. 4.11 and 4.12), which takes into consideration the increase of equilibrium vapor fraction due to the pressure difference between the mixture and the pure saturated vapor.

The fugacity coefficient $\phi_s$ can be expressed as a function of the second virial coefficient for pure water $B_{11}$:[90]

$$\phi_s = \exp\left(\frac{B_{11} p_s}{RT}\right). \tag{4.13}$$

The fugacity coefficient $\phi_{eq}$, can be written as follows[90]

$$\phi_{eq} = \exp\left[\left(2B_{11} y_{eq} + 2B_{12}(1 - y_{eq}) - B\right)\frac{p}{RT}\right], \tag{4.14}$$

with the second virial coefficient of the mixture $B$ defined as

$$B = B_{11} y_{eq}^2 + 2B_{12} y_{eq}(1 - y_{eq}) + B_{22}(1 - y_{eq})^2. \tag{4.15}$$

$B_{22}$ and $B_{12}$ are the second virial coefficients for the pure carrier gas and for the interacting components of the mixture, respectively. The analytical expression of $B_{12}$ in the form proposed by Hodges *et al.*[102,103] is

$$B_{12} = \sum_i a_i \left(\frac{T}{100}\right)^{b_i}, \tag{4.16}$$

with the temperature $T$ in K. The coefficients $a_i$ and $b_i$ were obtained by fitting computational quantum chemistry results[102,103,112] for the different water-gas mixtures analyzed in this chapter. The reader is referred to Sec. 2.1.1 for more details on carrier gas solubility in water and on the virial and cross-virial coefficients used for the present study. In FIG. 4.3, the results of this analysis are presented in terms of pressure (0.05 MPa – 5 MPa) and temperature (220 K – 300 K) dependency of real gas effect ($\phi_s/\phi_{eq}$), Poynting correction ($\exp[v_\ell (p - p_s)/kT]$) and total effect ($f_e$) for the three mixtures: water-nitrogen (FIG. 4.3a), water-argon (FIG. 4.3b) and water-helium (FIG. 4.3c). It should be noted that a link exists between the increase of enhancement factor $f_e$ and the reduction of water surface tension with the pressure, as pointed out by Luijten *et al.* (1997).[74] Both aspects account for the heteromolecular interaction taking place in the vapor-gas mixture. Extending this qualitative consideration to different gases at fixed thermodynamic conditions, a larger $f_e$ corresponds to a stronger reduction of the water surface tension. This outcome is confirmed by our calculations of $f_e$ (FIG. 4.3) and $\sigma$ (Sec. 4.2.2): at the same pressure and temperature conditions, $f_e$ for the water-argon mixture is smaller than the one for water-nitrogen and the same applies for the $\sigma$ reduction.
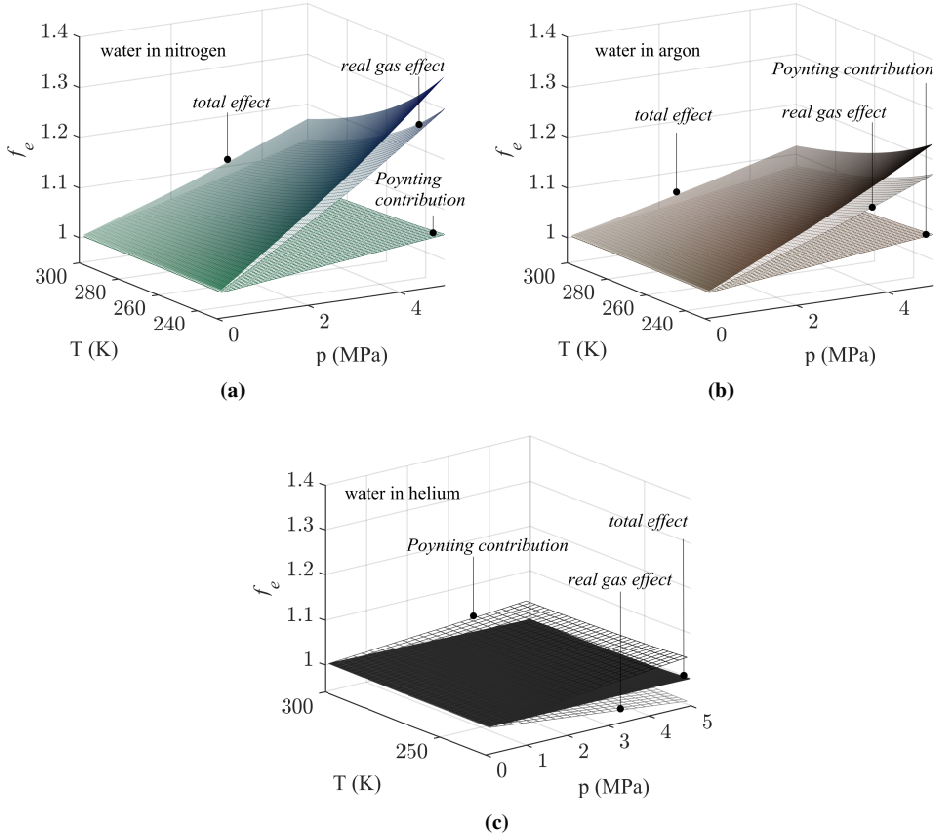
**FIG. 4.3.** Pressure and temperature dependency of Poynting correction ($\exp[v_\ell(p-p_s)/kT]$), real gas effect ($\phi_s/\phi_{eq}$) and the total effect ($f_e$) for water-nitrogen (4.3a), water-argon (4.3b) and water-helium (4.3c), between 0.05 MPa and 5 MPa and from 220 K to 300 K.

For a non-ideal vapor-gas mixture, the supersaturation of the condensing component can be defined as the ratio of its fugacities at the actual and at the corresponding equilibrium condition (see Eq. 2.15)

$$S = \frac{\mathscr{F}^g(p,T,y)}{\mathscr{F}^g(p,T,y_{eq})}, \tag{4.17}$$

with $y$ the vapor molar fraction. The fugacities $\mathscr{F}^g = \mathscr{F}^g(p,T,y)$ and $\mathscr{F}_{eq} = \mathscr{F}^g(p,T,y_{eq})$ can be expressed as a function of the chemical potential of the condensing component in the vapor state $\mu^g = \mu^g(p,T,y)$ and in the corresponding vapor-liquid equilibrium state $\mu_{eq} = \mu^g(p,T,y_{eq})$ as (see Sec 2.1)

$$\mu^g = \mu_{ref} + kT\ln\left(\frac{\mathscr{F}^g}{\mathscr{F}_{ref}}\right) \text{ and } \mu_{eq} = \mu_{ref} + kT\ln\left(\frac{\mathscr{F}_{eq}}{\mathscr{F}_{ref}}\right), \tag{4.18}$$

with the subscript 'ref' denoting the (arbitrary) reference properties of the pure condensing component. Hence, substituting Eq. 4.18 into Eq. 4.17, the supersaturation definition can be

reformulated as follows (see Eqs. 2.15 and 2.16)

$$S = \exp\left(\frac{\mu^{\mathrm{g}} - \mu_{\mathrm{eq}}}{kT}\right) \approx \frac{y}{y_{\mathrm{eq}}} = \frac{y\,p}{f_{\mathrm{e}}\,p_{\mathrm{s}}}, \tag{4.19}$$

with the last two equalities derived from the expression $\mathscr{F} = \phi\,y\,p$ (see Eq. 2.3) and by re-calling Eq. 4.11. The validity of $S \approx y/y_{\mathrm{eq}} = y\,p/(f_{\mathrm{e}}\,p_{\mathrm{s}})$ is restricted to the case in which the vapor monomers interact mostly with the diluent gas molecules and, consequently, $\phi \approx \phi_{eq}$. This condition is closely satisfied in the present application because of the small vapor molar fraction $y$. Note that the definition of supersaturation (Eq. 4.19) differs from that by Wedekind *et al.*,[113] who took the saturated state of the pure condensing component as reference (see Sec. 2.1.2 for more details).

## 4.3   Experimental

The experimental facility is a wave tube in which a well defined pattern of pressure waves can be generated. Geometrical details of the Pulse Expansion Wave Tube (PEWT) can be found in Chapter 3. A simplified schematic of the tube is represented in FIG. 4.4 (bottom-right). The device consists of a high pressure section HPS (0.65 m) and a low pressure section LPS (9.2 m), separated by a polyester diaphragm D. The cross section areas of HPS and LPS are the same, except for a local widening W (0.15 m long) of the LPS, placed at about 0.18 m from the diaphragm location.

The test mixture of water vapor and carrier gas is brought into the high pressure section. A well-defined composition of the mixture is obtained by sending a controlled carrier gas flow through a saturator and by flushing the test mixture through the HPS until the tube walls are saturated. This technique leads to a vapor molar fraction $y$ with a maximum estimated standard uncertainty of 1%. More details on the Mixture Preparation Device can be found in Sec. 3.3 and in Ref. 117.

The PEWT is designed to generate a specific wave pattern (see FIG. 4.4). The diaphragm rupture generates an expansion fan (E), moving towards the end wall of the HPS, and a shock wave (sh), in the opposite direction. The latter is reflected back as a weak expansion ($\mathrm{sh_1}$) at the widening cross-section enlargement $\mathrm{W_1}$ and as a small shock ($\mathrm{sh_2}$) at the restriction $\mathrm{W_2}$. In this way, at the observation point O, the test mixture undergoes a first large adiabatic expansion (E), immediately followed by an additional weak expansion ($\mathrm{sh_1}$) and a small re-compression ($\mathrm{sh_2}$), shortly after the weak expansion ($\mathrm{sh_1}$). This pressure-time pattern generated at the observation point O is able to greatly reproduce the features prescribed by the nucleation pulse method, represented in the two left diagrams of FIG. 4.4. The combination of the two expansions E and $\mathrm{sh_1}$ increases the saturation level of the initially under-saturated mixture far above unity ($S \gg 1$). The pressure drop is chosen such that the formation of a large number of droplets is triggered. This condition is maintained for a short period of time $\Delta t_{\mathrm{p}}$, the nucleation pulse. It is followed by a slight but sudden re-compression, which lowers the supersaturation level and inhibits the formation of new droplets. In this stage, the supersaturation is kept above unity ($S > 1$) for a long period of time leading to a cloud of growing droplets. As a consequence, separation in time of nucleation and droplet growth is achieved, both at reasonably constant thermodynamic conditions. Additionally, if $\Delta t_{\mathrm{p}}$ is much shorter than the growth time, the formed cloud of droplets can be assumed to be monodisperse to a large degree.[69] The nucleation pulse method has been successfully implemented by means
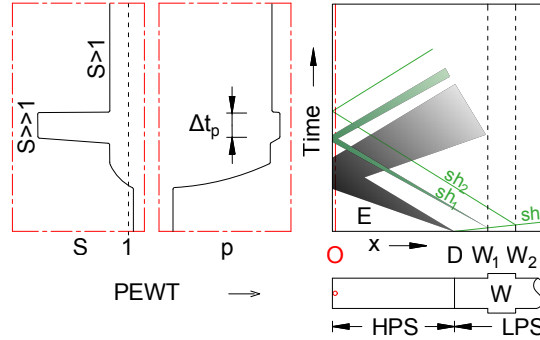
**FIG. 4.4.** Schematic of the PEWT principle of operation. The two left figures represent the pressure and supersaturation profiles in time prescribed by the nucleation pulse method and obtained at the PEWT observation point (O). The x-t wave diagram for the PEWT is represented in the right figure: the expansion wave is drawn in black (E), the shock (sh) and its reflections (sh$_1$ and sh$_2$) in green.

of several experimental facilities since 1965.[49,52,69,70] Peters[69] was the first to use a wave tube with this purpose. Looijmans and co-authors[70] later built the first version of the PEWT. The nucleation experiments presented in this chapter have been carried out with an upgraded version (see Chapter 3) of the Looijmans's design.

The pressure signal is measured via two pressure transducers, placed at the bottom wall of the observation plane: a piezo-resistive (Kistler 4073A50) and a piezo-electric (Kistler 603B). The combination of the two transducers leads to a pressure standard uncertainty of 0.2%.[44] With the pressure in time known, also $\Delta t_p$ can be measured with a maximum standard uncertainty of 3%. Before the test mixture undergoes the expansion E, its temperature $T_0$ is measured at the HPS wall via two platinum resistance thermometers (Tempcontrol PT-8316), placed at the walls of the observation plane. The time dependent temperature is calculated from the pressure signal as follows. Knowing the vapor molar fraction $y$, the entropy for the actual mixture can be calculated at the initial conditions. Assuming the process to be isentropic $\mathbb{S}(t) = \mathbb{S}(t=0) = const.$, the temperature as a function of time $T(t)$ can be finally derived for each known pressure condition $p(t)$.[91] A standard uncertainty of 0.1 K has been calculated for the pulse temperature. Once the thermodynamic conditions are known, the supersaturation can be computed from Eq. 4.19. The final standard uncertainty on the supersaturation has been calculated to be within 2%, depending on the experimental conditions.

The droplet monodispersity, obtained with the nucleation pulse method, leads to an accurate determination of the nucleation rate $J$ by optical means. It is calculated as the ratio of droplet number density $n_d$ and $\Delta t_p$

$$J = \frac{n_d}{\Delta t_p}, \tag{4.20}$$

with $\Delta t_p$ obtained from the pressure signal and $n_d$ measured by means of a dedicated optical setup represented in Fig. 4.5. The latter consists of a linearly polarized 100:1 laser light (Lasos Lasnova GLK 3220 T01 - wavelength of 532 nm), which probes the test section through the optical window $A_1$. A photomultiplier PM (Hamamatsu 1P28A) records the 90° scattered light at the optical window $A_2$ and a photodiode PD (Telefunken BPW 34) measures the light attenuation at the optical window $A_3$ ($A_1$, $A_2$ and $A_3$ are BK7 glass windows). The droplet radius in time is obtained by comparing the PM time signal with the theoretical (Mie theory) scat-
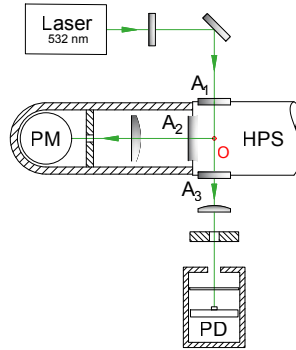
**FIG. 4.5.** Layout of the Optical Setup with PM the *Hamamatsu 1P28A* photomultiplier and PD the *Telefunken BPW 34* photodiode. The linearly polarized 100:1 laser light generated by the *Lasos Lasnova GLK 3220 T01* with a wavelength of 532 nm is shown in green. The optical access to the HPS test section is guaranteed by the three optical windows $A_1$, $A_2$ and $A_3$ (BK7 glass).

tered light as a function of the droplet radius. The PD time signal is used in combination with the Lambert-Beer law and the calculated droplet growth rate to obtain $n_d$. This technique is known as the Constant Angle Mie Scattering method (CAMS).[52,54,55] The estimated standard uncertainty of $J$ is within 20%. More details on the optical technique and the experimental setup can be found in Chapter 3.

## 4.4   Results and discussion

Novel homogeneous water nucleation experiments have been carried out

- in nitrogen at 240 K and 0.1 MPa, 1 MPa and 2 MPa,

- in argon at 236 K and 0.1 MPa, 1 MPa and 2 MPa,

- in argon at 240 K and 1 MPa and 2 MPa.

The obtained nucleation rates $J$ as a function of the supersaturation $S$ are presented in FIGS. 4.6 and 4.7. The $J_{CNT}(S)$ curves (Eqs. 4.1-4.3) at the investigated temperatures are also reported for reference. For each mixture, the $J$-$S$ data at fixed temperature and pressure conditions are fitted by means of the following regression curve

$$J_{exp} = C \exp\left[\frac{D}{(\ln S)^2}\right], \tag{4.21}$$

with the coefficients $C$ and $D$ calculated for each condition analyzed in this chapter. The reader is referred to the Appendix B for more details on experimental data and regression coefficients. The estimated standard uncertainties of $S$ and $J$ (see Sec. 4.3) are 2% and 20%, respectively. The $J$ standard uncertainty is within the represented symbol sizes. Therefore, only the $S$ standard uncertainty, combined with the regression error, is reported in the $J$-$S$ plots.

In FIG. 4.6, the water-nitrogen experiments are shown in comparison with the Fransen results.[61] The latter were obtained for the same mixture at 1 MPa and 240 K, by means of the

previous version of the PEWT. Most of these literature data[61] fall within the uncertainty bands identified in this study at the same conditions (water-nitrogen at 240 K and 1 MPa). However, a relevant data scatter is noticeable ($R^2 = 0.96$), which is not present for our data ($R^2 = 0.995$, see Appendix B). Hence, we can conclude that the new PEWT[116] has significantly improved the quality of the experiments, with a consistent reduction of the data scatter.
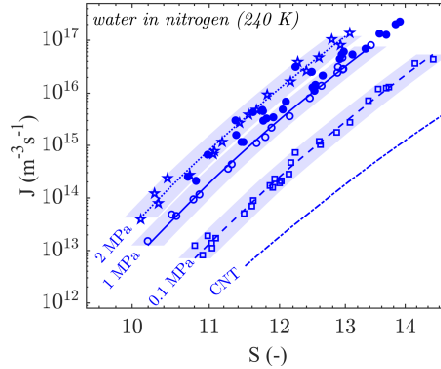


**FIG. 4.6.** *J-S* plot of the homogeneous water nucleation experiments in nitrogen. The lines refer to the $J_{\exp}(S)$ curves (Eq. 4.21) of the data obtained at 240 K and 0.1 MPa (blue open squares, blue dashed line), 1 MPa (blue open circles, blue solid line) and 2 MPa (blue stars, blue dotted line). The uncertainty bands are highlighted with a lighter color (shaded in light blue). The data obtained by Fransen *et al.*[61] at 1 MPa (blue filled circles) are shown for comparison. The $J_{CNT}(S)$ at 240 K (blue dashed-dotted line, Eqs. 4.1-4.3) is also reported.

FIG. 4.7a shows the nucleation data obtained for water in argon at 1 MPa and 2 MPa. These experiments have been carried out at 236 K (yellow data points and lines) and 240 K (red data point and lines) in order to test the Hale scaling model[86] of $S$

$$\ln S_{\mathrm{sc}} = \frac{C_0 \ln S}{\left( \dfrac{T_{\mathrm{c}}}{T} - 1 \right)^{3/2}}, \tag{4.22}$$

with $C_0 = (T_{\mathrm{c}}/T_{\mathrm{sc}} - 1)^{3/2}$, $T_{\mathrm{sc}}$ the target scaling temperature, $S$ the actual supersaturation at the temperature $T$ and with $T_{\mathrm{c}}$ the critical temperature of water. Using Hale's approach, the $J_{\exp}(S)$ fits of our data at 236 K for 1 MPa and 2 MPa are scaled to 240 K (red lines) as represented in FIG. 4.7a: solid line for 1 MPa and dotted line for 2 MPa. The actual *J-S* data obtained at 240 K for 1 MPa (red circles) and 2 MPa (red stars) are shown in FIG. 4.7a to fall on top of the 240 K scaled curves for both high pressure conditions. It should be considered that Eq. 4.22 was developed and verified by Hale[86] at low pressure (0.06 MPa).[43] In view of our experimental findings, this scaling model[86] appears to be also valid at high pressure conditions.

The water nucleation data in argon at 236 K and 0.1 MPa are compared with the Wölk and Strey *J-S* values[43] measured for the same mixture at 0.06 MPa and two temperatures: 230 K and 240 K. This comparison is reported in FIG. 4.7b. The intermediate *J-S* values of our experiments in comparison with the literature data[43] is consistent with the investigated thermodynamic conditions (water-argon at 236 K and 0.1 MPa). The Hale scaling model[86] is also tested for the latter case. The $J_{\exp}(S)$ fit of our 236 K and 0.1 MPa data is scaled to
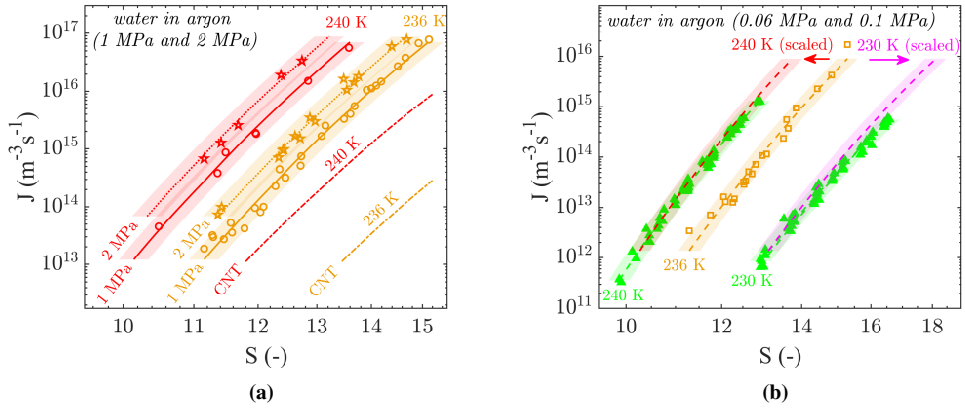
**FIG. 4.7.** *J-S* plot of the homogeneous water nucleation experiments in argon. The lines refer to $J_{\exp}(S)$ (Eq. 4.21). FIG. 4.7a shows the results of the high pressure experiments in argon: 236 K and 1 MPa (yellow circles, yellow solid line), 236 K and 2 MPa (yellow stars, yellow dotted line), 240 K and 1 MPa (red circles) and 240 K and 2 MPa (red stars). The $J_{\exp}(S)$ at 240 K and 1 MPa (red solid line) and 240 K and 2 MPa (red dotted line) are obtained from the data at 236 K and 1 MPa (yellow circles) and 236 K and 2 MPa (yellow stars) scaled [86] to 240 K. The $J_{CNT}(S)$ (Eqs. 4.1-4.3) at 240 K (red dashed-dotted line) and 236 K (yellow dashed-dotted line) are reported for reference. In FIG. 4.7b the tests performed at 236 K and 0.1 MPa (yellow squares, yellow dashed line) are shown in comparison with the data of Wölk and Strey [43] obtained for the same mixture at about 0.06 MPa and for 230 K and 240 K (green triangles, green dashed line). The $J_{\exp}(S)$ for 240 K and 0.1 MPa (red dashed line) is obtained by scaling [86] the 236 K-0.1 MPa data (yellow squares) to 240 K. The $J_{\exp}(S)$ for 230 K and 0.1 MPa (purple dashed line) is obtained by scaling [86] the 236 K-0.1 MPa data (yellow squares) to 230 K. The uncertainty bands are highlighted with a lighter color for the 240 K (shaded in red), 236 K (shaded in yellow), 230 K (shaded in purple) and the literature data [43] (shaded in green).

240 K and to 230 K, as shown in FIG. 4.7b with red and purple dashed lines respectively. These scaled curves are aligned with the 0.06 MPa water-argon data of Wölk and Strey at 240 K and 230 K [43] (green triangular markers in FIG. 4.7b). Such outcome confirms the validity of the Hale scaling function [86] at low pressure conditions, considering that, at 0.06 MPa and 0.1 MPa, negligible adsorption effects are present (see Sec. 4.2.2) and that the small pressure difference has a negligible influence on the thermalisation.

### 4.4.1  Critical cluster size

The nucleation theorem (Eq. 4.5) leads to experimental values of the critical cluster size $n^*$ from the *J-S* curves. These values can be compared with the theoretical ones $n^*_{\mathrm{GT}}$, based on the Gibbs-Thomson formulation (Eq. 4.4) and the capillarity approximation (CNT). Therefore, with the purpose of testing the Gibbs-Thomson equation, we calculate and compare $n^*$ and $n^*_{\mathrm{GT}}$. The results are presented in FIG. 4.8 for the conditions investigated in this chapter (more details in Appendix B).

A reasonable agreement is found, within the error bars, between the experimental and the theoretical values of the critical cluster sizes, as already pointed out by Wölk and Strey (2001). [43] As for them, we confirm that using the macroscopic values for surface tension and density leads to a reasonable approximation of $J_{\exp}(S)$ slopes and experimental critical cluster sizes.
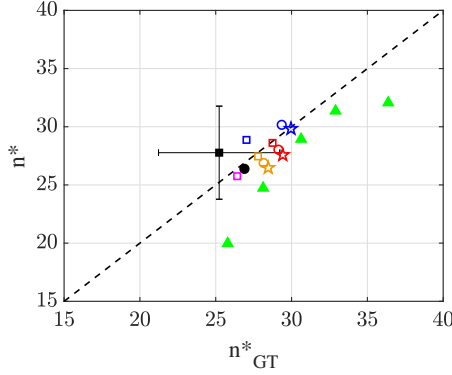
**FIG. 4.8.** Comparative plot of experimental $n^*$ (Eq. 4.5) *vs* theoretical $n^*_{GT}$ (Eq. 4.4) critical cluster sizes, calculated at the supersaturation mid-range $((S_{min} + S_{min})/2)$ for each condition: water-nitrogen at 240 K and 0.1 MPa (blue square), 1 MPa (blue circle) and 2 MPa (blue star); water-argon at 230 K and 0.1 MPa (purple square); water-argon at 236 K and 0.1 MPa (yellow square), 1 MPa (yellow circle) and 2 MPa (yellow star); water-argon at 240 K and 0.1 MPa (red square), 1 MPa (red circle) and 2 MPa (red star); water-helium [61,116] at 240 K and at 0.1 MPa (black filled square) and 1 MPa (black filled circle); water-argon between 220 K and 260 K at about 0.06 MPa [43] (green triangles). The dashed line represents the ideal perfect agreement between $n^*$ and $n^*_{GT}$. The standard uncertainty for each value ranges between 3 and 5 molecules, depending on the conditions (see Appendix B). The error bar for the only water-helium mixture at 240 K and 0.1 MPa is shown for reference.

## 4.4.2 Empirical correlation for the water nucleation rate

The CNT requires only bulk properties for the calculation of the nucleation rates $J_{CNT}$ (Eq. 4.1-4.3). This simplification makes possible to use the CNT relatively easily, but, on the other hand, does not lead to a quantitative agreement with the experimental nucleation rates as shown in FIGS. 4.6 and 4.7a. Therefore, we have investigated an empirical correction of $J_{CNT}$, leading to a one to one correspondence with the experimental values $J_{exp}(S)$ (see Eq. 4.21) discussed in this chapter. A similar approach has been proposed in the past by Wölk and Strey.[43] Their empirical correlation took into account the temperature dependency (between 200 K and 260 K) at about 0.06 MPa for water in argon. We propose a possible empirical expression for the water nucleation rate, which includes not only the temperature, but also the pressure and the carrier gas dependencies investigated in the present chapter. The proposed form of the empirical nucleation rate is

$$J_{emp} = \left(\frac{f_e\, p_s}{Z k T}\right)^2 S v_\ell \sqrt{\frac{2(\Psi\sigma)N_a}{\pi M}}\, \exp\left[\frac{-16\pi}{3}\left(\frac{v_\ell}{\ln S}\right)^2 \left(\frac{\Psi\sigma}{kT}\right)^3\right], \tag{4.23}$$

with $Z$ the compressibility factor of the mixture, approximated with the one of the carrier gas $Z_g$ (small $y$ for the fitted conditions) and with $\Psi = \Psi(p,T)$ the empirical correction function, given by following equation

$$\Psi(p,T) = c_1 T^2 + c_2 T + \frac{d_1 + d_2\, p}{1 + d_3 \sqrt{p}}. \tag{4.24}$$

The coefficients in Eq. 4.24 are $c_1 = -2.477 \cdot 10^{-5}$ K$^{-2}$, $c_2 = 13.5 \cdot 10^{-3}$ K$^{-1}$, $d_1 = -0.8324$, $d_2 = 0.0274$ MPa$^{-1}$, $d_3 = -0.0634$ MPa$^{-1/2}$, with $T$ in K and $p$ in MPa. The pressure-temperature dependency of $\Psi$ is shown in FIG. 4.9.
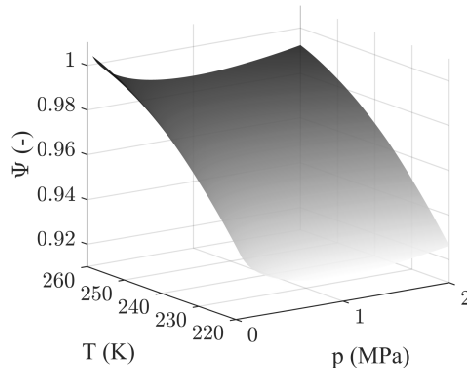
**FIG. 4.9.** Empirical correction function $\Psi(p, T)$ (Eq. 4.24).

It must be stressed that the proposed empirical correlation in Eq. 4.23 is obtained by fitting the experimental conditions discussed in this chapter (including literature sources),[43,85,116] and, therefore, the domain of $J_{\mathrm{emp}}$ is strictly limited to water-helium, water-argon and water-nitrogen mixtures with pressures between 0.05 MPa and 2 MPa and temperatures between 220 K and 260 K. For all the conditions analyzed, the $J_{\mathrm{emp}}(S)$ curves are shown in FIG. 4.10 to fall within the uncertainty bands of $J_{\mathrm{exp}}(S)$ (Eq. 4.21). It is worth mentioning that the empirical correlation of Wölk and Strey[43] consists in a temperature correction of $J_{\mathrm{CNT}}$ (Eq. 4.1 and 4.2 with kinetic prefactor $K$ calculated according to Becker and Döring)[5] such as a correspondence with their experimental data is achieved. Since the proposed function $J_{\mathrm{emp}}$ is shown in FIG. 4.10a to satisfactory reproduce such data,[43] the two temperature-dependent fits can be considered equivalent, albeit formally different.

Pressure, temperature and carrier gas dependencies are explicitly considered in $J_{\mathrm{emp}}$ through $\sigma$ (Eq. 4.6), $f_{\mathrm{e}}$ (Eq. 4.12) and $Z$, while $\Psi$ only accounts for residual pressure effects and almost completely for the temperature corrections (partially considered also in $\sigma$, $f_{\mathrm{e}}$ and $Z$). Additionally, the $(f_{\mathrm{e}}/Z)^2$ term accounts for the presence of the non-ideal carrier gas in the mixture, taking into consideration its compressibility factor ($Z \approx Z_{\mathrm{g}}$) and the enhancement effects ($f_{\mathrm{e}}$) of the non-ideal vapor-gas mixture discussed in Sec. 4.2.4 (see also Sec. 2.2.4). The parameters $\sigma/\sigma_{\ell}$, $f_{\mathrm{e}}$, $Z$ and $\Psi$ are all between 0.9 and 1.1, but because $\sigma$ and $\Psi$ appear cubed and in the exponent, they provide the major contribution to the pressure dependency of $J_{\mathrm{emp}}$.

The pressure dependency of $\Psi$ is obtained by fitting the experimental data at the four pressure conditions (0.06 MPa, 0.1 MPa, 1MPa and 2 MPa) analyzed in this chapter. Similarly, $\sigma$ is derived, in Sec. 4.2.2, by fitting the data available in literature. A slightly non-monotonic pressure dependency of $\Psi$ between 1 MPa and 2 MPa (see FIG. 4.9) is obtained as a result. We might speculate that the reason of the non-monotonicity is the fact that the correction includes non-isothermal effects at low pressure, whereas, at high pressures, it represents deviations from the true magnitudes of the modeled gas effects on surface tension and enhancement factor. Currently, the empirical correlation proposed in this chapter (Eq. 4.23) appears to be the solution that provides the most satisfactory reproducibility of the available data (see FIG. 4.10) with the minimum number of fitting coefficients possible.
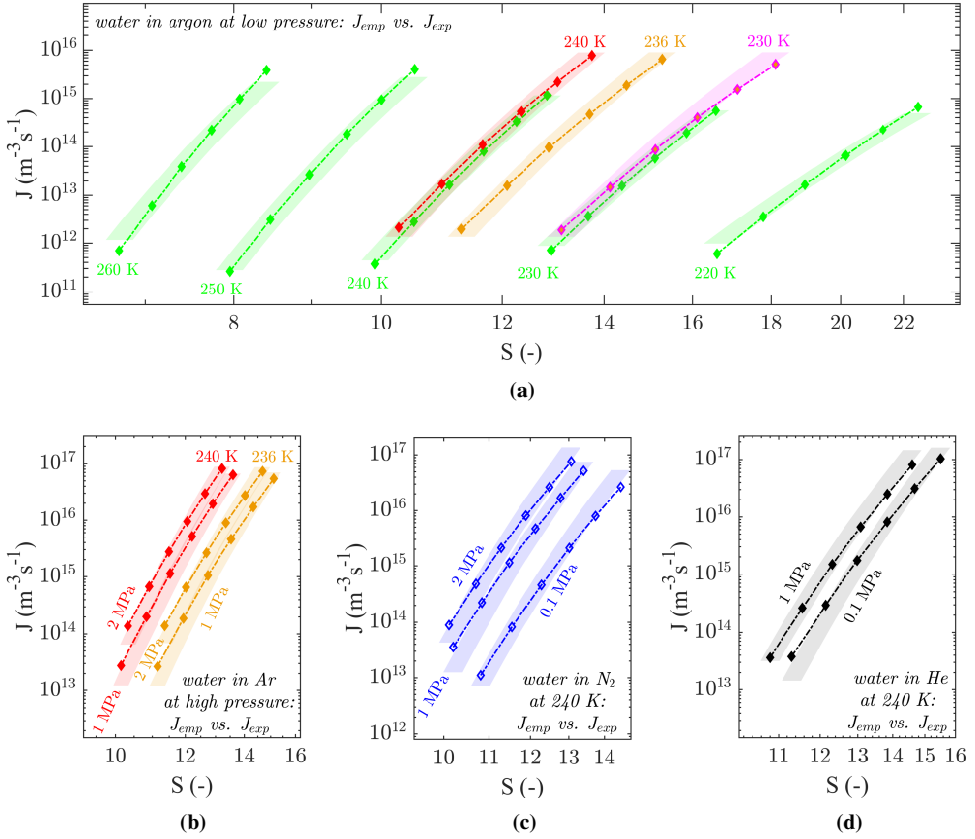
**FIG. 4.10.** Comparison between $J_{emp}$ (Eqs. 4.23 and 4.24) and $J_{exp}$ (Eq. 4.21) for all the conditions analyzed. The $J_{exp}(S)$ curves are identified only with the uncertainty bands (colored regions) and the $J_{emp}(S)$ curves with the diamond-spotted lines: water-argon at 0.06 MPa (shaded in green[43] and green diamond-spotted lines) [FIG. 4.10a], water-argon at 236 K (shaded in yellow and yellow diamond-spotted line) [FIGS. 4.10a and 4.10b], water-argon at 240 K (shaded in red and red diamond-spotted lines) [FIGS. 4.10a and 4.10b], water-argon at 230 K (shaded in purple and purple diamond-spotted lines) [FIG. 4.10a], water-nitrogen at 240 K (shaded in blue and blue diamond-spotted lines) [FIG. 4.10c], water-helium at 240 K (shaded in gray[85,116] and black diamond-spotted lines) [FIG. 4.10d]. In FIG. 4.10a, the 230 K and the 240 K conditions at 0.1 MPa (shaded in red and shaded in purple) refer to $J_{exp}(S)$ at 0.1 MPa and 236 K (shaded in yellow) scaled[86] to 240 K and 230 K (see FIG. 4.7b).

## 4.4.3 Effect of carrier gas adsorption on $J_{exp}$ at high pressure

The water-helium mixture at 1 MPa and 240 K[85,116] has been demonstrated to be rather insensitive to adsorption and thermalisation effects, as mentioned in Sec. 4.2.2 and 4.2.3 ($J/J_{iso} \approx 1$ and $\Delta\sigma/\sigma_\ell < -0.12\%$). Thus, its $J_{exp}(S)$ curve is used as experimental reference to analyze the water nucleation data at high and low pressure. Non-isothermal effect on nucleation can be reasonably excluded at high pressure ($J/J_{iso} \approx 1$, see Sec. 4.2.3). In a previous publication, Fransen *et al.*[85] compared the nucleation rates for water-nitrogen and the water-helium at 1 MPa and 240 K. They argued that the larger $J$ increase for water-nitrogen than for water-

helium was due to the significant pressure effect on the reduction of water surface tension. We have shown in Sec. 4.2.2 as this effect is expected to be somewhat smaller for argon than for nitrogen at the same pressure conditions. In order to verify this theoretical outcome, we compare the high pressure nucleation experiments carried out with water-nitrogen and water-argon at 1 Ma and 2 MPa, both at 240 K. The results of these experiments are collected in Fig. 4.11 for a comparative analysis. The reference water-helium $J_{exp}(S)$ curve at 1 MPa and 240 K [85,116] is also represented.
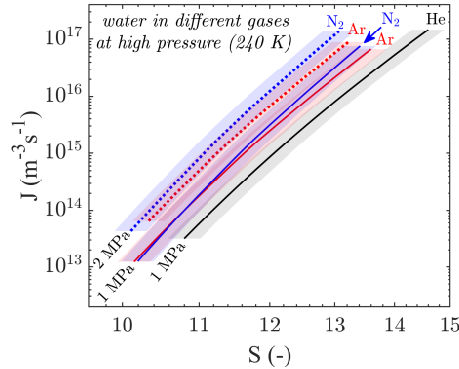


**FIG. 4.11.** $J_{exp}$-$S$ plot of the homogeneous water nucleation experiments in nitrogen and argon at 240 K and 1 MPa (blue solid line and red solid line) and 2 MPa (blue dotted line and red dotted line). $J_{exp}(S)$ of the water-helium data [61,116] at 240 K and 1 MPa (black solid line) is reported as reference condition. The uncertainty bands are highlighted for the different carrier gases: nitrogen (shaded in blue), argon (shaded in red) and helium [61,116] (shaded in gray).

The nucleation rates for water-argon at 240 K and 1 MPa are shown to overlap with the ones obtained with the water-nitrogen mixture at the same conditions. The differences are within the uncertainty bands. This is consistent with the predicted $\sigma$ reduction at 1 MPa for the two mixtures (see Sec. 4.2.2): $1.45\% \pm 0.55\%$ for argon and $1.53\% \pm 0.49\%$ for nitrogen. At 1 MPa and 240 K, the adsorption effect for argon and nitrogen appears to be significantly larger than for helium. The nucleation rates of water-nitrogen at 240 K and 2 MPa show larger values than water-argon at the same conditions, albeit a significant overlap of the uncertainty bands is still present. Nevertheless, the $J$ increase is shown to be more pronounced at 2 MPa than at 1 MPa for the two mixtures. This is in qualitative agreement with the larger $\sigma$ reduction at 2 MPa (see Sec. 4.2.2): $2.89\% \pm 0.98\%$ for argon and $3.06\% \pm 0.87\%$ for nitrogen. The qualitative agreement between experimental and predicted $J$ increase is further analyzed in TABLE 4.1. The expected nucleation rate enhancement $J/J_0$ is calculated according to the CNT (Eqs. 4.1-4.3) at the upper and lower uncertainty bands of the surface tension reduction (see Sec. 4.2.2). The experimental nucleation rate increase $(J/J_0)_{exp}$ is calculated as the ratio of $J_{exp}$ and reference $(J_0)_{exp}$, which is considered to be $J_{exp}$ of water-helium at 240 K and 1 MPa ($J/J_0 \approx 1$). The experimental increase $(J/J_0)_{exp}$ is shown to be systematically close to the lower limit of $(J/J_0)_{CNT}$ for all pressure conditions and mixtures analyzed at 240 K.

Additionally, we analyze the 236 K experiments carried out in water-argon at 1 MPa and 2 MPa. In this case, the reference experimental condition ($J/J_0 \approx 1$) is $(J_0)_{exp}$ of water-helium at 1 MPa and 236 K. Since this condition is not available in literature, we compute it as $J_{emp}$ by employing the proposed empirical correlation (see Eq. 4.23). Equivalently, the reference

**TABLE 4.1.** Pressure effect on the $\sigma$ reduction $(-\Delta\sigma/\sigma_\ell)$ for water in different carrier gases (see Sec. 4.2.2). Comparison between theoretical $(J/J_0)_{CNT}$ (Eqs. 4.1-4.3) and experimental $(J/J_0)_{exp}$ nucleation rate increases.

| T (K) | | p (MPa) | $S^a$ | $(-\Delta\sigma/\sigma_\ell)_\%$ | | $(J/J_0)_{CNT}$ | | $(J/J_0)_{exp}$ [b] | References[c] |
|---|---|---|---|---|---|---|---|---|---|
| | | | | min | max | min | max | | |
| 240 | He | 0.9968 | 12.7 | 0.10 | 0.14 | 1.11 | 1.15 | 1 | 85,116 |
| | Ar | 1.0002 | 11.9 | 0.89 | 2.00 | 2.6 | 8.2 | 2.9 | *c.w.* |
| | | 1.9939 | 11.8 | 1.91 | 3.88 | 7.6 | 56.7 | 8 | *c.w.* |
| | $N_2$ | 1.0018 | 11.8 | 1.03 | 2.02 | 3.0 | 8.5 | 3.5 | *c.w.* |
| | | 2.0004 | 11.6 | 2.19 | 3.93 | 10.5 | 63.1 | 14.2 | *c.w.* |
| 236 | He | 0.9968 | 13.2 | 0.10 | 0.14 | 1.11 | 1.16 | 1 | Eq. 4.23 |
| | Ar | 1.0002 | 13.1 | 0.97 | 2.08 | 2.8 | 9.0 | 3.5 | *c.w.* |
| | | 2.0004 | 13.0 | 2.07 | 4.03 | 9.1 | 68.2 | 9.4 | *c.w.* |

[a]Mid-range of $S$ for each experimental condition: $(S_{min} + S_{max})/2$.
[b]Ratio of $J_{exp}$ (Eq. 4.21) and experimental reference $(J_0)_{exp}$, both calculated at the same $S$-value.[a] The reference $(J_0)_{exp}$ is taken equal to $J_{exp}$ (Eq. 4.21) of water-helium at 1 MPa for 240 K (see FIG. 4.11) and to $J_{emp}$ (Eq. 4.23) of water-helium at 1 MPa for 236 K (see FIG 4.12).
[c]Literature and equation references, with *c.w.* (current work) denoting the new data.

condition can be obtained by scaling[86] the water-helium data at 1 MPa and 240 K to 236 K. The *J-S* plots of these conditions are shown in FIG. 4.12. Similarly to the 240 K case, the experimental nucleation rate increase $(J/J_0)_{exp}$ is found to be consistently close to the lower limit of $(J/J_0)_{CNT}$ for all pressure conditions analyzed at 236 K, as reported in TABLE 4.1.
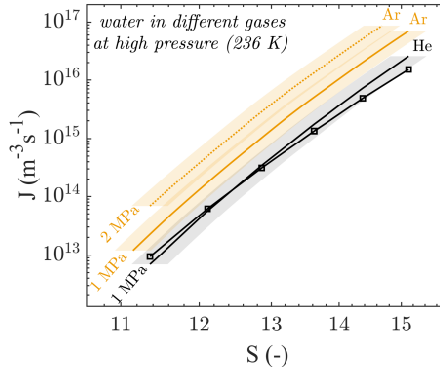


**FIG. 4.12.** $J_{exp}$-$S$ plot of the homogeneous water nucleation experiments in argon at 236 K and 1 MPa (yellow solid line) and 2 MPa (yellow dotted line) with the corresponding uncertainty bands (shaded in yellow). The $J_{emp}(S)$ curve (Eq. 4.23) for water-helium at 236 K and 1 MPa (black square-spotted line) is reported as reference condition. Equivalently, the latter can be derived from the water-helium data at 1 MPa and 240 K scaled[86] to 236 K [$J_{exp}(S)$ (black solid line), uncertainty band (shaded in black)].

Considering these experimental evidences, we can conclude that the adsorption phenomena and the corresponding water surface tension reduction seem to be the predominant causes of the nucleation rate increase at high pressures. For a definitive confirmation of our findings,

experiments at higher pressure conditions and with carrier gases that affect the surface tension more profoundly are needed. Further research studies should also be made in order to extend the few interfacial tension data, available above 298 K,[128–132] to the supercooled liquid region.

### 4.4.4  Thermalisation effect on $J_{\mathrm{exp}}$ at low pressure

Adsorption effects are not important at low pressure as discussed in Sec. 4.2.2 ($\Delta\sigma/\sigma_\ell < -0.2\%$). So, we assume that only thermalisation affects the nucleation rates at pressures up to the ambient condition. The experimental data at 0.1 MPa and 240 K for water-nitrogen and water-argon are analyzed in comparison with the 240 K water-helium data sets[85,116] at 0.1 MPa and 1 MPa. The 1 MPa case is taken as experimental isothermal reference ($J_{\mathrm{iso}}$)$_{\mathrm{exp}}$ at 240 K, being negligible thermalisation effects ($J/J_{\mathrm{iso}} = 0.97 \approx 1$, see TABLE 4.2) and adsorption phenomena ($\Delta\sigma/\sigma_\ell = -0.12\%$, see TABLE 4.1). The $J_{\mathrm{exp}}(S)$ curves of these conditions are collected in FIG. 4.13. The nucleation rates of water-argon and water-nitrogen at 0.1 MPa and 240 K are shown to be almost identical. The water-helium data at 0.1 MPa and 240 K present smaller nucleation rates than water-argon and water-nitrogen at the same conditions. Non-isothermal effects are investigated in order to explain the nucleation rate variations for the different carrier gases at low pressure. A quantitative analysis is presented in TABLE 4.2. According to the Barrett kinetic model,[87] the theoretical (CNT-based) nucleation rate reduction (see Eq. 4.7) is expected to be larger with increasing the molecular mass of the carrier gas, at fixed conditions (0.1 MPa and 240 K): smaller for water-helium ($J/J_{\mathrm{iso}} = 0.757$), intermediate for water-nitrogen ($J/J_{\mathrm{iso}} = 0.641$) and larger for water-argon ($J/J_{\mathrm{iso}} = 0.514$). At the same conditions, the experimental nucleation rate reduction is found to be in qualitative agreement with the predicted trend: smaller for water-nitrogen (($J/J_{\mathrm{iso}})_{\mathrm{exp}} = 0.328$) than for water-argon (($J/J_{\mathrm{iso}})_{\mathrm{exp}} = 0.258$). However, the predicted trend is not respected for water-helium, which experimentally shows the most significant nucleation rate reduction (($J/J_{\mathrm{iso}})_{\mathrm{exp}} = 0.187$), while it was expected to be least significant (($J/J_{\mathrm{iso}}) = 0.757$).

Additionally, we investigate the temperature dependency of the thermalisation effect. The
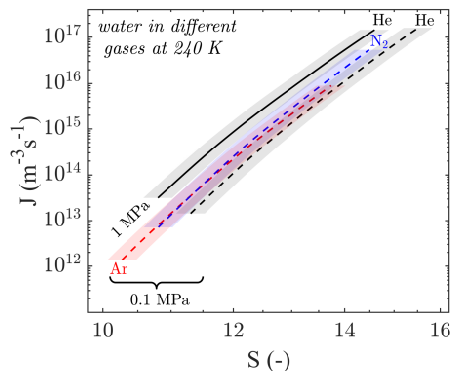


**FIG. 4.13.** $J_{\mathrm{exp}}$-$S$ plot of the homogeneous water nucleation experiments at 240 K and 0.1 MPa for different carrier gases: nitrogen (blue dashed line), argon (red dashed line) and helium[61,116] (black dashed line). The $J_{\mathrm{exp}}(S)$ curve of the water-helium data[61,116] at 240 K and 1 MPa (black solid line) is reported as reference condition. The uncertainty bands are highlighted for the different carrier gases: nitrogen (shaded in blue), argon (shaded in red) and helium[61,116] (shaded in black).

**TABLE 4.2.** Summary of the non-isothermal analysis for the 240 K nucleation experiments in water-helium, water-argon and water-nitrogen. The theoretical $J/J_{\text{iso}}$ (Eq. 4.7) are compared with the experimental values $(J/J_{\text{iso}})_{\text{exp}}$.

| | p (MPa) | $S^{\text{a}}$ | $\lambda$ | $J/J_{\text{iso}}$ | $(J/J_{\text{iso}})_{\text{exp}}^{\text{b}}$ | Ref.$^{\text{c}}$ |
|---|---|---|---|---|---|---|
| He | 0.1054 | 13.5 | 253 | 0.757 | 0.187 | 85,116 |
| | 0.9968 | 12.7 | 2526 | 0.968 | 1 | 85,116 |
| Ar | 0.1028 | 12.0 | 87 | 0.514 | 0.258 | *c.w.* |
| $N_2$ | 0.1017 | 12.6 | 147 | 0.641 | 0.328 | *c.w.* |

$^{\text{a}}$Mid-range of $S$ for each experimental condition: $(S_{\text{min}} + S_{\text{max}})/2$.
$^{\text{b}}$Ratio of $J_{\text{exp}}$ (Eq. 4.21) and experimental isothermal reference $(J_{\text{iso}})_{\text{exp}}$ at 240 K ($J_{\text{exp}}$ of water-helium at 1 MPa and 240 K), both calculated at the same $S$-value.$^{\text{a}}$
$^{\text{c}}$Literature references and new data from current work (*c.w.*).

Barrett model[87] is employed to predict the nucleation rate reduction for the water-argon experiments carried out at 0.06 MPa and different temperatures (220 K-260 K) by Wölk and Strey.[43] The results of this analysis are summarized in TABLE 4.3. The theory[87] predicts a larger nucleation rate reduction for increasing temperatures: from $J/J_{\text{iso}} = 0.681$ at 220 K to $(J/J_{\text{iso}}) = 0.163$ at 260 K. In order to verify the predicted temperature dependency of the thermalisation effect, the experimental isothermal references $(J_{\text{iso}})_{\text{exp}}$ at each temperature condition are needed. These references are chosen such as adsorption effects can be considered negligible and the theoretical $J/J_{\text{iso}} = const \approx 1$. Exploiting Eqs. 4.7-4.10, we have found that such requirements are met by a water-helium mixture ($\Delta\sigma/\sigma_\ell < -0.2\%$, see SEC. 4.2.2) at 0.219 MPa for 220 K, at 0.458 MPa for 230 K, at 0.922 MPa for 240 K, at 1.834 MPa for 250 K and at 3.339 MPa for 260 K. Since experimental data for these conditions are not available in literature, we calculate them as $J_{\text{emp}}(S)$ by employing the proposed empirical correlation (Eq. 4.23). Note that $J_{\text{emp}}$ for water-helium at 3.69 MPa and 260 K is not calculated because outside of the $J_{\text{emp}}$ domain (see Sec. 4.4.1). The comparison between $J_{\text{exp}}$ and $(J_{\text{iso}})_{\text{exp}}$ is

**TABLE 4.3.** Temperature dependency of non-isothermal effect for water-argon at about 0.06 MPa.[43] The theoretical $J/J_{\text{iso}}$ (Eq. 4.7) are compared with the experimental values $(J/J_{\text{iso}})_{\text{exp}}$.

| p (MPa) | T (K) | $S^{\text{a}}$ | $\lambda$ | $J/J_{\text{iso}}$ | $(J/J_{\text{iso}})_{\text{exp}}^{\text{b}}$ |
|---|---|---|---|---|---|
| 0.0482 | 220 | 19.5 | 217 | 0.681 | 0.446 |
| 0.0571 | 230 | 14.8 | 110 | 0.551 | 0.297 |
| 0.0611 | 240 | 11.4 | 55 | 0.397 | 0.205 |
| 0.0517 | 250 | 9.2 | 23 | 0.223 | 0.195 |
| 0.0631 | 260 | 7.6 | 14 | 0.163 | - |

$^{\text{a}}$Mid-range of $S$ for each experimental condition: $(S_{\text{min}} + S_{\text{max}})/2$.
$^{\text{b}}$Ratio of $J_{\text{exp}}$ (Eq. 4.21) and corresponding (same $S$-value)$^{\text{a}}$ isothermal references $(J_{\text{iso}})_{\text{exp}}$ at different temperature. The latter is taken equal to $J_{\text{emp}}$ (Eq. 4.23) of water-helium at 0.219 MPa for 220 K, at 0.458 MPa for 230 K, at 0.922 MPa for 240 K, at 1.834 MPa for 250 K, at 3.339 MPa for 260 K (out of $J_{\text{emp}}$ domain, see Sec. 4.4.1). These conditions are chosen such as the theoretical $J/J_{\text{iso}} = const \approx 1$ and adsorption effects can be considered negligible ($\Delta\sigma/\sigma_\ell < -0.2\%$).
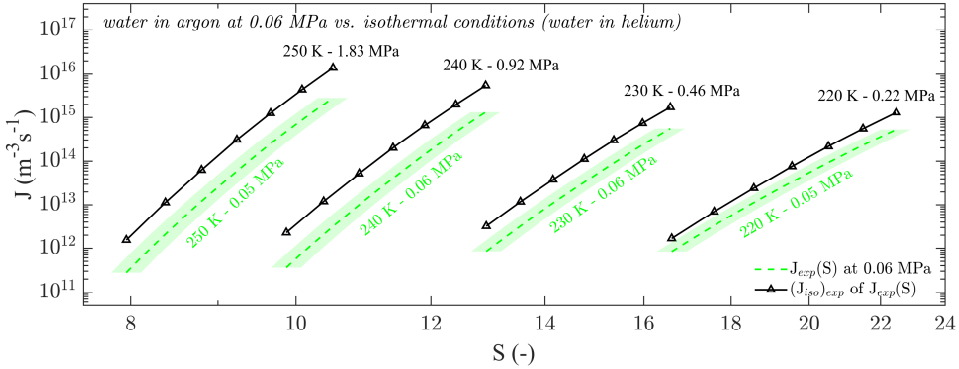
**FIG. 4.14.** Temperature dependency of the non-isothermal effect. Comparison between $J_{\text{exp}}$ (Eq. 4.21) for water-argon (shaded in green, green dashed line)[43] at 0.06 MPa and different temperatures (220 K-250 K) and the isothermal (experimental) references ($J_{\text{iso}}$)$_{\text{exp}}$ (black triangle-spotted line). The latter are computed as $J_{\text{emp}}$ (Eq. 4.23) of water-helium at 0.219 MPa for 220 K, at 0.458 MPa for 230 K, at 0.922 MPa for 240 K and at 1.834 MPa for 250 K.

shown in FIG. 4.14 as a function of $S$ at the different temperature conditions. As a result, the experimental nucleation rate reduction is also found to be larger with increasing temperatures: from $(J/J_{\text{iso}})_{\text{exp}} = 0.446$ at 220 K to $(J/J_{\text{iso}})_{\text{exp}} = 0.195$ at 250 K. The experimental trend is quantitatively well predicted by the Barrett model[87] at 250 K: $(J/J_{\text{iso}})_{\text{exp}} = 0.195$ and $J/J_{\text{iso}} = 0.223$. With decreasing temperatures, the theoretical nucleation rate reductions deviate from the experimental trend: $(J/J_{\text{iso}})_{\text{exp}} = 0.446$ and $J/J_{\text{iso}} = 0.681$ at 220 K. This outcome is not fully surprising since the Barrett model[87] was validated fo the water-argon case at 260 K and 0.06 MPa. However, at low as at high temperatures, the experimental trend is in qualitative agreement with the Barrett model,[87] albeit the theory quantitatively underestimates the thermalisation effect on the nucleation rate reduction, as already pointed out by Hrubý and co-authors.[141] This qualitative agreement is also confirmed when comparing water-argon and water-nitrogen at fixed temperature conditions (240 K). We argue that other aspects poorly treated by the classical nucleation theory are responsible for the lack of quantitative agreement. It is a matter of on-going research to find a possible reason for such discrepancy between theory and experiments.

## 4.5   Conclusions

Homogeneous nucleation of water has been experimentally studied in argon and nitrogen at about 240 K with the PEWT facility. Three different pressure conditions have been analyzed for both mixtures: 0.1 MPa, 1 MPa and 2 MPa. A substantial scatter reduction of the $J$-$S$ data has been found with respect to the experiments carried out with the previous version of the PEWT,[61] which confirms the improvements introduced with the new version of the setup.[116] A good agreement of the $J$-$S$ data has been found with the literature results, available at two of the investigated conditions (water-nitrogen[61] at 240 K and 1 MPa and water-argon[43] at 240 K and 0.06 MPa). The surface tension decrease due to adsorption effects appears to be the predominant cause of the nucleation rate enhancement at high pressure for both mixtures. Further research studies on the surface tension of water in diluent gases at supercooled conditions is

the key for a more accurate quantitative analysis. Higher pressure conditions and carrier gases with a larger influence on the surface tension are needed to give further confirmation of our findings. At fixed low pressure conditions, the theory of Barrett[87] on non-isothermal effects has been shown to qualitatively explain the experimental nucleation rate differences between water-argon and water-nitrogen at fixed temperature, as well as the temperature dependency of the thermalisation phenomenon in water-argon. For helium as carrier gas, the non-isothermal effects appear to be much stronger than predicted by the Barrett model.[87] The critical cluster size has been calculated from the experimental $J$-$S$ curves by means of the nucleation theorem. The comparison with the Gibbs-Thomson equation has revealed an agreement, within the experimental error bars, as already pointed out by Wölk and Strey.[43] This confirms that, at the analyzed conditions, the capillarity assumption can be considered an acceptable approximation to predict critical cluster size and slopes of the experimental $J(S)$ curves. On the other hand, using the macroscopic values of surface tension and density in the $J_{CNT}$, even with corrections for real gas, adsorption, and imperfect thermalisation, does not lead to quantitatively correct predictions of nucleation rates. Thus, we have introduced an empirical correction of $J_{CNT}$, based on the experimental values at the presented conditions. The proposed expression takes into account pressure, temperature and type of carrier gas, showing a one to one correspondence with the experimental nucleation rates within their uncertainty bands. This outcome suggests that the proposed empirical correlation can be used as a tool for the determination of actual nucleation rates within the following domain: water-argon, water-nitrogen and water-helium mixtures at pressures between 0.06 MPa and 2 MPa and temperatures from 220 K to 260 K.

# Homogeneous water nucleation in carbon dioxide-nitrogen mixtures

The content of this chapter is an unabridged version of the paper "M.M. Campagna, J. Hrubý, M.E.H. van Dongen, and D.M.J. Smeulders. Homogeneous water nucleation in carbon dioxide-nitrogen mixtures: experimental study on pressure and carrier gas effects. *J. Chem. Phys.* 154(15):154301, 2021" (Ref. 142).

***Abstract*** *New homogeneous nucleation experiments are presented at 240 K for water in carrier gas mixtures of nitrogen with carbon dioxide molar fractions of 5%, 15% and 25%. The Pulse Expansion Wave Tube (PEWT) is used to test three different pressure conditions, namely 0.1 MPa, 1 MPa and 2 MPa. In addition, a restricted series of nucleation experiments is presented for 25% carbon dioxide mixtures at temperatures of 234 and 236 K at 0.1 MPa. As pressure and carbon dioxide content are increased, the nucleation rate increases accordingly. This behavior is attributed to the reduction of the water surface tension by adsorption of carrier gas molecules. The new data are compared with theoretical predictions based on the Classical Nucleation Theory and on extrapolations of empirical surface tension data to the supercooled conditions at 240 K. The extrapolation is done on the basis of a theoretical adsorption/surface tension model, extended to multi-component mixtures. The theoretical model shows the expected trend, but appears to strongly overestimate the pressure and composition dependence. At relatively low pressures of 0.1 MPa, a reduction of the nucleation rates is found due to an incomplete thermalisation of colliding clusters and carrier gas molecules. The observed decrease of the nucleation rate is supported by the theoretical model of Barrett, generalized here for water in multi-component carrier gas mixtures. The temperature dependence of the nucleation rate at 0.1 MPa follows the scaling model proposed by Hale.*

## 5.1   Introduction

Dropwise condensation phenomena have been studied for over a century[1] with important implications in many industrial, technological and atmospheric applications.[2,143] In climate science, for example, cloud formation is of paramount importance but extremely difficult to model. This is because clouds both shade the Earth and trap heat. A recent study of Zelinnka *et al.*[144] suggests that in a warmer world, clouds would become thinner on average, resulting in additional global warming. This can be characterized as an indirect effect (cloud feedback) of

higher atmospheric carbon dioxide concentrations. In the present chapter we investigate the effect of carbon dioxide concentration and pressure on water nucleation in the absence of foreign particles or surfaces (homogeneous nucleation) in a nitrogen carrier gas, at low temperatures. Homogeneous nucleation is attractive because the number of stable droplets produced per unit of time and volume (nucleation rate) can directly be compared with the classical nucleation theory (CNT).[4–10] However it is not straightforward to realize experimentally, as nucleation is almost always heterogeneous. As shown in previous publications,[44,60,61,71,72,74–85,116,121] a Pulse Expansion Wave Tube (PEWT) is capable of eliminating contact of nuclei with foreign particles or surfaces and it enables experiments at different nucleation pressures, temperatures and various gas compositions.

In Chapter 4,[121] we investigated pressure and carrier gas effects on nucleation, pointing out the central role played by adsorption. In the present chapter, we present new homogeneous water nucleation experiments at 240 K and 0.1 MPa, 1 MPa and 2 MPa in nitrogen mixtures with carbon dioxide molar fractions of 0%,[121] 5%, 15% and 25%. The enhancement of the saturated vapor pressure due to the carrier gas presence in the mixture (enhancement factor) is accounted for in the experimental results. The observed trends are explained in terms of two different phenomena: adsorption and incomplete thermalisation. Adsorption of gas molecules on a liquid surface reduces the surface tension. Therefore, a theoretical analysis of the surface tension of water in presence of mixed carrier gas formed by nitrogen and carbon dioxide is proposed. The CNT is used to predict the effect of the calculated surface tension decrease on the nucleation rates and the results are compared with our experimental outcomes. At low pressure, the adsorption phenomena become negligible, while the collision frequency of gas molecules with clusters is too low for a full thermalisation of the clusters.[87,122,135–138] This effect is investigated theoretically according to the analytical model of Barrett.[87] Predictions of this model, generalized for water in a mixed carrier gas formed by nitrogen and carbon dioxide, are used to interpret our experimental findings at 0.1 MPa and 240 K. Additional 0.1 MPa experiments are carried out at 236 K and 234 K in nitrogen with 25% of carbon dioxide. The effect of the temperature on the experimental data is investigated by means of Hale's scaling model.[86] Apart from the comparison of the novel nucleation rate data with theoretical predictions, the combined effect of adsorption and insufficient thermalisation will also be shown by a comparison with reference nucleation rate data. These reference data are chosen such that both effects do not play a significant role.

## 5.2    Theoretical aspects

In this section, we shall discuss three phenomena with a common origin in the heteromolecular interaction taking place within the mixture: adsorption, incomplete thermalisation and enhancement effect.

### 5.2.1    Adsorption effects

The surface tension decrease of water in the presence of a diluent gas is related to the adsorption of gas molecules on the liquid surface.[133] As the pressure of the system increases or the temperature decreases, this effect becomes stronger.[85] The pressure and temperature dependency of the surface tension is also influenced by the type of carrier gas in the mixture (almost negligible effect in helium, stronger effects in nitrogen and argon).[85,121] We now extend this

analysis to water-carbon dioxide-nitrogen mixtures. To this end, we first need to generalize the theoretical treatment of the adsorption effect to the case of mixed carrier gas. The complete derivation is given in Appendix A. As a first step, we consider the general expression of the water surface tension in presence of one or more diluent gases

$$\sigma = \sigma_\ell - \frac{kT}{A_g} \ln\left(1 + \frac{p_g}{p_L}\right), \tag{5.1}$$

where $p_g = p - p_s(T)$, $p$ is the total pressure of the mixture, $p_s(T)$ and $\sigma_\ell$ are the equilibrium (saturation) vapor pressure[124] and the surface tension[125] of pure water at the temperature $T$, $A_g$ is the average surface area per adsorption site and $k$ is the Boltzmann constant. In the case of carbon dioxide and nitrogen as diluent gases (subscripts '2' and '3' respectively), the Langmuir pressure $p_L$ can be formulated as follows (see Eq. A.20)

$$p_L = (y_2 + y_3) \left[\frac{y_2}{p_{L,2}} + \frac{y_3}{p_{L,3}}\right]^{-1}, \tag{5.2}$$

where $y_2$ and $y_3$ are the molar fractions of carbon dioxide and nitrogen and

$$p_{L,i} = \frac{kT}{v_i^A} \exp\left(\frac{u_{g,i}^A}{kT}\right), \quad \text{with } i = 2,3. \tag{5.3}$$

The parameters $u_{g,i}^A$ and $v_i^A$ are the interaction potential energy of the $i$-th gas molecule with the liquid surface and the effective volume available for the translation of an adsorbed ($i$-th gas) molecule. The two quantities $u_{g,2}^A$ and $v_2^A$ (water-carbon dioxide case) are derived as follows. The surface tension data available in literature for water in carbon dioxide[145–147] are used to calculate the Langmuir pressures $p_{L,2}$ from Eq. 5.1 with $p_L = p_{L,2}$ and $A_g = 1.62 \cdot 10^{-19}$ m$^2$.[134] Finally, the $p_{L,2}(T)$ values are fitted with a regression curve in the form of Eq. 5.3, leading to the following regression parameters: $v_2^A = 1.37 \cdot 10^{-30}$ m$^3$ and $u_{g,2}^A = -2.8 \cdot 10^{-20}$ J. FIG. 5.1a shows the experimental Langmuir pressures as a function of temperature (black squares, pentagons and triangles) and their fit (black dashed line). The same procedure can be applied to the water-nitrogen case (surface tension data from Refs. 128–132), leading to $v_3^A = 6.94 \cdot 10^{-30}$ m$^3$ and $u_{g,3}^A = -1.18 \cdot 10^{-20}$ J (see FIG. 5.1b). In this way, the water surface tension reduction in carbon dioxide and nitrogen can be calculated (Eqs. 5.1-5.3) for the investigated experimental conditions. The final results are reported in FIG. 5.2.

For small ratios $p_g/p_L$, the $\ln(1 + p_g/p_L)$ term in Eq. 5.1 can be approximated by $p_g/p_L$ (see Eqs. A.21-A.23 in Appendix A). This approach was used in our previous publication[121] for the water-nitrogen case, leading to similar values for $v_3^A$ and $u_{g,3}^A$ ($8.85 \cdot 10^{-30}$ m$^3$ and $-1.03 \cdot 10^{-20}$ J). In the water-carbon dioxide case, the linear approximation is inaccurate, leading to a different $p_{L,2}(T)$ curve (red dashed-dotted line in FIG. 5.1a). For this reason, the general derivation is used in the present analysis for water in carbon dioxide and, in order to keep a consistent approach, for water in nitrogen as well.

## 5.2.2 Incomplete thermalisation effects

Nucleation in vapor-gas systems is generally affected by an incomplete thermalisation of the growing clusters.[87,122,135–138] This effect becomes more pronounced at lower pressures as the amount of the non-condensing component is insufficient to thermalize the clusters. The result
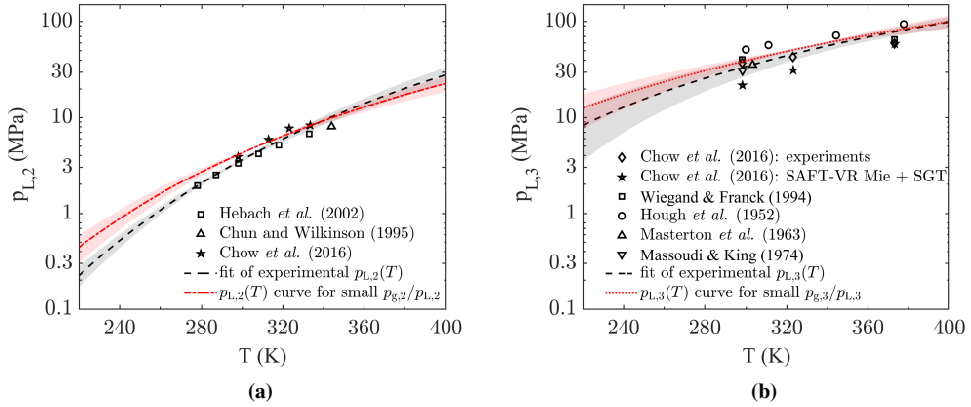
**FIG. 5.1.** Langmuir pressure for water in carbon dioxide $p_{L,2}$ (5.1a) and in nitrogen $p_{L,3}$ (5.1b) as a function of temperature. The experimental values in (5.1a) are derived from surface tension data for water in carbon dioxide atmosphere, available for above 278 K. [145–147] The experimental values in (5.1b) are derived from surface tension data for water in nitrogen atmosphere, available for above 298 K. [128–132] The corresponding values of $p_{L,2}$ and $p_{L,3}$ (black symbols) are fitted and extrapolated to the super-cooled region down to 220 K (black dashed line). The fit obtained assuming small $p_{g,2}/p_{L,2}$ and $p_{g,3}/p_{L,3}$ (red dashed-dotted line) is shown for comparison. The standard uncertainty is shaded around the lines.
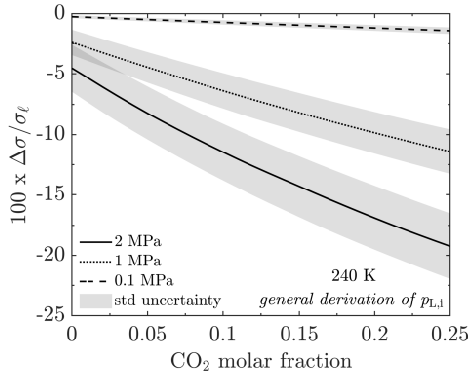


**FIG. 5.2.** Relative water surface tension reduction $(\sigma - \sigma_\ell)/\sigma_\ell$ as a function of carbon dioxide molar fraction in the water-nitrogen mixture at 240 K (Eqs. 5.1-5.3). The values are calculated at the investigated pressures: 0.1 MPa (dashed line), 1 MPa (dotted line) and 2 MPa (solid line). The standard uncertainty is shaded around the lines.

is a nucleation rate reduction, with respect to the isothermal case, modeled by Barrett as (in zeroth order approximation) [87,137,138]

$$\left(\frac{J}{J_{\text{iso}}}\right)_{\text{B}} = \left[1 + \frac{(\hat{c}_{\text{bv}} + H)^2}{\hat{c}_{\text{bv}}(1 + \lambda)}\right]^{-1}, \tag{5.4}$$

where $J_{\text{iso}}$ is the isothermal condition. In Eq. 5.4, $\hat{c}_{\text{bv}} = c_{\text{v}}/k + 1/2$ with $c_{\text{v}}$ the vapor monomer heat capacity at constant volume. The non-dimensional parameter $H$ is defined as

$$H = \frac{ML}{N_a kT} - \frac{1}{2} - \hat{c}_{\text{bv}} + \frac{2}{3(n_{\text{GT}}^*)^{1/3}} T \frac{d\Theta}{dT}, \tag{5.5}$$

with $M$ the molar mass of the vapor component, $L$ the latent heat of vaporization, $T$ the temperature, $n^*_{GT} = 32\pi v_\ell^2 \sigma_\ell^3 / [3(kT \ln S)^3]$ the critical cluster size as defined by Gibbs-Thomson (see Eq. 4.4), $v_\ell$ the molecular liquid volume of the pure vapor component,[123] $\Theta = A_{<1>} \sigma_\ell / kT$ the non-dimensional surface tension of the pure vapor component (see Eq. 2.37) and $A_{<1>} = (36\pi)^{1/3} v_\ell^{2/3}$ the surface area of the vapor monomer. In the Barrett model, the parameter $\lambda$ of Eq. 5.4 is defined for a vapor – (single) carrier gas mixture as $\lambda = c_{bg} \rho_g \overline{v}_g / c_{bv} \rho_1 \overline{v}_1$ (see Eq. 4.9), with $c_{bg} = c_g + k/2$ the enhanced heat capacity of the gas at constant volume, $\rho$ and $\overline{v}$ the number densities and the mean thermal velocities of gas and vapor components (subscripts 'g' and '1'). We propose the following generalization of this expression, accounting for the presence of two (or more) carrier gases (subscripts '2' and '3'):

$$\lambda = \frac{\sum_{i=2}^{3} c_{bg,i} \rho_{g,i} \overline{v}_{g,i}}{(c_{bv} \rho_1 \overline{v}_1)}. \tag{5.6}$$

We will use this approach to calculate $(J/J_{iso})_B$ at the investigated conditions and analyze the incomplete thermalisation influence on the experimental data.

### 5.2.3 Enhancement factor

Interactions between vapor and gas molecules cause an enhancement of the vapor molar fraction $y_{eq}$ in the gas phase in equilibrium with the liquid phase (see Sec. 2.1).[74,89,90,139,140] This effect can be quantified by the enhancement factor $f_e$ as (see Eq. 2.9)

$$f_e \equiv \frac{y_{eq} p}{p_s} = \frac{\phi_s}{\phi_{eq}} x_{1,eq} \exp\left[\frac{v_\ell (p - p_s)}{kT}\right], \tag{5.7}$$

with $p$ and $T$ the total pressure and temperature of the mixture and $x_{1,eq} = (1 - x_{2,eq} - x_{3,eq})$ the liquid fraction of the vapor component (see Eq. 2.14). In our analysis we shall neglect the solubility of nitrogen in water as $x_{3,eq} \leq 0.0015$ (see FIG. 2.3). It follows that $x_{1,eq}$ can be directly derived from the liquid fraction of carbon dioxide $x_{2,eq}$ (see Sec. 2.1.1). The parameter $\phi_s$ in Eq. 5.7 is the fugacity coefficient at equilibrium for pure water vapor and it is obtained as $\phi_s = \exp[B_{11} p_s / (RT)]$ (see Eq. 2.10), with $B_{11}$ standing for the second virial coefficient of pure water (see FIG. 2.1a).[91] The fugacity $\phi_{eq}$ for water vapor in presence of carbon dioxide and nitrogen is computed with the following expression

$$\ln \phi_{eq} = [y_{eq} B_{11} + y_2 B_{12} + y_3 B_{13}] \frac{2}{V} - \ln Z, \tag{5.8}$$

where $y_2$ and $y_3$ are the carbon dioxide and nitrogen molar fractions and where $B_{12}$ and $B_{13}$ are the second cross-virial coefficients for water-carbon dioxide[98] (see FIG. 2.2d) and water-nitrogen (see FIG. 2.2c),[148] respectively. The compressibility factor $Z = pV/RT$ can be expressed as $Z = 1 + B/V$, where $V$ is the molar volume and $B$ the second virial coefficient of the mixture

$$B = y_1^2 B_{11} + y_2^2 B_{22} + y_3^2 B_{33} + 2y_1 y_2 B_{12} + 2y_1 y_3 B_{13} + 2y_2 y_3 B_{23}. \tag{5.9}$$

with $B_{22}$ and $B_{33}$ the second virial coefficients of the pure carbon dioxide (see FIG. 2.1e) and nitrogen components (see FIG. 2.1d), while $B_{23}$ is the second cross-virial coefficients for
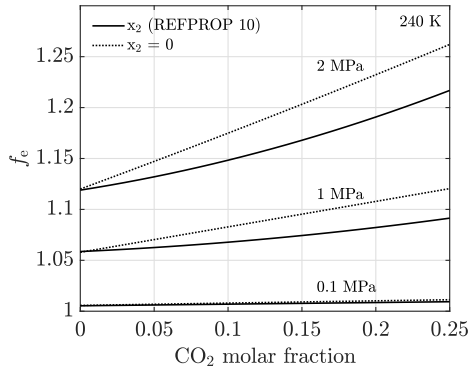
**FIG. 5.3.** Enhancement factor of water in carbon dioxide and nitrogen as a function of the carbon dioxide molar fraction at 240 K and 0.1 MPa, 1 MPa and 2 MPa (black solid lines). The figure shows also the comparison with the enhancement factor calculated assuming the liquid fraction of carbon dioxide to be negligible $x_2 = 0$ (dotted lines).

carbon dioxide-nitrogen (see FIG. 2.2e).[91] The enhancement factor calculated according to the present analysis is reported in FIG. 5.3 for the investigated conditions.

The reader is referred to Sec. 2.1.1 for more details on the carbon dioxide and the nitrogen solubility in water and on the virial and cross-virial coefficients used for the present study.

## 5.3    Experimental methodology

The experimental setup used for the present work is the Pulse Expansion Wave Tube (PEWT) (see Chapter 3),[116] a specially designed shock tube, implementing the so called nucleation pulse method.[69] This technique enables the nucleation and the droplet growth phenomena to be effectively decoupled, leading to a monodisperse cloud of condensing clusters.[116] In this way, the nucleation rate $J$ — the number of critical clusters generated per unit of time and volume — can be determined as $J = n_d/\Delta t_p$, with $\Delta t_p$ the nucleation pulse duration[116] and $n_d$ the droplet number density. The Constant Angle Mie Scattering method (CAMS)[52,54,55] is used to measure $n_d$ by means of an optical setup placed at the observation section of the PEWT.[116] A maximum standard uncertainty of 20% is calculated for $J$ (see Chapter 4).[121]

The other key parameter in homogeneous nucleation studies is the supersaturation. It quantifies the deviation of the current state for the vapor component from its corresponding (same $p$ and $T$) phase equilibrium and can be approximated as $S \approx y/y_{eq}$ (see Eq. 2.16), where $y_{eq}$ (Eq. 5.7) is the equilibrium vapor molar fraction for water in carbon dioxide and nitrogen at the nucleation conditions $p$ and $T$. The pressure $p$ is measured via two pressure transducers at the PEWT test section, while the temperature $T$ is derived from the pressure signal, by assuming isentropic conditions for the real mixture and measuring the initial temperature at the test section walls.[116,121] A controlled vapor molar fraction $y$ is obtained by means of the mixture preparation device (MPD) shown in FIG. 5.4. Pure nitrogen flowing from gas bottle $G_I$ (99.999% purity) is split into two controlled flows A and B (normal volume flow rates $Q_A$ and $Q_B$). Flow A is fully saturated with the pure water contained inside the saturators $sat_a$ and $sat_b$,[116] while flow B remains dry. A third flow (normal volume flow rate $Q_C$) of nitrogen and carbon dioxide is let into the MPD from the premixed gas bottle $G_{II}$. As a result, a well

**FIG. 5.4.** Schematic of the Mixture Preparation Device (MPD).

defined total flow rate $Q_{tot} = Q_A + Q_B + Q_C + Q_{H_2O}$ is obtained at the MPD outlet, with $Q_{H_2O}$ the water flow rate added to the mixture after $Q_A$ passes through $sat_a$ and $sat_b$. Once the thermodynamic conditions $p_{mpd}$ and $T_{mpd}$ and the three flow rates $Q_A$, $Q_B$ and $Q_C$ are known, the vapor molar fraction of water in the mixture can be determined as

$$y = \frac{Q_{H_2O}}{Q_{tot}} = \frac{y'_{eq}}{1 + (1 - y'_{eq})\dfrac{Q_B + Q_C}{Q_A}}, \tag{5.10}$$

where $y'_{eq}$ is the equilibrium vapor molar fraction calculated at the MPD conditions as

$$y'_{eq} = \frac{Q_{H_2O}}{Q_{H_2O} + Q_A} = f_{e,mpd}\frac{p_s(T_{mpd})}{p_{mpd}} \tag{5.11}$$

and where $f_{e,mpd} = f_{e,13}(p_{mpd}, T_{mpd})$ is the enhancement factor for water in nitrogen at $p_{mpd}$ and $T_{mpd}$. By controlling the MPD thermodynamic conditions ($p_{mpd}$ and $T_{mpd}$) and flow rates ($Q_A$, $Q_B$ and $Q_C$), the desired vapor molar fraction of carbon dioxide can be derived as

$$y_2 = \frac{Q_2}{Q_{tot}} = \frac{y_2^C Q_C}{\dfrac{Q_A}{1 - y'_{eq}} + Q_B + Q_C}, \tag{5.12}$$

with $Q_2 = y_2^C Q_C$ the carbon dioxide flow rate and $y_2^C = 0.5$ the molar fraction of carbon dioxide in $G_{II}$. This experimental methodology leads to a maximum standard uncertainty for $S$ of 2.5%. A more extensive description of the MPD can be found in Refs. 92, 117 and in Chapter 3. The calculation of the described quantities at the investigated conditions is reported in Appendix B.

## 5.4 Results and discussion

In this section, the experimental results will be presented and, afterwards, interpreted with reference to adsorption (Sec. 5.2.1) and incomplete thermalisation effects (Sec. 5.2.2). The

enhancement of the equilibrium vapor pressure (enhancement factor), discussed in Sec. 5.2.3, is accounted for in the presented supersaturation values as described in Sec. 5.3.

### 5.4.1   Experiments at 240 K for various pressures and carbon dioxide contents

Homogeneous water nucleation experiments have been carried out at 240 K and 0.1 MPa, 1 MPa and 2 MPa in nitrogen with 5%, 15% and 25% of carbon dioxide.[a] The resulting nucleation rate data $J$ as a function of the supersaturation $S$ are summarized in FIG. 5.5 for each pressure condition: 2 MPa (FIG. 5.5a), 1 MPa (FIG. 5.5b) and 0.1 MPa (FIG. 5.5c). The $J$-$S$ data are represented for variable carbon dioxide molar fractions: 5% (green circles), 15% (red squares) and 25% (blue triangles). The whole set of data is fitted according to the following regression curve $J_{exp} = C \exp[D/(\ln S)^2]$ (see Eq. 4.21), with the coefficients $C$ and $D$ calculated for each pressure and temperature condition and for each carbon dioxide vapor molar fraction. Different $J_{exp}(S)$ line types are used to distinguish the pressure conditions: dashed lines for 0.1 MPa, dotted lines for 1 MPa and solid lines for 2 MPa. The standard uncertainties for $J$ (20% at the most - within the symbol sizes) and for $S$ (2.5%) are shaded around the regression curves (FIG. 5.5). The experimental nucleation rates presented in Chapter 4 for water in nitrogen at the investigated pressures (0.1 MPa, 1 MPa and 2 MPa) and temperature (240 K) are also included in the analysis, denoted as 0% carbon dioxide (FIG. 5.5). The $J_{exp}(S)$ lines are colored according to the carbon dioxide content. Details on regression coefficients ($C$ and $D$), fitting quality ($R^2_{adj}$) and experimental $J$-$S$ data can be found in Appendix B. As pointed in Chapter 4, both surface tension reduction and incomplete thermalisation effects can be considered negligible at 240 K for homogeneous water nucleation in helium at 1 MPa. Therefore, also for the current analysis, this condition is used as experimental reference at 240 K and it is denoted as $J_{id,exp}$ (dashed dotted lines in FIG. 5.5).

The $J$-$S$ data at 2 MPa and 240 K in FIG. 5.5a show that $J_{exp}$ is higher than $J_{id,exp}$ from about an order of magnitude at 0% of carbon dioxide to about three orders of magnitude at 25% of carbon dioxide. Consistently, intermediate results are found for $J_{exp}$ with 5% and 15% of carbon dioxide in the mixture. In TABLE 5.1, $J_{exp}/J_{id,exp}$ is quantified at the supersaturation mid-range value $[(S_{max} + S_{min})/2]$ for each condition.

The data at 1 MPa and 240 K with 5%, 15% and 25% of carbon dioxide in FIG. 5.5b show a smaller nucleation rate increase than the 2 MPa case.

At 0.1 MPa, the increasing trend of $J_{exp}$ with increasing the carbon dioxide content, albeit present, is within the uncertainty bands. Moreover, the nucleation rates at 0.1 MPa and 240 K are found to be lower than the nucleation rates at the ideal experimental condition $J_{id,exp}$. Later we will show that this can be attributed to the effect of incomplete thermalisation.

#### 5.4.1.1   Comparison of the 240 K high pressure experiments with the theoretical predictions: effect of adsorption of carrier gases on nucleation rates

The described experimental behavior can be qualitatively explained by taking into account adsorption phenomena and incomplete thermalisation effects. The surface tension of water in nitrogen and carbon dioxide decreases with respect to the surface tension of pure water $\sigma_\ell$ as pressure and carbon dioxide content increase (see Sec. 5.2.1 [Eqs. 5.1-5.3]). The values of

---

[a]Note that the nucleation phenomena investigated in the present work can be considered as essentially unary (water) nucleation,[77,114] as pointed out at the end of Sec. 2.1.2.
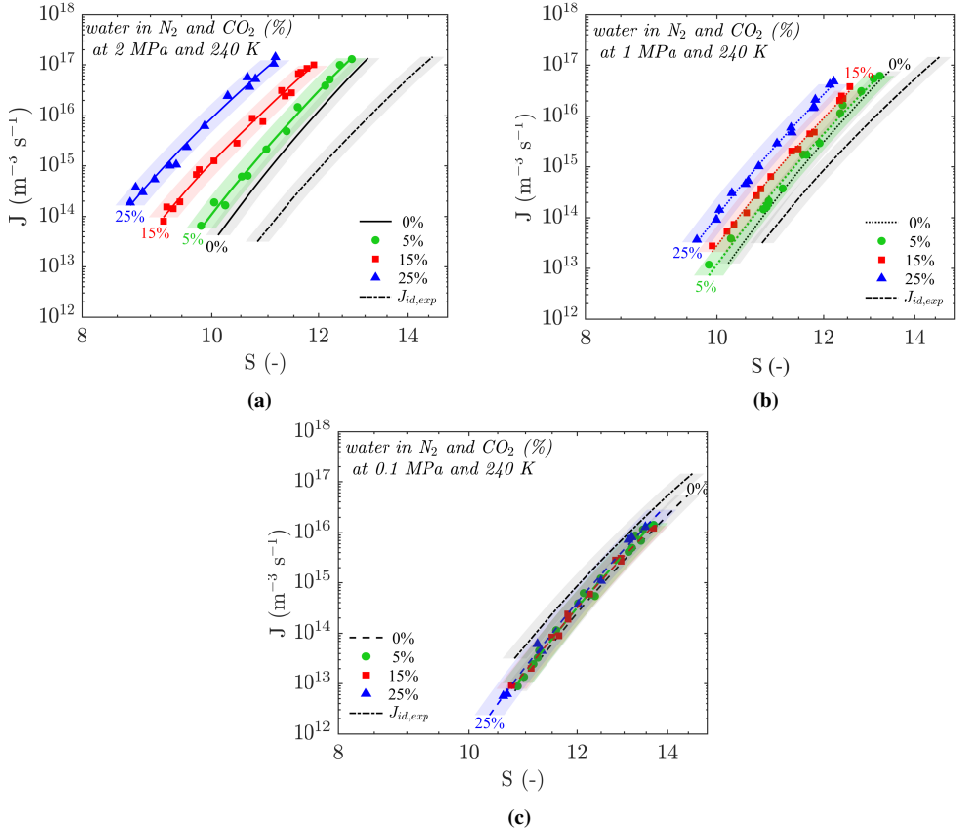
**FIG. 5.5.** *J-S* plot of the 240 K homogeneous water nucleation experiments in carbon dioxide and nitrogen at 2 MPa (FIG. 5.5a), 1 MPa (FIG. 5.5b) and 0.1 MPa (FIG. 5.5c). The data are represented as a function of the carbon dioxide molar fraction: 5% (green circles), 15% (red squares) and 25% (blue triangles). The lines refer to the data fitting curve $J_{exp} = C \exp[D/(\ln S)^2]$ (see text in Sec. 5.4). The standard uncertainties are shaded around the regression curves. The $J_{exp}(S)$ curves for water in nitrogen[121] at 240 K and 0.1 MPa (black dashed line), 1 MPa (black dotted line) and 2 MPa (black solid line) are denoted as 0% carbon dioxide. The lines are colored according to the carbon dioxide content: 0% (black lines), 5% (green lines), 15% (red lines) and 25% (blue lines). The experimental ideal reference $J_{id,exp}(S)$ corresponds to the $J_{exp}(S)$ of the water-helium condition at 240 K and 1 MPa (black dashed-dotted lines with black shaded band for the standard uncertainty).[121]

the relative water surface tension decrease $(-\Delta\sigma/\sigma_\ell)$ for the investigated conditions and their standard uncertainties are reported in FIG. 5.2 (mean values in TABLE 5.1). This reduction is caused by the adsorption of gas monomers on the cluster surface. A theoretical estimate of this effect on the nucleation rates can be made by employing the Classical Nucleation Theory (CNT) expression (see Eqs. 4.1-4.3)

$$J_{CNT} = \left(\frac{p_s}{kT}\right)^2 S v_\ell \sqrt{\frac{2\sigma N_a}{\pi M}} \exp\left[-\frac{16\pi v_\ell^2}{3(\ln S)^2}\left(\frac{\sigma}{kT}\right)^3\right]. \tag{5.13}$$

The nucleation rates calculated according to the CNT will be indicated as $J_{CNT}$ when it is assumed $\sigma = \sigma(p, T, y_2, y_3)$ [Eqs. 5.1-5.3]. The nucleation rate increase predicted by the CNT can be estimated with the ratio $J_{CNT}/J_{0,CNT}$, where $J_{0,CNT}$ is the value for $\sigma = \sigma_\ell$. These ratios

are calculated for each experimental condition and the results are reported in TABLE 5.1.

At 2 MPa and 1 MPa, incomplete thermalisation phenomena do not play a role as $(J/J_{\mathrm{iso}})_\mathrm{B}$ is 0.98 and 0.95 respectively (TABLE 5.1). On the contrary, $J_{\mathrm{CNT}}/J_{0,\mathrm{CNT}}$ progressively increases with pressure and carbon dioxide content as the surface tension decreases. At 1 MPa, $J_{\mathrm{CNT}}/J_{0,\mathrm{CNT}}$ goes from 27 for 0% of carbon dioxide up to $1.7 \cdot 10^5$ for 25% of carbon dioxide. At 2 MPa, $J_{\mathrm{CNT}}/J_{0,\mathrm{CNT}}$ increases from 410 for 0% of carbon dioxide up to $5.2 \cdot 10^8$ for 25% of carbon dioxide.

We observe that the theoretical predictions $J_{\mathrm{CNT}}/J_{0,\mathrm{CNT}}$ appear to strongly overestimate the nucleation rate increase, due to gas adsorption, for all the analyzed conditions. This is not fully surprising considering that the CNT assumes bulk properties (capillarity approximation), which poorly describes the nucleation process in case of clusters consisting of a few molecules only. This is the case for the experimental conditions presented in the current investigation: the critical cluster size, as determined using the nucleation theorem,[126,127] is of about 30 molecules (see TABLE 6.1). Hence, for the present analysis, $J_{\mathrm{CNT}}/J_{0,\mathrm{CNT}}$ can only be used as qualitative reference to predict the trend of the nucleation rate increase as a function of pressure and carbon dioxide content. We can conclude that our experimental findings at 240 K and high pressure (2 MPa and 1 MPa) seem to confirm the central role played by the adsorption

**TABLE 5.1.** Summary of experimental nucleation rate variation $J_{\mathrm{exp}}/J_{\mathrm{id,exp}}$ as a function of the investigated $CO_2$ molar fractions (%) and pressures $p$ at 240 K. These values are compared to the theoretical (CNT) nucleation rate increase $J_{\mathrm{CNT}}/J_{0,\mathrm{CNT}}$ (Eq. 5.13), due to the surface tension reduction $(-\Delta\sigma/\sigma_\ell)\%$. The predicted decrease of the nucleation rate according to the Barrett model[87] $(J/J_{\mathrm{iso}})_\mathrm{B}$ [Eq. 5.4] is also reported.

| $(CO_2)_\%$ | $p$ (MPa) | $S$[a] | $J_{\mathrm{exp}}/J_{\mathrm{id,exp}}$[b] | $(-\Delta\sigma/\sigma_0)_\%$[c] | $J_{\mathrm{CNT}}/J_{0,\mathrm{CNT}}$ | $(J/J_{\mathrm{iso}})_\mathrm{B}$ |
|---|---|---|---|---|---|---|
| 0 | 0.10172 | 12.6 | 0.33 | 0.25 | 1.4 | 0.6404 |
| 5 | 0.10095 | 12.3 | 0.39 | 0.48 | 1.8 | 0.6439 |
| 15 | 0.10067 | 12.2 | 0.38 | 0.97 | 3.0 | 0.6432 |
| 25 | 0.10072 | 12.0 | 0.48 | 1.42 | 4.8 | 0.6451 |
| 0 | 1.0018 | 11.9 | 3.5 | 2.35 | 27 | 0.9487 |
| 5 | 1.0020 | 11.5 | 5.3 | 4.41 | 208 | 0.9495 |
| 15 | 0.9960 | 11.2 | 11 | 8.11 | $7.4 \cdot 10^3$ | 0.9500 |
| 25 | 1.0051 | 10.9 | 40 | 11.39 | $1.7 \cdot 10^5$ | 0.9513 |
| 0 | 2.0004 | 11.6 | 14 | 4.46 | 410 | 0.9740 |
| 5 | 1.9957 | 11.3 | 40 | 8.10 | $1.2 \cdot 10^4$ | 0.9745 |
| 15 | 2.0003 | 10.6 | 350 | 14.2 | $1.8 \cdot 10^6$ | 0.9757 |
| 25 | 2.0002 | 9.9 | $4.6 \cdot 10^3$ | 19.08 | $5.2 \cdot 10^8$ | 0.9767 |

[a]Mid-range of $S$ for each experimental condition: $(S_{\mathrm{min}} + S_{\mathrm{max}})/2$.

[b]Ratio of $J_{\mathrm{exp}}(S)$ and $J_{\mathrm{id,exp}}(S)$, both calculated at the same $S$-value.[a] As an example, consider the case with 25% of carbon dioxide at 2 MPa and $S = 9.9$ (last line in TABLE 5.1): $J_{\mathrm{exp}}(S = 9.9) = 7.2 \cdot 10^{15}$, $J_{\mathrm{id,exp}}(S = 9.9) = 1.6 \cdot 10^{12}$ and $J_{\mathrm{exp}}/J_{\mathrm{id,exp}} = 4.6 \cdot 10^3$. Note that $J_{\mathrm{id,exp}}(S)$ is the regression curve of the water-helium data at 1 MPa and 240 K (reference experimental case), with $J_{\mathrm{id,exp}}(S) = C \exp[D/(\ln S)^2]$, $C = 5.5 \cdot 10^{30}$ and $D = -224.7$ (Ref. 121). The reader is referred to the Appendix B for the regression curves $J_{\mathrm{exp}}(S)$ of each condition in the current work.

[c]$\Delta\sigma = \sigma - \sigma_\ell(T)$ (see Sec. 5.2.1, Eqs. 5.1-5.3).

[d]Literature references, with *c.w.* (current work) denoting the new data.

phenomena in increasing the nucleation rate when pressure and carbon dioxide content are increased.

### 5.4.1.2 Comparison of the 240 K low pressure experiments with the theoretical predictions: effect of incomplete thermalisation on nucleation rates

At 0.1 MPa and 240 K, $J_{CNT}/J_{0,CNT}$ ranges from 1.4 with no carbon dioxide up to about 4 with 25% carbon dioxide. Considering that the theory strongly overpredicts the nucleation rate at high pressure, we postulate that $J_{CNT}/J_{0,CNT}$ is overpredicted at low pressure as well and is close to unity in practice. On the other hand, incomplete thermalisation (Barrett theory) at ambient pressure tends to decrease the nucleation rate with respect to the isothermal condition, with a $(J/J_{iso})_B$ of about 0.64 for any carbon dioxide content (TABLE 5.1). Hence, incomplete thermalisation at 0.1 MPa explains the experimental data at this condition, within the uncertainty bands. It is clear that, for a more detailed check of the Barrett model, experiments at much lower pressures would be indispensable.

## 5.4.2 Experiments at 0.1 MPa and 25% of $CO_2$: temperature effect on nucleation rate and Hale scaling

Additional water nucleation experiments in nitrogen and 25% of carbon dioxide have been conducted at 0.1 MPa for 236 K and 234 K. The corresponding *J-S* data, fitting curves and uncertainty bands are represented in FIG. 5.6. The reader is referred to the Appendix B for more details. A nucleation rate decrease of about 2 order of magnitude is observed when the temperature is reduced from 240 K to 236 K. This result is in agreement with the nucleation rate reduction observed in Chapter 4 for water in argon. As pointed out, the *J-S* data can be successfully scaled to different temperatures by employing the Hale model:[86] $S_{sc} = \exp[C_0 \ln S/(T_c/T - 1)^{3/2}]$ with $C_0 = (T_c/T_{sc} - 1)^{3/2}$, $T_{sc}$ the target scaling temperature, $S$ the actual supersaturation at the temperature $T$ and with $T_c$ the critical temperature of water.
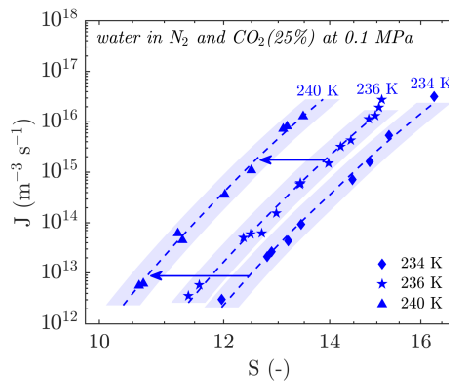


**FIG. 5.6.** *J-S* plot of the 0.1 MPa homogeneous water nucleation experiments in carbon dioxide (25%) and nitrogen at 240 K (blue triangles), 236 K (blue pentagons) and 234 K (blue diamonds). The two blue dashed lines at 236 K and 234 K are the fitting curves $J_{exp}(S)$ of the data at these two temperature conditions. The blue dashed line at 240 K represents the $J_{exp}(S)$ curve that fits the 236 K and the 234 K data scaled[86] to 240 K. The uncertainty bands are shaded in blue.

We now verify the Hale scaling for our water-nitrogen-25% carbon dioxide mixture at 0.1 MPa. The 0.1 MPa *J-S* data obtained at 234 K (blue diamonds) and 236 K (blue pentagons) are shown in FIG. 5.6. These data are scaled[86] to 240 K and the regression curve for the scaled data is represented as blue dashed line at 240 K in FIG. 5.6. The comparison between the scaled curve (blue dashed line at 240 K) and the actual *J-S* values at 240 K (blue triangles) shows a perfect agreement, which demonstrates the validity of the Hale scaling model[86] for the current water-nitrogen-carbon dioxide mixture as well as for the water-argon case discussed in Chapter 4.

## 5.5   Conclusions

Homogeneous water nucleation experiments were carried out with the Pulse Expansion Wave Tube in mixtures of nitrogen and 5%, 15% and 25% carbon dioxide molar fractions. Most experiments were performed at a temperature of 240 K. Various pressures were tested: 0.1 MPa, 1 MPa, and 2 MPa. Nucleation rates were determined as functions of the supersaturation for a fixed pressure, temperature and carrier gas composition. An experimental reference was identified in literature for which adsorption and thermalisation effects do not play a role (Sec. 5.4.1).[116,121]

As the pressure is increased from 1 MPa to 2 MPa, the experimental nucleation rates are found to increase. This effect is stronger when the fraction of carbon dioxide increases (Sec. 5.4.1 and FIG. 5.5) and it can be attributed to the surface tension reduction (Sec. 5.4.1.1). The adsorption of carrier gas molecules on a liquid surface reduces the surface tension. To compute this, use is made of an adsorption/surface tension theory, extended to multi components (Sec. 5.2.1 and Appendix A). Empirical literature data in the temperature range of 280 K - 350 K for the Langmuir pressure were extrapolated to 240 K. The surface tension data are substituted in the Classical Nucleation Theory (CNT). The predicted effects of pressure and composition are in qualitative agreement with the experimental trend (Sec. 5.4.1.1 and TABLE 5.1), as extensively pointed out in literature.[78,84,85,121] A strong quantitative overestimation of the model is found, mainly due to the CNT (Sec. 5.4.1.1).

At 0.1 MPa and 240 K, the increase of carbon dioxide from 0% to 25% does not appear to affect the nucleation rates. Additionally, they are found to be smaller than the experimental isothermal reference (Sec. 5.4.1 and FIG. 5.5c). This can be explained by incomplete thermalisation of the colliding clusters and carrier gas molecules. These results were confirmed, within the experimental uncertainty, by the theoretical model of Barrett[87] (Sec. 5.4.1.1 and TABLE 5.1). It is recognized that adsorption phenomena are negligible at 0.1 MPa and 240 K.

Additional experiments were performed at 0.1 MPa, 25% carbon dioxide and two different temperatures: 234 K and 236 K. The nucleation rates decrease with temperature and perfectly follow the scaling model of Hale (Sec. 5.4.2 and FIG 5.6).

# Chapter 6

# Critical cluster composition from homogeneous nucleation data: application to water in carbon dioxide-nitrogen

The content of this chapter is an unabridged version of the paper "M.M. Campagna, J. Hrubý, M.E.H. van Dongen, and D.M.J. Smeulders. Critical cluster composition from homogeneous nucleation data: application to water in carbon dioxide–nitrogen carrier gases. *Exp. Fluids* 62(9):189, 2021" (Ref. 149).

**Abstract** *Knowledge on critical cluster composition is important for improving the nucleation theory. Thus, homogeneous water nucleation experiments previously carried out in nitrogen and 0%, 5%, 15% and 25% of carbon dioxide (Refs. 121, 142) are analyzed. The tests were conducted at 240 K and 0.1 MPa, 1 MPa and 2 MPa. The observed nucleation rates are strongly dependent on supersaturation, pressure, temperature and mixture composition. These experimentally found dependencies can be used to derive the composition of critical clusters by means of the nucleation theorem. In this way, a macroscopic quantity, nucleation rate, reveals properties of critical clusters consisting of a few tens of molecules. Two novel methods are presented for the detailed application of the nucleation theorem. The first method extends to mixtures of N > 2 components the approach used in literature for two components. The second method not only applies to N > 2 mixtures in a more straightforward manner, but it can also be used for unary as well as for binary and multi-component nucleation cases. To the best of our knowledge, for the first time the critical cluster composition is computed for high pressure nucleation data of a vapor (here water) in mixtures of two carrier gases (here carbon dioxide-nitrogen). After a proper parameterization of the nucleation rate data, both methods consistently lead to the same critical nuclei compositions within the experimental uncertainty. Increasing pressure and carbon dioxide molar fraction at fixed supersaturation leads to a decrease of the water content of the critical cluster, while the adsorbed number of nitrogen and carbon dioxide molecules increases. As a consequence, the surface tension decreases. This outcome explains the observed increase of the nucleation rate with increasing pressure and carbon dioxide molar fraction at constant supersaturation.*

## 6.1   Introduction

Water condensation processes have important implications for a great variety of technological and climate related processes.[2] Water condensation is considered homogeneous when the vapor-to-liquid transition takes place in absence of surfaces or foreign particles such as dust or ions.  Under these circumstances, Wilson[1] speculated that aggregates of water molecules, called nuclei, must act as condensation centers.  Molecular clusters grow by collision with the free vapor molecules, while they also shrink by evaporation in a stochastic process.  The probabilities of growth and decay are equal for the critical cluster.  The number of supercritical clusters/droplets formed per unit time and volume is the so-called nucleation rate $J$. This quantity can be experimentally determined.[116,121,142] The homogeneous nucleation rate $J$ strongly depends on temperature $T$, pressure $p$, supersaturation $S$ of the condensing vapor and presence of carrier gases in the mixture. The supersaturation $S$ represents the driving force of the nucleation process and quantifies the current state deviation of the condensing component from its corresponding (same $p$ and $T$) phase equilibrium.  A generally accepted expression for the nucleation rate $J$ is (see Eq. 2.43)

$$J = K \exp\left(\frac{-W^*}{kT}\right),$$
(6.1)

with $W^*$ the work of formation of a critical cluster, $K$ a pre-exponential factor, $k$ the Boltzmann constant, and $T$ the temperature.

According to the Classical Nucleation Theory (CNT) the size of a critical cluster can be estimated by means of the Gibbs-Thompson equation (see Eq. 2.39). This approach relies on the capillarity approximation, which assigns macroscopic surface energy properties to small clusters (typically some tens of molecules). In addition, the classical model does not account for the presence of carrier gas molecules at the cluster. As a result, the CNT does not lead to a satisfactory agreement with experiments. In 1994, Oxtoby and Kashchiev[126] proposed an alternative to the Gibbs-Thompson equation to evaluate the critical cluster content in a model-independent way: the nucleation theorem. They showed that, for a generic component $i$, its excess number of molecules in the critical cluster, $\Delta n_i^*$, relates to the partial derivative of the work of critical cluster formation $W^*$ as follows

$$\left.\frac{\partial W^*}{\partial \mu_i^g}\right|_{\mu_{j\neq i}^g, T} = -\Delta n_i^* \quad \text{for } i = 1, 2, .., N,$$
(6.2)

with $\mu_i^g$ the chemical potential of component $i$ in its gaseous phase and $N$ the number of components in the mixture. The excess number $\Delta n_i^*$ is defined as the number of molecules in the critical cluster minus the number of molecules in the gas phase occupying the same volume of the cluster.

Combining Eqs. 6.1 and 6.2 enables to relate the excess number of molecules in the critical cluster to the measured nucleation rates $J$ at different pressure $p$, supersaturation $S$ and carrier gas molar fractions. For the present analysis, the condensing component is denoted as $i = 1$, while the other components are not supersaturated. These components can enter the cluster by means of dissolution and adsorption.

Several examples can be found in literature on the analysis of the cluster composition by exploiting the nucleation theorem.[3,43,76,78,84,127,150] At high pressure ($>0.2$ MPa), only few studies can be found in literature on the analysis of the critical cluster composition for

water-carrier gas mixtures.[78,84] Luijten *et al.*[78] analyzed water-helium, water–nitrogen and n-nonane-methane mixtures at 240 K and 1 MPa, 2.5 MPa and 4 MPa. Using the supersaturation and pressure dependence of the experimental nucleation rates, they estimated the cluster composition for their binary mixtures (vapor in a single carrier gas). Following the same approach as Luijten *et al.*,[78] water-carbon dioxide-methane mixtures at 235 K and 1 MPa were analyzed by Holten *et al.*.[84] In this case, only the number of water and methane molecules in the critical cluster was determined.

The analysis presented in this chapter aims to cope with the lack of research studies on the critical cluster composition for mixtures of water in multiple carrier gas environments ($N > 2$) at high pressures. Providing information on the critical cluster composition is of paramount importance for improving the existing nucleation theory. For this purpose, two methods based on the nucleation theorem will be presented. With the first method, the approach generally used in literature for systems with two components is extended to mixtures with $N > 2$ components (Sec. 6.3.1). In addition, a more straightforward method to determine the critical cluster composition will be provided (Sec. 6.3.2), which can be used in case of unary as well as multi-component nucleation. Both methods will be applied to the experimental nucleation data of water-carbon dioxide-nitrogen mixtures at 240 K[a] and various pressures (0.1 MPa, 1 MPa and 2 MPa) and carbon dioxide molar fractions (0%, 5%, 15% and 25%) previously published by the authors.[121,142] After careful parameterization of the nucleation data (Eqs. 6.9 and Eqs. 6.10), the cluster composition will be deduced for these experimental conditions (Sec. 6.4) by exploiting the nucleation rate dependence on supersaturation, pressure and carbon dioxide molar fraction (Method 1) and on the fugacities (Method 2).

## 6.2    Experimental methodology overview

The experiments used for the analysis of the present chapter were carried out with the Pulse Expansion Wave Tube (PEWT).[121,142] A schematic of the facility is reported in FIG. 6.1 (more geometrical details in Chapter 3). The PEWT is a special shock tube[60] implementing the nucleation pulse method.[69] This technique enables an effective decoupling of nucleation and the droplet growth phenomena, which generates an almost monodisperse cloud of growing clusters/droplets (see Chapter 3).[116] The number of critical clusters per unit of time and volume $J$ (nucleation rate) is experimentally determined as $J = n_d/\Delta t_p$, with $n_d$ the droplet number density and $\Delta t_p$ the nucleation pulse duration. The quantity $n_d$ is measured via a dedicated optical setup placed at the PEWT test section as sketched in Fig. 6.1. It consists of a 100:1 linearly polarized laser beam with a wavelength of 532 nm, a photodiode PD and a photomultiplier PM. By means of the optical setup, Constant Angle Mie Scattering CAMS[52,54,55] is applied and $n_d$ can be determined. The nucleation pulse duration $\Delta t_p$ is obtained from the pressure signal, which is measured at the test section wall of the PEWT with two pressure transducers (see Chapter 3).[116] The temperature $T$ at the pulse condition is determined by measuring the initial temperature of the test section wall and assuming isentropic expansion as explained in Chapters 3-5.[116,121,142] A well-defined mixture composition ($y_1, y_2, y_3$) is gen-

---

[a]The Pulse Expansion Wave Tube (PEWT) allows to study homogeneous nucleation by experimental means at temperatures ranging from 220 K to 260 K (see Ref. 116). The temperature range is limited to avoid the formation of ice crystals (for $T < 220$ K) and by PEWT gas dynamics constraints (for $T > 260$ K). Within this temperature range, the choice of working at the intermediate temperature of 240 K is driven by the temperature conditions used in literature (Refs. 61, 78, 84, 85) and adopted as references for our previous publications (Refs. 116, 121, 142).
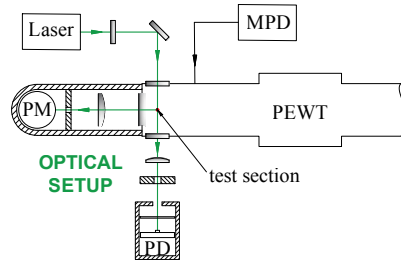
**FIG. 6.1.** Sketch of the experimental facility. The Pulse Expansion Wave Tube (PEWT) has a local widening at the low pressure section, enabling the application of the nucleation pulse method. The optical setup is placed at the test section and consists of a linearly polarized laser light with a wavelength of 532nm, a photodiode PD and a photomultiplier PM. The two pressure transducers are placed at the test section wall. The mixture preparation device is denoted as MPD.

erated in the mixture preparation device (MPD) connected to the PEWT (see FIG. 6.1). In this way, knowing the thermodynamic conditions at the pulse ($p$ and $T$), the supersaturation can be determined as $S \approx y_1/y_{1,\text{eq}}$ (Eq. 2.16), $y_{1,\text{eq}}$ being dependent on $(p, T, y_1, y_2, y_3)$ (see Chapter 5).[142] For a more extensive description of the experimental methodology, the reader is referred to the Chapters 4 and 5.

For the analysis presented in this chapter, we use the homogeneous water nucleation experiments carried out in nitrogen and 0%, 5%, 15% and 25% of carbon dioxide, previously presented in Chapters 4 and 5. The tests were carried out at 240 K and three pressure conditions, 0.1 MPa, 1 MPa and 2 MPa. The results are shown in terms of nucleation rate $J$ and supersaturation $S$ in FIG. 6.4 (blue lines and symbols, with the standard uncertainty blue-shaded around the lines). It must be stressed that the experimental nucleation conditions were chosen such that the carrier gases were always in the undersaturated state. In fact, the saturation pressure of the pure carrier components was always larger than their partial pressure at the investigated conditions. In addition, the molar fractions of the carrier gases were so large that any carrier component in the gas phase was in chemical equilibrium with the corresponding carrier gas in the cluster and the nucleation kinetics only depended on impingement/evaporation of the condensing component molecules. In 1999, Luijten and van Dongen showed that nucleation phenomena of condensable vapors in a carrier gas can be considered as unary nucleation if $x_{\text{g,eq}} << (S-1)/S$, with $x_{\text{g,eq}}$ the dissolved gas fraction in the bulk liquid. With a maximum carrier gas solubility $x_{\text{CO}_2,\text{eq}} < 0.038$ in our experiments (see FIG. 2.4), this condition was always fulfilled. For carrier gases with a much larger $x_{\text{g,eq}}$, the full binary nucleation model applies.[114] Thus, we consider the nucleation phenomena analyzed in the present work as essentially unary, with water the only (supersaturated) component providing the driving force for the nucleation process.

## 6.3   Application of the nucleation theorem to mixtures of $N$ components at constant temperature

For a mixture with $N$ components at constant temperature $T$, the nucleation rate $J$ and the work of critical cluster formation $W^*$ depend on a set of $N$ independent thermodynamic variables: $(\mu_1^{\text{g}}, \mu_2^{\text{g}}, \mu_3^{\text{g}}, .., \mu_N^{\text{g}})$ or equivalently $(S, p, y_2, .., y_{N-1})$. The partial derivative of $J$ with

respect to these variables, can be used in combination with the nucleation theorem in Eq. 6.2 to compute the $N$ unknowns $(\Delta n_1^*, \Delta n_2^*, \Delta n_3^*, ..., \Delta n_N^*)$.

The dependence of $J$ and $W^*$ on $S$ and $p$, in combination with the nucleation theorem, is the method that has been explored in literature to determine the cluster composition for mixtures with a maximum of two components, one of which being the condensing component.[3,78,84] We will extend this procedure to a mixture of $N > 2$ components in subsection 6.3.1 by exploiting the $J$ and $W^*$ dependence on on $(S, p, y_2, .., y_{N-1})$. Hereafter, this method will be denoted as Method 1. In addition, we will present in subsection 6.3.2 a novel methodology, based on the $J$ and $W^*$ dependence on the $N$ fugacities $(\mathscr{F}_1^g, \mathscr{F}_2^g, \mathscr{F}_3^g, .., \mathscr{F}_N^g)$. Hereafter, this method will be referred to as Method 2. Such method will be shown to be more straightforward and easily applicable to multi-component nucleation cases.

## 6.3.1  Method 1

We now consider the dependence of nucleation rate $J$ and work of cluster formation $W^*$ on the set of $N$ independent variables $(S, p, y_2, .., y_{N-1})$. The expression of the partial derivative of $J$ with respect to $S$ can be obtained by employing Eq. 6.1 and the chain rule as follows

$$
\begin{aligned}
\left.\frac{\partial \ln J}{\partial \ln S}\right|_{p,y_2,..,y_{N-1}} &= -\frac{1}{kT} \sum_{i=1}^{N} \left.\frac{\partial W^*}{\partial \mu_i^g}\right|_{\mu_{j \neq i}^g} \left.\frac{\partial \mu_i^g}{\partial \ln S}\right|_{p,y_2,..,y_{N-1}} + 1 \\
&= \frac{1}{kT} \sum_{i=1}^{N} \Delta n_i^* \left.\frac{\partial \mu_i^g}{\partial \ln S}\right|_{p,y_2,..,y_{N-1}} + 1,
\end{aligned}
\tag{6.3}
$$

with the second equality obtained by substituting the nucleation theorem in Eq. 6.2. Note that $\partial \ln K / \partial \ln S = 1$ in Eq. 6.3 for the following reason. In order to express the pre-exponential factor $K$, a kinetic model of nucleation needs to be considered. However, regardless of the model, the impingement rate of the vapor molecules is proportional to the vapor concentration. Thus, $K$ is proportional to $S$, which leads to $\partial \ln K / \partial \ln S = 1$.

Analogously to Eq. 6.3, $J$ can be derived with respect to $p$ leading to

$$
\begin{aligned}
\left.\frac{\partial \ln J}{\partial \ln p}\right|_{S,y_2,..,y_{N-1}} &= -\frac{p}{kT} \sum_{i=1}^{N} \left.\frac{\partial W^*}{\partial \mu_i^g}\right|_{\mu_{j \neq i}^g} \left.\frac{\partial \mu_i^g}{\partial p}\right|_{S,y_2,..,y_{N-1}} \\
&= \frac{p}{kT} \sum_{i=1}^{N} \Delta n_i^* \left.\frac{\partial \mu_i^g}{\partial p}\right|_{S,y_2,..,y_{N-1}},
\end{aligned}
\tag{6.4}
$$

where $\partial \ln K / \partial \ln p \approx 0$. In order to justify the latter approximation, it must be considered that the expression of $K$ as a function of $(p, y_2, .., y_{N-1})$ at constant $S$ depends on the kinetic model. We employed the kinetic model in the form of Courtney[9,10] extended to the case of non-ideal mixtures.[121] For our conditions, $\partial \ln K / \partial \ln p$ has been found to be much smaller than the uncertainty of $\partial \ln J / \partial \ln p$. Thus, $\partial \ln K / \partial \ln p$ can be safely neglected in deriving Eq. 6.4.

At this point, two linear equations 6.3 and 6.4 are available with $N$ unknowns to be obtained. The remaining $(N-2)$ equations to close the system are given by the $(N-2)$ deriva-

tives of $J$ with respect to each of the molar fractions $(y_2, .., y_q, .., y_{N-1})$ as

$$
\begin{aligned}
\left.\frac{\partial \ln J}{\partial y_q}\right|_{S,p,y_{j\neq\{1,q,N\}}} &= -\frac{1}{kT}\sum_{i=1}^{N}\left.\frac{\partial W^*}{\partial \mu_i^g}\right|_{\mu_{j\neq i}^g}\left.\frac{\partial \mu_i^g}{\partial y_q}\right|_{S,p,y_{j\neq\{1,q,N\}}} \\
&= \frac{1}{kT}\sum_{i=1}^{N}\Delta n_i^*\left.\frac{\partial \mu_i^g}{\partial y_q}\right|_{S,p,y_{j\neq\{1,q,N\}}},
\end{aligned}
\tag{6.5}
$$

for $q = 2, 3, .., (N-1)$. Note that $\partial \ln K/\partial y_q$ is neglected in Eq. 6.5 for the same reason given for neglecting $\partial \ln K/\partial p$.

The left hand sides of Eqs. 6.3-6.5 can be directly obtained from the experimental nucleation rates $J$ as a function of $(S, p, y_2, .., y_{N-1})$. For our practical applications ($N = 3$), details will be given in Sec. 6.4 (see Eqs. 6.9 and Figs. 6.2 and 6.4).

Finally, in order to determine $(\Delta n_1^*, \Delta n_2^*, \Delta n_3^*, ..., \Delta n_N^*)$ from Eqs. 6.3-6.5, each of the chemical potentials $(\mu_1^g, \mu_2^g, \mu_3^g, .., \mu_N^g)$ needs to be differentiated with respect to $(S, p, y_2, .., y_{N-1})$. Details are given in Appendix C.

## 6.3.2   Method 2

The definition of fugacity $\mathscr{F}_i^g$ (see Eq. C.7) leads to $d\mu_i^g = kT d\ln\mathscr{F}_i^g$ and Eq. 6.2 can be written as

$$
\left.\frac{\partial W^*}{\partial \mu_i^g}\right|_{\mu_{j\neq i}^g} = \frac{1}{kT}\left.\frac{\partial W^*}{\partial \ln\mathscr{F}_i^g}\right|_{\mathscr{F}_{j\neq i}^g} = -\Delta n_i^*.
\tag{6.6}
$$

We now consider the $J$, $K$ and $W^*$ dependence on $(\mathscr{F}_1^g, \mathscr{F}_2^g, \mathscr{F}_3^g, .., \mathscr{F}_N^g)$. From Eq. 6.1, the partial derivative of $J/K$ with respect to $\mathscr{F}_i^g$ leads to

$$
\left.\frac{\partial \ln(J/K)}{\partial \ln\mathscr{F}_i}\right|_{\mathscr{F}_{j\neq i}} = -\frac{1}{kT}\left.\frac{\partial W^*}{\partial \ln\mathscr{F}_i^g}\right|_{\mathscr{F}_{j\neq i}^g}.
\tag{6.7}
$$

Finally, by employing the nucleation theorem in the form of Eq. 6.6, we obtain that

$$
\left.\frac{\partial \ln(J/K)}{\partial \ln\mathscr{F}_i}\right|_{\mathscr{F}_{j\neq i}} = \Delta n_i^* \quad \text{for } i = 1, 2, .., N,
\tag{6.8}
$$

where, analogously to Method 1 (Sec. 6.3.1), it can be considered $\partial \ln K/\partial \ln\mathscr{F}_1^g \approx 1$ and $\partial \ln K/\partial \ln\mathscr{F}_i^g \approx 0$ for $i = 2, 3, .., N$.

Eq. 6.8 enables a straightforward derivation of the cluster composition $(\Delta n_1^*, \Delta n_2^*, \Delta n_3^*, ..., \Delta n_N^*)$ from the experimental $J$ data expressed as a function of the corresponding $(\mathscr{F}_1^g, \mathscr{F}_2^g, \mathscr{F}_3^g, .., \mathscr{F}_N^g)$. In addition, Eq. 6.8 can be directly applied to multi-component as well as to unary nucleation cases, which makes this methodology more general than Method 1. For our practical applications ($N = 3$), details will be given in Sec. 6.4 (see Eqs. 6.10 and FIGS. 6.3 and 6.5).

## 6.4 Critical cluster composition for water-carbon dioxide-nitrogen mixtures at 240 K

The cluster composition is determined for mixtures of water in nitrogen with 0%, 5%, 15% and 25% of carbon dioxide, at 240 K and 0.1 MPa, 1 MPa and 2 MPa (presented in Chapters 4 and 5).[121,142] The analysis is based on the two methods derived in Secs. 6.3.1 and 6.3.2, applied to the case of three components ($N = 3$), where the unknowns are the excess number of water $\Delta n^*_{H_2O}$, carbon dioxide $\Delta n^*_{CO_2}$ and nitrogen $\Delta n^*_{N_2}$. Note that, hereafter, the subscript for the condensing component "1" will be assigned to water, "2" to carbon dioxide and "3" to nitrogen.

In order to determine $\Delta n^*_{H_2O}$, $\Delta n^*_{CO_2}$ and $\Delta n^*_{N_2}$, the calculation of the partial derivatives given in Eqs. 6.3-6.5 are required: $\partial \ln J / \partial \ln S$, $\partial \ln J / \partial \ln p$ and $\partial \ln J / \partial y_{CO_2}$ (Method 1). For Method 2, determining the excess numbers of water, carbon dioxide and nitrogen requires the following partial derivatives to be computed from Eq. 6.8: $\partial \ln J / \partial \ln \mathscr{F}^g_{H_2O}$, $\partial \ln J / \partial \ln \mathscr{F}^g_{CO_2}$ and $\partial \ln J / \partial \ln \mathscr{F}^g_{N_2}$. To this end, we parameterize $J$ as a function $(S, p, y_{CO_2})$ and as a function of $(\mathscr{F}^g_{H_2O}, \mathscr{F}^g_{CO_2}, \mathscr{F}^g_{N_2})$ to the experimental data. The following expressions are found to efficiently describe the data set for any experimental condition investigated in the present chapter (see Figs. 6.4 and 6.5).

- Method 1

$$\ln J = A_1 + \frac{C_1}{(\ln S)^2} \tag{6.9a}$$

where

$$A_1 = a_{10} + a_{12}\, p + a_{13}\, p\, y_{CO_2} \tag{6.9b}$$
$$C_1 = c_{10} + c_{12}\, p + c_{13}\, p\, y_{CO_2} \tag{6.9c}$$

with $a_{10} = 73.4$, $a_{12} = -4.39 \cdot 10^{-8}$, $a_{13} = -1.42 \cdot 10^{-5}$, $c_{10} = -247$, $c_{12} = 1.24 \cdot 10^{-5}$, $c_{13} = 1.36 \cdot 10^{-4}$, for $J$ in m$^{-3}$s$^{-1}$, $p$ in Pa and $S$ non dimensional.

In Fig. 6.2, the function $J(S, p, y_{CO_2})$ as from Eqs. 6.9 is represented for $S = 11$.

- Method 2

$$\ln J = A_2 + C_2 \ln \mathscr{F}^g_{H_2O} \tag{6.10a}$$

where

$$A_2 = a_{20} + a_{22}\, \mathscr{F}^g_{CO_2} + a_{23}\, \mathscr{F}^g_{N_2} \tag{6.10b}$$
$$C_2 = c_{20} + c_{22}\, \mathscr{F}^g_{CO_2} + c_{23}\, \mathscr{F}^g_{N_2} \tag{6.10c}$$

with $a_{20} = 162$, $a_{22} = 7.97 \cdot 10^{-5}$, $a_{23} = 4.90 \cdot 10^{-6}$, $c_{20} = 31.9$, $c_{22} = -1.05 \cdot 10^{-5}$, $c_{23} = -5.10 \cdot 10^{-7}$, for $J$ in m$^{-3}$s$^{-1}$ and $\mathscr{F}^g_{H_2O}, \mathscr{F}^g_{CO_2}, \mathscr{F}^g_{N_2}$ in Pa.

In Fig. 6.3, the function $J(\mathscr{F}^g_{H_2O}, \mathscr{F}^g_{CO_2}, \mathscr{F}^g_{N_2})$ as from Eqs. 6.10 is represented for $\mathscr{F}^g_{H_2O} = 410$ MPa.

Finally, $\Delta n^*_{H_2O}$, $\Delta n^*_{CO_2}$ and $\Delta n^*_{N_2}$ can be calculated and the outcomes for Method 1 and 2 are reported in TABLE 6.1.
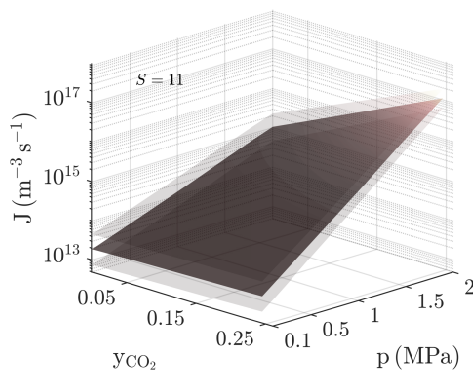
**FIG. 6.2.** 3D view of $J$ parameterized as a function of $(S, p, y_{CO_2})$, represented here for $S = 11$. The standard uncertainty is also reported as thinner upper and lower layers.
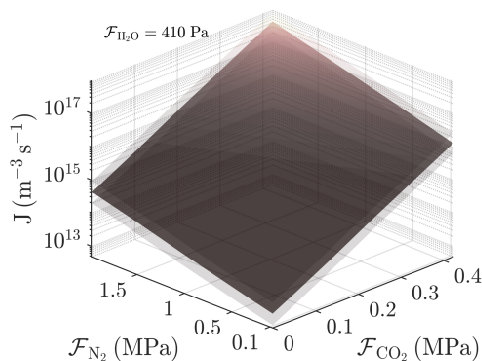


**FIG. 6.3.** 3D view of $J$ parameterized as a function of $(\mathcal{F}_{H_2O}^g, \mathcal{F}_{CO_2}^g, \mathcal{F}_{N_2}^g)$, represented here for $\mathcal{F}_{H_2O}^g = 410$ Pa. The standard uncertainty is also reported as thinner upper and lower layers.

The results obtained with both methods show a good agreement within the uncertainty bands (see TABLE 6.1). This finding supports the validity of both methods, with Method 2 being more straightforward and easily applicable to unary as well as to multi-component nucleation cases (Sec. 6.3). It must be noted that a small difference between the outcomes of the two methods can be observed. We argue that this difference can be attributed to the different ways with which the data are parameterized (see Eqs. 6.9 and Eqs. 6.10). However, the agreement between the two methods proves that the parameterizations are consistent. Given the equivalence of the two methods, we refer to Method 1 only.

At fixed carbon dioxide molar fraction $y_{CO_2}$ and supersaturation $S$, $\Delta n_{H_2O}^*$ decreases with pressure, while $\Delta n_{CO_2}^*$ and $\Delta n_{N_2}^*$ increase (see TABLE 6.1). For $y_{CO_2} = 0.25$, $\Delta n_{H_2O}^*$ ranges form $34.2 \pm 5.2$ at 0.1 MPa to $21.5 \pm 4.0$ at 2 MPa. On the other hand, $\Delta n_{CO_2}^*$ and $\Delta n_{N_2}^*$ increase with the pressure: $\Delta n_{CO_2}^*$ vary from $0.41 \pm 0.09$ at 0.1 MPa to $6.33 \pm 1.63$ at 2 MPa and $\Delta n_{N_2}^*$ ranges from $0.12 \pm 0.05$ at 0.1 MPa to $3.20 \pm 1.45$ at 2 MPa. This behavior consistently repeats itself at smaller $y_{CO_2}$, becoming less pronounced with decreasing the carbon

**TABLE 6.1.** Method 1 vs. Method 2: excess numbers at the experimental conditions analyzed in the present chapter for 240 K. The data reported here refer to $S = 11$ for Method 1 and to $\mathscr{F}_{H_2O}^g = 410$ Pa for Method 2. These two reference values are the only $S$ and $\mathscr{F}_{H_2O}^g$ in common to all $p$ and $y_{CO_2}$ conditions (see FIGS. 6.4 and 6.5).

| | | Method 1 | | | Method 2 | | |
|---|---|---|---|---|---|---|---|
| $y_{CO_2}$ | $p$ (MPa) | $\Delta n_{H_2O}$ | $\Delta n_{CO_2}$ | $\Delta n_{N_2}$ | $\Delta n_{H_2O}$ | $\Delta n_{CO_2}$ | $\Delta n_{N_2}$ |
| 0 | 0.10172 | $34.7 \pm 4.3$ | | $0.16 \pm 0.07$ | $30.9 \pm 4.2$ | | $0.17 \pm 0.08$ |
| 0.05 | 0.10095 | $34.6 \pm 5.2$ | $0.09 \pm 0.02$ | $0.15 \pm 0.07$ | $30.8 \pm 5.2$ | $0.08 \pm 0.02$ | $0.16 \pm 0.08$ |
| 0.15 | 0.10067 | $34.4 \pm 5.2$ | $0.25 \pm 0.05$ | $0.14 \pm 0.06$ | $30.7 \pm 5.3$ | $0.24 \pm 0.05$ | $0.14 \pm 0.07$ |
| 0.25 | 0.10072 | $34.2 \pm 5.2$ | $0.41 \pm 0.09$ | $0.12 \pm 0.05$ | $30.6 \pm 4.4$ | $0.39 \pm 0.09$ | $0.13 \pm 0.06$ |
| 0 | 1.0018 | $33.1 \pm 4.4$ | | $1.70 \pm 0.77$ | $30.4 \pm 4.6$ | | $1.69 \pm 0.82$ |
| 0.05 | 1.0020 | $30.1 \pm 4.9$ | $0.80 \pm 0.20$ | $1.64 \pm 0.74$ | $30.0 \pm 4.3$ | $0.72 \pm 0.16$ | $1.61 \pm 0.78$ |
| 0.15 | 0.9960 | $30.1 \pm 5.5$ | $2.11 \pm 0.48$ | $1.54 \pm 0.70$ | $29.0 \pm 5.1$ | $2.15 \pm 0.49$ | $1.43 \pm 0.69$ |
| 0.25 | 1.0051 | $28.1 \pm 5.2$ | $3.28 \pm 0.73$ | $1.38 \pm 0.32$ | $28.1 \pm 5.0$ | $3.57 \pm 0.81$ | $1.28 \pm 0.62$ |
| 0 | 2.0004 | $31.3 \pm 4.4$ | | $3.47 \pm 1.57$ | $29.9 \pm 4.8$ | | $3.34 \pm 1.62$ |
| 0.05 | 1.9957 | $29.3 \pm 5.0$ | $1.48 \pm 0.34$ | $3.46 \pm 1.56$ | $29.1 \pm 4.7$ | $1.33 \pm 0.30$ | $3.17 \pm 1.54$ |
| 0.15 | 2.0003 | $25.4 \pm 4.4$ | $3.90 \pm 0.90$ | $3.34 \pm 1.51$ | $27.4 \pm 4.4$ | $3.95 \pm 0.89$ | $2.85 \pm 1.38$ |
| 0.25 | 2.0002 | $21.5 \pm 4.0$ | $6.33 \pm 1.63$ | $3.20 \pm 1.45$ | $25.8 \pm 4.0$ | $6.49 \pm 1.47$ | $2.53 \pm 1.23$ |

dioxide molar fraction.

At fixed pressure $p$ and supersaturation $S$, $\Delta n_{H_2O}^*$ decreases with increasing $y_{CO_2}$, while $\Delta n_{CO_2}^*$ increase and $\Delta n_{N_2}^*$ somewhat decreases (see TABLE 6.1). For 2 MPa, the values of $\Delta n_{H_2O}^*$ vary from $31.3 \pm 4.4$ for $y_{CO_2} = 0$ to $21.5 \pm 4.0$ for $y_{CO_2} = 0.25$. At 2 MPa, the $\Delta n_{CO_2}^*$ values increase from $1.48 \pm 0.34$ for $y_{CO_2} = 0.05$ to $6.33 \pm 1.63$ for $y_{CO_2} = 0.25$. The values of $\Delta n_{N_2}^*$ slightly decrease with increasing $y_{CO_2}$ at 2 MPa. However, this small decrease remains well within the uncertainty bands (for both methods) and $\Delta n_{N_2}^*$ can be considered approximately constant. The behavior observed at 2 MPa is also found at 1 MPa and 0.1 MPa, but with consistently bigger values of $\Delta n_{H_2O}^*$ and smaller $\Delta n_{CO_2}^*$ and $\Delta n_{N_2}^*$.

The microscopic picture given by the critical cluster composition in TABLE 6.1 provides important information. At constant supersaturation (the driving force of nucleation), increasing $p$ and $y_{CO_2}$ facilitates the nucleation process as $J$ increases (see Fig. 6.4). This effect is due to more and more carrier gas molecules adsorbed at the cluster surface. Their increasing excess numbers with increasing $p$ and $y_{CO_2}$ reduces the energy of formation available for the water molecules, which explains the smaller $\Delta n_{H_2O}^*$. The larger number of carrier gas molecules adsorbed[b] at the cluster surface causes a decrease of the surface tension, leading to the observed increase of $J$ with $p$ and $y_{CO_2}$ (see FIG. 6.4).[121,142] An estimate of the surface tension reduction for the analyzed nucleation condition was given in FIG. 5.2: with $y_{CO_2} = 0$, the surface tension decrease is of about 0.25% at 0.1 MPa and 4.5% at 2 MPa; with $y_{CO_2} = 0.25$, the surface tension decrease is consistently larger and of about 1.4% at 0.1 MPa and 19.1% at 2 MPa. This causes the experimental work of critical cluster formation to decrease and, as a consequence, the observed nucleation rates increase with $p$ and $y_{CO_2}$. By increasing the

---

[b]As demonstrated by Luijten *et al.*,[77] the carrier gas bulk fractions are smaller than its equilibrium liquid fractions. Therefore, the carrier gas molecules at the critical cluster can be all considered as located at the surface.

pressure from 0.1 MPa to 2 MPa, in fact, the magnitude of decrease in the critical work of cluster formation is $\sim$10% with $y_{CO_2} = 0$ and $\sim$36% with $y_{CO_2} = 0.25$.

It is worth mentioning that, even though $y_{CO_2} < y_{N_2}$ for any investigated condition, the presence of carbon dioxide at high pressure (1 MPa and 2 MPa) significantly increases $J$ with respect to the case of $y_{CO_2} = 0$. This is coherent with the much stronger effect that carbon dioxide has on the surface tension reduction, even for the conditions in which $\Delta n^*_{CO_2}$ is smaller than or comparable to $\Delta n^*_{N_2}$.

## 6.5   Conclusions

The nucleation theorem is used to deduce the cluster compositions at constant temperature $T$ by experimental means. Two novel methods (Method 1 and 2) are derived from the nucleation theorem for mixtures of $N$ components, with one being supersaturated (Sec. 6.3). The nucleation rate dependence on supersaturation, pressure and mixture composition is used in Method 1 (Sec. 6.3.1). This method extends to mixtures of $N > 2$ components the approach used in literature for two components only.[3,43,76,78,84,127,150] Method 2 (Sec. 6.3.2) relies on the nucleation rate dependence on the $N$ fugacities. It can be used in case of unary as well as multi-component nucleation and it greatly simplifies the calculations with respect to the first method.

The two methods are applied to homogeneous water nucleation experiments in nitrogen and 0%, 5%, 15% and 25% of carbon dioxide, presented in Chapters 4 and 5.[121,142] The experiments were carried out at 240 K and 0.1 MPa, 1 MPa and 2 MPa. As a result, the excess numbers of water, carbon dioxide and nitrogen are deduced for the whole set of analyzed experimental conditions (Table 6.1). To the best of our knowledge, for the first time the critical cluster composition is deduced for mixtures of water in more than one carrier gas at high pressure ($>$0.2 MPa). After parameterization of the nucleation rate data (see Eqs. 6.9 and Eqs. 6.10), Method 1 and 2 gave equivalent results in terms of critical cluster composition. This finding supports the validity of both methods and proves the used parameterizations to be consistent.

At constant carbon dioxide fractions, the excess number of water molecules decreases with increasing the pressure, while the excess number of carbon dioxide and nitrogen increase. At constant pressure, the water molecules in the critical cluster decrease with increasing the carbon dioxide content, while the excess number of carbon dioxide predictably increases. In this case, the nitrogen excess number remains approximately constant.

The microscopic overview that results from this analysis can be interpreted as follows. Increasing pressure and carbon dioxide fraction at constant supersaturation (the driving force of nucleation), increases the nucleation rate, meaning that the nucleation process is greatly facilitated ($J$ increases). This is due to a larger number of carbon dioxide and nitrogen molecules adsorbed at the cluster surface. Adsorption phenomena cause a surface tension decrease, thus explaining the observed nucleation rate increase with pressure and carbon dioxide molar fraction.[121,142] The pulse expansion wave tube experiments can thus successfully be used to unravel the composition of condensing clusters on the molecular scale, which is crucial for the advancement of the existing nucleation theory.
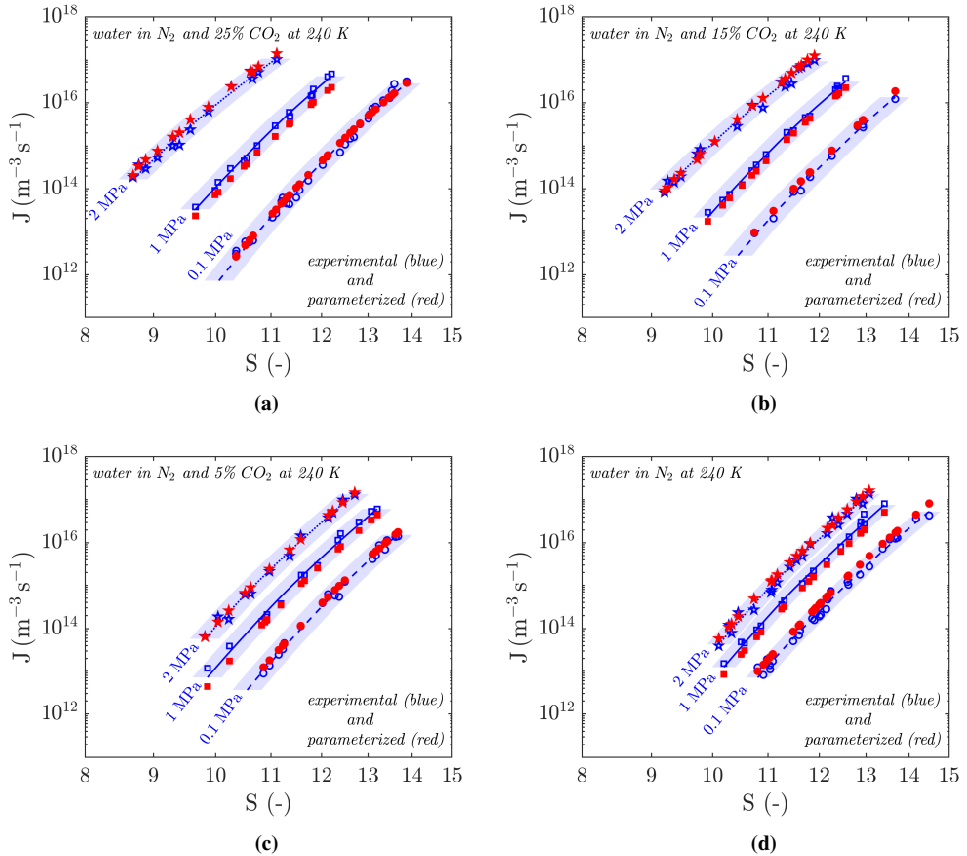
**FIG. 6.4.** Method 1: *J-S* plots of the homogeneous water nucleation experiments [121,142] (blue lines and symbols) carried out in nitrogen and 25% (FIG. 6.4a), 15% (FIG. 6.4b), 5% (FIG. 6.4c) and 0% (FIG. 6.4d) of carbon dioxide at 0.1 MPa (dashed lines), 1 MPa (solid lines) and 2 MPa (dotted lines). The standard uncertainty is blue-shaded around the lines. The experimental *J-S* data are compared to the values of *J* calculated from Eqs. 6.9 (red symbols) at the experimental $(S, p, y_{CO_2})$.
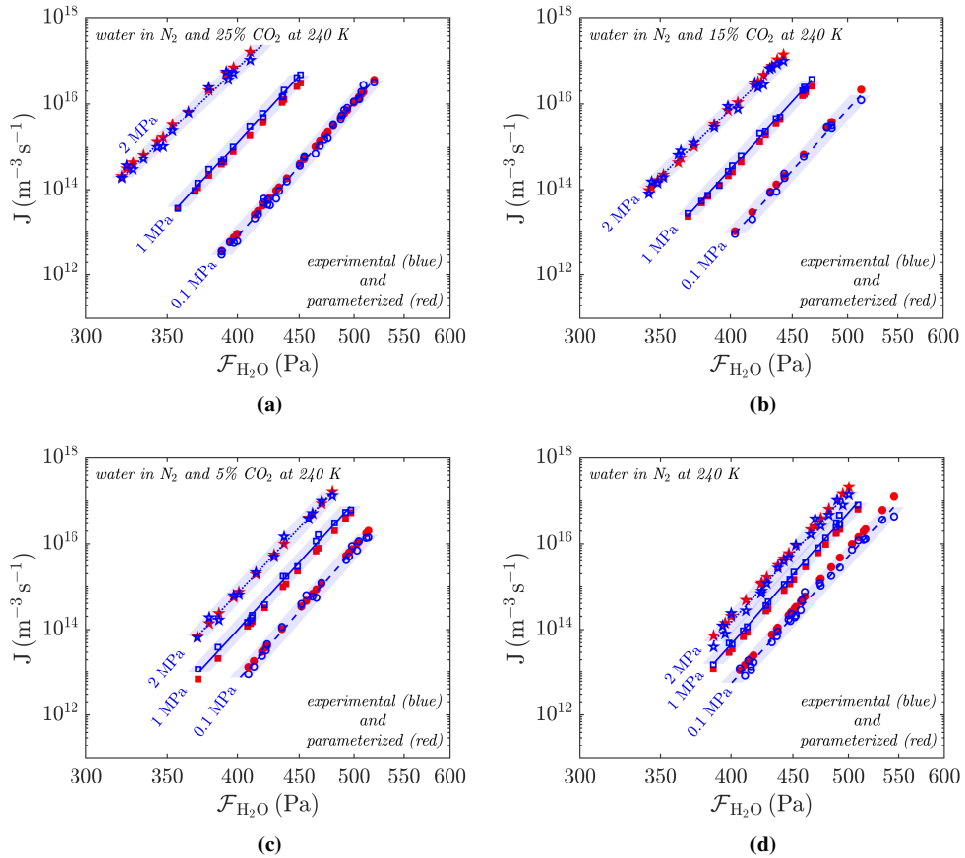
**FIG. 6.5.**   Method 2: $J$-$\mathcal{F}_{H_2O}^g$ plots of the homogeneous water nucleation experiments [121,142] (blue lines and symbols) carried out in nitrogen and 25% (FIG. 6.5a), 15% (FIG. 6.5b), 5% (FIG. 6.5c) and 0% (FIG. 6.5d) of carbon dioxide at 0.1 MPa (dashed lines), 1 MPa (solid lines) and 2 MPa (dotted lines). The standard uncertainty is blue-shaded around the lines. The experimental $J$-$\mathcal{F}_{H_2O}^g$ data are compared to the values of $J$ calculated from Eqs. 6.10 (red symbols) at the experimental $(\mathcal{F}_{H_2O}^g, \mathcal{F}_{CO_2}^g, \mathcal{F}_{N_2}^g)$.

# Chapter 7

# Conclusions

The final goal of the present thesis was to provide new findings on the pressure and carrier gas effects on homogeneous nucleation of water by experimental means. The Pulse Expansion Wave Tube (PEWT) was used for this purpose.

The high pressure section of the PEWT was redesigned. A square-shape cross-section was chosen for the test section in order to avoid geometrical mismatches with pressure transducers and optical windows. In addition, the high pressure section was halved in length to reduce the gas consumption and accelerate the experimental procedure. The gas-dynamic performances of the re-designed PEWT were verified by performing a preliminary test campaign. These experiments demonstrated that the combination of accurate piezoresistive pressure transducers and fast responding piezoelectric transducers - with coating reducing the thermal shock - allows accurate measurements of thermodynamic conditions. In addition, the importance of choosing the thinnest diaphragm thickness possible was shown to be important in order to minimize the intrusiveness of the diaphragm opening process. A 2D numerical model was developed. It was shown to correctly predict the gasdynamic features of the PEWT, as well as the opening process and the total opening time of the diaphragm. The numerical model allowed to exclude the presence of disturbances on the flow field at the observation point during the experiments. A second experimental campaign was carried out to test the nucleation rate – supersaturation data quality after redesigning the PEWT test section. Thus, homogeneous water nucleation experiments were carried out in helium at 240 K and two pressure conditions, 0.1 MPa and 1 MPa. The data were found to be in perfect agreement with measurements performed at the same conditions by Fransen *et al.*[61] with the previous version of the PEWT. This demonstrated the proper functionality of the newly designed test section, additionally implying that the slight geometrical mismatches present in the previous version of the high pressure section did not significantly affect the quality of the data.

Homogeneous water nucleation in argon and nitrogen was experimentally investigated by means of the PEWT. At about 240 K, three pressure conditions were tested for both mixtures: 0.1 MPa, 1 MPa and 2 MPa. The comparison with the *J-S* data obtained by Fransen *et al.*[85] in nitrogen at 240 K and 1 MPa showed a significant scatter reduction, confirming the improvements introduced with the new design of the PEWT test section. The nucleation rate significantly increases with the gas pressure. The physical explanation is that the surface tension of water decreases with pressure due to adsorption of carrier gas molecules. The observed enhancement of the water nucleation rate at high pressure was found somewhat stronger for nitrogen than for argon. At 0.1 MPa, non-isothermal effects theoretically predicted by Barrett[87]

qualitatively explain the measured nucleation rate differences between water-argon and water-nitrogen at fixed temperature. At the same pressure condition, the temperature dependence of the water nucleation rates in argon was also shown to qualitatively agree with the predictions of the Barrett theory. By employing the nucleation theorem, the experimental $J$-$S$ curves were used to calculate the critical cluster size in terms of number of water molecules. These calculations agreed reasonably well with the Gibbs-Thomson predictions, similarly to Wölk and Strey.[43] On the other hand, the CNT incorrectly predicted the experimental nucleation rates. An empirical correction of the CNT $J$-expression was proposed, based on the analyzed data and, thus, accounting for pressure, temperature and type of carrier gas dependencies. The proposed $J$-expression was shown to agree well with the experimental $J$-values (within their uncertainty) for water-argon, water-nitrogen and water-helium mixtures, between 0.06 MPa and 2 MPa and from 220 K to 260 K.

In order to further confirm that the surface tension decrease is responsible for the increase of the nucleation rate, homogeneous water nucleation experiments were carried out in carrier gas mixtures of nitrogen and 5%, 15% and 25% of carbon dioxide. The tests were conducted at 240 K and for 0.1 MPa, 1 MPa, and 2 MPa. As expected, the experimental nucleation rates increased with pressure. This increase was much more pronounced by adding carbon dioxide to the carrier gas mixture. An adsorption/surface tension model, extended to multi component mixtures, was derived. Empirical literature data in the temperature range of 280 – 350 K for the Langmuir pressure were extrapolated to 240 K. The surface tensions calculated at the investigated temperature, pressure and carrier gas conditions were substituted in the CNT $J$-expression. The predicted nucleation rate increase with pressure and carbon dioxide molar fraction qualitatively agreed with the experimental trend, substantiating the previous findings. A substantial overestimation of the modeled nucleation rate enhancement was observed, which was attributed the inherent weaknesses of the CNT. At 0.1 MPa and 240 K, the increase of carbon dioxide from 0% to 25% did not affect the nucleation rates, which are observed to be smaller than the isothermal reference. Incomplete thermalisation of colliding clusters and carrier gas molecules justifies this behavior, as confirmed by the theoretical model of Barrett.[87] At 0.1 MPa, a series of homogeneous water nucleation experiments were conducted in nitrogen and 25% of carbon dioxide for 234 K and 236 K. The scaling model by Hale[86] explained the observed effect of temperature on the measured nucleation rates.

Finally, the critical cluster compositions were deduced from the water-nitrogen-carbon dioxide data. By employing the nucleation theorem, two methods were derived for mixtures of $N > 2$ components, one being supersaturated. The first method exploited the nucleation rate dependence on supersaturation, pressure and mixture composition. The nucleation rate dependence on the $N$ fugacities was used to derive the second method. The application of the two methods to the experimental data led to equivalent values for the critical cluster compositions. In this way, the macroscopic quantities measured with the PEWT setup can successfully be used to unravel the composition of condensing clusters on the molecular scale. At constant temperature and carbon dioxide fractions, the number of water molecules in the critical cluster were found to decrease with pressure, while the number of carbon dioxide and nitrogen molecules increases. At constant temperature and pressure, the number of water molecules in the critical cluster decreases with increasing the carbon dioxide content. In this case, the number of carbon dioxide molecules increases, with the nitrogen content in the critical cluster remaining constant. These outcomes were interpreted as follows. Increasing the pressure and the carbon dioxide molar fraction causes a larger number of carbon dioxide and nitrogen molecules to be adsorbed at the critical cluster surface. The gas adsorption is substantially

stronger for carbon dioxide, which is explained by a stronger attraction between carbon dioxide and water molecules. In consequence of the gas adsorption, the surface tension decreases, thus increasing the nucleation rates and, following the Gibbs – Thomson equation, reducing the number of water molecules contained in the critical cluster.

# Appendix A

# Generalized derivation of the Langmuir adsorption for multiple adsorbates

The present section has been published as appendix to the paper "M.M. Campagna, J. Hrubý, M.E.H. van Dongen, and D.M.J. Smeulders. Homogeneous water nucleation in carbon dioxide-nitrogen mixtures: experimental study on pressure and carrier gas effects. *J. Chem. Phys.* 154(15):154301, 2021" (Ref. 142).

The derivation of the Langmuir adsorption was extensively discussed by Fransen *et al.*[85] for a single type of gas molecules adsorbed at the condensing water cluster surfaces. That approach is now generalized to the case of $(N-1)$ gases. Given $\chi$ available adsorption sites at the condensing cluster surfaces, one can consider that $N_{g,i}^A$ sites are occupied by the adsorbed (superscript 'A') molecules of the $i$-th gas. The number of possible configurations for the adsorbed layer can be calculated as

$$\mathbb{C} = \frac{\chi!}{(\chi - \sum\limits_{i=2}^{N} N_{g,i}^A)! \prod\limits_{i=2}^{N} N_{g,i}^A!}, \tag{A.1}$$

assuming no multiple occupation of the adsorption sites and mutual indistinguishability of the adsorbed molecules. The equilibrium condition between the adsorbed and the free molecules (superscript 'G') of the $i$-th gas is given by the chemical potential equality

$$\mu_{g,i}^A = \mu_{g,i}^G. \tag{A.2}$$

The chemical potentials in Eq A.2 can be found as follows. For the adsorbed case, we first consider the Helmholtz free energy

$$F^A = U^A - T\mathbb{S}^A, \tag{A.3}$$

with the internal energy

$$U^A = \sum_{i=2}^{N} N_{g,i}^A \left( u_{g,i}^{int} + \frac{3}{2}kT + u_{g,i}^A \right). \tag{A.4}$$

For the $i$-th gas, $u_{g,i}^{int}$ and $(3/2)kT$ are the internal molecular energy and the translation degrees of freedom, while $u_{g,i}^A$ is the potential energy of the interaction between the adsorbed gas

molecules and the liquid surface. For our case, the potential energy of the interaction between adsorbed gas molecules is neglected, being weaker than the one between gas molecules and the liquid surface. In Eq. A.3, the quantity $\mathbb{S}^A$ denotes the entropy of the adsorbate

$$\mathbb{S}^A = \sum_{i=2}^{N} N_{g,i}^A \left[ s_{g,i}^{int} + k \ln \left( \frac{v_i^A}{V_{ref}} \right) \right] + \mathbb{S}_c, \tag{A.5}$$

where, for the $i$-th gas, $s_{g,i}^{int}$ is the internal molecular entropy, $V_{ref}$ and $v_i^A$ are, respectively, a reference volume and the effective volume available for translation of an adsorbed molecule. The configurational entropy $\mathbb{S}_c$ on a per molecule basis is given by

$$\mathbb{S}_c = -k \sum_{j=1}^{\mathbb{C}} \mathbb{P}_j \ln \mathbb{P}_j = k \ln \mathbb{C}, \tag{A.6}$$

where the probability of the $j$-th configuration $\mathbb{P}_j$ is considered equal for any configuration, i.e. $\mathbb{P}_j = 1/\mathbb{C}$. Being the surface coverage of the $i$-th gas component $\theta_i = N_{g,i}^A/\chi$ and applying Stirling's approximation[151] $\ln x! \approx x \ln x - x$, Eq. A.6 becomes

$$\mathbb{S}_c = -k \chi \left[ (1 - \sum_{i=2}^{N} \theta_i) \ln(1 - \sum_{i=2}^{N} \theta_i) + \sum_{i=2}^{N} \theta_i \ln \theta_i \right]. \tag{A.7}$$

We now consider the differential of the Helmholtz free energy of the adsorbed phase

$$dF^A = -\mathbb{S}^A dT + \sigma_g dA + \sum_{i=2}^{N} \mu_{g,i}^A dN_{g,i}^A, \tag{A.8}$$

with $\sigma_g$ the contribution of the adsorbate to the surface tension and $A$ surface area. Recalling Eq. A.3, the chemical potential for the adsorbed molecules of the $i$-th gas can be expressed as

$$\mu_{g,i}^A = \left( \frac{\partial F^A}{\partial N_{g,i}^A} \right)_{T,A,N_{g,t \neq i}^A} = \left( \frac{\partial U^A}{\partial N_{g,i}^A} - T \frac{\partial S^A}{\partial N_{g,i}^A} \right)_{T,A,N_{g,t \neq i}^A} \tag{A.9}$$

with the partial derivative of the configurational entropy that can be decomposed as follows $\partial \mathbb{S}_c / \partial N_{g,i}^A = (\partial \mathbb{S}_c / \partial \theta_{g,i})(\partial \theta_{g,i} / \partial N_{g,i}^A)$ and then calculated by recalling Eq. A.7:

$$\left( \frac{\partial \mathbb{S}_c}{\partial N_{g,i}^A} \right)_{T,A,N_{g,t \neq i}^A} = k \ln \left[ (1 - \sum_{i=2}^{N} \theta_i)/\theta_i \right]. \tag{A.10}$$

Finally, $\mu_{g,i}^A$ can be derived by plugging Eqs. A.4 and A.10 in Eq. A.9:

$$\mu_{g,i}^A = u_{g,i}^{int} + \frac{3}{2} k T + u_{g,i}^A - T s_{g,i}^{int} +$$
$$-k T \ln \left( \frac{v_i^A}{V_{ref}} \right) - k T \ln \left[ (1 - \sum_{i=2}^{N} \theta_i)/\theta_i \right]. \tag{A.11}$$

The chemical potential for the free gas molecules of the $i$-th gas $\mu_{g,i}^G$ can be derived in a similar manner, assuming $v_i = kT/p_{g,i}$ (ideal gas law):

$$\mu_{g,i}^G = u_{g,i}^{int} + \frac{3}{2} k T - T s_{g,i}^{int} + k T \ln \left( \frac{p_{g,i} V_{ref}}{k T} \right). \tag{A.12}$$

The equilibrium condition of Eq. A.2, combined with Eq. A.11 and A.12, leads to the following expression

$$(1 - \sum_{i=2}^{N} \theta_i)/\theta_i = \frac{kT}{p_{g,i} v_i^A} \exp\left(\frac{u_{g,i}^A}{kT}\right). \tag{A.13}$$

The change of surface tension due to the chemical potential variation of the $(N-1)$ gases can be derived from the Gibbs adsorption equation[115]

$$\mathbb{S} \, dT + A \, d\sigma + N_v \, d\mu_v + \sum_{i=2}^{N} N_{g,i} \, d\mu_{g,i} = 0 \tag{A.14}$$

at constant temperature and vapor chemical potential as

$$d\sigma = - \sum_{i=2}^{N} \frac{N_{g,i}^A}{A_g \chi} d\mu_{g,i}, \tag{A.15}$$

where $A = A_g \chi$ and $A_g$ the average surface area per adsorption site. It must be stressed that this derivation considers the same $A_g$ for the $(N-1)$ gases. The term $d\mu_{g,i}$ in Eq. A.15 can be calculated as

$$d\mu_{g,i} = v_{g,i} \, dp_g = kT \frac{dp_g}{p_g}, \tag{A.16}$$

with the second equality obtained from the ideal gas law under the assumption of constant temperature, pressure and $N_{g,t \neq i}$. The combination of Eq. A.15 and A.16 leads to

$$d\sigma = - \sum_{i=2}^{N} \frac{\theta_i \, kT}{A_g} \frac{dp_g}{p_g}. \tag{A.17}$$

Finally, considering the derivation of $\theta_i$ from Eq. A.13

$$\theta_i = \frac{\dfrac{p_{g,i} v_i^A}{kT} \exp\left(-\dfrac{u_{g,i}^A}{kT}\right)}{1 + \displaystyle\sum_{j=2}^{N} \dfrac{p_{g,j} v_j^A}{kT} \exp\left(-\dfrac{u_{g,j}^A}{kT}\right)}, \tag{A.18}$$

the integration of Eq. A.17 leads to the following general expression for the surface tension

$$\sigma = \sigma_\ell - \frac{kT}{A_g} \ln\left(\frac{p_g + p_L}{p_L}\right), \tag{A.19}$$

where the Langmuir pressure is defined as

$$p_L = \left(\sum_{i=2}^{N} z_{g,i} p_{L,i}^{-1}\right)^{-1} \tag{A.20}$$

and $p_{L,i}$ is the Langmuir pressure for individual gas $i$, whose temperature dependence is given in Eq. 5.3. In Eq. A.20, $z_{g,i} = y_i / \sum_{i=2}^{N} y_i$ with $y_i$ the molar fraction of the $i$-th gas. If the

Langmuir pressure is much grater than the gas pressure, the general expression of the surface tension in Eq. A.19 becomes a linear function of pressure:

$$\sigma = \sigma_\ell + \sigma_{p0} p_g, \tag{A.21}$$

where

$$\sigma_{p0} = \left( \sum_{i=2}^{N} z_{g,i} \, \sigma_{p0,i}^{-1} \right)^{-1}, \tag{A.22}$$

and

$$\sigma_{p0,i} = \frac{v_i^A}{A_g} \exp\left( -\frac{u_{g,i}^A}{kT} \right) \tag{A.23}$$

the coefficient of the linearized dependence of the surface tension on pressure for the case of pure gas $i$.

# Experimental data

The meaning of the symbols used in the following tables is listed in nomenclature. Their definitions and derivations can be found in Chapters 3-6.

**TABLE B1.** Experimental regression coefficients $C$ and $D$ (Eq. 4.21) and corresponding numbers of water molecules of the critical clusters $n^*$ (Eq. 4.5) and $n^*_{GT}$ (Eq. 4.4) for the $J$-$S$ data presented in Chapters 3 and 4. The quality of the regression analysis is reported as $R^2_{adj}$. The standard uncertainty of $n^*$ is denoted as $U(n^*)$.

| | p (MPa) | T (K) | S min | S max | C (m$^{-3}$ s$^{-1}$) | D | $R^2_{adj}$ | $n^{*a}$ | $n^*_{GT}$ | $U(n^*)$ | |
|---|---|---|---|---|---|---|---|---|---|---|---|
| He | 0.10545 | 240 | 11.3 | 15.5 | 5.612E+31 | -251.8 | 0.988 | 28 | 25 | 4 | TABLE B4[b] |
| | 0.99678 | 240 | 10.8 | 14.6 | 5.509E+30 | -224.7 | 0.988 | 26 | 27 | 4 | TABLE B4[b] |
| Ar | 0.04815 | 220 | 16.6 | 22.5 | 1.183E+27 | -275.5 | 0.970 | 20 | 26 | 3 | Ref. 43 |
| | 0.05715 | 230 | 12.9 | 16.6 | 3.677E+28 | -251.0 | 0.989 | 25 | 28 | 4 | Ref. 43 |
| | 0.10281 | 230 | 13.1 | 18.1 | 2.184E+30 | -277.9 | 0.973 | 26 | 26 | 3 | TABLE B6[c] |
| | 0.10281 | 236 | 11.3 | 15.3 | 2.184E+30 | -246.3 | 0.973 | 27 | 28 | 4 | TABLE B6 |
| | 0.10281 | 240 | 10.3 | 13.7 | 2.184E+30 | -227.4 | 0.973 | 29 | 29 | 4 | TABLE B6[c] |
| | 0.06109 | 240 | 9.9 | 12.9 | 2.709E+29 | -215.8 | 0.993 | 29 | 31 | 5 | Ref. 43 |
| | 0.05171 | 250 | 8.0 | 10.5 | 2.463E+29 | -177.7 | 0.993 | 31 | 33 | 5 | Ref. 43 |
| | 0.06314 | 260 | 6.7 | 8.4 | 3.174E+28 | -137.2 | 0.922 | 32 | 36 | 6 | Ref. 43 |
| | 0.99999 | 236 | 11.2 | 15.1 | 7.452E+30 | -238.2 | 0.987 | 27 | 28 | 4 | TABLE B8 |
| | 1.00020 | 240 | 10.1 | 13.6 | 7.452E+30 | -220.0 | 0.987 | 28 | 29 | 4 | TABLE B8 |
| | 1.99449 | 236 | 11.4 | 14.7 | 8.203E+30 | -232.3 | 0.991 | 26 | 28 | 4 | TABLE B10 |
| | 1.99389 | 240 | 10.3 | 13.2 | 8.2203E+30 | -214.5 | 0.991 | 28 | 29 | 5 | TABLE B10 |
| N$_2$ | 0.10172 | 240 | 10.8 | 14.5 | 7.204E+31 | -246.0 | 0.991 | 29 | 27 | 4 | TABLE B12 |
| | 1.00177 | 240 | 10.2 | 13.4 | 6.924E+31 | -234.8 | 0.995 | 30 | 29 | 5 | TABLE B14 |
| | 2.00041 | 240 | 10.1 | 13.1 | 6.627E+31 | -222.4 | 0.989 | 30 | 30 | 5 | TABLE B16 |

[a]Calculated at the mid-range of $S$ for each experimental condition: $(S_{min} + S_{max})/2$.
[b]Condition in agreement with the data obtained by Fransen *et al.*[61] with the previous version of the PEWT.
[c]Condition derived from the data in TABLE B6 scaled to the temperature T (K) according to the Hale's model.[86]

**TABLE B2.** Regression coefficients $C$ and $D$ for the water-carbon dioxide-nitrogen $J$-$S$ data presented in Chapter 5. The quality of the regression curves is given by the $R^2_{adj}$ values.

| $y_{CO_2}$ | p (MPa) | T (K) | S min | S max | $C$ ($m^{-3}\,s^{-1}$) | D | $R^2_{adj}$ | |
|---|---|---|---|---|---|---|---|---|
| 0.05 | 0.10095 | 240 | 10.9 | 13.7 | 6.711E+31 | -245.3 | 0.994 | TABLE B19 |
| 0.15 | 0.10067 | 240 | 10.7 | 13.7 | 5.794E+31 | -243.9 | 0.994 | TABLE B19 |
| 0.25 | 0.10072 | 240 | 10.6 | 13.5 | 5.036E+31 | -242.6 | 0.991 | TABLE B20 |
| 0.25 | 0.10139 | 236 | 11.4 | 15.1 | 6.431E+31 | -264.3 | 0.991 | TABLE B20 |
| 0.25 | 0.09970 | 234 | 12.0 | 16.3 | 4.345E+31 | -273.9 | 0.992 | TABLE B20 |
| 0.05 | 1.0020 | 240 | 9.9 | 13.2 | 3.434E+31 | -228.1 | 0.989 | TABLE B22 |
| 0.15 | 0.9960 | 240 | 9.9 | 12.6 | 8.339E+30 | -214.6 | 0.996 | TABLE B22 |
| 0.25 | 1.0051 | 240 | 9.7 | 12.2 | 2.000E+30 | -200.8 | 0.996 | TABLE B22 |
| 0.05 | 1.9957 | 240 | 9.8 | 12.7 | 1.644E+31 | -209.1 | 0.992 | TABLE B24 |
| 0.15 | 2.0003 | 240 | 9.2 | 11.9 | 9.783E+29 | -182.0 | 0.990 | TABLE B24 |
| 0.25 | 2.0002 | 240 | 8.7 | 11.1 | 5.919E+28 | -155.1 | 0.987 | TABLE B24 |

**TABLE B3.** Water-helium experiments analyzed in Chapter 3: mixture preparation data.

| $p_{mpd}$ (MPa) | $T_{mpd}$ (K) | $Q_A$ (ln/min) | $Q_B$ (ln/min) | $f_{e,mpd}$ | $y$ (ppm)[a] |
|---|---|---|---|---|---|
| 0.400 | 291.01 | 3.341 | 0.704 | 1.0005 | 4233 |
| 0.400 | 291.01 | 3.276 | 0.752 | 1.0005 | 4166 |
| 0.300 | 291.03 | 2.760 | 1.186 | 1.0007 | 4790 |
| 0.300 | 291.02 | 2.724 | 1.171 | 1.0007 | 4788 |
| 0.300 | 291.02 | 2.786 | 1.191 | 1.0007 | 4796 |
| 0.300 | 291.02 | 3.075 | 0.891 | 1.0007 | 5305 |
| 0.300 | 291.01 | 2.928 | 1.175 | 1.0007 | 4881 |
| 0.300 | 291.01 | 2.833 | 1.142 | 1.0007 | 4876 |
| 0.300 | 291.01 | 3.186 | 1.020 | 1.0007 | 5180 |
| 0.300 | 291.02 | 3.085 | 0.895 | 1.0007 | 5302 |
| 0.300 | 291.02 | 3.064 | 0.888 | 1.0007 | 5303 |
| 2.575 | 291.08 | 1.103 | 0.904 | 0.9973 | 438 |
| 2.575 | 291.11 | 1.108 | 0.908 | 0.9973 | 439 |
| 3.200 | 296.38 | 1.079 | 0.873 | 0.9965 | 491 |
| 2.575 | 291.12 | 1.190 | 0.796 | 0.9973 | 478 |
| 3.200 | 296.68 | 1.075 | 0.869 | 0.9965 | 500 |
| 2.575 | 291.08 | 1.204 | 0.803 | 0.9973 | 478 |
| 3.200 | 296.15 | 1.084 | 0.889 | 0.9965 | 481 |
| 2.575 | 291.07 | 1.209 | 0.807 | 0.9973 | 477 |
| 3.200 | 296.64 | 1.108 | 0.908 | 0.9965 | 496 |
| 3.200 | 296.14 | 1.099 | 0.900 | 0.9965 | 481 |
| 2.575 | 291.06 | 1.281 | 0.737 | 0.9973 | 505 |
| 2.575 | 291.08 | 1.310 | 0.706 | 0.9973 | 517 |

[a]Water molar fraction in the mixture.

**TABLE B4.** Water-helium experiments analyzed in Chapter 3: nucleation data.

| $y$ (ppm)[a] | $p_0$ (MPa) | $T_0$ (K) | $p$ (MPa)[b] | $T$ (K)[b] | $f_e$[b] | $\Delta t_p$ (ms) | $J$ (m$^{-3}$s$^{-1}$) | S |
|---|---|---|---|---|---|---|---|---|
| 4233 | 0.17851 | 297.17 | 0.10397 | 239.5 | 1.0001 | 0.14 | $8.7 \cdot 10^{13}$ | 12.1 |
| 4166 | 0.17892 | 297.19 | 0.10385 | 239.2 | 1.0000 | 0.14 | $1.6 \cdot 10^{14}$ | 12.2 |
| 4790 | 0.17660 | 296.74 | 0.10446 | 240.7 | 1.0000 | 0.15 | $6.6 \cdot 10^{14}$ | 12.7 |
| 4788 | 0.17685 | 297.38 | 0.10311 | 239.8 | 1.0001 | 0.15 | $2.6 \cdot 10^{15}$ | 13.3 |
| 4796 | 0.17697 | 296.60 | 0.10399 | 239.9 | 1.0001 | 0.14 | $3.0 \cdot 10^{15}$ | 13.3 |
| 5305 | 0.17692 | 297.32 | 0.10490 | 241.4 | 1.0001 | 0.15 | $3.1 \cdot 10^{15}$ | 13.4 |
| 4881 | 0.17839 | 297.12 | 0.10433 | 239.9 | 1.0001 | 0.14 | $5.9 \cdot 10^{15}$ | 13.6 |
| 4876 | 0.17895 | 297.06 | 0.10424 | 239.5 | 1.0001 | 0.13 | $6.5 \cdot 10^{15}$ | 14.0 |
| 5180 | 0.17674 | 296.75 | 0.10295 | 239.2 | 1.0001 | 0.15 | $8.4 \cdot 10^{16}$ | 15.0 |
| 5302 | 0.17600 | 296.96 | 0.10263 | 239.5 | 1.0001 | 0.14 | $6.6 \cdot 10^{16}$ | 15.0 |
| 5303 | 0.17639 | 296.93 | 0.10258 | 239.2 | 1.0001 | 0.14 | $9.6 \cdot 10^{16}$ | 15.3 |
| 438 | 1.7197 | 299.34 | 0.9977 | 240.8 | 0.9995 | 0.21 | $5.9 \cdot 10^{13}$ | 11.0 |
| 439 | 1.7245 | 299.54 | 0.9894 | 239.8 | 0.9995 | 0.20 | $2.5 \cdot 10^{14}$ | 11.7 |
| 491 | 1.6894 | 296.69 | 1.0095 | 241.5 | 0.9995 | 0.21 | $1.0 \cdot 10^{15}$ | 11.8 |
| 478 | 1.7360 | 301.65 | 0.9880 | 240.8 | 0.9995 | 0.20 | $5.9 \cdot 10^{14}$ | 11.9 |
| 500 | 1.6880 | 297.08 | 1.0038 | 241.3 | 0.9995 | 0.20 | $1.4 \cdot 10^{15}$ | 12.1 |
| 478 | 1.7172 | 299.61 | 0.9900 | 240.4 | 0.9995 | 0.20 | $1.0 \cdot 10^{15}$ | 12.2 |
| 481 | 1.6945 | 296.99 | 0.9991 | 240.4 | 0.9995 | 0.21 | $2.5 \cdot 10^{15}$ | 12.4 |
| 477 | 1.7235 | 299.61 | 0.9886 | 239.9 | 0.9995 | 0.20 | $4.3 \cdot 10^{15}$ | 12.6 |
| 496 | 1.6956 | 297.41 | 0.9951 | 240.3 | 0.9995 | 0.21 | $6.9 \cdot 10^{15}$ | 12.8 |
| 481 | 1.6949 | 296.94 | 0.9929 | 239.8 | 0.9995 | 0.20 | $6.7 \cdot 10^{15}$ | 12.9 |
| 505 | 1.7089 | 298.35 | 0.9893 | 239.8 | 0.9995 | 0.21 | $2.2 \cdot 10^{16}$ | 13.5 |
| 517 | 1.7113 | 298.17 | 0.9934 | 239.9 | 0.9995 | 0.20 | $3.8 \cdot 10^{16}$ | 13.8 |

[a]Water molar fraction in the mixture.
[b]Nucleation (pulse) quantity.

**TABLE B5.** Water-argon experiments at about 0.1 MPa (nucleation pressure) analyzed in Chapter 4: mixture preparation data.

| $p_{mpd}$ (MPa) | $T_{mpd}$ (K) | $Q_A$ (ln/min) | $Q_B$ (ln/min) | $f_{e,mpd}$ | $y$ (ppm)[a] |
|---|---|---|---|---|---|
| 0.5003 | 291.02 | 1.733 | 0.781 | 1.0158 | 2870 |
| 0.5003 | 291.01 | 1.336 | 0.656 | 1.0158 | 2792 |
| 0.5251 | 291.01 | 1.757 | 0.752 | 1.0165 | 2779 |
| 0.5003 | 291.01 | 1.400 | 0.612 | 1.0158 | 2896 |
| 0.4748 | 291.05 | 1.867 | 0.651 | 1.0150 | 3256 |
| 0.4748 | 291.04 | 1.749 | 0.704 | 1.0150 | 3129 |
| 0.4748 | 291.03 | 1.934 | 0.574 | 1.0150 | 3382 |
| 0.4748 | 291.04 | 1.812 | 0.702 | 1.0150 | 3164 |
| 0.4748 | 291.03 | 1.741 | 0.741 | 1.0150 | 3077 |
| 0.4748 | 291.01 | 1.757 | 0.764 | 1.0150 | 3052 |
| 0.5003 | 291.01 | 1.468 | 0.553 | 1.0158 | 3022 |
| 0.4748 | 291.05 | 1.875 | 0.643 | 1.0150 | 3269 |
| 0.4748 | 291.04 | 1.804 | 0.697 | 1.0150 | 3165 |
| 0.4748 | 291.03 | 1.511 | 0.513 | 1.0150 | 3274 |
| 0.4748 | 291.03 | 1.611 | 0.412 | 1.0150 | 3491 |
| 0.4097 | 291.03 | 1.272 | 0.459 | 1.0131 | 3731 |
| 0.4748 | 291.03 | 1.923 | 0.591 | 1.0150 | 3355 |
| 0.4748 | 291.02 | 1.607 | 0.400 | 1.0150 | 3509 |
| 0.4748 | 291.03 | 1.599 | 0.398 | 1.0150 | 3510 |
| 0.4500 | 291.02 | 1.511 | 0.488 | 1.0143 | 3493 |
| 0.4500 | 291.02 | 1.559 | 0.436 | 1.0143 | 3612 |
| 0.4500 | 291.02 | 1.615 | 0.415 | 1.0143 | 3675 |

[a]Water molar fraction in the mixture.

**TABLE B6.** Water-argon experiments at about 0.1 MPa (nucleation pressure) analyzed in Chapter 4: nucleation data.

| $y$ (ppm)[a] | $p_0$ (MPa) | $T_0$ (K) | $p$ (MPa)[b] | $T$ (K)[b] | $f_e$[b] | $\Delta t_p$ (ms) | $J$ (m$^{-3}$s$^{-1}$) | $S$ |
|---|---|---|---|---|---|---|---|---|
| 2870 | 0.18204 | 296.61 | 0.10311 | 236.4 | 1.0055 | 0.60 | $3.4 \cdot 10^{12}$ | 10.3 |
| 2792 | 0.18149 | 295.31 | 0.10296 | 235.5 | 1.0055 | 0.66 | $7.1 \cdot 10^{12}$ | 10.7 |
| 2779 | 0.18261 | 295.64 | 0.10286 | 235.1 | 1.0056 | 0.60 | $1.6 \cdot 10^{13}$ | 10.9 |
| 2896 | 0.18142 | 295.45 | 0.10290 | 235.6 | 1.0055 | 0.65 | $1.3 \cdot 10^{13}$ | 11.0 |
| 3256 | 0.18122 | 296.52 | 0.10339 | 237.0 | 1.0055 | 0.62 | $1.3 \cdot 10^{13}$ | 11.1 |
| 3129 | 0.18014 | 296.24 | 0.10225 | 236.3 | 1.0055 | 0.62 | $1.5 \cdot 10^{13}$ | 11.1 |
| 3382 | 0.18081 | 296.76 | 0.10316 | 237.2 | 1.0055 | 0.62 | $3.2 \cdot 10^{13}$ | 11.3 |
| 3164 | 0.18283 | 297.33 | 0.10280 | 236.3 | 1.0055 | 0.64 | $2.9 \cdot 10^{13}$ | 11.3 |
| 3077 | 0.18157 | 296.22 | 0.10256 | 235.8 | 1.0055 | 0.63 | $3.4 \cdot 10^{13}$ | 11.4 |
| 3052 | 0.18246 | 296.58 | 0.10256 | 235.6 | 1.0055 | 0.61 | $5.2 \cdot 10^{13}$ | 11.4 |
| 3022 | 0.18144 | 295.07 | 0.10313 | 235.5 | 1.0056 | 0.65 | $4.7 \cdot 10^{13}$ | 11.5 |
| 3269 | 0.18264 | 296.93 | 0.10324 | 236.4 | 1.0055 | 0.62 | $7.2 \cdot 10^{13}$ | 11.6 |
| 3165 | 0.18349 | 297.46 | 0.10251 | 235.8 | 1.0055 | 0.63 | $1.1 \cdot 10^{14}$ | 11.7 |
| 3274 | 0.18127 | 296.26 | 0.10268 | 236.1 | 1.0055 | 0.60 | $1.1 \cdot 10^{14}$ | 11.8 |
| 3491 | 0.18153 | 296.57 | 0.10307 | 236.6 | 1.0055 | 0.63 | $2.3 \cdot 10^{14}$ | 12.2 |
| 3731 | 0.18042 | 297.25 | 0.10267 | 237.3 | 1.0054 | 0.65 | $5.5 \cdot 10^{14}$ | 12.3 |
| 3355 | 0.18276 | 297.33 | 0.10229 | 235.8 | 1.0055 | 0.64 | $3.7 \cdot 10^{14}$ | 12.3 |
| 3509 | 0.18205 | 296.68 | 0.10298 | 236.3 | 1.0055 | 0.62 | $9.4 \cdot 10^{14}$ | 12.5 |
| 3510 | 0.18205 | 296.73 | 0.10292 | 236.3 | 1.0055 | 0.60 | $9.5 \cdot 10^{14}$ | 12.5 |
| 3493 | 0.18261 | 296.78 | 0.10247 | 235.6 | 1.0055 | 0.63 | $2.3 \cdot 10^{15}$ | 13.0 |
| 3612 | 0.18261 | 296.85 | 0.10249 | 235.7 | 1.0055 | 0.63 | $4.3 \cdot 10^{15}$ | 13.3 |
| 3675 | 0.18153 | 295.61 | 0.10281 | 235.6 | 1.0055 | 0.63 | $1.7 \cdot 10^{16}$ | 13.7 |

[a]Water molar fraction in the mixture.
[b]Nucleation (pulse) quantity.

**TABLE B7.** Water-argon experiments at about 1 MPa (nucleation pressure) analyzed in Chapter 4: mixture preparation data.

| $p_{mpd}$ (MPa) | $T_{mpd}$ (K) | $Q_A$ (ln/min) | $Q_B$ (ln/min) | $f_{e,mpd}$ | $y$ (ppm)[a] |
|---|---|---|---|---|---|
| 2.599 | 291.00 | 0.709 | 1.274 | 1.0801 | 304 |
| 2.501 | 291.00 | 0.668 | 1.288 | 1.0770 | 301 |
| 2.599 | 291.02 | 0.696 | 1.305 | 1.0801 | 296 |
| 2.599 | 291.02 | 0.692 | 1.268 | 1.0801 | 301 |
| 2.599 | 291.04 | 0.733 | 1.251 | 1.0800 | 315 |
| 2.599 | 291.01 | 0.733 | 1.270 | 1.0801 | 311 |
| 2.599 | 291.00 | 0.717 | 1.286 | 1.0801 | 304 |
| 2.599 | 291.05 | 0.757 | 1.249 | 1.0800 | 322 |
| 2.501 | 291.01 | 0.717 | 1.313 | 1.0770 | 311 |
| 2.599 | 291.02 | 0.729 | 1.239 | 1.0801 | 315 |
| 2.599 | 291.03 | 0.733 | 1.216 | 1.0801 | 320 |
| 2.599 | 291.04 | 0.818 | 1.154 | 1.0800 | 354 |
| 2.599 | 291.02 | 0.745 | 1.272 | 1.0801 | 314 |
| 2.599 | 291.04 | 0.785 | 1.262 | 1.0801 | 327 |
| 2.599 | 291.04 | 0.806 | 1.235 | 1.0800 | 337 |
| 2.599 | 291.05 | 0.842 | 1.183 | 1.0800 | 355 |
| 2.599 | 291.03 | 0.802 | 1.204 | 1.0801 | 341 |
| 2.599 | 291.02 | 0.846 | 1.123 | 1.0801 | 366 |
| 2.599 | 291.05 | 0.830 | 1.158 | 1.0800 | 356 |
| 2.599 | 291.05 | 0.842 | 1.185 | 1.0800 | 354 |
| 2.599 | 291.01 | 0.858 | 1.158 | 1.0801 | 362 |
| 2.599 | 291.01 | 0.874 | 1.140 | 1.0801 | 369 |
| 2.599 | 291.02 | 0.882 | 1.101 | 1.0801 | 379 |
| 2.599 | 291.04 | 0.874 | 1.142 | 1.0800 | 370 |
| 2.599 | 291.05 | 0.850 | 1.113 | 1.0800 | 369 |
| 2.599 | 291.02 | 0.866 | 1.132 | 1.0801 | 369 |
| 2.599 | 291.01 | 0.903 | 1.057 | 1.0801 | 392 |
| 2.599 | 291.01 | 0.907 | 1.061 | 1.0801 | 392 |
| 2.599 | 291.00 | 1.011 | 0.999 | 1.0801 | 428 |
| 2.599 | 291.02 | 1.072 | 0.949 | 1.0801 | 451 |
| 2.599 | 291.04 | 1.007 | 1.003 | 1.0801 | 427 |
| 2.599 | 291.02 | 1.128 | 0.883 | 1.0801 | 478 |
| 2.599 | 291.01 | 1.268 | 0.720 | 1.0801 | 542 |
| 2.599 | 291.03 | 1.200 | 0.827 | 1.0801 | 504 |
| 2.599 | 291.00 | 1.244 | 0.706 | 1.0801 | 543 |

[a]Water molar fraction in the mixture.

**TABLE B8.** Water-argon experiments at about 1 MPa (nucleation pressure) analyzed in Chapter 4: nucleation data.

| $y$ (ppm)[a] | $p_0$ (MPa) | $T_0$ (K) | $p$ (MPa)[b] | $T$ (K)[b] | $f_e$[b] | $\Delta t_p$ (ms) | $J$ (m$^{-3}$s$^{-1}$) | $S$ |
|---|---|---|---|---|---|---|---|---|
| 304 | 1.7572 | 295.28 | 1.0080 | 236.4 | 1.0543 | 0.68 | $1.9 \cdot 10^{13}$ | 10.1 |
| 301 | 1.7564 | 294.99 | 1.0069 | 236.1 | 1.0544 | 0.67 | $3.2 \cdot 10^{13}$ | 10.3 |
| 296 | 1.7676 | 296.33 | 0.9985 | 235.8 | 1.0541 | 0.69 | $3.0 \cdot 10^{13}$ | 10.3 |
| 301 | 1.7673 | 296.20 | 0.9996 | 235.8 | 1.0542 | 0.68 | $2.7 \cdot 10^{13}$ | 10.4 |
| 315 | 1.7606 | 296.41 | 0.9991 | 236.2 | 1.0538 | 0.69 | $5.3 \cdot 10^{13}$ | 10.5 |
| 311 | 1.7578 | 294.93 | 1.0097 | 236.2 | 1.0545 | 0.67 | $3.6 \cdot 10^{13}$ | 10.5 |
| 304 | 1.7568 | 295.10 | 1.0008 | 235.6 | 1.0544 | 0.66 | $4.2 \cdot 10^{13}$ | 10.7 |
| 322 | 1.7711 | 296.85 | 0.9998 | 236.1 | 1.0540 | 0.68 | $9.6 \cdot 10^{13}$ | 10.8 |
| 311 | 1.7564 | 295.01 | 1.0016 | 235.6 | 1.0544 | 0.65 | $8.1 \cdot 10^{13}$ | 10.9 |
| 315 | 1.7671 | 296.05 | 0.9999 | 235.7 | 1.0543 | 0.65 | $1.0 \cdot 10^{14}$ | 11.0 |
| 320 | 1.7773 | 297.31 | 0.9942 | 235.6 | 1.0540 | 0.68 | $2.3 \cdot 10^{14}$ | 11.1 |
| 354 | 1.7473 | 295.95 | 1.0029 | 237.0 | 1.0536 | 0.66 | $4.5 \cdot 10^{14}$ | 11.2 |
| 314 | 1.7731 | 295.82 | 1.0007 | 235.3 | 1.0546 | 0.69 | $3.2 \cdot 10^{14}$ | 11.3 |
| 327 | 1.7666 | 295.94 | 0.9983 | 235.5 | 1.0543 | 0.69 | $5.2 \cdot 10^{14}$ | 11.5 |
| 337 | 1.7763 | 297.41 | 0.9949 | 235.8 | 1.0539 | 0.63 | $7.4 \cdot 10^{14}$ | 11.5 |
| 355 | 1.7661 | 296.43 | 1.0017 | 236.2 | 1.0540 | 0.68 | $1.7 \cdot 10^{15}$ | 11.8 |
| 341 | 1.7577 | 295.50 | 0.9979 | 235.6 | 1.0542 | 0.68 | $2.5 \cdot 10^{15}$ | 11.9 |
| 366 | 1.7674 | 296.49 | 1.0021 | 236.2 | 1.0540 | 0.65 | $3.3 \cdot 10^{15}$ | 12.2 |
| 356 | 1.7763 | 296.97 | 0.9973 | 235.7 | 1.0541 | 0.68 | $4.1 \cdot 10^{15}$ | 12.3 |
| 354 | 1.7744 | 296.73 | 0.9967 | 235.5 | 1.0542 | 0.69 | $5.5 \cdot 10^{15}$ | 12.4 |
| 362 | 1.7573 | 295.11 | 1.0021 | 235.7 | 1.0544 | 0.67 | $1.1 \cdot 10^{16}$ | 12.6 |
| 369 | 1.7570 | 295.22 | 1.0031 | 235.9 | 1.0543 | 0.66 | $1.1 \cdot 10^{16}$ | 12.6 |
| 379 | 1.7676 | 296.50 | 1.0007 | 236.1 | 1.0540 | 0.68 | $1.3 \cdot 10^{16}$ | 12.7 |
| 370 | 1.7780 | 297.13 | 0.9962 | 235.6 | 1.0541 | 0.67 | $1.5 \cdot 10^{16}$ | 12.8 |
| 369 | 1.7741 | 297.12 | 0.9899 | 235.2 | 1.0540 | 0.66 | $2.7 \cdot 10^{16}$ | 13.1 |
| 369 | 1.7678 | 295.25 | 1.0021 | 235.2 | 1.0547 | 0.68 | $3.8 \cdot 10^{16}$ | 13.2 |
| 392 | 1.7668 | 296.18 | 0.9994 | 235.8 | 1.0542 | 0.69 | $6.8 \cdot 10^{16}$ | 13.4 |
| 392 | 1.7671 | 296.37 | 0.9955 | 235.5 | 1.0541 | 0.68 | $7.8 \cdot 10^{16}$ | 13.6 |
| 428 | 1.6658 | 294.65 | 1.0023 | 240.4 | 1.0513 | 0.70 | $4.5 \cdot 10^{13}$ | 10.5 |
| 451 | 1.6922 | 296.37 | 0.9996 | 240.0 | 1.0514 | 0.66 | $3.8 \cdot 10^{14}$ | 11.4 |
| 427 | 1.7049 | 296.57 | 0.9953 | 239.1 | 1.0518 | 0.68 | $8.7 \cdot 10^{14}$ | 11.5 |
| 478 | 1.6920 | 296.44 | 0.9995 | 240.1 | 1.0514 | 0.68 | $1.9 \cdot 10^{15}$ | 12.0 |
| 542 | 1.6575 | 294.80 | 1.0131 | 242.1 | 1.0509 | 0.67 | $1.8 \cdot 10^{15}$ | 12.0 |
| 504 | 1.6916 | 296.38 | 0.9970 | 239.8 | 1.0514 | 0.68 | $1.5 \cdot 10^{16}$ | 12.8 |
| 543 | 1.6714 | 294.90 | 1.0005 | 240.1 | 1.0514 | 0.62 | $5.6 \cdot 10^{16}$ | 13.6 |

[a]Water molar fraction in the mixture.
[b]Nucleation (pulse) quantity.

**TABLE B9.** Water-argon experiments at about 2 MPa (nucleation pressure) analyzed in Chapter 4: mixture preparation data.

| $p_{mpd}$ (MPa) | $T_{mpd}$ (K) | $Q_A$ (ln/min) | $Q_B$ (ln/min) | $f_{e,mpd}$ | $y$ (ppm)[a] |
|---|---|---|---|---|---|
| 4.499 | 291.02 | 0.631 | 1.381 | 1.1123 | 159 |
| 4.499 | 291.02 | 0.623 | 1.371 | 1.1123 | 158 |
| 4.499 | 291.01 | 0.692 | 1.309 | 1.1123 | 175 |
| 4.499 | 291.03 | 0.648 | 1.348 | 1.1123 | 164 |
| 4.499 | 291.01 | 0.684 | 1.327 | 1.1123 | 172 |
| 4.499 | 291.02 | 0.761 | 1.309 | 1.1123 | 186 |
| 4.499 | 291.00 | 0.692 | 1.309 | 1.1123 | 175 |
| 4.499 | 291.01 | 0.704 | 1.301 | 1.1123 | 178 |
| 4.499 | 291.02 | 0.700 | 1.286 | 1.1123 | 179 |
| 4.499 | 291.02 | 0.692 | 1.313 | 1.1123 | 175 |
| 4.499 | 291.01 | 0.700 | 1.266 | 1.1123 | 180 |
| 4.499 | 291.01 | 0.745 | 1.251 | 1.1123 | 189 |
| 4.499 | 291.01 | 0.749 | 1.257 | 1.1123 | 189 |
| 4.499 | 291.02 | 0.785 | 1.251 | 1.1123 | 195 |
| 4.499 | 291.00 | 0.761 | 1.210 | 1.1123 | 195 |
| 4.499 | 291.01 | 0.874 | 1.146 | 1.1123 | 219 |
| 4.499 | 291.02 | 0.907 | 1.103 | 1.1123 | 229 |
| 4.499 | 291.02 | 1.015 | 1.014 | 1.1123 | 253 |
| 4.499 | 291.02 | 0.995 | 0.995 | 1.1123 | 253 |
| 4.499 | 291.02 | 1.020 | 0.960 | 1.1123 | 261 |

[a]Water molar fraction in the mixture.

**TABLE B10.** Water-argon experiments at about 2 MPa (nucleation pressure) analyzed in Chapter 4: nucleation data.

| $y$ (ppm)[a] | $p_0$ (MPa) | $T_0$ (K) | $p$ (MPa)[b] | $T$ (K)[b] | $f_e$[b] | $\Delta t_p$ (ms) | $J$ (m$^{-3}$s$^{-1}$) | $S$ |
|---|---|---|---|---|---|---|---|---|
| 159 | 3.4878 | 295.55 | 1.9930 | 236.2 | 1.0806 | 0.62 | $7.3 \cdot 10^{13}$ | 10.3 |
| 158 | 3.4920 | 295.45 | 1.9948 | 236.1 | 1.0807 | 0.67 | $9.9 \cdot 10^{13}$ | 10.4 |
| 175 | 3.4880 | 295.42 | 2.0004 | 236.5 | 1.0807 | 0.68 | $7.1 \cdot 10^{14}$ | 11.2 |
| 164 | 3.5059 | 295.43 | 1.9897 | 235.5 | 1.0811 | 0.66 | $9.4 \cdot 10^{14}$ | 11.2 |
| 172 | 3.4858 | 295.21 | 1.9950 | 236.1 | 1.0808 | 0.68 | $9.8 \cdot 10^{14}$ | 11.3 |
| 186 | 3.5029 | 296.46 | 2.0028 | 237.0 | 1.0803 | 0.62 | $1.7 \cdot 10^{15}$ | 11.4 |
| 175 | 3.4919 | 295.44 | 1.9928 | 236.0 | 1.0807 | 0.67 | $1.5 \cdot 10^{15}$ | 11.5 |
| 178 | 3.4841 | 295.06 | 1.9959 | 236.1 | 1.0808 | 0.62 | $3.5 \cdot 10^{15}$ | 11.7 |
| 179 | 3.5053 | 295.81 | 1.9942 | 236.0 | 1.0808 | 0.66 | $3.0 \cdot 10^{15}$ | 11.7 |
| 175 | 3.5400 | 294.93 | 2.0146 | 235.4 | 1.0823 | 0.62 | $1.7 \cdot 10^{16}$ | 12.2 |
| 180 | 3.5039 | 295.46 | 1.9893 | 235.6 | 1.0810 | 0.68 | $1.1 \cdot 10^{16}$ | 12.2 |
| 189 | 3.5024 | 296.02 | 1.9896 | 236.1 | 1.0806 | 0.66 | $1.4 \cdot 10^{16}$ | 12.3 |
| 189 | 3.5255 | 296.59 | 1.9917 | 236.0 | 1.0807 | 0.68 | $1.8 \cdot 10^{16}$ | 12.4 |
| 195 | 3.5117 | 296.04 | 1.9893 | 235.8 | 1.0808 | 0.66 | $6.0 \cdot 10^{16}$ | 13.0 |
| 195 | 3.5098 | 295.89 | 1.9842 | 235.5 | 1.0808 | 0.67 | $7.8 \cdot 10^{16}$ | 13.2 |
| 219 | 3.3994 | 296.88 | 1.9873 | 239.5 | 1.0775 | 0.63 | $6.8 \cdot 10^{14}$ | 11.2 |
| 229 | 3.4003 | 297.01 | 1.9916 | 239.8 | 1.0775 | 0.66 | $1.3 \cdot 10^{15}$ | 11.4 |
| 253 | 3.3364 | 296.10 | 1.9923 | 240.9 | 1.0766 | 0.63 | $2.6 \cdot 10^{15}$ | 11.7 |
| 253 | 3.3741 | 296.49 | 1.9911 | 240.1 | 1.0772 | 0.64 | $1.9 \cdot 10^{16}$ | 12.4 |
| 261 | 3.4012 | 297.09 | 1.9981 | 240.1 | 1.0774 | 0.65 | $3.4 \cdot 10^{16}$ | 12.7 |

[a]Water molar fraction in the mixture.
[b]Nucleation (pulse) quantity.

**TABLE B11.** Water-nitrogen experiments at about 0.1 MPa (nucleation pressure) analyzed in Chapter 4: mixture preparation data.

| $p_{mpd}$ (MPa) | $T_{mpd}$ (K) | $Q_A$ (ln/min) | $Q_B$ (ln/min) | $f_{e,mpd}$ | $y$ (ppm)[a] |
|---|---|---|---|---|---|
| 0.3998 | 291.03 | 1.575 | 0.262 | 1.0146 | 4464 |
| 0.3998 | 291.04 | 1.563 | 0.282 | 1.0146 | 4412 |
| 0.3998 | 291.04 | 1.553 | 0.280 | 1.0146 | 4412 |
| 0.3998 | 291.02 | 1.563 | 0.284 | 1.0146 | 4404 |
| 0.3998 | 291.04 | 1.501 | 0.349 | 1.0146 | 4228 |
| 0.3998 | 291.03 | 1.596 | 0.229 | 1.0146 | 4551 |
| 0.3998 | 291.04 | 1.596 | 0.229 | 1.0146 | 4554 |
| 0.3998 | 291.03 | 1.578 | 0.262 | 1.0146 | 4463 |
| 0.3998 | 291.02 | 1.538 | 0.305 | 1.0146 | 4342 |
| 0.3998 | 291.03 | 1.584 | 0.228 | 1.0146 | 4551 |
| 0.3502 | 291.03 | 1.405 | 0.449 | 1.0130 | 4497 |
| 0.3502 | 291.03 | 1.572 | 0.260 | 1.0130 | 5088 |
| 0.3998 | 291.03 | 1.587 | 0.228 | 1.0146 | 4551 |
| 0.3502 | 291.03 | 1.454 | 0.403 | 1.0130 | 4649 |
| 0.3502 | 291.03 | 1.516 | 0.358 | 1.0130 | 4801 |
| 0.3502 | 291.02 | 1.405 | 0.449 | 1.0130 | 4496 |
| 0.3502 | 290.99 | 1.581 | 0.285 | 1.0130 | 5014 |
| 0.3502 | 291.03 | 1.448 | 0.401 | 1.0130 | 4648 |
| 0.3502 | 291.03 | 1.566 | 0.282 | 1.0130 | 5029 |
| 0.3502 | 291.03 | 1.516 | 0.358 | 1.0130 | 4802 |
| 0.3502 | 291.04 | 1.501 | 0.355 | 1.0130 | 4801 |
| 0.3502 | 290.99 | 1.581 | 0.285 | 1.0130 | 5014 |
| 0.3502 | 291.01 | 1.584 | 0.263 | 1.0130 | 5081 |
| 0.3502 | 291.00 | 1.581 | 0.285 | 1.0130 | 5017 |
| 0.3502 | 290.99 | 1.584 | 0.287 | 1.0130 | 5011 |
| 0.3502 | 291.00 | 1.587 | 0.263 | 1.0130 | 5077 |
| 0.3502 | 291.02 | 1.646 | 0.201 | 1.0130 | 5283 |

[a]Water molar fraction in the mixture.

**TABLE B12.** Water-nitrogen experiments at about 0.1 MPa (nucleation pressure) analyzed in Chapter 4: nucleation data.

| $y$ (ppm)[a] | $p_0$ (MPa) | $T_0$ (K) | $p$ (MPa)[b] | $T$ (K)[b] | $f_e$[b] | $\Delta t_p$ (ms) | $J$ (m$^{-3}$s$^{-1}$) | $S$ |
|---|---|---|---|---|---|---|---|---|
| 4464 | 0.21366 | 297.12 | 0.10374 | 241.7 | 1.0058 | 0.53 | $1.2 \cdot 10^{13}$ | 10.8 |
| 4412 | 0.21058 | 296.89 | 0.10168 | 241.1 | 1.0057 | 0.55 | $8.2 \cdot 10^{12}$ | 10.9 |
| 4412 | 0.21168 | 297.16 | 0.10178 | 241.0 | 1.0057 | 0.59 | $1.9 \cdot 10^{13}$ | 11.0 |
| 4404 | 0.21052 | 297.03 | 0.10111 | 240.9 | 1.0057 | 0.53 | $1.4 \cdot 10^{13}$ | 11.0 |
| 4228 | 0.21369 | 297.12 | 0.10182 | 240.4 | 1.0058 | 0.51 | $1.1 \cdot 10^{13}$ | 11.0 |
| 4551 | 0.21216 | 297.42 | 0.10222 | 241.4 | 1.0057 | 0.58 | $1.7 \cdot 10^{13}$ | 11.1 |
| 4554 | 0.21169 | 297.42 | 0.10107 | 240.8 | 1.0057 | 0.52 | $5.1 \cdot 10^{13}$ | 11.5 |
| 4463 | 0.21363 | 297.07 | 0.10199 | 240.5 | 1.0058 | 0.60 | $7.1 \cdot 10^{13}$ | 11.6 |
| 4342 | 0.21366 | 297.02 | 0.10134 | 240.0 | 1.0058 | 0.55 | $9.0 \cdot 10^{13}$ | 11.6 |
| 4551 | 0.21169 | 297.06 | 0.10078 | 240.3 | 1.0057 | 0.56 | $1.7 \cdot 10^{14}$ | 11.9 |
| 4497 | 0.21071 | 296.49 | 0.10066 | 240.1 | 1.0057 | 0.51 | $1.6 \cdot 10^{14}$ | 11.9 |
| 5088 | 0.21349 | 296.93 | 0.10482 | 242.3 | 1.0058 | 0.60 | $2.3 \cdot 10^{14}$ | 11.9 |
| 4551 | 0.21148 | 297.16 | 0.10022 | 240.0 | 1.0057 | 0.43 | $1.9 \cdot 10^{14}$ | 12.0 |
| 4649 | 0.21209 | 296.96 | 0.10135 | 240.5 | 1.0057 | 0.59 | $2.1 \cdot 10^{14}$ | 12.0 |
| 4801 | 0.21111 | 297.08 | 0.10117 | 240.8 | 1.0057 | 0.57 | $2.8 \cdot 10^{14}$ | 12.1 |
| 4496 | 0.21193 | 296.90 | 0.10020 | 239.7 | 1.0057 | 0.53 | $4.7 \cdot 10^{14}$ | 12.2 |
| 5014 | 0.21057 | 294.87 | 0.10515 | 241.8 | 1.0059 | 0.60 | $7.3 \cdot 10^{14}$ | 12.2 |
| 4648 | 0.21208 | 296.55 | 0.10078 | 239.7 | 1.0058 | 0.54 | $1.2 \cdot 10^{15}$ | 12.6 |
| 5029 | 0.21254 | 296.43 | 0.10324 | 241.2 | 1.0058 | 0.58 | $1.0 \cdot 10^{15}$ | 12.6 |
| 4802 | 0.21211 | 297.16 | 0.10018 | 239.8 | 1.0057 | 0.54 | $1.8 \cdot 10^{15}$ | 12.9 |
| 4801 | 0.21260 | 297.18 | 0.10002 | 239.6 | 1.0057 | 0.51 | $2.8 \cdot 10^{15}$ | 13.1 |
| 5014 | 0.21018 | 294.75 | 0.10274 | 240.2 | 1.0058 | 0.57 | $7.2 \cdot 10^{15}$ | 13.4 |
| 5081 | 0.21366 | 296.78 | 0.10180 | 240.1 | 1.0058 | 0.59 | $1.2 \cdot 10^{16}$ | 13.5 |
| 5017 | 0.21103 | 295.40 | 0.10171 | 239.8 | 1.0058 | 0.51 | $1.3 \cdot 10^{16}$ | 13.7 |
| 5011 | 0.21073 | 294.79 | 0.10233 | 239.8 | 1.0058 | 0.57 | $1.3 \cdot 10^{16}$ | 13.7 |
| 5077 | 0.21178 | 295.41 | 0.10153 | 239.4 | 1.0058 | 0.61 | $3.7 \cdot 10^{16}$ | 14.2 |
| 5283 | 0.21361 | 296.82 | 0.10093 | 239.6 | 1.0058 | 0.53 | $4.4 \cdot 10^{16}$ | 14.5 |

[a]Water molar fraction in the mixture.
[b]Nucleation (pulse) quantity.

**TABLE B13.** Water-nitrogen experiments at about 1 MPa (nucleation pressure) analyzed in Chapter 4: mixture preparation data.

| $p_{mpd}$ (MPa) | $T_{mpd}$ (K) | $Q_A$ (ln/min) | $Q_B$ (ln/min) | $f_{e,mpd}$ | $y$ (ppm)[a] |
|---|---|---|---|---|---|
| 2.599 | 291.08 | 0.984 | 1.097 | 1.0925 | 409 |
| 2.599 | 291.07 | 0.947 | 1.035 | 1.0925 | 413 |
| 2.599 | 291.09 | 0.978 | 1.047 | 1.0925 | 418 |
| 2.599 | 291.11 | 0.965 | 1.057 | 1.0925 | 414 |
| 2.599 | 291.07 | 1.027 | 1.027 | 1.0925 | 432 |
| 2.599 | 291.07 | 1.092 | 0.990 | 1.0925 | 453 |
| 2.599 | 291.08 | 1.027 | 1.026 | 1.0925 | 433 |
| 2.599 | 291.10 | 1.092 | 0.978 | 1.0925 | 457 |
| 2.599 | 291.11 | 1.108 | 0.899 | 1.0925 | 478 |
| 2.599 | 291.06 | 1.154 | 0.965 | 1.0925 | 470 |
| 2.599 | 291.07 | 1.157 | 0.937 | 1.0925 | 477 |
| 2.599 | 291.08 | 1.176 | 0.908 | 1.0925 | 488 |
| 2.599 | 291.05 | 1.176 | 0.889 | 1.0925 | 491 |
| 2.599 | 291.09 | 1.244 | 0.832 | 1.0925 | 518 |
| 2.599 | 291.06 | 1.160 | 0.886 | 1.0925 | 489 |
| 2.599 | 291.01 | 1.337 | 0.741 | 1.0926 | 554 |
| 2.599 | 291.10 | 1.259 | 0.807 | 1.0925 | 528 |
| 2.599 | 291.09 | 1.294 | 0.823 | 1.0925 | 528 |
| 2.599 | 291.08 | 1.297 | 0.807 | 1.0925 | 533 |

[a]Water molar fraction in the mixture.

**TABLE B14.** Water-nitrogen experiments at about 1 MPa (nucleation pressure) analyzed in Chapter 4: nucleation data.

| $y$ (ppm)[a] | $p_0$ (MPa) | $T_0$ (K) | p (MPa)[b] | T (K)[b] | $f_e$[b] | $\Delta t_p$ (ms) | J (m$^{-3}$s$^{-1}$) | S |
|---|---|---|---|---|---|---|---|---|
| 409 | 2.1145 | 298.04 | 1.0017 | 240.1 | 1.0575 | 0.54 | $1.5 \cdot 10^{13}$ | 10.2 |
| 413 | 2.1056 | 297.54 | 0.9987 | 239.8 | 1.0575 | 0.54 | $4.9 \cdot 10^{13}$ | 10.5 |
| 418 | 2.1308 | 298.46 | 1.0019 | 239.9 | 1.0576 | 0.54 | $4.6 \cdot 10^{13}$ | 10.6 |
| 414 | 2.1542 | 299.15 | 0.9979 | 239.5 | 1.0577 | 0.55 | $9.4 \cdot 10^{13}$ | 10.8 |
| 432 | 2.1098 | 297.76 | 1.0008 | 240.0 | 1.0575 | 0.55 | $1.2 \cdot 10^{14}$ | 10.9 |
| 453 | 2.1090 | 297.59 | 1.0058 | 240.2 | 1.0577 | 0.54 | $3.6 \cdot 10^{14}$ | 11.3 |
| 433 | 2.1246 | 298.09 | 0.9953 | 239.4 | 1.0576 | 0.54 | $4.3 \cdot 10^{14}$ | 11.3 |
| 457 | 2.1388 | 298.86 | 0.9983 | 239.7 | 1.0575 | 0.55 | $1.1 \cdot 10^{15}$ | 11.7 |
| 478 | 2.1437 | 299.24 | 1.0043 | 240.3 | 1.0575 | 0.61 | $1.4 \cdot 10^{15}$ | 11.8 |
| 470 | 2.0988 | 296.97 | 1.0046 | 240.0 | 1.0578 | 0.56 | $2.2 \cdot 10^{15}$ | 11.9 |
| 477 | 2.1103 | 297.69 | 0.9992 | 239.8 | 1.0576 | 0.55 | $3.6 \cdot 10^{15}$ | 12.2 |
| 488 | 2.1141 | 297.92 | 0.9974 | 239.7 | 1.0575 | 0.56 | $8.1 \cdot 10^{15}$ | 12.4 |
| 491 | 2.0953 | 296.62 | 1.0034 | 239.7 | 1.0579 | 0.56 | $1.4 \cdot 10^{16}$ | 12.6 |
| 518 | 2.1144 | 298.30 | 0.9988 | 240.1 | 1.0573 | 0.55 | $2.5 \cdot 10^{16}$ | 12.9 |
| 489 | 2.1301 | 297.19 | 1.0097 | 239.5 | 1.0584 | 0.54 | $3.1 \cdot 10^{16}$ | 12.9 |
| 554 | 2.0741 | 296.70 | 1.0132 | 241.2 | 1.0575 | 0.56 | $4.7 \cdot 10^{16}$ | 13.0 |
| 528 | 2.1295 | 298.70 | 1.0047 | 240.4 | 1.0575 | 0.56 | $2.8 \cdot 10^{16}$ | 13.0 |
| 528 | 2.1091 | 298.14 | 1.0011 | 240.3 | 1.0573 | 0.56 | $2.9 \cdot 10^{16}$ | 13.0 |
| 533 | 2.1037 | 297.75 | 0.9968 | 239.9 | 1.0573 | 0.56 | $8.1 \cdot 10^{16}$ | 13.4 |

[a]Water molar fraction in the mixture.
[b]Nucleation (pulse) quantity.

**TABLE B15.** Water-nitrogen experiments at about 2 MPa (nucleation pressure) analyzed in Chapter 4: mixture preparation data.

| $p_{mpd}$ (MPa) | $T_{mpd}$ (K) | $Q_A$ (ln/min) | $Q_B$ (ln/min) | $f_{e,mpd}$ | $y$ (ppm)[a] |
|---|---|---|---|---|---|
| 5.001 | 291.07 | 0.882 | 1.150 | 1.1845 | 211 |
| 5.499 | 291.05 | 0.962 | 1.040 | 1.2045 | 216 |
| 5.001 | 291.06 | 0.876 | 1.125 | 1.1845 | 213 |
| 5.001 | 291.05 | 0.922 | 1.112 | 1.1845 | 220 |
| 5.001 | 291.05 | 0.938 | 1.063 | 1.1846 | 228 |
| 5.001 | 291.05 | 0.916 | 1.103 | 1.1846 | 221 |
| 5.001 | 291.04 | 0.972 | 1.071 | 1.1846 | 231 |
| 5.001 | 291.03 | 1.006 | 1.057 | 1.1846 | 237 |
| 5.001 | 291.07 | 0.993 | 1.023 | 1.1845 | 240 |
| 5.001 | 291.06 | 1.003 | 1.001 | 1.1845 | 243 |
| 5.001 | 291.05 | 0.956 | 1.033 | 1.1845 | 234 |
| 5.001 | 291.04 | 0.981 | 1.041 | 1.1846 | 236 |
| 5.001 | 291.08 | 1.052 | 0.975 | 1.1845 | 253 |
| 5.499 | 291.06 | 1.133 | 0.909 | 1.2045 | 250 |
| 5.001 | 291.10 | 1.074 | 0.968 | 1.1845 | 256 |
| 5.001 | 291.05 | 1.120 | 0.947 | 1.1846 | 263 |
| 5.001 | 291.03 | 1.148 | 0.896 | 1.1846 | 273 |
| 5.001 | 291.04 | 1.139 | 0.922 | 1.1846 | 268 |
| 5.001 | 291.04 | 1.145 | 0.857 | 1.1846 | 278 |

[a]Water molar fraction in the mixture.

**TABLE B16.** Water-nitrogen experiments at about 2 MPa (nucleation pressure) analyzed in Chapter 4: nucleation data.

| $y$ (ppm)[a] | $p_0$ (MPa) | $T_0$ (K) | $p$ (MPa)[b] | $T$ (K)[b] | $f_e$[b] | $\Delta t_p$ (ms) | $J$ (m$^{-3}$s$^{-1}$) | S |
|---|---|---|---|---|---|---|---|---|
| 211 | 4.1612 | 297.23 | 1.9982 | 239.9 | 1.1182 | 0.57 | $4.0 \cdot 10^{13}$ | 10.1 |
| 216 | 4.1271 | 296.41 | 2.0041 | 240.0 | 1.1184 | 0.57 | $1.2 \cdot 10^{14}$ | 10.3 |
| 213 | 4.1419 | 296.62 | 1.9972 | 239.7 | 1.1184 | 0.57 | $8.0 \cdot 10^{13}$ | 10.3 |
| 220 | 4.1029 | 295.95 | 2.0041 | 240.0 | 1.1183 | 0.58 | $2.4 \cdot 10^{14}$ | 10.4 |
| 228 | 4.1429 | 296.84 | 2.0055 | 240.1 | 1.1183 | 0.60 | $2.7 \cdot 10^{14}$ | 10.7 |
| 221 | 4.1900 | 297.11 | 1.9960 | 239.2 | 1.1190 | 0.60 | $6.8 \cdot 10^{14}$ | 11.1 |
| 231 | 4.1323 | 296.42 | 2.0034 | 239.9 | 1.1185 | 0.59 | $7.7 \cdot 10^{14}$ | 11.1 |
| 237 | 4.1083 | 295.93 | 2.0099 | 240.1 | 1.1185 | 0.57 | $1.2 \cdot 10^{15}$ | 11.2 |
| 240 | 4.1832 | 297.65 | 2.0014 | 240.0 | 1.1183 | 0.55 | $2.7 \cdot 10^{15}$ | 11.4 |
| 243 | 4.1633 | 297.19 | 2.0044 | 240.0 | 1.1183 | 0.55 | $3.9 \cdot 10^{15}$ | 11.5 |
| 234 | 4.1724 | 296.81 | 1.9960 | 239.3 | 1.1189 | 0.55 | $4.8 \cdot 10^{15}$ | 11.7 |
| 236 | 4.1497 | 295.81 | 2.0087 | 239.3 | 1.1197 | 0.56 | $9.4 \cdot 10^{15}$ | 11.8 |
| 253 | 4.2136 | 298.14 | 2.0006 | 239.8 | 1.1184 | 0.54 | $1.7 \cdot 10^{16}$ | 12.2 |
| 250 | 4.0733 | 296.72 | 1.9472 | 239.2 | 1.1160 | 0.56 | $3.9 \cdot 10^{16}$ | 12.3 |
| 256 | 4.2372 | 298.61 | 1.9982 | 239.7 | 1.1184 | 0.54 | $2.6 \cdot 10^{16}$ | 12.4 |
| 263 | 4.1477 | 296.37 | 2.0151 | 240.0 | 1.1191 | 0.57 | $4.7 \cdot 10^{16}$ | 12.6 |
| 273 | 4.0989 | 295.78 | 2.0123 | 240.3 | 1.1185 | 0.57 | $1.0 \cdot 10^{17}$ | 12.8 |
| 268 | 4.1467 | 296.64 | 2.0031 | 239.8 | 1.1186 | 0.55 | $8.1 \cdot 10^{16}$ | 12.9 |
| 278 | 4.1316 | 296.75 | 2.0023 | 240.1 | 1.1180 | 0.55 | $1.4 \cdot 10^{17}$ | 13.1 |

[a]Water molar fraction in the mixture.
[b]Nucleation (pulse) quantity.

**TABLE B17.** Water-carbon dioxide-nitrogen experiments at about 0.1 MPa (nucleation pressure) analyzed in Chapter 5: mixture preparation data, **I part**.

| $p_{mpd}$ (MPa) | $T_{mpd}$ (K) | $Q_A$ (ln/min) | $Q_B$ (ln/min) | $Q_C$ (ln/min) | $f_{e,mpd}$ | $y$ (ppm)[a] | $y_{CO_2}$ |
|---|---|---|---|---|---|---|---|
| 0.2997 | 291.07 | 1.163 | 0.647 | 0.200 | 1.0112 | 4023 | 0.0495 |
| 0.2997 | 291.07 | 1.160 | 0.647 | 0.198 | 1.0112 | 4020 | 0.0493 |
| 0.2997 | 291.08 | 1.228 | 0.613 | 0.202 | 1.0112 | 4180 | 0.0492 |
| 0.2997 | 291.07 | 1.197 | 0.596 | 0.196 | 1.0112 | 4182 | 0.0491 |
| 0.2997 | 291.06 | 1.166 | 0.650 | 0.200 | 1.0112 | 4020 | 0.0493 |
| 0.2997 | 291.08 | 1.147 | 0.572 | 0.189 | 1.0112 | 4183 | 0.0493 |
| 0.2997 | 291.07 | 1.240 | 0.400 | 0.180 | 1.0112 | 4736 | 0.0491 |
| 0.2997 | 291.08 | 1.252 | 0.528 | 0.196 | 1.0112 | 4405 | 0.0494 |
| 0.2997 | 291.07 | 1.234 | 0.615 | 0.203 | 1.0112 | 4181 | 0.0493 |
| 0.2997 | 291.08 | 1.197 | 0.596 | 0.197 | 1.0112 | 4182 | 0.0494 |
| 0.2997 | 291.08 | 1.361 | 0.442 | 0.198 | 1.0112 | 4726 | 0.0494 |
| 0.2997 | 291.08 | 1.410 | 0.411 | 0.201 | 1.0112 | 4848 | 0.0494 |
| 0.2997 | 291.08 | 1.388 | 0.405 | 0.197 | 1.0112 | 4848 | 0.0493 |
| 0.2997 | 291.07 | 1.410 | 0.411 | 0.200 | 1.0112 | 4849 | 0.0492 |
| 0.2997 | 291.08 | 1.432 | 0.368 | 0.198 | 1.0112 | 4980 | 0.0494 |
| 0.2997 | 291.08 | 1.382 | 0.422 | 0.198 | 1.0112 | 4797 | 0.0493 |
| 0.2997 | 291.07 | 1.509 | 0.321 | 0.201 | 1.0112 | 5161 | 0.0492 |
| 0.2997 | 291.07 | 1.425 | 0.434 | 0.204 | 1.0112 | 4799 | 0.0493 |
| 0.2997 | 291.06 | 1.184 | 0.229 | 0.601 | 1.0112 | 4087 | 0.1486 |
| 0.2997 | 291.06 | 1.223 | 0.189 | 0.601 | 1.0112 | 4221 | 0.1487 |
| 0.2997 | 293.02 | 1.169 | 0.226 | 0.594 | 1.0111 | 4618 | 0.1487 |
| 0.2997 | 293.01 | 1.201 | 0.232 | 0.692 | 1.0111 | 4440 | 0.1621 |
| 0.2997 | 293.03 | 1.169 | 0.226 | 0.594 | 1.0111 | 4620 | 0.1487 |
| 0.2997 | 291.05 | 1.279 | 0.135 | 0.601 | 1.0112 | 4406 | 0.1486 |
| 0.2997 | 291.07 | 1.322 | 0.079 | 0.595 | 1.0112 | 4601 | 0.1484 |
| 0.2997 | 291.05 | 1.385 | 0.030 | 0.602 | 1.0112 | 4764 | 0.1486 |
| 0.2997 | 293.02 | 1.117 | 0.216 | 0.641 | 1.0111 | 4443 | 0.1617 |
| 0.2997 | 293.01 | 1.231 | 0.190 | 0.677 | 1.0111 | 4606 | 0.1606 |
| 0.2997 | 295.03 | 1.206 | 0.233 | 0.608 | 1.0111 | 5238 | 0.1478 |

[a]Water molar fraction in the mixture.

**TABLE B18.** Water-carbon dioxide-nitrogen experiments at about 0.1 MPa (nucleation pressure) analyzed in Chapter 5: mixture preparation data, **II part**.

| $p_{mpd}$ (MPa) | $T_{mpd}$ (K) | $Q_A$ (ln/min) | $Q_B$ (ln/min) | $Q_C$ (ln/min) | $f_{e,mpd}$ | $y$ (ppm)[a] | $y_{CO_2}$ |
|---|---|---|---|---|---|---|---|
| 0.2997 | 294.99 | 0.907 | 0.088 | 0.997 | 1.0111 | 4044 | 0.2493 |
| 0.2997 | 295.00 | 0.930 | 0.069 | 0.997 | 1.0111 | 4139 | 0.2488 |
| 0.2997 | 294.99 | 0.964 | 0.029 | 0.997 | 1.0111 | 4299 | 0.2494 |
| 0.2502 | 294.99 | 0.837 | 0.150 | 0.997 | 1.0094 | 4486 | 0.2501 |
| 0.2502 | 294.99 | 0.859 | 0.126 | 0.997 | 1.0094 | 4608 | 0.2504 |
| 0.2502 | 294.99 | 0.914 | 0.062 | 0.997 | 1.0094 | 4926 | 0.2513 |
| 0.2502 | 295.01 | 0.930 | 0.064 | 0.997 | 1.0094 | 4972 | 0.2492 |
| 0.2502 | 295.02 | 0.920 | 0.063 | 0.997 | 1.0094 | 4950 | 0.2505 |
| 0.2502 | 294.99 | 0.911 | 0.062 | 0.997 | 1.0094 | 4915 | 0.2518 |
| 0.2997 | 291.06 | 0.868 | 0.116 | 0.997 | 1.0112 | 3048 | 0.2509 |
| 0.2997 | 291.03 | 0.842 | 0.163 | 0.997 | 1.0112 | 2920 | 0.2484 |
| 0.2997 | 291.03 | 0.973 | 0.019 | 0.997 | 1.0112 | 3394 | 0.2497 |
| 0.2997 | 291.03 | 0.970 | 0.019 | 0.997 | 1.0112 | 3388 | 0.2501 |
| 0.2997 | 293.04 | 0.828 | 0.160 | 0.997 | 1.0111 | 3285 | 0.2504 |
| 0.2997 | 293.03 | 0.837 | 0.161 | 0.997 | 1.0111 | 3303 | 0.2490 |
| 0.2997 | 293.02 | 0.822 | 0.159 | 0.997 | 1.0111 | 3270 | 0.2513 |
| 0.2997 | 293.03 | 0.831 | 0.160 | 0.997 | 1.0111 | 3290 | 0.2499 |
| 0.2997 | 295.02 | 0.842 | 0.163 | 0.997 | 1.0111 | 3744 | 0.2482 |
| 0.2997 | 291.04 | 0.970 | 0.010 | 0.997 | 1.0112 | 3407 | 0.2513 |
| 0.2997 | 293.04 | 0.967 | 0.029 | 0.997 | 1.0111 | 3818 | 0.2492 |
| 0.2997 | 293.05 | 0.959 | 0.046 | 0.997 | 1.0111 | 3772 | 0.2480 |
| 0.2997 | 293.04 | 0.945 | 0.046 | 0.997 | 1.0111 | 3743 | 0.2498 |
| 0.2997 | 293.04 | 0.970 | 0.029 | 0.997 | 1.0111 | 3824 | 0.2488 |
| 0.2997 | 293.04 | 0.931 | 0.045 | 0.997 | 1.0111 | 3716 | 0.2517 |
| 0.3498 | 291.04 | 0.887 | 0.102 | 0.997 | 1.0129 | 2660 | 0.2504 |
| 0.3498 | 291.03 | 0.887 | 0.102 | 0.997 | 1.0129 | 2658 | 0.2504 |
| 0.3498 | 291.03 | 0.939 | 0.069 | 0.997 | 1.0129 | 2788 | 0.2479 |
| 0.4000 | 295.02 | 0.840 | 0.162 | 0.997 | 1.0144 | 2807 | 0.2487 |
| 0.2997 | 291.03 | 0.839 | 0.162 | 0.997 | 1.0112 | 2915 | 0.2488 |
| 0.2997 | 293.03 | 0.831 | 0.160 | 0.997 | 1.0111 | 3289 | 0.2499 |
| 0.3498 | 295.02 | 0.851 | 0.147 | 0.997 | 1.0127 | 3255 | 0.2491 |
| 0.2997 | 293.03 | 0.819 | 0.158 | 0.997 | 1.0111 | 3265 | 0.2518 |
| 0.3498 | 295.02 | 0.854 | 0.147 | 0.997 | 1.0127 | 3262 | 0.2486 |

[a]Water molar fraction in the mixture.

**TABLE B19.** Water-carbon dioxide-nitrogen experiments at about 0.1 MPa (nucleation pressure) analyzed in Chapter 5: nucleation data, **I part**.

| $y$ (ppm)[a] | $y_{CO_2}$ | $p_0$ (MPa) | $T_0$ (K) | $p$ (MPa)[b] | $T$ (K)[b] | $f_e$[b] | $\Delta t_p$ (ms) | $J$ (m$^{-3}$s$^{-1}$) | S |
|---|---|---|---|---|---|---|---|---|---|
| 4023 | 0.0495 | 0.21216 | 296.61 | 0.09982 | 239.7 | 1.0061 | 0.56 | $8.9 \cdot 10^{12}$ | 10.9 |
| 4020 | 0.0493 | 0.21165 | 295.71 | 0.10059 | 239.6 | 1.0062 | 0.54 | $1.4 \cdot 10^{13}$ | 11.0 |
| 4180 | 0.0492 | 0.21066 | 294.26 | 0.10280 | 240.2 | 1.0063 | 0.58 | $2.5 \cdot 10^{13}$ | 11.1 |
| 4182 | 0.0491 | 0.21175 | 295.53 | 0.10134 | 239.9 | 1.0062 | 0.56 | $3.3 \cdot 10^{13}$ | 11.2 |
| 4020 | 0.0493 | 0.21173 | 295.43 | 0.10042 | 239.3 | 1.0062 | 0.55 | $4.6 \cdot 10^{13}$ | 11.3 |
| 4183 | 0.0493 | 0.21338 | 295.89 | 0.10097 | 239.5 | 1.0062 | 0.57 | $1.1 \cdot 10^{14}$ | 11.6 |
| 4736 | 0.0491 | 0.21215 | 296.02 | 0.10228 | 240.8 | 1.0062 | 0.54 | $3.9 \cdot 10^{14}$ | 12.0 |
| 4405 | 0.0494 | 0.21218 | 295.13 | 0.10153 | 239.6 | 1.0062 | 0.57 | $6.2 \cdot 10^{14}$ | 12.1 |
| 4181 | 0.0493 | 0.21203 | 294.47 | 0.10081 | 238.6 | 1.0062 | 0.53 | $5.8 \cdot 10^{14}$ | 12.3 |
| 4182 | 0.0494 | 0.21521 | 295.56 | 0.10085 | 238.5 | 1.0062 | 0.54 | $5.4 \cdot 10^{14}$ | 12.4 |
| 4726 | 0.0494 | 0.21268 | 296.38 | 0.10099 | 240.1 | 1.0062 | 0.54 | $1.2 \cdot 10^{15}$ | 12.5 |
| 4848 | 0.0494 | 0.21281 | 296.18 | 0.10079 | 239.8 | 1.0062 | 0.56 | $4.1 \cdot 10^{15}$ | 13.1 |
| 4848 | 0.0493 | 0.21274 | 296.46 | 0.10018 | 239.6 | 1.0061 | 0.53 | $5.0 \cdot 10^{15}$ | 13.2 |
| 4849 | 0.0492 | 0.21277 | 296.45 | 0.10009 | 239.5 | 1.0061 | 0.53 | $8.8 \cdot 10^{15}$ | 13.2 |
| 4980 | 0.0494 | 0.21286 | 295.91 | 0.10139 | 239.9 | 1.0062 | 0.57 | $6.9 \cdot 10^{15}$ | 13.4 |
| 4797 | 0.0493 | 0.21221 | 296.13 | 0.09961 | 239.1 | 1.0061 | 0.52 | $1.2 \cdot 10^{16}$ | 13.4 |
| 5161 | 0.0492 | 0.21217 | 296.38 | 0.10073 | 240.1 | 1.0061 | 0.52 | $1.4 \cdot 10^{16}$ | 13.6 |
| 4799 | 0.0493 | 0.21255 | 294.41 | 0.10197 | 239.2 | 1.0063 | 0.58 | $1.4 \cdot 10^{16}$ | 13.7 |
| 4087 | 0.1486 | 0.21468 | 296.56 | 0.09993 | 240.0 | 1.0082 | 0.53 | $9.1 \cdot 10^{12}$ | 10.7 |
| 4221 | 0.1487 | 0.21480 | 296.59 | 0.09994 | 240.0 | 1.0082 | 0.53 | $2.0 \cdot 10^{13}$ | 11.1 |
| 4618 | 0.1487 | 0.21413 | 294.88 | 0.10370 | 241.3 | 1.0075 | 0.54 | $8.5 \cdot 10^{13}$ | 11.5 |
| 4440 | 0.1621 | 0.21215 | 294.68 | 0.10119 | 240.2 | 1.0077 | 0.62 | $9.0 \cdot 10^{13}$ | 11.6 |
| 4620 | 0.1487 | 0.21418 | 294.75 | 0.10324 | 240.9 | 1.0075 | 0.57 | $2.4 \cdot 10^{14}$ | 11.8 |
| 4406 | 0.1486 | 0.21413 | 296.05 | 0.09988 | 239.7 | 1.0082 | 0.58 | $1.9 \cdot 10^{14}$ | 11.8 |
| 4601 | 0.1484 | 0.21465 | 296.34 | 0.09991 | 239.8 | 1.0082 | 0.52 | $5.9 \cdot 10^{14}$ | 12.3 |
| 4764 | 0.1486 | 0.21433 | 295.98 | 0.10003 | 239.7 | 1.0082 | 0.60 | $2.8 \cdot 10^{15}$ | 12.8 |
| 4443 | 0.1617 | 0.21304 | 294.48 | 0.09929 | 238.5 | 1.0075 | 0.59 | $3.1 \cdot 10^{15}$ | 12.9 |
| 4606 | 0.1606 | 0.21222 | 294.60 | 0.09956 | 239.1 | 1.0075 | 0.59 | $2.7 \cdot 10^{15}$ | 12.9 |
| 5238 | 0.1478 | 0.21295 | 295.57 | 0.10065 | 240.2 | 1.0082 | 0.56 | $1.2 \cdot 10^{16}$ | 13.7 |

[a]Water molar fraction in the mixture.
[b]Nucleation (pulse) quantity.

**TABLE B20.** Water-carbon dioxide-nitrogen experiments at about 0.1 MPa (nucleation pressure) analyzed in Chapter 5: nucleation data, **II part**.

| $y$ (ppm)[a] | $y_{CO_2}$ | $p_0$ (MPa) | $T_0$ (K) | $p$ (MPa)[b] | $T$ (K)[b] | $f_e$[b] | $\Delta t_p$ (ms) | $J$ (m$^{-3}$s$^{-1}$) | $S$ |
|---|---|---|---|---|---|---|---|---|---|
| 4044 | 0.2493 | 0.21562 | 295.78 | 0.09969 | 240.0 | 1.0093 | 0.55 | $5.7 \cdot 10^{12}$ | 10.6 |
| 4139 | 0.2488 | 0.21672 | 296.11 | 0.10025 | 240.3 | 1.0093 | 0.53 | $6.2 \cdot 10^{12}$ | 10.7 |
| 4299 | 0.2494 | 0.21467 | 295.34 | 0.09994 | 240.1 | 1.0093 | 0.53 | $6.2 \cdot 10^{13}$ | 11.2 |
| 4486 | 0.2501 | 0.21786 | 296.27 | 0.10128 | 240.8 | 1.0081 | 0.54 | $4.5 \cdot 10^{13}$ | 11.3 |
| 4608 | 0.2504 | 0.21969 | 296.34 | 0.10130 | 240.3 | 1.0081 | 0.55 | $3.6 \cdot 10^{14}$ | 12.0 |
| 4926 | 0.2513 | 0.21872 | 296.20 | 0.10169 | 240.8 | 1.0081 | 0.58 | $1.1 \cdot 10^{15}$ | 12.5 |
| 4972 | 0.2492 | 0.22020 | 296.61 | 0.10093 | 240.1 | 1.0080 | 0.56 | $7.2 \cdot 10^{15}$ | 13.1 |
| 4950 | 0.2505 | 0.22019 | 296.48 | 0.10083 | 240.0 | 1.0080 | 0.53 | $8.1 \cdot 10^{15}$ | 13.2 |
| 4915 | 0.2518 | 0.22080 | 296.34 | 0.10056 | 239.5 | 1.0080 | 0.53 | $1.3 \cdot 10^{16}$ | 13.5 |
| 3048 | 0.2509 | 0.23380 | 296.32 | 0.10240 | 236.9 | 1.0080 | 0.54 | $3.6 \cdot 10^{12}$ | 11.4 |
| 2920 | 0.2484 | 0.23324 | 295.95 | 0.10123 | 236.0 | 1.0078 | 0.54 | $5.8 \cdot 10^{12}$ | 11.6 |
| 3394 | 0.2497 | 0.23173 | 296.10 | 0.10236 | 237.3 | 1.0080 | 0.55 | $5.0 \cdot 10^{13}$ | 12.4 |
| 3388 | 0.2501 | 0.23231 | 296.19 | 0.10220 | 237.1 | 1.0080 | 0.54 | $5.9 \cdot 10^{13}$ | 12.5 |
| 3285 | 0.2504 | 0.22976 | 295.76 | 0.10026 | 236.2 | 1.0077 | 0.52 | $6.2 \cdot 10^{13}$ | 12.7 |
| 3303 | 0.2490 | 0.23492 | 296.02 | 0.10229 | 236.3 | 1.0079 | 0.60 | $1.6 \cdot 10^{14}$ | 13.0 |
| 3270 | 0.2513 | 0.23126 | 295.01 | 0.10070 | 235.5 | 1.0078 | 0.56 | $5.8 \cdot 10^{14}$ | 13.4 |
| 3290 | 0.2499 | 0.23545 | 295.93 | 0.10169 | 235.7 | 1.0079 | 0.22 | $6.1 \cdot 10^{14}$ | 13.4 |
| 3744 | 0.2482 | 0.23336 | 296.04 | 0.10275 | 237.0 | 1.0080 | 0.53 | $1.5 \cdot 10^{15}$ | 14.0 |
| 3407 | 0.2513 | 0.23479 | 296.27 | 0.10015 | 235.2 | 1.0077 | 0.56 | $3.2 \cdot 10^{15}$ | 14.2 |
| 3818 | 0.2492 | 0.22981 | 296.12 | 0.10024 | 236.5 | 1.0098 | 0.54 | $4.3 \cdot 10^{15}$ | 14.4 |
| 3772 | 0.2480 | 0.23634 | 296.68 | 0.10198 | 236.2 | 1.0079 | 0.56 | $1.1 \cdot 10^{16}$ | 14.8 |
| 3743 | 0.2498 | 0.23436 | 296.38 | 0.10089 | 235.8 | 1.0078 | 0.55 | $1.3 \cdot 10^{16}$ | 15.0 |
| 3824 | 0.2488 | 0.23290 | 296.36 | 0.10058 | 236.0 | 1.0077 | 0.52 | $1.9 \cdot 10^{16}$ | 15.0 |
| 3716 | 0.2517 | 0.23636 | 296.64 | 0.10107 | 235.6 | 1.0078 | 0.57 | $2.8 \cdot 10^{16}$ | 15.1 |
| 2660 | 0.2504 | 0.23488 | 295.85 | 0.10029 | 234.9 | 1.0076 | 0.52 | $3.0 \cdot 10^{12}$ | 12.0 |
| 2658 | 0.2504 | 0.23314 | 295.11 | 0.09880 | 233.8 | 1.0101 | 0.56 | $2.1 \cdot 10^{13}$ | 12.8 |
| 2788 | 0.2479 | 0.23524 | 295.96 | 0.09966 | 234.4 | 1.0100 | 0.52 | $2.6 \cdot 10^{13}$ | 12.9 |
| 2807 | 0.2487 | 0.23562 | 295.85 | 0.09959 | 234.2 | 1.0101 | 0.51 | $4.4 \cdot 10^{13}$ | 13.2 |
| 2915 | 0.2488 | 0.23369 | 295.64 | 0.09937 | 234.4 | 1.0100 | 0.52 | $9.3 \cdot 10^{13}$ | 13.4 |
| 3289 | 0.2499 | 0.23082 | 295.38 | 0.09940 | 235.0 | 1.0100 | 0.55 | $7.2 \cdot 10^{14}$ | 14.5 |
| 3255 | 0.2491 | 0.23676 | 295.98 | 0.10082 | 234.8 | 1.0077 | 0.56 | $1.6 \cdot 10^{15}$ | 14.8 |
| 3265 | 0.2518 | 0.23528 | 296.10 | 0.09906 | 234.2 | 1.0101 | 0.58 | $5.4 \cdot 10^{15}$ | 15.3 |
| 3262 | 0.2486 | 0.24083 | 296.07 | 0.10036 | 233.5 | 1.0103 | 0.56 | $3.2 \cdot 10^{16}$ | 16.3 |

[a]Water molar fraction in the mixture.
[b]Nucleation (pulse) quantity.

**TABLE B21.** Water-carbon dioxide-nitrogen experiments at about 1 MPa (nucleation pressure) analyzed in Chapter 5: mixture preparation data.

| $p_{mpd}$ (MPa) | $T_{mpd}$ (K) | $Q_A$ (ln/min) | $Q_B$ (ln/min) | $Q_C$ (ln/min) | $f_{e,mpd}$ | $y$ (ppm)[a] | $y_{CO_2}$ |
|---|---|---|---|---|---|---|---|
| 2.599 | 291.08 | 1.009 | 0.855 | 0.203 | 1.0931 | 422 | 0.0491 |
| 2.599 | 291.07 | 0.972 | 0.823 | 0.196 | 1.0931 | 422 | 0.0492 |
| 2.599 | 291.03 | 1.123 | 0.744 | 0.203 | 1.0931 | 468 | 0.0491 |
| 2.599 | 291.06 | 1.040 | 0.843 | 0.206 | 1.0931 | 430 | 0.0492 |
| 2.599 | 291.09 | 1.018 | 0.792 | 0.198 | 1.0931 | 439 | 0.0494 |
| 2.599 | 291.08 | 1.015 | 0.860 | 0.204 | 1.0931 | 422 | 0.0491 |
| 2.599 | 291.07 | 1.027 | 0.869 | 0.207 | 1.0931 | 422 | 0.0491 |
| 2.599 | 291.09 | 1.061 | 0.702 | 0.193 | 1.0931 | 469 | 0.0492 |
| 2.599 | 291.09 | 1.061 | 0.793 | 0.202 | 1.0931 | 446 | 0.0491 |
| 2.599 | 291.06 | 1.099 | 0.663 | 0.194 | 1.0931 | 485 | 0.0495 |
| 2.599 | 291.07 | 1.173 | 0.677 | 0.202 | 1.0931 | 494 | 0.0492 |
| 2.599 | 291.09 | 1.114 | 0.736 | 0.202 | 1.0931 | 470 | 0.0492 |
| 2.599 | 291.06 | 1.151 | 0.607 | 0.193 | 1.0931 | 510 | 0.0493 |
| 2.599 | 291.06 | 1.222 | 0.645 | 0.203 | 1.0931 | 510 | 0.0491 |
| 2.599 | 291.08 | 1.247 | 0.659 | 0.208 | 1.0931 | 510 | 0.0492 |
| 2.599 | 291.06 | 0.922 | 0.454 | 0.601 | 1.0931 | 403 | 0.1520 |
| 2.599 | 291.04 | 0.953 | 0.440 | 0.601 | 1.0931 | 412 | 0.1507 |
| 2.599 | 291.06 | 0.928 | 0.457 | 0.601 | 1.0931 | 404 | 0.1513 |
| 2.599 | 291.07 | 1.021 | 0.420 | 0.612 | 1.0931 | 430 | 0.1489 |
| 2.599 | 291.06 | 1.052 | 0.383 | 0.601 | 1.0931 | 446 | 0.1476 |
| 2.599 | 291.07 | 1.034 | 0.426 | 0.607 | 1.0931 | 432 | 0.1468 |
| 2.599 | 291.07 | 1.034 | 0.377 | 0.605 | 1.0931 | 443 | 0.1500 |
| 2.599 | 291.06 | 1.064 | 0.338 | 0.601 | 1.0931 | 459 | 0.1500 |
| 2.599 | 291.06 | 1.058 | 0.311 | 0.601 | 1.0931 | 464 | 0.1525 |
| 2.599 | 291.06 | 1.154 | 0.288 | 0.613 | 1.0931 | 485 | 0.1490 |
| 2.599 | 291.06 | 1.195 | 0.271 | 0.618 | 1.0931 | 495 | 0.1482 |
| 2.599 | 291.05 | 1.160 | 0.256 | 0.601 | 1.0931 | 496 | 0.1489 |
| 2.599 | 291.05 | 1.195 | 0.262 | 0.608 | 1.0931 | 499 | 0.1472 |
| 2.599 | 291.08 | 1.201 | 0.208 | 0.601 | 1.0931 | 517 | 0.1495 |
| 2.599 | 291.07 | 1.244 | 0.239 | 0.627 | 1.0931 | 510 | 0.1485 |
| 2.400 | 294.97 | 0.668 | 0.350 | 1.006 | 1.0829 | 390 | 0.2485 |
| 2.400 | 294.97 | 0.677 | 0.335 | 1.006 | 1.0829 | 396 | 0.2492 |
| 2.400 | 294.96 | 0.686 | 0.324 | 1.012 | 1.0829 | 401 | 0.2501 |
| 2.400 | 294.97 | 0.693 | 0.294 | 1.006 | 1.0829 | 410 | 0.2523 |
| 2.400 | 294.95 | 0.755 | 0.262 | 1.004 | 1.0829 | 441 | 0.2483 |
| 2.400 | 294.96 | 0.714 | 0.322 | 1.009 | 1.0829 | 412 | 0.2465 |
| 2.400 | 294.95 | 0.724 | 0.268 | 1.006 | 1.0829 | 427 | 0.2517 |
| 2.400 | 294.95 | 0.786 | 0.274 | 1.024 | 1.0829 | 445 | 0.2456 |
| 2.299 | 294.94 | 0.770 | 0.268 | 1.012 | 1.0793 | 461 | 0.2467 |
| 2.400 | 294.96 | 0.820 | 0.245 | 1.030 | 1.0829 | 462 | 0.2457 |
| 2.400 | 294.97 | 0.792 | 0.276 | 1.020 | 1.0829 | 448 | 0.2442 |
| 2.400 | 294.95 | 0.795 | 0.220 | 1.006 | 1.0829 | 464 | 0.2488 |
| 2.400 | 294.97 | 0.826 | 0.211 | 1.024 | 1.0829 | 474 | 0.2483 |
| 2.400 | 294.96 | 0.820 | 0.209 | 1.006 | 1.0829 | 476 | 0.2471 |
| 2.400 | 294.95 | 0.832 | 0.212 | 1.010 | 1.0829 | 478 | 0.2457 |

[a]Water molar fraction in the mixture.

**TABLE B22.**  Water-carbon dioxide-nitrogen experiments at about 1 MPa (nucleation pressure) analyzed in Chapter 5: nucleation data.

| $y$ (ppm)[a] | $y_{CO_2}$ | $p_0$ (MPa) | $T_0$ (K) | $p$ (MPa)[b] | $T$ (K)[b] | $f_e$[b] | $\Delta t_p$ (ms) | $J$ (m$^{-3}$s$^{-1}$) | $S$ |
|---|---|---|---|---|---|---|---|---|---|
| 422 | 0.0491 | 2.1315 | 298.17 | 1.0152 | 241.1 | 1.0632 | 0.55 | $1.2 \cdot 10^{13}$ | 9.9 |
| 422 | 0.0492 | 2.1228 | 297.62 | 1.0090 | 240.5 | 1.0630 | 0.56 | $3.9 \cdot 10^{13}$ | 10.2 |
| 468 | 0.0491 | 2.0922 | 297.06 | 1.0110 | 241.2 | 1.0628 | 0.56 | $1.5 \cdot 10^{14}$ | 10.8 |
| 430 | 0.0492 | 2.1421 | 298.51 | 0.9971 | 239.8 | 1.0623 | 0.60 | $1.6 \cdot 10^{14}$ | 10.9 |
| 439 | 0.0494 | 2.1527 | 298.79 | 1.0033 | 240.1 | 1.0627 | 0.55 | $1.9 \cdot 10^{14}$ | 10.9 |
| 422 | 0.0491 | 2.1443 | 297.93 | 1.0014 | 239.5 | 1.0626 | 0.55 | $2.1 \cdot 10^{14}$ | 10.9 |
| 422 | 0.0491 | 2.1244 | 297.25 | 0.9939 | 239.1 | 1.0622 | 0.55 | $3.7 \cdot 10^{14}$ | 11.2 |
| 469 | 0.0492 | 2.1383 | 298.06 | 1.0076 | 240.3 | 1.0629 | 0.58 | $1.8 \cdot 10^{15}$ | 11.6 |
| 446 | 0.0491 | 2.1564 | 298.41 | 0.9993 | 239.4 | 1.0625 | 0.56 | $1.7 \cdot 10^{15}$ | 11.7 |
| 485 | 0.0495 | 2.1365 | 298.35 | 1.0034 | 240.3 | 1.0627 | 0.59 | $2.9 \cdot 10^{15}$ | 11.9 |
| 494 | 0.0492 | 2.1055 | 297.24 | 0.9971 | 240.0 | 1.0622 | 0.56 | $1.2 \cdot 10^{16}$ | 12.3 |
| 470 | 0.0492 | 2.1558 | 297.67 | 1.0068 | 239.3 | 1.0631 | 0.55 | $1.7 \cdot 10^{16}$ | 12.4 |
| 510 | 0.0493 | 2.0988 | 296.89 | 0.9972 | 239.9 | 1.0623 | 0.57 | $3.1 \cdot 10^{16}$ | 12.8 |
| 510 | 0.0491 | 2.0975 | 296.67 | 0.9945 | 239.6 | 1.0621 | 0.55 | $5.4 \cdot 10^{16}$ | 13.1 |
| 510 | 0.0492 | 2.1437 | 298.46 | 0.9930 | 239.4 | 1.0621 | 0.55 | $6.1 \cdot 10^{16}$ | 13.2 |
| 403 | 0.1520 | 2.1398 | 297.20 | 1.0000 | 240.0 | 1.0746 | 0.55 | $2.8 \cdot 10^{13}$ | 9.9 |
| 412 | 0.1507 | 2.1235 | 296.74 | 0.9972 | 240.0 | 1.0740 | 0.58 | $5.4 \cdot 10^{13}$ | 10.2 |
| 404 | 0.1513 | 2.1365 | 296.91 | 0.9939 | 239.5 | 1.0739 | 0.53 | $7.4 \cdot 10^{13}$ | 10.3 |
| 430 | 0.1489 | 2.1465 | 298.28 | 0.9900 | 240.0 | 1.0731 | 0.54 | $1.3 \cdot 10^{14}$ | 10.5 |
| 446 | 0.1476 | 2.1249 | 297.65 | 0.9924 | 240.3 | 1.0730 | 0.55 | $2.7 \cdot 10^{14}$ | 10.7 |
| 432 | 0.1468 | 2.1471 | 298.14 | 0.9883 | 239.7 | 1.0724 | 0.57 | $3.6 \cdot 10^{14}$ | 10.8 |
| 443 | 0.1500 | 2.1389 | 297.94 | 0.9878 | 239.8 | 1.0732 | 0.55 | $6.4 \cdot 10^{14}$ | 11.0 |
| 459 | 0.1500 | 2.1638 | 298.12 | 0.9991 | 240.0 | 1.0743 | 0.53 | $2.1 \cdot 10^{15}$ | 11.4 |
| 464 | 0.1525 | 2.1420 | 297.56 | 0.9943 | 239.9 | 1.0742 | 0.55 | $2.3 \cdot 10^{15}$ | 11.5 |
| 485 | 0.1490 | 2.1550 | 297.88 | 1.0040 | 240.4 | 1.0745 | 0.55 | $4.5 \cdot 10^{15}$ | 11.7 |
| 495 | 0.1482 | 2.1477 | 297.90 | 1.0031 | 240.5 | 1.0742 | 0.59 | $4.9 \cdot 10^{15}$ | 11.8 |
| 496 | 0.1489 | 2.1518 | 297.61 | 0.9993 | 239.9 | 1.0740 | 0.57 | $2.0 \cdot 10^{16}$ | 12.3 |
| 499 | 0.1472 | 2.1452 | 297.67 | 0.9957 | 239.9 | 1.0733 | 0.55 | $2.5 \cdot 10^{16}$ | 12.4 |
| 517 | 0.1495 | 2.1630 | 298.55 | 1.0001 | 240.4 | 1.0743 | 0.57 | $2.2 \cdot 10^{16}$ | 12.4 |
| 510 | 0.1485 | 2.1563 | 298.23 | 0.9949 | 240.0 | 1.0735 | 0.57 | $3.8 \cdot 10^{16}$ | 12.6 |
| 390 | 0.2485 | 2.2083 | 297.77 | 1.0072 | 239.8 | 1.0916 | 0.57 | $3.7 \cdot 10^{13}$ | 9.7 |
| 396 | 0.2492 | 2.2335 | 298.18 | 1.0109 | 239.7 | 1.0923 | 0.54 | $9.2 \cdot 10^{13}$ | 10.0 |
| 401 | 0.2501 | 2.2015 | 297.51 | 1.0045 | 239.7 | 1.0917 | 0.58 | $1.4 \cdot 10^{14}$ | 10.0 |
| 410 | 0.2523 | 2.2229 | 297.98 | 1.0094 | 239.7 | 1.0929 | 0.57 | $3.0 \cdot 10^{14}$ | 10.3 |
| 441 | 0.2483 | 2.1687 | 297.19 | 1.0037 | 240.3 | 1.0911 | 0.55 | $4.5 \cdot 10^{14}$ | 10.5 |
| 412 | 0.2465 | 2.1996 | 297.30 | 1.0022 | 239.4 | 1.0907 | 0.57 | $5.2 \cdot 10^{14}$ | 10.5 |
| 427 | 0.2517 | 2.1893 | 296.69 | 1.0088 | 239.7 | 1.0927 | 0.56 | $1.0 \cdot 10^{15}$ | 10.7 |
| 445 | 0.2456 | 2.1916 | 297.14 | 1.0070 | 239.8 | 1.0910 | 0.55 | $2.9 \cdot 10^{15}$ | 11.1 |
| 461 | 0.2467 | 2.1613 | 296.90 | 0.9961 | 239.8 | 1.0899 | 0.54 | $6.0 \cdot 10^{15}$ | 11.3 |
| 462 | 0.2457 | 2.1889 | 297.38 | 1.0048 | 239.9 | 1.0907 | 0.57 | $4.8 \cdot 10^{15}$ | 11.4 |
| 448 | 0.2442 | 2.2430 | 298.32 | 1.0044 | 239.0 | 1.0905 | 0.56 | $1.5 \cdot 10^{16}$ | 11.8 |
| 464 | 0.2488 | 2.1971 | 296.93 | 1.0072 | 239.5 | 1.0918 | 0.55 | $1.5 \cdot 10^{16}$ | 11.8 |
| 474 | 0.2483 | 2.2089 | 297.90 | 1.0037 | 239.7 | 1.0913 | 0.56 | $2.1 \cdot 10^{16}$ | 11.8 |
| 476 | 0.2471 | 2.2073 | 297.61 | 1.0022 | 239.4 | 1.0909 | 0.56 | $4.2 \cdot 10^{16}$ | 12.1 |
| 478 | 0.2457 | 2.2023 | 297.34 | 1.0036 | 239.4 | 1.0907 | 0.57 | $4.8 \cdot 10^{16}$ | 12.2 |

[a]Water molar fraction in the mixture.
[b]Nucleation (pulse) quantity.

**TABLE B23.**   Water-carbon dioxide-nitrogen experiments at about 2 MPa (nucleation pressure) analyzed in Chapter 5: mixture preparation data.

| $p_{mpd}$ (MPa) | $T_{mpd}$ (K) | $Q_A$ (ln/min) | $Q_B$ (ln/min) | $Q_C$ (ln/min) | $f_{e,mpd}$ | $y$ (ppm)[a] | $y_{CO_2}$ |
|---|---|---|---|---|---|---|---|
| 5.001 | 291.07 | 0.879 | 0.961 | 0.200 | 1.1866 | 210 | 0.0490 |
| 5.001 | 291.06 | 0.903 | 0.944 | 0.200 | 1.1866 | 215 | 0.0488 |
| 5.001 | 291.07 | 0.879 | 0.957 | 0.200 | 1.1866 | 210 | 0.0490 |
| 5.001 | 291.11 | 0.959 | 0.860 | 0.198 | 1.1865 | 232 | 0.0492 |
| 5.001 | 291.08 | 0.931 | 0.891 | 0.200 | 1.1866 | 225 | 0.0494 |
| 5.001 | 291.08 | 0.968 | 0.866 | 0.200 | 1.1866 | 232 | 0.0491 |
| 5.001 | 291.07 | 1.009 | 0.827 | 0.200 | 1.1866 | 242 | 0.0490 |
| 5.001 | 291.08 | 1.049 | 0.806 | 0.200 | 1.1866 | 249 | 0.0486 |
| 5.001 | 291.09 | 1.046 | 0.767 | 0.200 | 1.1866 | 254 | 0.0496 |
| 5.001 | 291.07 | 1.071 | 0.741 | 0.200 | 1.1866 | 260 | 0.0496 |
| 5.001 | 291.07 | 1.111 | 0.717 | 0.200 | 1.1866 | 267 | 0.0492 |
| 5.001 | 291.07 | 1.136 | 0.710 | 0.200 | 1.1866 | 271 | 0.0488 |
| 4.501 | 291.05 | 0.773 | 0.652 | 0.601 | 1.1664 | 203 | 0.1483 |
| 4.501 | 294.96 | 0.631 | 0.823 | 0.612 | 1.1605 | 206 | 0.1481 |
| 4.501 | 294.94 | 0.637 | 0.795 | 0.604 | 1.1605 | 211 | 0.1483 |
| 4.501 | 291.06 | 0.789 | 0.618 | 0.601 | 1.1664 | 209 | 0.1497 |
| 4.501 | 291.06 | 0.832 | 0.607 | 0.601 | 1.1664 | 217 | 0.1473 |
| 4.501 | 294.97 | 0.668 | 0.799 | 0.621 | 1.1605 | 216 | 0.1487 |
| 4.501 | 291.06 | 0.860 | 0.575 | 0.601 | 1.1664 | 225 | 0.1476 |
| 4.501 | 291.05 | 0.879 | 0.564 | 0.601 | 1.1664 | 229 | 0.1471 |
| 4.501 | 291.07 | 0.891 | 0.514 | 0.601 | 1.1664 | 236 | 0.1498 |
| 4.501 | 291.06 | 0.922 | 0.533 | 0.601 | 1.1664 | 239 | 0.1462 |
| 4.501 | 291.06 | 0.972 | 0.491 | 0.601 | 1.1664 | 251 | 0.1456 |
| 4.501 | 291.05 | 0.975 | 0.493 | 0.601 | 1.1664 | 251 | 0.1453 |
| 4.501 | 291.05 | 0.981 | 0.456 | 0.601 | 1.1664 | 256 | 0.1475 |
| 4.501 | 294.96 | 0.764 | 0.652 | 0.604 | 1.1605 | 255 | 0.1494 |
| 4.501 | 294.97 | 0.773 | 0.648 | 0.607 | 1.1605 | 257 | 0.1496 |
| 4.501 | 291.06 | 0.972 | 0.408 | 0.601 | 1.1664 | 261 | 0.1518 |
| 4.501 | 291.06 | 0.981 | 0.440 | 0.601 | 1.1664 | 258 | 0.1486 |
| 4.299 | 291.05 | 0.730 | 0.339 | 1.012 | 1.1584 | 194 | 0.2431 |
| 4.501 | 291.06 | 0.767 | 0.248 | 1.005 | 1.1664 | 202 | 0.2487 |
| 4.501 | 291.07 | 0.786 | 0.240 | 1.005 | 1.1664 | 206 | 0.2474 |
| 4.299 | 291.05 | 0.752 | 0.304 | 1.008 | 1.1584 | 201 | 0.2442 |
| 4.501 | 291.06 | 0.817 | 0.222 | 1.004 | 1.1664 | 213 | 0.2458 |
| 4.501 | 291.06 | 0.804 | 0.259 | 1.005 | 1.1664 | 207 | 0.2430 |
| 4.299 | 291.06 | 0.789 | 0.234 | 1.012 | 1.1584 | 215 | 0.2486 |
| 4.501 | 291.06 | 0.841 | 0.195 | 1.004 | 1.1664 | 219 | 0.2459 |
| 4.501 | 291.05 | 0.891 | 0.122 | 1.006 | 1.1664 | 235 | 0.2491 |
| 4.501 | 294.98 | 0.730 | 0.291 | 1.018 | 1.1605 | 242 | 0.2496 |
| 4.501 | 291.05 | 0.888 | 0.158 | 1.005 | 1.1664 | 230 | 0.2450 |
| 4.501 | 291.05 | 0.922 | 0.099 | 1.006 | 1.1664 | 242 | 0.2481 |
| 4.501 | 291.05 | 0.941 | 0.073 | 1.008 | 1.1664 | 248 | 0.2492 |

[a]Water molar fraction in the mixture.

**TABLE B24.** Water-carbon dioxide-nitrogen experiments at about 2 MPa (nucleation pressure) analyzed in Chapter 5: nucleation data.

| $y$ (ppm)[a] | $y_{CO_2}$ | $p_0$ (MPa) | $T_0$ (K) | $p$ (MPa)[b] | $T$ (K)[b] | $f_e$[b] | $\Delta t_p$ (ms) | $J$ (m$^{-3}$s$^{-1}$) | $S$ |
|---|---|---|---|---|---|---|---|---|---|
| 210 | 0.0490 | 4.1858 | 297.54 | 1.9942 | 240.0 | 1.1298 | 0.55 | $6.6 \cdot 10^{13}$ | 9.8 |
| 215 | 0.0488 | 4.1612 | 296.73 | 2.0034 | 240.1 | 1.1304 | 0.56 | $1.9 \cdot 10^{14}$ | 10.0 |
| 210 | 0.0490 | 4.1876 | 297.03 | 1.9911 | 239.5 | 1.1300 | 0.58 | $1.7 \cdot 10^{14}$ | 10.2 |
| 232 | 0.0492 | 4.2221 | 298.73 | 1.9966 | 240.5 | 1.1298 | 0.52 | $6.1 \cdot 10^{14}$ | 10.5 |
| 225 | 0.0494 | 4.2168 | 298.09 | 1.9912 | 239.9 | 1.1299 | 0.56 | $6.4 \cdot 10^{14}$ | 10.6 |
| 232 | 0.0491 | 4.2036 | 297.79 | 1.9925 | 239.9 | 1.1299 | 0.55 | $2.1 \cdot 10^{15}$ | 11.0 |
| 242 | 0.0490 | 4.1803 | 297.24 | 1.9966 | 240.0 | 1.1301 | 0.57 | $4.9 \cdot 10^{15}$ | 11.4 |
| 249 | 0.0486 | 4.2001 | 297.57 | 2.0045 | 240.2 | 1.1303 | 0.55 | $1.5 \cdot 10^{16}$ | 11.6 |
| 254 | 0.0496 | 4.2275 | 298.07 | 1.9916 | 239.7 | 1.1302 | 0.55 | $3.9 \cdot 10^{16}$ | 12.1 |
| 260 | 0.0496 | 4.1811 | 297.22 | 1.9962 | 239.9 | 1.1304 | 0.56 | $5.1 \cdot 10^{16}$ | 12.2 |
| 267 | 0.0492 | 4.1903 | 297.64 | 1.9952 | 240.1 | 1.1300 | 0.56 | $9.9 \cdot 10^{16}$ | 12.4 |
| 271 | 0.0488 | 4.1713 | 297.12 | 1.9959 | 240.0 | 1.1299 | 0.55 | $1.3 \cdot 10^{17}$ | 12.7 |
| 203 | 0.1483 | 4.1410 | 295.16 | 2.0036 | 240.1 | 1.1679 | 0.54 | $8.1 \cdot 10^{13}$ | 9.2 |
| 206 | 0.1481 | 4.2269 | 297.12 | 2.0013 | 240.2 | 1.1674 | 0.55 | $1.5 \cdot 10^{14}$ | 9.3 |
| 211 | 0.1483 | 4.2253 | 296.64 | 2.0197 | 240.4 | 1.1691 | 0.57 | $1.4 \cdot 10^{14}$ | 9.4 |
| 209 | 0.1497 | 4.1840 | 296.04 | 2.0031 | 240.1 | 1.1686 | 0.55 | $1.9 \cdot 10^{14}$ | 9.5 |
| 217 | 0.1473 | 4.2216 | 297.79 | 1.9802 | 240.1 | 1.1652 | 0.54 | $6.7 \cdot 10^{14}$ | 9.7 |
| 216 | 0.1487 | 4.2865 | 298.03 | 2.0044 | 240.1 | 1.1682 | 0.56 | $8.4 \cdot 10^{14}$ | 9.8 |
| 225 | 0.1476 | 4.1846 | 296.79 | 1.9897 | 240.2 | 1.1662 | 0.57 | $1.3 \cdot 10^{15}$ | 10.0 |
| 229 | 0.1471 | 4.2113 | 296.48 | 2.0039 | 240.0 | 1.1678 | 0.54 | $2.8 \cdot 10^{15}$ | 10.4 |
| 236 | 0.1498 | 4.2390 | 297.42 | 1.9953 | 240.0 | 1.1678 | 0.57 | $8.9 \cdot 10^{15}$ | 10.7 |
| 239 | 0.1462 | 4.2177 | 297.05 | 1.9912 | 239.9 | 1.1660 | 0.55 | $7.7 \cdot 10^{15}$ | 10.9 |
| 251 | 0.1456 | 4.2199 | 297.22 | 1.9957 | 240.2 | 1.1659 | 0.55 | $3.1 \cdot 10^{16}$ | 11.3 |
| 251 | 0.1453 | 4.2020 | 296.42 | 2.0060 | 240.1 | 1.1668 | 0.58 | $2.4 \cdot 10^{16}$ | 11.3 |
| 256 | 0.1475 | 4.1912 | 296.31 | 2.0068 | 240.3 | 1.1675 | 0.54 | $2.8 \cdot 10^{16}$ | 11.5 |
| 255 | 0.1494 | 4.2536 | 297.52 | 1.9991 | 240.0 | 1.1681 | 0.56 | $6.6 \cdot 10^{16}$ | 11.6 |
| 257 | 0.1496 | 4.2751 | 297.90 | 2.0022 | 240.1 | 1.1685 | 0.56 | $7.1 \cdot 10^{16}$ | 11.6 |
| 261 | 0.1518 | 4.2260 | 296.95 | 2.0029 | 240.1 | 1.1695 | 0.56 | $8.5 \cdot 10^{16}$ | 11.8 |
| 258 | 0.1486 | 4.2209 | 296.61 | 1.9998 | 239.8 | 1.1680 | 0.55 | $1.0 \cdot 10^{17}$ | 11.9 |
| 194 | 0.2431 | 4.2791 | 296.52 | 2.0015 | 239.7 | 1.2130 | 0.56 | $1.9 \cdot 10^{14}$ | 8.7 |
| 202 | 0.2487 | 4.2862 | 296.97 | 2.0044 | 240.1 | 1.2152 | 0.56 | $3.7 \cdot 10^{14}$ | 8.8 |
| 206 | 0.2474 | 4.3149 | 297.35 | 2.0132 | 240.3 | 1.2154 | 0.55 | $3.0 \cdot 10^{14}$ | 8.9 |
| 201 | 0.2442 | 4.2736 | 296.20 | 2.0052 | 239.7 | 1.2142 | 0.55 | $5.4 \cdot 10^{14}$ | 9.1 |
| 213 | 0.2458 | 4.2310 | 296.11 | 1.9963 | 240.0 | 1.2129 | 0.56 | $1.0 \cdot 10^{15}$ | 9.3 |
| 207 | 0.2430 | 4.2803 | 296.57 | 1.9936 | 239.5 | 1.2127 | 0.57 | $1.1 \cdot 10^{15}$ | 9.4 |
| 215 | 0.2486 | 4.2985 | 296.83 | 2.0015 | 239.7 | 1.2158 | 0.54 | $2.4 \cdot 10^{15}$ | 9.6 |
| 219 | 0.2459 | 4.2851 | 296.85 | 1.9910 | 239.6 | 1.2134 | 0.55 | $6.3 \cdot 10^{15}$ | 9.9 |
| 235 | 0.2491 | 4.2670 | 296.58 | 2.0007 | 240.0 | 1.2152 | 0.55 | $2.4 \cdot 10^{16}$ | 10.3 |
| 242 | 0.2496 | 4.3705 | 298.36 | 2.0044 | 239.9 | 1.2160 | 0.55 | $5.6 \cdot 10^{16}$ | 10.6 |
| 230 | 0.2450 | 4.2931 | 296.30 | 1.9985 | 239.2 | 1.2149 | 0.54 | $3.7 \cdot 10^{16}$ | 10.7 |
| 242 | 0.2481 | 4.2903 | 296.82 | 1.9994 | 239.8 | 1.2150 | 0.55 | $5.2 \cdot 10^{16}$ | 10.8 |
| 248 | 0.2492 | 4.2974 | 297.00 | 1.9934 | 239.6 | 1.2152 | 0.52 | $1.1 \cdot 10^{17}$ | 11.1 |

[a]Water molar fraction in the mixture.
[b]Nucleation (pulse) quantity.

# Appendix C

# Chemical potentials and partial derivatives

In this section, more details will be given on the partial derivatives of the chemical potentials in Eqs. 6.3-6.5. To this end, each of the chemical potentials $(\mu_1^g, \mu_2^g, \mu_3^g, .., \mu_N^g)$ needs to be expressed as a function of $(S, p, y_2, .., y_{N-1})$.[a]

We start with the partial derivative of the chemical potentials $(\mu_1^g, \mu_2^g, \mu_3^g, .., \mu_N^g)$ to the logarithm of $S$ at constant $(p, y_2, .., y_{N-1})$ in Eq. 6.3. From the definition of supersaturation $S = \mathscr{F}_1^g / \mathscr{F}_{1,\mathrm{eq}}$ (see Eq. 2.15),

$$\mu_1^g = \mu_{1,\mathrm{eq}} + kT \ln S$$

$$= \mu_{1,\mathrm{s}} + kT \ln x_{1,\mathrm{eq}} + \int_{p_{1,\mathrm{s}}}^{p} v_1^\ell \, dp + kT \ln S, \tag{C.1}$$

with $\mu_{1,\mathrm{eq}}$ the chemical potential of the condensing component "1" with its gaseous and liquid phase at equilibrium, $x_{1,\mathrm{eq}}$ the liquid fraction of "1" at equilibrium, $(\int_{p_{1,\mathrm{s}}}^{p} v_1^\ell \, dp)$ the Poynting contribution and with $\mu_{1,\mathrm{s}}$ and $p_{1,\mathrm{s}}$ the chemical potential and the pressure of the pure component "1" at saturation (see Sec. 2.1). It follows that

$$\left. \frac{\partial \mu_1^g}{\partial \ln S} \right|_{p,y_2,..,y_{N-1}} = kT. \tag{C.2}$$

In addition, for $y_1 \ll (y_2, y_3, .., y_N)$, it can be safely assumed that $(\mu_2^g, \mu_3^g, .., \mu_N^g)$ are not influenced by the variations of $S$ due to the variation of $y_1$ at constant $T$ and $(p, y_2, .., y_{N-1})$. Hence,

$$\left. \frac{\partial \mu_i^g}{\partial \ln S} \right|_{p,y_2,..,y_{N-1}} = 0 \quad \text{for } i = 2,3,..,N. \tag{C.3}$$

Finally, Eq. 6.3 simplifies as follows

$$\left. \frac{\partial \ln J}{\partial \ln S} \right|_{p,y_2,..,y_{N-1}} = \Delta n_1^* + 1, \tag{C.4}$$

which enables a straightforward calculation of $\Delta n_1^*$ from the experimental $J$-$S$ curves at constant $T$ and $(p, y_2, .., y_{N-1})$.

---

[a] Note that the temperature $T$ is not included, being $T = const$ for the present analysis.

The partial derivative of $\mu_1^g$ with respect to $p$ in Eq. 6.4 and with respect to $\partial y_q$ in Eq. 6.5 can be obtained from Eq. C.1 as

$$\left.\frac{\partial \mu_1^g}{\partial p}\right|_{S,y_2,..,y_{N-1}} = v_1^\ell + \frac{kT}{x_{1,eq}}\left.\frac{\partial x_{1,eq}}{\partial p}\right|_{S,y_2,..,y_{N-1}} \tag{C.5}$$

and

$$\left.\frac{\partial \mu_1^g}{\partial y_q}\right|_{S,p,y_{j\neq\{1,q,N\}}} = \frac{kT}{x_{1,eq}}\left.\frac{\partial x_{1,eq}}{\partial y_q}\right|_{p,y_{j\neq\{1,q,N\}}}. \tag{C.6}$$

The partial derivative of the chemical potentials ($\mu_1^g$, $\mu_2^g$, $\mu_3^g$, .., $\mu_N^g$) to the pressure $p$ at constant ($S$, $y_2$, .., $y_{N-1}$) in Eq. 6.4 can be obtained as follows. We now introduce the correlation between chemical potential $\mu_i^g$ and fugacity $\mathscr{F}_i^g$ for the generic $i^{th}$ component in its gaseous phase

$$\mu_i^g = \mu_{i,ref}(p_{ref},T) + kT\ln\left[\frac{\mathscr{F}_i^g}{\mathscr{F}_{i,ref}(p_{ref},T)}\right], \tag{C.7}$$

where $\mu_{i,ref}$ and $\mathscr{F}_{i,ref}$ are the chemical potential and the fugacity of the pure component $i$ at the temperature $T$ and an arbitrary reference pressure $p_{ref}$. Thus, at constant temperature $T$

$$\left.\frac{\partial \mu_i^g}{\partial p}\right|_{S,y_2,..,y_{N-1}} = \frac{kT}{\mathscr{F}_i^g}\left.\frac{\partial \mathscr{F}_i^g}{\partial p}\right|_{y_2,..,y_{N-1}} \tag{C.8}$$

and

$$\left.\frac{\partial \mu_i^g}{\partial y_q}\right|_{S,p,y_{j\neq\{1,q,N\}}} = \frac{kT}{\mathscr{F}_i^g}\left.\frac{\partial \mathscr{F}_i^g}{\partial y_q}\right|_{p,y_{j\neq\{1,q,N\}}}, \tag{C.9}$$

with

$$\mathscr{F}_i^g = \phi_i y_i p. \tag{C.10}$$

The parameter $\phi_i$ in Eq. C.10 denotes the fugacity coefficient, which can be defined by means of the virial EOS as

$$\ln\phi_i = \left[2\sum_{j=1}^{N} B_{ij}y_j - B\right]\frac{p}{RT}, \tag{C.11}$$

where $B$ is the second virial coefficient of the mixture, defined as

$$B = \sum_{i=1}^{N}\sum_{j=1}^{N} y_i y_j B_{ij}. \tag{C.12}$$

In Eqs. C.11 and C.12, $B_{ii}$ denotes the second virial coefficient of the pure $i^{th}$ component and $B_{ij\neq i}$ stands for the second cross-virial coefficient of the $i$-th and $j$-th interacting components (see Chapter 2.1.1).

# Nomenclature

## Roman

| | | |
|---|---|---|
| $a$ | - | coefficient of the diaphragm opening function in the 2D model |
| $a_i$ | - | computational quantum chemistry (empirical) coefficient of $B_{ij \neq i}$ |
| $A$ | $m^2$ | open diaphragm surface area at the time $t$ in the 2D model |
| $A_{<1>}$ | $m^2$ | monomer surface area |
| $A_{diaph}$ | $m^2$ | total diaphragm surface area |
| $A_{<n>}$ | $m^2$ | surface area of a cluster with $n$ molecules ($n$-mer) |
| $A_g$ | $m^2$ | average surface area per adsorption site |
| $b_i$ | - | computational quantum chemistry (empirical) coefficient of $B_{ij \neq i}$ |
| $B$ | $m^{-3} \, mol^{-1}$ | second virial coefficient of a mixture |
| $B_{ij \neq i}$ | $m^{-3} \, mol^{-1}$ | second cross virial coefficient for a system of two $i$ and $j \neq i$ interacting components |
| $B_{ii}$ | $m^{-3} \, mol^{-1}$ | second virial coefficient of a pure component $i$ |
| $C$ | $m^{-3} \, s^{-1}$ | coefficient of $J_{exp}$ |
| $\mathbb{C}$ | | number of possible configurations for the adsorbed layer |
| $C_0$ | $m^{-3} \, s^{-1}$ | non-dimensional coefficient of the Hale scaling model[86] |
| $c_1$ | $J \, K^{-1}$ | isochoric heat capacity per molecule in the liquid |
| $c_1$ | $K^{-2}$ | coefficient of $J_{emp}$ |
| $c_2$ | $K^{-1}$ | coefficient of $J_{exp}$ |
| $c_{bg}$ | $J \, K^{-1}$ | enhanced heat capacity of the (carrier) gas at constant volume |
| $\hat{c}_{bv}$ | - | non dimensional $c_{bv}$ |
| $c_{bv}$ | $J \, K^{-1}$ | enhanced $c_v$ (increased collision rate of the high energy monomers) |
| $c_g$ | $J \, K^{-1}$ | isochoric heat capacity of the (carrier) gas |
| $c_p$ | $J \, K^{-1}$ | isobaric vapor monomer heat capacity |
| $c_v$ | $J \, K^{-1}$ | isochoric vapor monomer heat capacity |
| $d$ | m | open diaphragm dimension at the time $t$ in the 2D model |
| $d_1$ | - | coefficient of $J_{emp}$ |
| $d_2$ | $MPa^{-1}$ | coefficient of $J_{exp}$ |
| $d_3$ | $MPa^{-1/2}$ | coefficient of $J_{exp}$ |
| $D$ | - | coefficient of $J_{exp}$ |
| $d_{diaph}$ | m | total diaphragm dimension |
| $D$ | $m^2 \, s^{-1}$ | diffusion coefficient |
| $\mathscr{F}$ | Pa | fugacity |
| $f_e$ | - | enhancement factor |
| $F^A$ | J | Helmholtz free energy of the adsorbates |
| $f_{e,mpd}$ | - | enhancement factor at the MPD conditions |

| | | |
|---|---|---|
| $g$ | m s$^{-2}$ | gravitation acceleration |
| $G$ | J | Gibbs free energy |
| $h$ | m | height |
| $H$ | - | dimensionless parameter in non-isothermal nucleation |
| $I$ | J m$^{-2}$ s$^{-1}$ | transmitted irradiance |
| $I_0$ | J m$^{-2}$ s$^{-1}$ | transmitted irradiance before expansion |
| $I_{\mathrm{sca}}$ | J m$^{-2}$ s$^{-1}$ | scattered irradiance |
| $I_{\mathrm{sca,Th}}$ | J m$^{-2}$ s$^{-1}$ | scattered irradiance from Mie theory |
| $J$ | m$^{-3}$ s$^{-1}$ | nucleation rate |
| $J_{\mathrm{emp}}$ | m$^{-3}$ s$^{-1}$ | nucleation rate calculated from the empirical expression |
| $J_{\mathrm{exp}}$ | m$^{-3}$ s$^{-1}$ | nucleation rate calculated from experimental $J$-$S$ data fitting |
| $J_{\mathrm{iso}}$ | m$^{-3}$ s$^{-1}$ | isothermal nucleation rate |
| $J_{<n>}$ | m$^{-3}$ s$^{-1}$ | net transition rate between clusters of size n and size (n $+$ 1) |
| $J_{\mathrm{CNT}}$ | m$^{-3}$ s$^{-1}$ | nucleation rate predicted by CNT |
| $k$ | J K$^{-1}$ | Boltzmann constant |
| $K$ | m$^{-3}$ s$^{-1}$ | pre-exponential factor |
| $l$ | m | extinction length |
| $l_n$ | normal liters | volume |
| $L$ | J kg$^{-1}$ | latent heat of evaporation |
| $m$ | kg | mass |
| $m$ | - | refractive index |
| $M$ | kg mol$^{-1}$ | molar mass |
| $n$ | - | number of cluster molecules |
| $n^*$ | - | critical cluster size |
| $n_0$ | - | total number of molecules at the initial gaseous state |
| $n_{\mathrm{d}}$ | m$^{-3}$ | number density of droplets |
| $n^{\mathrm{g}}$ | - | number of vapor monomers (gaseous phase) |
| $n_{\mathrm{GT}}^*$ | - | critical cluster size according to the Gibbs-Thomson equation (CNT) |
| $n^{\ell}$ | - | number of molecules in the cluster core (liquid phase) |
| $n^{\mathrm{s}}$ | - | number of molecules at the cluster surface |
| $N$ | - | number of mixture components |
| $N_{\mathrm{A}}$ | mol$^{-1}$ | Avogadro's number |
| $N_{\mathrm{g,i}}^{\mathrm{A}}$ | | number of sites occupied by the adsorbed molecules of the $i$-th carrier gas |
| $p$ | Pa | pressure |
| $p^{\mathrm{g}}$ | Pa | partial pressure of the gaseous phase |
| $\mathbb{P}_{\mathrm{j}}$ | - | probability of the $j$-th configuration |
| $p_{\mathrm{L}}$ | Pa | Langmuir pressure |
| $p^{\ell}$ | Pa | partial pressure of the liquid phase |
| $p_{\mathrm{L}}$ | Pa | Langmuir pressure |
| $p_{\mathrm{mpd}}$ | Pa | pressure condition at the MPD |
| $p_{\mathrm{s}}$ | Pa | saturated vapor pressure |
| $p_{\mathrm{v}}$ | Pa | partial vapor (condensing component) pressure |
| $Q$ | $l_n$ min$^{-1}$ | flow rate |
| $Q'$ | $l_n$ min$^{-1}$ | flow rate at the exit of sat$_{\mathrm{a}}$ and sat$_{\mathrm{b}}$ |
| $Q_{\mathrm{A}}$ | $l_n$ min$^{-1}$ | flow rate to sat$_{\mathrm{a}}$ and sat$_{\mathrm{b}}$ |

| | | |
|---|---|---|
| $Q_B$ | $l_n \, min^{-1}$ | dilution flow rate |
| $Q_C$ | $l_n \, min^{-1}$ | dilution flow rate of $CO_2$ |
| $Q_{H_2O}$ | $l_n \, min^{-1}$ | water flow rate |
| $Q_{ext}$ | - | extinction efficiency |
| $Q_{tot}$ | $l_n \, min^{-1}$ | total flow rate at the exit of the MPD |
| $r$ | m | droplet radius |
| $r_{<1>}$ | m | monomer radius |
| $r_{<n>}$ | m | radius of cluster with $n$ molecules ($n$-mers) |
| $R$ | $J \, mol^{-1} \, K^{-1}$ | universal gas constant |
| $S$ | - | supersaturation |
| $S'$ | - | supersaturation according to Wedekind *et al.*[113] |
| $\mathbb{S}$ | $J \, K^{-1}$ | entropy |
| $\mathbb{S}_0$ | $J \, K^{-1}$ | entropy of the system at the initial (gaseous) state |
| $\mathbb{S}^A$ | $J \, K^{-1}$ | entropy of the adsorbates |
| $\mathbb{S}^g$ | $J \, K^{-1}$ | entropy of vapor monomers (gaseous phase) |
| $s_{g,i}^{int}$ | $J \, K^{-1}$ | internal molecular entropy of a gas molecule ($i^{th}$ carrier gas) |
| $\mathbb{S}^\ell$ | $J \, K^{-1}$ | entropy of cluster core (liquid phase) |
| $\mathbb{S}^s$ | $J \, K^{-1}$ | entropy of cluster surface |
| $\mathbb{S}_c$ | $J \, K^{-1}$ | configurational entropy on a per molecule basis |
| $t$ | s | time |
| $t_{diaph}$ | s | total opening time of the diaphragm |
| $T$ | K | temperature |
| $T_0$ | K | temperature HPS wall temperature |
| $T_c$ | K | critical temperature of water |
| $T_{hb}$ | K | temperature at the heated box |
| $T_{mpd}$ | K | temperature at the MPD |
| $T_{sc}$ | K | target scaling temperature in the Hale model[86] |
| $u$ | - | extended uncertainty with 95% confidence interval |
| $u$ | $m \, s^{-1}$ | velocity component in the axial direction |
| $u_{g,i}^A$ | J | potential energy of the interaction between the adsorbed gas molecules ($i^{th}$ carrier gas) and the liquid surface |
| $u_{g,i}^{int}$ | J | internal molecular energy of a gas molecule ($i^{th}$ carrier gas) |
| $U$ | - | standard uncertainty |
| $U$ | J | internal energy |
| $\mathbb{U}$ | | vector of unknowns |
| $U^A$ | J | internal energy of the adsorbates |
| $U_0$ | J | internal energy of the system at the initial (gaseous) state |
| $U^g$ | J | internal energy of vapor monomers (gaseous phase) |
| $U^\ell$ | J | internal energy of cluster core (liquid phase) |
| $U^s$ | J | internal energy of cluster surface |
| $v$ | $m^3$ | molecular volume |
| $v$ | $m \, s^{-1}$ | velocity component in the radial direction |
| $v^A$ | $m^3$ | effective volume available for the translation of an adsorbed molecule |
| $v^G$ | $m^3$ | molecular volume of the carrier gas ( free molecules) |
| $v^\ell$ | $m^3$ | molecular liquid volume |

| | | |
|---|---|---|
| $v_\ell$ | $m^3$ | molecular bulk liquid volume |
| $v_1^\ell$ | $m^3$ | molecular liquid volume of component '1' |
| $v_{<n>}$ | $m^3$ | volume of clusters with $n$ molecules |
| $V$ | $m^3\,mol^{-1}$ | molar volume |
| $V_0$ | $m^3$ | volume occupied at the initial (gaseous) state |
| $V^g$ | $m^3$ | volume occupied by the vapor monomers (gaseous phase) |
| $V^\ell$ | $m^3$ | total volume occupied by the liquid phase (cluster) |
| $V^{ref}$ | $m^3$ | reference volume |
| $W$ | J | work of cluster formation |
| $x$ | - | liquid molar fraction |
| $x$ | m | axial coordinate |
| $X$ | - | non-dimensional parameter in non-isothermal nucleation |
| $\mathbf{X}$ | | convective flux in x direction |
| $x_g$ | - | carrier gas solubility in the liquid phase |
| $y$ | m | radial coordinate |
| $y$ | - | gaseous molar fraction |
| $y_1$ | - | gaseous molar fraction of the condensing component '1' |
| $y'_{eq}$ | - | equilibrium molar fraction at the MPD conditions |
| $\mathbf{Y}$ | | convective flux in y direction |
| $Z$ | - | compressibility factor |
| $\mathscr{Z}$ | - | Zeldovich factor |

# Greek

| | | |
|---|---|---|
| $\alpha$ | - | non-dimensional droplet radius |
| $\beta$ | $m^{-1}$ | extinction coefficient |
| $\beta_{<n>}$ | $s^{-1}$ | condensation rate of $n$-mers |
| $\gamma_{<n>}$ | $s^{-1}$ | evaporation rate of $n$-mers |
| $\Delta G$ | J | Gibbs energy of cluster formation |
| $\Delta G^*$ | J | Gibbs energy of critical cluster formation |
| $\Delta t_p$ | s | nucleation pulse duration |
| $\theta_i$ | | surface coverage of the $i$-th gas component |
| $\Theta$ | - | non-dimensional surface tension |
| $\lambda$ | m | wavelength of light |
| $\lambda$ | - | non-dimensional parameter in non-isothermal nucleation |
| $\mu$ | J | chemical potential |
| $\mu_0$ | $J\,K^{-1}$ | chemical potential of the system at the initial (gaseous) state |
| $\mu^g$ | $J\,K^{-1}$ | chemical potential of vapor monomers (gaseous phase) |
| $\mu_{g,i}^A$ | $J\,K^{-1}$ | chemical potential of $i^{th}$ carrier gas molecules adsorbed at the cluster surface |
| $\mu_{g,i}^G$ | $J\,K^{-1}$ | chemical potential of $i^{th}$ carrier gas free molecules |
| $\mu^\ell$ | $J\,K^{-1}$ | chemical potential of cluster core (liquid phase) |
| $\mu^s$ | $J\,K^{-1}$ | chemical potential of cluster surface |
| $\overline{v}_1$ | $m\,s^{-1}$ | the mean molecular (thermal) velocity of component '1' |
| $\overline{v}_g$ | $m\,s^{-1}$ | mean molecular (thermal) velocity of the (carrier) gas |
| $\rho$ | $m^{-3}$ | total number density of the mixture |
| $\rho_1$ | $m^{-3}$ | partial molecular number density of component '1' |

| | | |
|---|---|---|
| $\rho_{<1>}$ | $m^{-3}$ | number density of monomers |
| $\rho_g$ | $m^{-3}$ | the molecular gas and vapor number densities |
| $\rho_{<n>}$ | $m^{-3}$ | number density of clusters with $n$ molecules |
| $\rho_\ell$ | $kg\ m^{-3}$ | bulk liquid density |
| $\rho_1^\ell$ | $kg\ m^{-3}$ | liquid density of component '1' |
| $\sigma$ | $N\ m^{-1}$ | surface tension |
| $\sigma_g$ | $N\ m^{-1}$ | the contribution of the adsorbate to the surface tension |
| $\sigma_\ell$ | $N\ m^{-1}$ | bulk liquid surface tension |
| $\sigma_{p0,i}$ | $m$ | coefficient of the linearized dependence of the surface tension on pressure for the case of pure gas $i$ |
| $\phi$ | - | fugacity coefficient |
| $\phi_w$ | $m$ | diameter of the widening |
| $\chi$ | | available adsorption sites at the condensing cluster surfaces |
| $\Psi$ | - | empirical correction function of $J_{emp}$ |

## Subscripts

| | |
|---|---|
| eq | equilibrium condition |
| emp | empirical |
| exp | experimental |
| g | (carrier) gas |
| GT | Gibbs-Thomson |
| id | ideal |
| $\ell$ | bulk liquid |
| p | pulse |
| ref | reference state |
| s | saturated (pure component) state |
| 0 | initial gaseous state |

## Superscripts

| | |
|---|---|
| A | denotes a quantity associated to the adsorbate |
| $*$ | denotes a quantity associated to critical clusters |
| eq | equilibrium condition |
| g | gaseous state |
| G | denotes a quantity associated to the free molecules |
| $\ell$ | liquid state |
| s | liquid-gaseous interface (cluster surface) |

## Operators

| | |
|---|---|
| d | derivative of |
| $\partial$ | partial derivative of |
| $\Delta$ | difference or variation of |

## Acronyms

| | |
|---|---|
| 2D | 2 dimensional |
| 3D | 3 dimensional |
| $A_1$ | optical window (laser access to test section) |
| $A_2$ | optical window (PM access to test section) |
| $A_3$ | optical window (PD access to test section) |
| AUSM | Advection Upstream Splitting Method |
| b | pressure ripple |
| C | reduction section in the LPS of Peter's tube [69] |
| CAMS | constant angle Mie scattering |
| CI | confidence interval |
| CNT | Classical Nucleation Theory |
| D | diaphragm section |
| E | expansion wave |
| ECC | expansion cloud chamber |
| EoS | Equation of State |
| $G_I$ | gas bottle of pure dry gas at the MPD |
| $G_{II}$ | gas bottle of pure dry gases ($N_2+CO_2$) |
| $G_L$ | gas bottle of pure dry gas at the LPS |
| HPS | high pressure side of the PEWT |
| $HPS_1$ | element of HPS with square-shaped section |
| $HPS_2$ | transition element of HPS from square to circular section-shape |
| $HPS_3$ | element of HPS with circular-shape section |
| IAPWS | International Association for the Properties of Water and Steam |
| LFDC | laminar flow diffusion chamber |
| LFTR | laminar flow tube reactor |
| LPS | low pressure side of the PEWT |
| MFC | mass flow controller |
| MPD | Mixture Preparation Device |
| MUSCL | Third Order Monotone Upstream - Centered Scheme |
| $n_{PEWT}$ | nucleation pulse in the PEWT |
| nP | nucleation pulse in the Peter's tube [69] |
| O | observation point ( axial position of test section) |
| $O_w$ | radial projection of O at the HPS wall |
| $P_a$ | vacuum manometer at the HPS |
| $P_b$ | vacuum manometer at the LPS |
| PD | photodiode |
| PE | piezoelectric transducer |
| PEWT | Pulse-Expansion Wave Tube |
| PM | photomultiplier |
| PR | piezoresistive transducer |
| rE | expansion wave E reflected at the HPS end-wall |
| $rE_a$ | rE reflected at $W_1$ (or C for the Peter's tube) [69] |
| $rE_{W2}$ | rE reflected at $W_2$ |
| $rSh_1$ | $sh_1$ reflection at the HPS end-wall |
| $rSh_1c$ | $rSh_1$ reflection at $W_1$ (or C for the Peter's tube) [69] |

| | |
|---|---|
| RH | relative humidity sensor |
| SAFT-VR | statistical associating fluid theory - variable range |
| SGT | square-gradient theory |
| $sat_a$ | saturator a |
| $sat_b$ | saturator b |
| sh | shock wave |
| $sh_1$ | shock wave reflection at $W_1$ (or C for the Peter's tube)[69] |
| sP | second nucleation pulse in the Peter's tube[69] |
| SSN | supersonic nozzles |
| TDCC | thermal diffusion cloud chamber |
| TPEC | two pistons expansion chamber |
| TVEC | two valve expansion chamber |
| UPC | upstream pressure controller |
| $V_b$ | bypass valve at the HPS |
| $V_{H1}$ | HPS inlet valve |
| $V_{H2}$ | HPS outlet valve |
| $V_{H3}$ | valve between HPS and $VP_H$ |
| $V_{hb}$ | metering valve at the heated box |
| $V_{L1}$ | LPS valve to $VP_L$ and $G_L$ |
| $V_{L2}$ | LPS valve to waste |
| $V_{L3}$ | LPS valve to $VP_L$ |
| $VP_H$ | HPS vacuum pump |
| $VP_L$ | LPS vacuum pump |
| W | widening at the LPS |
| $W_1$ | enlargement section of W |
| $W_2$ | reduction section of W |

# Bibliography

[1] C. T. R. Wilson and J. J. Thomson. Condensation of water vapour in the presence of dust-free air and other gases. *Philos. Trans. R. Soc. London, Ser. A*, 189:265–307, 1897. doi:10.1098/rsta.1897.0011.

[2] B. E. Wyslouzil and J. Wölk. Overview: Homogeneous nucleation from the vapor phase - the experimental science. *J. Chem. Phys.*, 145(21):211702, 2016. doi:10.1063/1.4962283.

[3] V.I. Kalikmanov, M. Betting, J. Bruining, and D.M.J. Smeulders. New developments in nucleation theory and their impact on natural gas separation. In *Proceedings of the SPE Annual Technical Conference and Exhibition, 11-14 November 2007, Anaheim, California*, pages 11–14, 2007.

[4] L. Farkas. Keimbildungsgeschwindigkeit in übersättigten dämpfen. *Zeitschrift für physikalische Chemie*, 125(1), 1927. doi:10.1515/zpch-1927-12513.

[5] R. Becker and W. Döring. Kinetische behandlung der keimbildung in übersättigten dämpfen. *Annalen der Physik*, 416(8):719–752, 1935. doi:10.1002/andp.19354160806.

[6] M. Volmer and A. Weber. Keimbildung in übersattigen Gebilden. *J. Phys. Chem.*, 119:277–301, 1926. doi:10.1515/zpch-1926-11927.

[7] Y. B. Zeldovich. On the theory of new phase formation: cavitation. *Acta Physicochem., USSR*, 18:1, 1943. doi:10.1515/9781400862979.120.

[8] J. Frenkel. A general theory of heterophase fluctuations and pretransition phenomena. *J. Chem. Phys.*, 7(7):538–547, 1939. doi:10.1063/1.1750484.

[9] W. G. Courtney. Remarks on homogeneous nucleation. *J. Chem. Phys.*, 35:2249–2250, 1961. doi:10.1063/1.1732252.

[10] G. Wilemski. The Kelvin equation and self-consistent nucleation theory. *J. Chem. Phys.*, 103:1119–1126, 1995. doi:10.1063/1.469822.

[11] D. Kashchiev. Chapter 9 - master equation. In Dimo Kashchiev, editor, *Nucleation*, pages 115–135. Butterworth-Heinemann, Oxford, 2000. doi:10.1016/B978-075064682-6/50010-X.

[12] V. I. Kalikmanov. *Nucleation Theory, Lecture Notes in Physics*. Springer, Dordrecht, 2013. ISBN 978-90-481-3642-1. doi:10.1007/978-90-481-3643-8.

[13] Howard Reiss. The kinetics of phase transitions in binary systems. *J. Chem. Phys.*, 18(6):840–848, 1950. doi:10.1063/1.1747784.

[14] J.L. Katz, H. Saltsburg, and H. Reiss. Nucleation in associated vapors. *Journal of Colloid and Interface Science*, 21(5):560–568, 1966. doi:10.1016/0095-8522(66)90053-5.

[15] J. O. Hirschfelder. Kinetics of homogeneous nucleation on many-component systems. *J. Chem. Phys.*, 61(7):2690–2694, 1974. doi:10.1063/1.1682400.

[16] W. Studziński, G. H. Spiegel, and R. A. Zahoransky. Binary nucleation and condensation in associated vapors. *J. Chem. Phys.*, 84(7):4008–4014, 1986. doi:10.1063/1.450111.

[17] A. Jaecker-Voirol, P. Mirabel, and H. Reiss. Hydrates in supersaturated binary sulfuric acid–water vapor: A reexamination. *J. Chem. Phys.*, 87(8):4849–4852, 1987. doi:10.1063/1.452847.

[18] J. Lothe and G. M. Pound. Reconsiderations of nucleation theory. *J. Chem. Phys.*, 36(8):2080–2085, 1962. doi:10.1063/1.1732832.

[19] M. Blander and J. L. Katz. The thermodynamics of cluster formation in nucleation theory. *J. Stat. Phys.*, 4(1):55–59, 1972. doi:10.1007/BF01008471.

[20] S. L. Girshick and C.-P. Chiu. Kinetic nucleation theory: A new expression for the rate of homogeneous nucleation from an ideal supersaturated vapor. *J. Chem. Phys.*, 93(2):1273–1277, 1990. doi:10.1063/1.459191.

[21] K. Nishioka and I. Kusaka. Thermodynamic formulas of liquid phase nucleation from vapor in multicomponent systems. *J. Chem. Phys.*, 96(7):5370–5376, 1992. doi:10.1063/1.462721.

[22] H. Reiss, W. K. Kegel, and J. L. Katz. Resolution of the problems of replacement free energy, $1/S$, and internal consistency in nucleation theory by consideration of the length scale for mixing entropy. *Phys. Rev. Lett.*, 78:4506–4509, 1997. doi:10.1103/PhysRevLett.78.4506.

[23] A. Obeidat and G. Wilemski. Gradient theory of nucleation in polar fluids. *Atmospheric Research*, 82(3):481–488, 2006. doi:10.1016/j.atmosres.2006.02.005. 16th International Conference on Nucleation and Atmospheric Aerosols.

[24] V. I. Kalikmanov. Mean-field kinetic nucleation theory. *J. Chem. Phys.*, 124(12):124505, 2006. doi:10.1063/1.2178812.

[25] V. I. Kalikmanov. Binary nucleation beyond capillarity approximation. *Phys. Rev. E*, 81:050601–050604, 2010. doi:10.1103/PhysRevE.81.050601.

[26] Ø. Wilhelmsen, D. Bedeaux, and D. Reguera. Communication: Tolman length and rigidity constants of water and their role in nucleation. *J. Chem. Phys.*, 142(17):171103, 2015. doi:10.1063/1.4919689.

[27] X. C. Zeng and D. W. Oxtoby. Binary homogeneous nucleation theory for the gas–liquid transition: A nonclassical approach. *J. Chem. Phys.*, 95(8):5940–5947, 1991. doi:10.1063/1.461615.

[28] C. L. Weakliem and H. Reiss. Toward a molecular theory of vapor phase nucleation. iv. rate theory using the modified liquid drop model. *J. Chem. Phys.*, 101(3):2398–2406, 1994. doi:10.1063/1.467680.

[29] B. Senger, P. Schaaf, D. S. Corti, R. Bowles, J.-C. Voegel, and H. Reiss. A molecular theory of the homogeneous nucleation rate. i. formulation and fundamental issues. *J. Chem. Phys.*, 110 (13):6421–6437, 1999. doi:10.1063/1.478545.

[30] D. Reguera, R. K. Bowles, Y. Djikaev, and H. Reiss. Phase transitions in systems small enough to be clusters. *J. Chem. Phys.*, 118(1):340–353, 2003. doi:10.1063/1.1524192.

[31] R. Zandi, D. Reguera, and H. Reiss. Nucleation rates in a new phenomenological model. *J. Phys. Chem. B*, 110(44):22251–22260, 2006. doi:10.1021/jp057418+.

[32] J. Wedekind, D. Reguera, and R. Strey. Finite-size effects in simulations of nucleation. *J. Chem. Phys.*, 125(21):214505, 2006. doi:10.1063/1.2402167.

[33] J. Wedekind and D. Reguera. What is the best definition of a liquid cluster at the molecular scale? *J. Chem. Phys.*, 127(15):154516, 2007. doi:10.1063/1.2786457.

[34] G. K. Schenter, S. M. Kathmann, and B. C. Garrett. Dynamical nucleation theory: A new molecular approach to vapor-liquid nucleation. *Phys. Rev. Lett.*, 82:3484–3487, Apr 1999. doi:10.1103/PhysRevLett.82.3484.

[35] S. M. Kathmann, G. K. Schenter, and B. C. Garrett. Multicomponent dynamical nucleation theory and sensitivity analysis. *J. Chem. Phys.*, 120(19):9133–9141, 2004. doi:10.1063/1.1695323.

[36] A. Langsdorf. A continuously sensitive diffusion cloud chamber. *Review of Scientific Instruments*, 10(3):91–103, 1939. doi:10.1063/1.1751494.

[37] J. L. Katz and B. J. Ostermier. Diffusion cloud-chamber investigation of homogeneous nucleation. *The Journal of Chemical Physics*, 47(2):478–487, 1967. doi:10.1063/1.1711920.

[38] R. H. Heist and H. Reiss. Investigation of the homogeneous nucleation of water vapor using a diffusion cloud chamber. *J. Chem. Phys.*, 59(2):665–671, 1973. doi:10.1063/1.1680073.

[39] D. Brus, V. Ždímal, and J. Smolík. Homogeneous nucleation rate measurements in supersaturated water vapor. *J. Chem. Phys.*, 129(17):174501, 2008. doi:10.1063/1.3000629.

[40] D. Brus, V. Ždímal, and H. Uchtmann. Homogeneous nucleation rate measurements in supersaturated water vapor ii. *J. Chem. Phys.*, 131(7):074507, 2009. doi:10.1063/1.3211105.

[41] V. B. Mikheev, P. M. Irving, N. S. Laulainen, S. E. Barlow, and V. V. Pervukhin. Laboratory measurement of water nucleation using a laminar flow tube reactor. *J. Chem. Phys.*, 116(24): 10772–10786, 2002. doi:10.1063/1.1480274.

[42] A. A. Manka, D. Brus, A. Hyvärinen, H. Lihavainen, J. Wölk, and R. Strey. Homogeneous water nucleation in a laminar flow diffusion chamber. *J. Chem. Phys.*, 132(24):244505, 2010. doi:10.1063/1.3427537.

[43] J. Wölk and R. Strey. Homogeneous nucleation of $H_2O$ and $D_2O$ in comparison: the isotope effect. *J. Phys. Chem. B*, 105:11683–11701, 2001. doi:10.1021/jp0115805.

[44] V. Holten, D. G. Labetski, and M. E. H. van Dongen. Homogeneous nucleation of water between 200 and 240 k: New wave tube data and estimation of the tolman length. *J. Chem. Phys.*, 123: 104505, 2005. doi:10.1063/1.2018638.

[45] Y. Viisanen, R. Strey, and H. Reiss. Homogeneous nucleation rates for water. *J. Chem. Phys.*, 99(6):4680–4692, 1993. doi:10.1063/1.466066.

[46] R. C. Miller, R. J. Anderson, J. L. Kassner, and D. E. Hagen. Homogeneous nucleation rate measurements for water over a wide range of temperature and nucleation rate. *J. Chem. Phys.*, 78(6):3204–3211, 1983. doi:10.1063/1.445236.

[47] Y. J. Kim, B. E. Wyslouzil, G. Wilemski, J. Wölk, and R. Strey. Isothermal nucleation rates in supersonic nozzles and the properties of small water clusters. *J. Phys. Chem. A*, 108(20): 4365–4377, 2004. doi:10.1021/jp037030j.

[48] A.-P. Hyvärinen, D. Brus, J. Wedekind, and H. Lihavainen. How ambient pressure influences water droplet nucleation at tropospheric conditions. *Geophysical Research Letters*, 37(21), 2010. doi:10.1029/2010GL045013.

[49] E. F. Allard and J. L. Kassner. New cloud-chamber method for the determination of homogeneous nucleation rates. *J. Chem. Phys.*, 42(4):1401–1405, 1965. doi:10.1063/1.1696129.

[50] L. B. Allen and J. L. Kassner. The nucleation of water vapor in the absence of particulate matter and ions. *Journal of Colloid and Interface Science*, 30(1):81–93, 1969. doi:10.1016/0021-9797(69)90381-6.

[51] J. L. Schmitt. Precision expansion cloud chamber for homogeneous nucleation studies. *Review of Scientific Instruments*, 52(11):1749–1754, 1981. doi:10.1063/1.1136524.

[52] P. E. Wagner and R. Strey. Homogeneous nucleation rates of water vapor measured in a two-piston expansion chamber. *J. Phys. Chem.*, 85:2694–2698, 1981. doi:10.1021/j150618a026.

[53] R. Strey and P. E. Wagner. Homogeneous nucleation rates measured in a two-piston expansion chamber. *Journal of Aerosol Science*, 12(3):199–201, 1981. doi:10.1016/0021-8502(81)90093-8.

[54] R. Strey, P. E. Wagner, and Y. Viisanen. The problem of measuring homogeneous nucleation rates and the molecular contents of nuclei: progress in the form of nucleation pulse measurements. *J. Phys. Chem.*, 98(32):7748–7758, 1994. doi:10.1021/j100083a003.

[55] P. E. Wagner. A constant-angle mie scattering method (CAMS) for investigation of particle formation processes. *Journal of colloid and interface science*, 105(2):456–467, 1985. doi:10.1016/0021-9797(85)90319-4.

[56] R. Strey, Y. Viisanen, and P. E. Wagner. Measurement of the molecular content of binary nuclei. iii. use of the nucleation rate surfaces for the water-n-alcohol series. *J. Chem. Phys.*, 103(10): 4333–4345, 1995. doi:10.1063/1.470672.

[57] Y. Viisanen and R. Strey. Composition of critical clusters in ternary nucleation of water–n-nonane–n-butanol. *J. Chem. Phys.*, 105(18):8293–8299, 1996. doi:10.1063/1.472683.

[58] Y. Viisanen, P. E. Wagner, and R. Strey. Measurement of the molecular content of binary nuclei. iv. use of the nucleation rate surfaces for the n-nonane-n-alcohol series. *J. Chem. Phys.*, 108 (10):4257–4266, 1998. doi:10.1063/1.475825.

[59] P. E. Wagner and R. Strey. Two pathway homogeneous nucleation in supersaturated water–n-nonane vapor mixtures. *J. Phys. Chem. B*, 105(47):11656–11661, 2001. doi:10.1021/jp011460x.

[60] K. N. H. Looijmans and M. E. H. van Dongen. A pulse-expansion wave tube for nucleation studies at high pressures. *Exp. Fluids*, 23:54–63, 1997. doi:10.1007/s003480050086.

[61] M. A. L. J. Fransen, E. Sachteleben, J. Hrubý, and D. M. J. Smeulders. On the growth of homogeneously nucleated water droplets in nitrogen: an experimental study. *Exp. Fluids*, 55(7): 1780, 2014. doi:10.1007/s00348-014-1780-y.

[62] Kl. Oswatitsch. Kondensationserscheinungen in Überschalldüsen . *ZAMM - Journal of Applied Mathematics and Mechanics / Zeitschrift für Angewandte Mathematik und Mechanik*, 22(1): 1–14, 1942. doi:10.1002/zamm.19420220102.

[63] B. E. Wyslouzil, G. Wilemski, M. G. Beals, and M. B. Frish. Effect of carrier gas pressure on condensation in a supersonic nozzle. *Physics of Fluids*, 6(8):2845–2854, 1994. doi:10.1063/1.868107.

[64] C. H. Heath, K. Streletzky, B. E. Wyslouzil, J. Wölk, and R. Strey. H2O–D2O condensation in a supersonic nozzle. *J. Chem. Phys.*, 117(13):6176–6185, 2002. doi:10.1063/1.1502644.

[65] S. Sinha, B. E. Wyslouzil, and G. Wilemski. Modeling of h2o/d2o condensation in supersonic nozzles. *Aerosol Science and Technology*, 43(1):9–24, 2009. doi:10.1080/02786820802441771.

[66] B. E. Wyslouzil, G. Wilemski, R. Strey, S. Seifert, and R. E. Winans. Small angle x-ray scattering measurements probe water nanodroplet evolution under highly non-equilibrium conditions. *Phys. Chem. Chem. Phys.*, 9:5353–5358, 2007. doi:10.1039/B709363B.

[67] A. Manka, H. Pathak, S. Tanimura, J. Wölk, R. Strey, and B. E. Wyslouzil. Freezing water in no-man's land. *Phys. Chem. Chem. Phys.*, 14:4505–4516, 2012. doi:10.1039/C2CP23116F.

[68] D. Barschdorff. Carrier gas effects on homogeneous nucleation of water vapor in a shock tube. *The Physics of Fluids*, 18(5):529–535, 1975. doi:10.1063/1.861185.

[69] F. Peters. A new method to measure homogeneous nucleation rates in shock tubes. *Exp. Fluids*, 1:143–148, 1983. doi:10.1007/bf00272013.

[70] K. N. H. Looijmans, P. C. Kriesels, and M. E. H. van Dongen. Gasdynamic aspects of a modified expansion-shock tube for nucleation and condensation studies. *Exp. Fluids*, 15(1):61–64, 1993. doi:10.1007/BF00195596.

[71] K. N. H. Looijmans, C. C. M. Luijten, and M. E. H. van Dongen. Binary nucleation rate measurements of n-nonane/methane at high pressures. *J. Chem. Phys.*, 103:1714–1717, 1995. doi:10.1063/1.469742.

[72] C. C. M. Luijten, O. D. E. Baas, and M. E. H. van Dongen. Homogeneous nucleation rates for *n*-pentanol from expansion wave tube experiments. *J. Chem. Phys.*, 106:4152–4156, 1997. doi:10.1063/1.473125.

[73] C. C. M. Luijten, K. J. Bosschaart, and M. E. H. van Dongen. High pressure nucleation in water/nitrogen systems. *J. Chem. Phys.*, 106:8116–8123, 1997. doi:10.1063/1.473818.

[74] C. C. M. Luijten, O. D. E. Baas, and M. E. H. van Dongen. Homogeneous nucleation rates for *n*-pentanol from expansion wave tube experiments. *J. Chem. Phys.*, 106:4152–4156, 1997. doi:10.1063/1.473125.

[75] C. C. M. Luijten, M. E. H. van Dongen, and L. E. Stormbom. Pressure influence in capacitive humidity measurement. *Sens. Act.: B. Chem.*, 49:279–282, 1998. doi:10.1016/s0925-4005(98)00148-8.

[76] C. C. M. Luijten, R. G. P. van Hooy, J. W. F. Janssen, and M. E. H. van Dongen. Multicomponent nucleation and droplet growth in natural gas. *J. Chem. Phys.*, 109:3553, 1998. doi:10.1063/1.476950.

[77] C. C. M. Luijten and M. E. H. van Dongen. Nucleation at high pressure. I. Theoretical considerations. *J. Chem. Phys*, 111:8524–8534, 1999. doi:10.1063/1.480193.

[78] C. C. M. Luijten, P. Peeters, and M. E. H. van Dongen. Nucleation at high pressure. II. Wave tube data and analysis. *J. Chem. Phys*, 111:8535–8544, 1999. doi:10.1063/1.480194.

[79] P. Peeters, J. Hrubý, and M. E. H. van Dongen. High pressure nucleation experiments in binary and ternary mixtures. *J. Phys. Chem. B*, 105:11763–11771, 2001. doi:10.1021/jp011670+.

[80] P. Peeters, C. C. M. Luijten, and M. E. H. van Dongen. Transitional droplet growth and diffusion coefficients. *Int. J. Heat Mass Transfer*, 44:181–193, 2001. doi:10.1016/s0017-9310(00)00098-3.

[81] P. Peeters, J.J.H. Gielis, and M.E.H. van Dongen. The nucleation behavior of supercooled water vapor in helium. *J. Chem. Phys.*, 117:5647–5653, 2002. doi:10.1063/1.1501885.

[82] P. Peeters, G. Pieterse, J. Hrubý, and M. E. H. van Dongen. Multi-component droplet growth. I. experiments with supersaturated *n*-nonane vapor and water vapor in methane. *Phys. Fluids*, 16: 2567–2574, 2004. doi:10.1063/1.1751191.

[83] P. Peeters, J. Hrubý, and M.E.H. van Dongen. Multi-component droplet growth. II. a theoretical model. *Phys. Fluids*, 16:2575–2586, 2004. doi:10.1063/1.1751192.

[84] V. Holten and M.E.H. van Dongen. Homogeneous water nucleation and droplet growth in methane and carbon dioxide mixtures at 235 K and 10 bar. *J. Chem. Phys.*, 132:204504, 2010. doi:10.1063/1.3432623.

[85] M. A. L. J. Fransen, J. Hrubý, D. M. J. Smeulders, and M. E. H. van Dongen. On the effect of pressure and carrier gas on homogeneous water nucleation. *J. Chem. Phys.*, 142(16):164307, 2015. doi:10.1063/1.4919249.

[86] B. N. Hale. Temperature dependence of homogeneous nucleation rates for water: Near equivalence of the empirical fit of Wölk and Strey, and the scaled nucleation model. *J. Chem. Phys.*, 122(20):204509, 2005. doi:10.1063/1.1906213.

[87] J. C. Barrett. A stochastic simulation of nonisothermal nucleation. *J. Chem. Phys.*, 128(16): 164519, 2008. doi:10.1063/1.2913051.

[88] C.C.M. Luijten. *Nucleation and droplet growth at high pressure*. PhD thesis, Technische Universiteit Eindhoven - Department of Applied Physics, 1998.

[89] J. M. Prausnitz, R. N. Lichtenthaler, and E. G. de Azevedo. *Molecular Thermodynamics of Fluid-Phase Equilibria*. Prentice Hall Inc., 3rd edition edition, 1999.

[90] A. V. Plyasunov and Everett L. Shock. Second cross virial coefficients for interactions involving water. critical data compilation. *Journal of Chemical & Engineering Data*, 48:808–821, 2003. doi:10.1021/je034046u.

[91] E. W. Lemmon, , Ian H. Bell, M. L. Huber, and M. O. McLinden. NIST Standard Reference Database 23: Reference Fluid Thermodynamic and Transport Properties-REFPROP, Version 10.0, National Institute of Standards and Technology, 2018.

[92] V. Holten. *Water nucleation: wave tube experiments and theoretical considerations*. PhD thesis, Technische Universiteit Eindhoven - Department of Applied Physics, 2009.

[93] S.-X. Hou, G. C. Maitland, and J. P. M. Trusler. Measurement and modeling of the phase behavior of the (carbon dioxide+water) mixture at temperatures from 298.15k to 448.15k. *The Journal of Supercritical Fluids*, 73:87–96, 2013. ISSN 0896–8446. doi:10.1016/j.supflu.2012.11.011.

[94] W. S. Dodds, L. F. Stutzman, and B. J. Sollami. Carbon dioxide solubility in water. *Industrial & Engineering Chemistry Chemical & Engineering Data Series*, 1(1):92–95, 1956. doi:10.1021/i460001a018.

[95] A. H. Harvey and E. W. Lemmon. Correlation for the second virial coefficient of water. *Journal of Physical and Chemical Reference Data*, 33(1):369–376, 2004. doi:10.1063/1.1587731.

[96] Andrew J. Schultz, David A. Kofke, and Allan H. Harvey. Molecular-based virial coefficients of $CO_2$-$H_2O$ mixtures. *AIChE Journal*, 61(9):3029–3037, 2015. doi:10.1002/aic.14880.

[97] C. R. Coan and A. D. King. Solubility of water in compressed carbon dioxide, nitrous oxide, and ethane. evidence for hydration of carbon dioxide and nitrous oxide in the gas phase. *Journal of the American Chemical Society*, 93(8):1857–1862, 1971. doi:10.1021/ja00737a004.

[98] Richard J. Wheatley and Allan H. Harvey. Intermolecular potential energy surface and second virial coefficients for the water–$CO_2$ dimer. *J. Chem. Phys.*, 134(13):134309, 2011. doi:10.1063/1.3574345.

[99] O. Kunz and W. Wagner. The GERG-2008 wide-range equation of state for natural gases and other mixtures: An expansion of GERG-2004. *Journal of Chemical & Engineering Data*, 57 (11):3032–3091, 2012. doi:10.1021/je300655b.

[100] H. B. Brugge, C.-A. Hwang, W. J. Rogers, J. C. Holste, K. R. Hall, W. Lemming, G. J. Esper, K. N. Marsh, and B. E. Gammon. Experimental cross virial coefficients for binary mixtures of carbon dioxide with nitrogen, methane and ethane at 300 and 320 k. *Physica A: Statistical Mechanics and its Applications*, 156(1):382–416, 1989. doi:10.1016/0378-4371(89)90131-3.

[101] T. L. Cottrell, R. A. Hamilton, and R. P. Taubinger. The second virial coefficients of gases and mixtures. Part 2.—mixtures of carbon dioxide with nitrogen, oxygen, carbon monoxide, argon and hydrogen. *Trans. Faraday Soc.*, 52:1310–1312, 1956. doi:10.1039/TF9565201310.

[102] M. P. Hodges, R. J. Wheatley, and A. H. Harvey. Intermolecular potential and second virial coefficient of the water–helium complex. *J. Chem. Phys.*, 116(4):1397–1405, 2002. doi:10.1063/1.1421065.

[103] M. P. Hodges, R. J. Wheatley, and A. H. Harvey. Intermolecular potentials and second virial coefficients of the water–neon and water–argon complexes. *J. Chem. Phys.*, 117(15):7169–7179, 2002. doi:10.1063/1.1504703.

[104] J. J. Hurly and M. R. Moldover. Ab initio values of the thermophysical properties of helium as standards. *J. Res. Natl. Inst. Stand. Technol.*, 105(5), 2000. doi:10.6028/jres.105.054.

[105] B. Schramm, E. Elias, L. Kern, Gh. Natour, A. Schmitt, and Ch. Weber. Precise measurements of second virial coefficients of simple gases and gas mixtures in the temperature range below 300 k. *Berichte der Bunsengesellschaft für physikalische Chemie*, 95(5):615–621, 1991. doi:10.1002/bbpc.19910950513.

[106] W. Zhang, J. A. Schouten, H. M. Hinze, and M. Jaeschke. Pvt-x behavior of helium-nitrogen mixtures from 270 to 353 k and up to 280 bar. *Journal of Chemical & Engineering Data*, 37(1): 114–119, 1992. doi:10.1021/je00005a030.

[107] B. Schramm and W. Müller. Messungen des zweiten virialkoeffizienten von gasen und gasmischungen bei zimmertemperatur mit einer expansionsapparatur. *Berichte der Bunsengesellschaft für physikalische Chemie*, 86(2):110–112, 1982. doi:10.1002/bbpc.19820860204.

[108] M. Duschek, R. Kleinrahm, W. Wagner, and M. Jaeschke. Measurement and correlation of the (pressure, density, temperature) relation of nitrogen in the temperature range from 273.15 to 323.15 k at pressures up to 8 mpa. *J. Chem. Thermodyn.*, 20(9):1069–1077, 1988. doi:10.1016/0021-9614(88)90113-9.

[109] P. J. Mcelroy and S. S. Buchanan. Second virial coefficients of fuel-gas components: (carbon monoxide + nitrogen) and (carbon monoxide + ethene). *J. Chem. Thermodyn.*, 27(7):755–761, 1995. doi:10.1006/jcht.1995.0078.

[110] M. R. Patel, L. Lane Joffrion, and P. T. Eubank. A simple procedure for estimating virial coefficients from burnett pvt data. *AIChE Journal*, 34(7):1229–1232, 1988. doi:10.1002/aic.690340722.

[111] M. P. Hodges, R. J. Wheatley, and A. H. Harvey. Intermolecular potential and second virial coefficient of the water–helium complex. *J. Chem. Phys.*, 116(4):1397–1405, 2002. doi:10.1063/1.1421065.

[112] A. S. Tulegenov, R. J. Wheatley, M. P. Hodges, and A. H. Harvey. Intermolecular potential and second virial coefficient of the water-nitrogen complex. *J. Chem. Phys.*, 126(9):094305, 2007. doi:10.1063/1.2446843.

[113] J. Wedekind, A.-P. Hyvärinen, D. Brus, and D. Reguera. Unraveling the "pressure effect" in nucleation. *Phys. Rev. Lett.*, 101:125703, 2008. doi:10.1103/physrevlett.101.125703.

[114] K. N. H. Looijmans, C. C. M. Luijten, G. C. J. Hofmans, and M. E. H. van Dongen. Classical binary nucleation theory applied to the real mixture n-nonane/methane at high pressures. *J. Chem. Phys.*, 102(11):4531–4537, 1995. doi:10.1063/1.469501.

[115] H. Vehkamäki. *Classical nucleation theory in multicomponent systems*. Springer, Heidelberg, Germany, 1st edition, 2006. doi:10.1007/3-540-31218-8.

[116] M. M. Campagna, M. E. H. van Dongen, and D. M. J. Smeulders. Novel test section for homogeneous nucleation studies in a pulse expansion wave tube: experimental verification and gasdynamic 2d numerical model. *Exp. Fluids*, 61(4):108, 2020. doi:10.1007/s00348-020-02945-3.

[117] J. Hrubý. New mixture-preparation device for investigation of nucleation and droplet growth in natural gas-like systems. Technical Report R-1489-D, Eindhoven University of Technology, 1999.

[118] M.I. Mishchenko, L.D. Travis, and A.A. Lacis. *Scattering, absorption, and emission of light by small particles*. Cambridge University Press, 1st edition, 2002.

[119] X. Luo. *Unsteady flows with phase transition, p.64-66*. PhD thesis, Department of Applied Physics, 2004.

[120] K. R. Arun, H. D. Kim, and T. Setoguchi. Effect of finite diaphragm rupture process on microshock tube flows. *J. Fluids Eng.*, 135(8):081203, 2013. doi:10.1115/1.4024196.

[121] M. M. Campagna, J. Hrubý, M. E. H. van Dongen, and D. M. J. Smeulders. Homogeneous water nucleation: Experimental study on pressure and carrier gas effects. *J. Chem. Phys.*, 153 (16):164303, 2020. doi:10.1063/5.0021477.

[122] J. Feder, K. C. Russell, J. Lothe, and G. M. Pound. Homogeneous nucleation and growth of droplets in vapours. *Adv. Phys.*, 15:111–178, 1966. doi:10.1080/00018736600101264.

[123] J. Malila and A. Laaksonen. Properties of supercooled water clusters from nucleation rate data with the effect of non-ideal vapour phase. In R. Span and I. Weber, editors, *Proceedings–ICPWS XV*, Berlin, 2008. VDI–The Association of German Engineers.

[124] D. M. Murphy and T. Koop. Review of the vapour pressures of ice and supercooled water for atmospheric applications. *Q. J. R. Meterol. Soc.*, 131:1539–1565, 2005. doi:10.1256/qj.04.94.

[125] W. Wagner and A. Pruss. The IAPWS formulation 1995 for the thermodynamic properties of ordinary water substance for general and scientific use. *J. Phys. Chem. Ref. Data*, 31:387–535, 2002. doi:10.1063/1.1461829.

[126] D. W. Oxtoby and D. Kashchiev. A general relation between the nucleation work and the size of the nucleus in multicomponent nucleation. *J. Chem. Phys.*, 100(10):7665–7671, 1994. doi:10.1063/1.466859.

[127] D. Kashchiev. On the relation between nucleation work, nucleus size, and nucleation rate. *J. Chem. Phys.*, 76(10):5098–5102, 1982. doi:10.1063/1.442808.

[128] W. L. Masterton, J. Bianchi, and E. J. Slowinski Jr. Surface tension and adsorption in gas-liquid systems at moderate pressures. *J. Phys. Chem.*, 67:615–618, 1963. doi:10.1021/j100797a018.

[129] R. Massoudi and A. D. King Jr. Effect of pressure on the surface tension of water. Adsorption of low molecular weight gases on water at 25°. *J. Phys. Chem.*, 78:2262–2266, 1974. doi:10.1021/j100615a017.

[130] G. Wiegand and E. U. Franck. Interfacial tension between water and non-polar fluids up to 473 K and 2800 bar. *Ber. Bunsenges. Phys. Chem.*, 98:809–817, 1994. doi:10.1002/bbpc.19940980608.

[131] Y. T. F. Chow, D. K. Eriksen, A. Galindo, A. J. Haslam, G. Jackson, G. C. Maitland, and J. P. M. Trusler. Interfacial tensions of systems comprising water, carbon dioxide and diluent gases at high pressures: Experimental measurements and modelling with saft-vr mie and square-gradient theory. *Fluid Phase Equilibria*, 407:159–176, 2016. doi:10.1016/j.fluid.2015.07.026.

[132] E. W. Hough, B. B. Wood Jr., and M. J. Rzasa. Adsorption at water-helium, -methane, and -nitrogen interfaces at pressures to 15,000 psia. *J. Phys. Chem.*, 56:996–999, 1952. doi:10.1021/j150500a017.

[133] J. W. Gibbs. *Collected Works I*. Yale University Press, New Haven, United States, 1st edition, 1948.

[134] A. L. McClellan and H. F. Harnsberger. Cross-sectional areas of molecules adsorbed on solid surfaces. *Journal of Colloid and Interface Science*, 23(4):577–599, 1967. doi:10.1016/0021-9797(67)90204-4.

[135] B. E. Wyslouzil and J. H. Seinfeld. Nonisothermal homogeneous nucleation. *J. Chem. Phys.*, 97:2661–2670, 1992. doi:10.1063/1.463055.

[136] J. H. ter Horst, D. Bedeaux, and S. Kjelstrup. The role of temperature in nucleation processes. *J. Chem. Phys.*, 134:054703, 2011. doi:10.1063/1.3544689.

[137] J. C. Barrett, C. F. Clement, and I. J. Ford. Energy fluctuations in homogeneous nucleation theory for aerosols. *Journal of Physics A: Mathematical and General*, 26(3):529–548, feb 1993. doi:10.1088/0305-4470/26/3/016.

[138] J. C. Barrett. Equilibrium and steady-state distributions of vapour clusters in nucleation theory. *Journal of Physics A: Mathematical and General*, 27(15):5053–5068, aug 1994. doi:10.1088/0305-4470/27/15/007.

[139] V. A. Rabinovich and V. G. Beketov. *Moist gases: thermodynamic properties.* New York, Begell House, 1995.

[140] J. A. Fisk and J. L. Katz. Condensation of supersaturated vapors. x. pressure and nonideal gas effects. *J. Chem. Phys.*, 104(21):8649–8656, 1996. doi:10.1063/1.471553.

[141] J. Hrubý, M. Duska, T. Nemec, and M. Kolovratnık. Nucleation rates of droplets in supersaturated steam and water vapour–carrier gas mixtures between 200 and 450k. *Institution of Mechanical Engineers*, 232(5):536–549, 2018. doi:10.1177/0957650918770939.

[142] M. M. Campagna, J. Hrubý, M. E. H. van Dongen, and D. M. J. Smeulders. Homogeneous water nucleation in carbon dioxide–nitrogen mixtures: Experimental study on pressure and carrier gas effects. *J. Chem. Phys.*, 154(15):154301, 2021. doi:10.1063/5.0044898.

[143] C. Li, J. Krohn, M. Lippe, and R. Signorell. How volatile components catalyze vapor nucleation. *Science Advances*, 7(3), 2021. doi:10.1126/sciadv.abd9954.

[144] Mark D. Zelinka, Timothy A. Myers, Daniel T. McCoy, Stephen Po-Chedley, Peter M. Caldwell, Paulo Ceppi, Stephen A. Klein, and Karl E. Taylor. Causes of higher climate sensitivity in cmip6 models. *Geophysical Research Letters*, 47(1), 2020. doi:10.1029/2019GL085782.

[145] A. Hebach, A. Oberhof, N. Dahmen, A. Kögel, H. Ederer, and E. Dinjus. Interfacial tension at elevated pressures - measurements and correlations in the water + carbon dioxide system. *Journal of Chemical & Engineering Data*, 47(6):1540–1546, 2002. doi:10.1021/je025569p.

[146] B. Chun and G. T. Wilkinson. Interfacial tension in high-pressure carbon dioxide mixtures. *Industrial & Engineering Chemistry Research*, 34(12):4371–4377, 1995. doi:10.1021/ie00039a029.

[147] Y. T. F. Chow, G. C. Maitland, and J. P. M. Trusler. Interfacial tensions of the $(CO_2+N_2+H_2O)$ system at temperatures of 298 to 448 K and pressures up to 40 MPa. *J. Chem. Thermodyn.*, 93: 392–403, 2016. doi:10.1016/j.jct.2015.08.006.

[148] A. S. Tulegenov, R. J. Wheatley, M. P. Hodges, and A. H. Harvey. Intermolecular potential and second virial coefficient of the water-nitrogen complex. *J. Chem. Phys.*, 126(9):094305, 2007. doi:10.1063/1.2446843.

[149] M. M. Campagna, J. Hrubý, M. E. H. van Dongen, and D. M. J. Smeulders. Critical cluster composition from homogeneous nucleation data: application to water in carbon dioxide–nitrogen carrier gases. *Exp. Fluids*, 62(9):189, 2021. doi:10.1007/s00348-021-03270-z.

[150] D. W. Oxtoby and A. Laaksonen. Some consequences of the nucleation theorem for binary fluids. *J. Chem. Phys.*, 102(17):6846–6850, 1995. doi:10.1063/1.469121.

[151] M. Abramowitz and I. A. Stegun. *Handbook of mathematical functions.* Dover publications, New York, United States, 9th edition, 1970.

# Curriculum Vitae

| | |
|---|---|
| 15 January 1984 | Born in San Giovanni Rotondo (FG), Italy |

## Education

| | |
|---|---|
| Sep 1997 - July 2002 | Scientific High School diploma (8.5/10)<br>Liceo Scientifico Checchia Rispoli<br>San Severo (FG), Italy |
| Sep 2003 - Nov 2007 | Bachelor's Degree in Mechanical Engineering (9/10)<br>Department of Mechanical Engineering<br>Polytechnic University of Bari<br>Bari, Italy |
| Sep 2007 - July 2014 | Master's Degree in Mechanical Engineering (10/10)<br>Department of Mechanical Engineering<br>Polytechnic University of Bari<br>Bari, Italy |
| Oct 2015 - June 2016 | Research Master in Fluid Dynamics (cum laude)<br>Environmental and Applied Fluid Dynamics group<br>von Karman Institute for Fluid Dynamics<br>Sint-Genesius-Rode, Belgium |
| Jan 2017 - Sep 2021 | PhD Candidate<br>Department of Mechanical Engineering<br>Energy Technology & Fluid Dynamics group<br>Eindhoven University of Technology<br>Eindhoven, The Netherlands |

## Work Experience

| | |
|---|---|
| July 2014 - Oct 2014 | Post-Graduate Researcher<br>Department of Mechanical Engineering<br>Polytechnic University of Bari<br>Bari, Italy |

| Nov 2014 - Aug 2015 | Design and Production Engineer |
| | Nuova Ci. Mo.Sa Dauna |
| | Castelnuovo della Daunia (FG), Italy |

| July 2016 - Dec 2016 | Researcher |
| | Environmental and Applied Fluid Dynamics group |
| | von Karman Institute for Fluid Dynamics |
| | Sint-Genesius-Rode, Belgium |

## List of Publications

- M.M. Campagna, J. Hrubý, M.E.H. van Dongen, and D.M.J. Smeulders. Critical cluster composition from homogeneous nucleation data: application to water in carbon dioxide–nitrogen carrier gases. *Exp. Fluids* 62(9):189, 2021. doi:10.1007/s00348-021-03270-z

- M.M. Campagna, J. Hrubý, M.E.H. van Dongen, and D.M.J. Smeulders. Homogeneous water nucleation in carbon dioxide-nitrogen mixtures: Experimental study on pressure and carrier gas effects. *J. Chem. Phys.* 154(15):154301, 2021. doi:10.1063/5.0044898

- M.M. Campagna, J. Hrubý, M.E.H. van Dongen, and D.M.J. Smeulders. Homogeneous water nucleation: Experimental study on pressure and carrier gas effects. *J. Chem. Phys.* 153(16):164303, 2020. doi:10.1063/5.0021477

- M.M. Campagna, M.E.H. van Dongen, and D.M.J. Smeulders. Novel test section for homogeneous nucleation studies in a Pulse Expansion Wave Tube. Experimental verification and gas dynamic 2D numerical model. *Exp. Fluids* 61(4):108, 2020. doi:10.1007/s00348-020-02945-3

- M.M. Campagna, G. Dinardo, L. Fabbiano, and G. Vacca. Fluid flow measurements by means of vibration monitoring. *Meas. Sci. Technol.* 26 115306, 2015. doi:10.1088/0957-0233/26/11/115306